Prediction of the Ultimate Behaviour of Tubular Joints in Offshore Jacket Structures Using Nonlinear Finite Element Methods

by

Hartanta Tarigan

A Thesis submitted for the degree of
Doctor of Philosophy

Marine Technology

The University of Newcastle upon Tyne
1992

Abstract

Tubular joints are of great importance in offshore jacket structures. This thesis examines the ultimate state behaviour of tubular joints in offshore structures. In particular, the validity of a nonlinear finite element method was investigated and it was subsequently used to determine the ultimate load behaviour of a range of tubular joints.

A geometrically nonlinear, eight node isoparametric shell finite element program is developed which allows six degrees of freedom per node. The material laws in the model include elastic and elastoplastic multilayer solution with integration across the thickness. Strain hardening effects can be included.

The nonlinear solution strategies are based on the Newton-Raphson Method. The load is applied in increments where for each step, equilibrium iterations are carried out to establish equilibrium, subject to a given error criterion. To cross the limit point and to select load increments, iterative solution strategies such as the arc length and automatic load increments method are adopted.

To analyse tubular joints, a simple mesh generator has been developed. Structural symmetry is exploited to reduce the number of elements. The tubular joint is divided into a few regions and by means of a blending function. each region is discretised into a number of elements.

A wide range of tubular joints have been analysed using this finite element method. The numerical results have been compared with experimental tests undertaken by the Wimpey Offshore Laboratory using large scale specimens.

Finally, the applicability of the nonlinear finite element developed here is briefly discussed and potential areas of research in the ultimate behaviour of tubular joints are proposed.

Acknowledgements

The author would like to take the opportunity to express his sincerest gratitude to his supervisor, Prof. P. Bettess of the Department of Marine Technology. His careful guidance and enthusiastic encouragement during the period of research is deeply appreciated.

The author is a staff member of Surabaya Institute Technology (ITS) in Indonesia and his research was sponsored by the British Council. He would like to thank them for their financial support. In particular, the author wishes to express his gratitute to Mr.Soegiono (former dean of Faculty of Marine Technology ITS) and Mr.Soeweify (dean of Faculty of Marine Technology ITS).

The author would like to thank to his collegues, in particular, Mr. E. Panunggal and Dr. M. Chipalo for reading the draft of this thesis and Dr. D. Petty and Dr. H.S. Urm for their suggestions and discussion and Mr. B.A. Murray for his help with various operating system problems in Sun computer.

Most of all, the author is deeply gratefull to his parents for their unlimited patience and support.

Contents

LIST OF TABLES

Chapter I

Introduction

1.1 Hydrocarbons

Hydrocarbons are chemical compounds composed of the elements carbon and hydrogen. At normal temperature and normal pressure, they may be liquid, gas or solid depending on their composition. Accumulations of hydrocarbons can be found in many places of the world. All hydrocarbons which occur naturally in the earths crust are termed petroleum. In the commercial sense the word is usually restricted to the liquid deposit crude oil, the gaseous form is termed natural gas, and the solid forms are called bitumen, asphalt or wax according to their composition. In general, the proportion of carbon and hydrogen does not vary appreciably among the different varieties of petroleum : carbon comprises 82% to 87% and hydrogen 12% to 15% by molecular weight [Chapman 1983]. Hydrocarbons are extremely economically important, and are the concern of a multibillion pound international industry. They are overwhelmingly important as fuels (after refining), but also have a myriad other uses.

1.1.1 Oil Fields

A petroleum reservoir can be defined as the part of geologic trap in which oil and gas accumulate, while an accumulation comprises one or more reservoirs of oil and gas fields. An oil field contains one or more reservoirs related to their geological structure. There are over 500 known giant oil and gas fields in different parts of the world. A giant field is defined as having 500 million barrels of recoverable oil or equivalent gas. About third of those discovered have produced [Carmalt 1986].

According to the BP Statistical Riview [1988], the total oil reseves in 1967 were 418 billion barrels and this had doubled by 1987. The oil reserves in 1987 were

896 billion barrel. Most oil reserves are located in Middle East (see Fig. 1.1a-b). However, most gas reserves are located in what used to be the Centrally Planned Economies. Since 1977, the world gas reserves have increased from 2159 trillion cubic feet to 3797 trillion cubic feet in 1987.

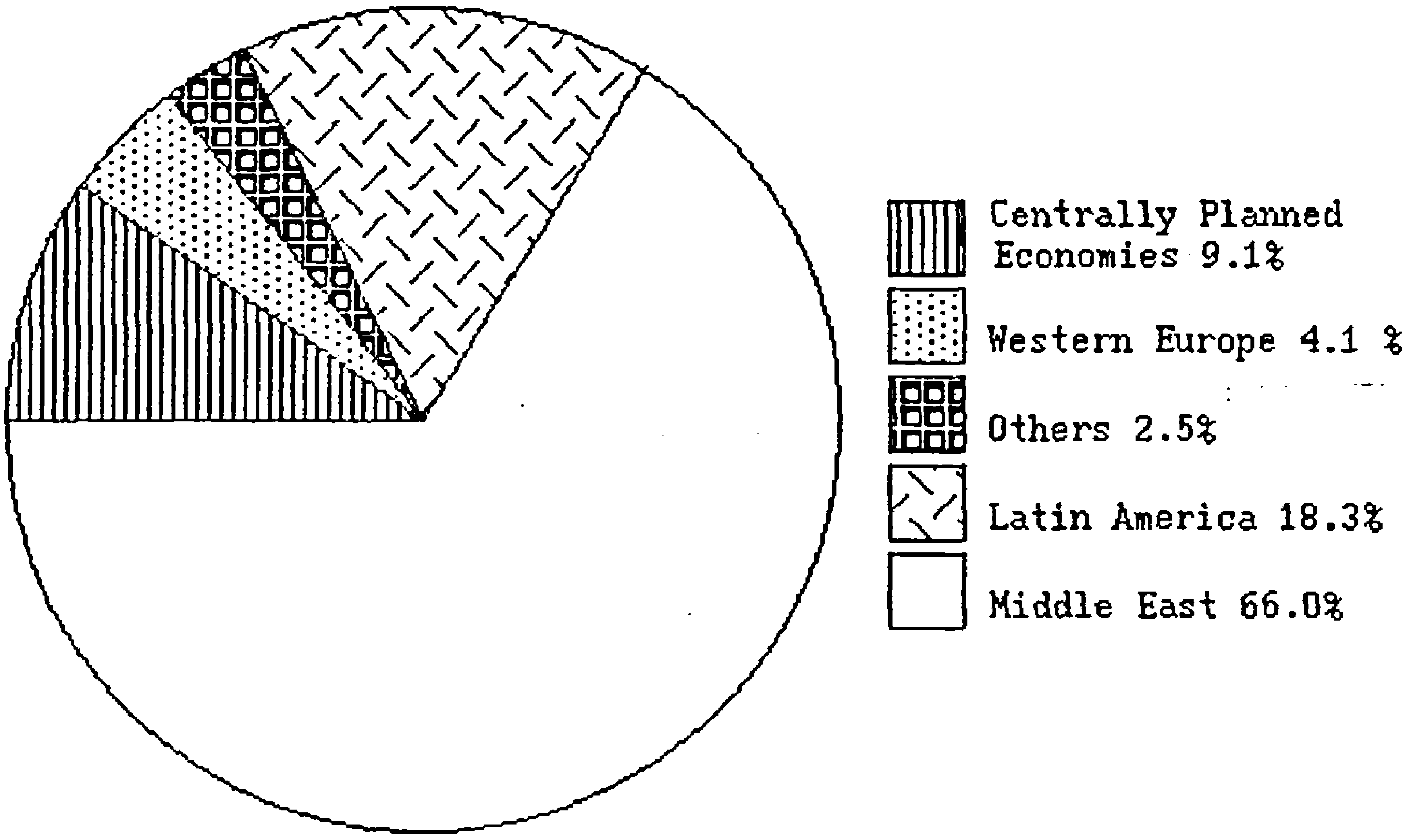

Figure 1.1a : Percentage of oil reserves in the world 1987

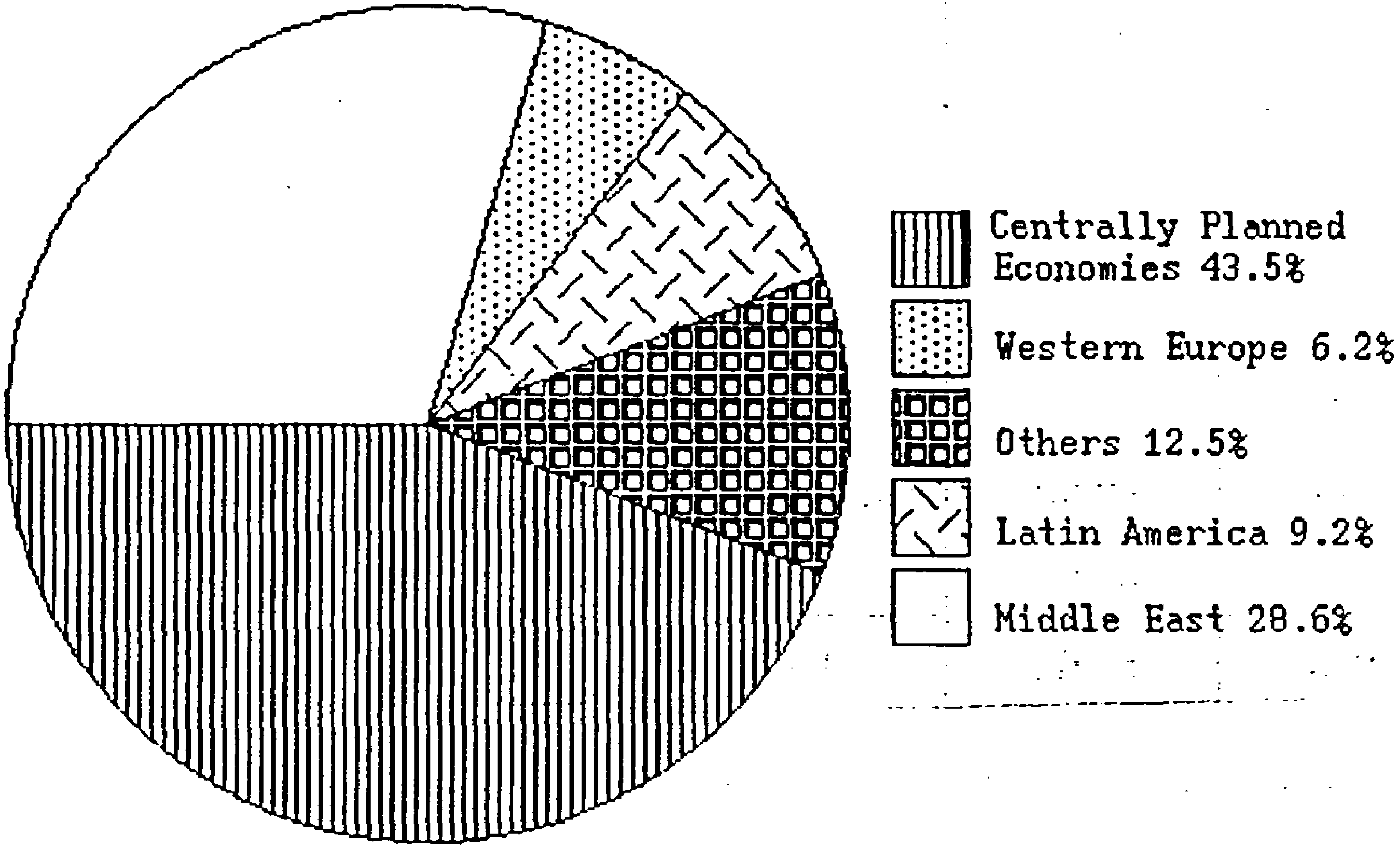

Figure 1.1b : Percentage of gas reserves in the world 1987

Many explorations have been carried out in the sedimentary basins of the world which were expected to have oil accumulation. The result of exploration can be classified into 4 groups, which are intensively explored, moderately explored, partially explored and essentially unexplored. 27% of prospective sedimentary basins in the world currently produce hydrocarbons, another 40% of the basins have been partially or moderately explored and tested but do not produce commercial quantities of petroleum. The total of the world's prospective sedimentary basin area is approximately 77,643,000 sq. km. About 26,395,000 sq. km of this area lies in the world's oceans (see Table 1.1) [Halbouty, 1986].

Location	Total (1000 sq km)	Onshore (1000 sq km)	Offshore (1000 sq km)
Japan	644	80	564
Eastern Europe	1015	900	115
Antartica	1042	0	1042
Republic of China	2472	1787	685
Middle East	3669	2152	1517
Western Europe	3848	1944	1904
Canada	5167	3084	2083
Australia-NZ	6604	4424	2180
Latin America	7851	4843	3008
U S A	8247	6604	1643
S and SE Asia	8916	3705	5211
Africa/Madagascar	13223	11725	1498
U S S R	14945	10000	4945
TOTAL	77643	51248	26395

Table 1.1 — Approximate prospective areas of the sedimentary basins of the world [Halbouty 1986]

1.1.2 Offshore Oil Production

Now oil drilling has spread to the offshore area in almost every part of the world. About 17% of the worlds annual crude oil output came from offshore oil fields in 1970 and this proportion increased until it reach 23% in 1980 (see Table1.2). As mentioned above, more than one third of the prospective basin area lies in the oceans basin (Table 1.1). This means that, the prospect of offshore oil production in the future is excellent.

Year	billion barel	% of total oil production
1970	2.75	17.1
1971	3.00	17.0
1972	3.24	17.4
1973	3.63	17.8
1974	3.40	16.6
1975	3.19	16.3
1976	3.53	16.6
1977	4.15	19.0
1978	4.20	18.9
1979	4.56	20.0
1980	5.00	23.0

Table 1.2 — World Offshore Crude Oil Production 1970-1980 [Tiratsou,1984]

1.2 Offshore Structures Type

The first offshore structural platform, which was built in 1896 on the coast of California, used a wharf which was built out into the water. Futhermore, a wooden platform was used in Ferry Lake in Caddo Parish Lousiana on 1909/1910. This platform was used for drilling, and was built on top of cypress tree piling. After that year, several wooden platforms were built in offshore fields. In 1946, the Magnolia oil company used steel piles for an offshore platform. This was the first offshore platform to use steel piles. The choice of steel piles was because of problem with teredo, a marine borer, which attacked the wooden piles. Three years later, in 1949, mobile drilling units mounted on barges were introduced. Now many types of offshore structure have been developed. The most common type is the jacket structure. Some offshore structure type will now be briefly listed [Bettess 1989, Gerwick 1986, Graff 1981].

1.2.1 Jack-ups

Jack-ups rigs are normally operated in a range of water depth from 30 m to 75m. Jack-ups are used in drilling operations, but may be used as a production support. The jack-ups consist of a barge as a deck section and several tubular legs usually 3 or 4 at the side of the deck section. The legs can be lowered to the seabed on site, then the deck section of platform is raised to a certain level above sea. In transit the legs are raised and the barge can be towed.

1.2.2 Semi-Submersibles

Semi-submersibles are the most popular form of floating production system. These have been used as early as 1975 on the Argyll field in the North Sea. They are basically buoyant structures which consist of 2 pontoons and several columns to support the deck platform. When they are operating, they are moored to the seabed and the pontoons are fully submerged. This mooring system allows a large heave motion in extreme wave enviroments and this can cause problems with the risers. However, the semisubmersible can operate in water depths of up to 1000 m.

1.2.3 Monohulls

Monohulls are designed for the development of small fields. The design concept takes a small oil tanker, with elaborate dynamic positioning equipment, and facilities to locate the well head and to process the oil production. The Petrojarll is a turret moored monohull production vessel. It started work in the Oseberg field in September 1986.

1.2.4 Tension Leg Platform (TLP)

The basic design of all tension leg platform is a buoyant structure which is connected to the seabed by taut vertical mooring lines. The buoyancy force of the platform creates an upward force keeping the mooring lines under constant tension. The first tension leg platform was the Hutton field platform in 147 m depth of water in the North Sea, developed by Conoco. TLP has been prefered for the Jolliet field in the Gulf of Mexico which has 536 m water depth. The Jolliet TLP has been installed, despite problems with tendons. The TLP scheme has great potential for operation in great water depth.

1.2.5 Monopole Platforms

Monopole platforms are sometimes called guyed tower platform. One was installed by Exxon in 1983 in the Gulf of Mexico in a depth of 350 m of water. The basic idea of this platform is a tower with a flexible joint at the base held in position by means of positive buoyancy and mooring lines.

1.2.6 Tripod Tower Platforms

The concept of the steel tripod has been developed by Heerema/Aker. The design looks like a tetrahedron of steel tubing. One large central colounm is supported by three smaller diameter inclined tubes. Some bracing frames are connected between the central column and the inclined leg. The structure is pinned to the seabed by the piles. A number of small tripod structures have been installed in shallow water, in the south north sea. The large tripod structure have been studied for Norske Shell and a design study was carried out for the Norwegian Troll gas field. It would have been very large structure in a water depth of 340 m and with deck loading of 60000 tonnes. However it was not built, a conventional concrete gravity structure being prefered.

1.2.7 Concrete Gravity

Most concrete offshore structures are situated in the North Sea, especially in the Norwegian sector and a few concrete gravity structures are also used off the coast of Brazil. The first major concrete gravity structures was the Ekofisk storage tank, Ekofisk 1. It was built by C. G. Dorris for Phillips petroleum and it has storage capacity of 5.6 million cubic feet.

The concrete gravity structures are founded at the sea floor, transfering their load to the soil by means of shallow footings. They offer integrated oil storage and a short installation time since no piling is required. Platforms usually have short skirt piles. It is also possible to install the topside facilities at a sheltered inshore location. These gravity platforms are huge structures and they are only suited to large field developments. The final design for the Norwegian Troll gas field was a concrete gravity structure.

1.2.8 Jacket Structures

Jacket or template structures have evolved from simple piled jetties or platforms, originally used in only a few metres of water, just off the coast. Now, these structures are in depths of more than 300 m. The huge jacket structure, Shell Bullwinkle, has just been built and it stands in a water depth of 412 m in the US Gulf of Mexico [Anon. 1988]. Although designs have become more complicated and sophisticated over the years, the original layout has proved to surprisingly flexible and effective.

Table 1.3, lists known, completed structures located in waters exceeding 140 metres while Fig. 1.2 depicts major historical developments.

Name/Owner/Location	Water depth (m)	No. of wells	Jacket weight (tonnes)	Foundation Type
Iwakv Exxon/Japan	153	24	13600	Extended skirt
Murchison/Conoco, North Sea	156	27	21300	Cluster
North Cormorant/Shell, North Sea	160	40	17000	Cluster
Casablanca/Chevron, Spain	160	9	7200	Extended skirt
Thistle/BNOC, North Sea	161	60	26000	Cluster
Nomorado II/Petrobas, Brazil	170	24	16500	Extended skirt
Magnus/B.P North Sea	184	24	35400	Extended skirt
Mississippl Canyon, 1484/ARCO, Gulf of Mexico	198	29	7500	Extended skirt
Zapata, Gulf of Mexico	200	18	6500	Extended skirt
Garden Banks 230A / Chevron, Gulf of Mexico	209	20	10200	Extended skirt
Eureka/Shell, offshore Eureka/Shell, offshore California	259	28	11000	Extended skirt
Cerveza ligera/ Union, Gulf of Mexico	285	40	20900	Extended skirt
Cerveza/Union, Gulf of Mexico	312	62	30400	Extended skirt
Northern Ninian/ Chevron, North Sea	141	25	13000	Extended skirt
Bullwinkle/Shell, Gulf of Mexico	412	60	44789	-

Table 1.3 — Fixed steel offshore platforms located in water depths exceeding 140 metres

The principal structural components of a fixed offshore structure are the jacket, the deck, and piles. The jacket consists of a three dimensional frame structure, the main members of which are vertical or slightly inclined and which extended from the seabed to above the water surface. They are called legs. The other members, which are usually smaller are horizontal members and diagonal bracing. K bracing, X bracing or more complicated bracing schemes are used. The members are invariably cylindrical tubes and some of the members are sometimes internally or externally stiffened. Gusset plates are also sometimes used at joints. The intersections of members are called nodes or joints.

The jacket is prefabricated onshore as a space frame and is transported to the site. At the offshore site the jacket, the pile and the deck will be installed together. The tubular members are fabricated from plates which are rolled to the correct radius and welded up. At intersection of a member and braces, the radius of the member is enlarged, firstly to strengtehen the joint area and secondly to provide sufficient spacing between neighbouring braces for welding purposes. The enlarged part of a memeber is called a can. Before tubes are constructed into the space frame, the tubes have to prepared for welding of the joint. The nodes have to be profiled at the end of the tubes, so that the nodes can be welded together. Another way to prepare the joints, is to fabricate the joint from pieces of tube by welding or it may be cast in one unit. A typical structure might have 600 members and 100 joints. The framework of the jacket tends to have many features attached to it. These include guides for the conductors, risers and other oppurtenances, including fenders and sacrificial anodes.

As the foundation of the jacket structure, the piles project downward through the inside of leg, which form the template. The piles can also be driven alongside the leg. To do this, the base of leg is fitted with a bottle or pile cluster, consisting

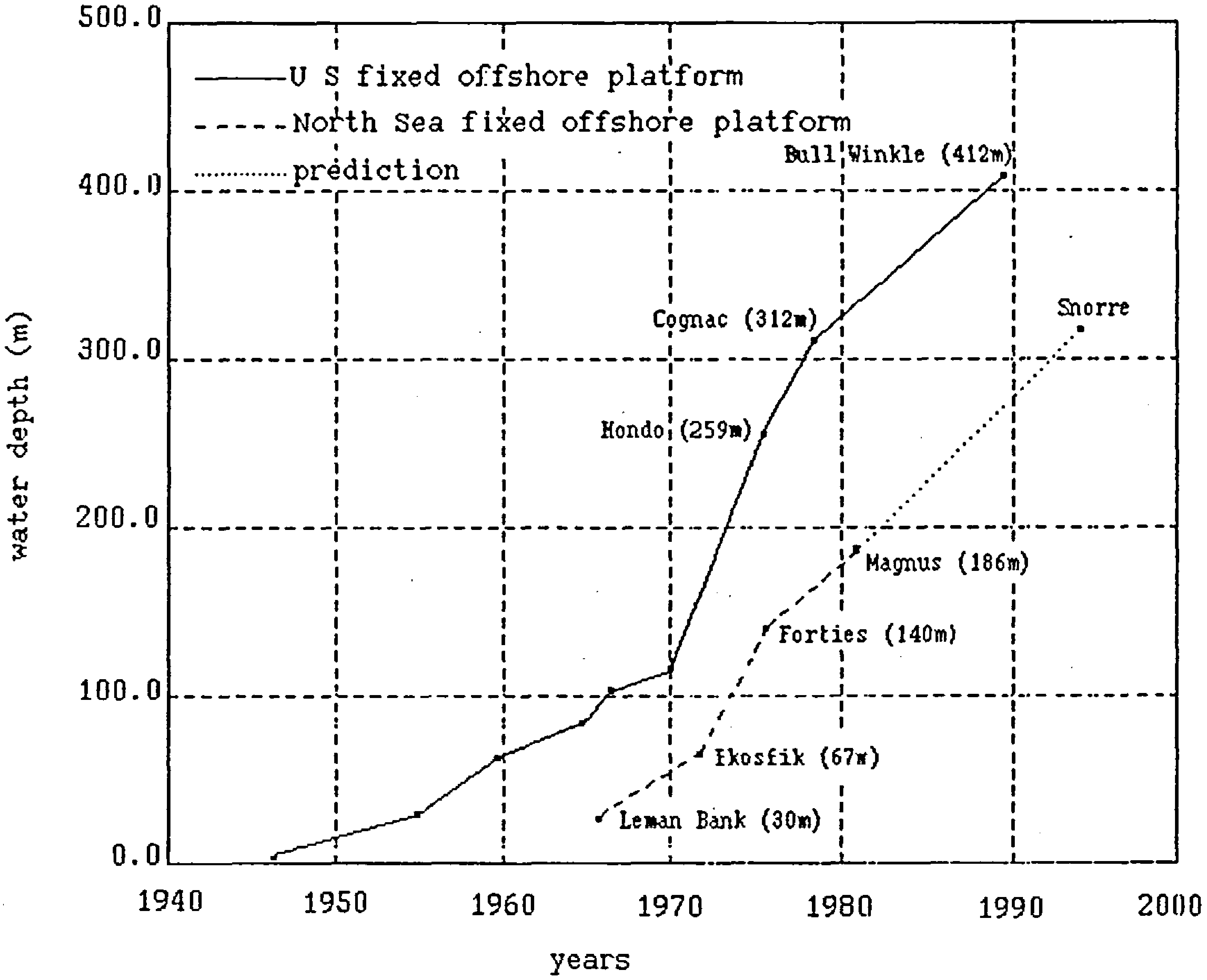

Figure 1.2 : Water depth vs years for fixed platforms.

of several hollow steel cylinders, which hold and guide the piles, in clusters. Some jacket structures use additional skirt piles in between the jacket legs. The skirt pile is driven through the skirt pile sleeve which is attached to the bracing members. The depth of piling depends on the condition of soil. If necessary additional lengths of pile may be welded on. When the driving has finished the piles are firmly fixed to the jacket by pumping grout into the annulus between pile and leg or bottle cylinder.

Modules are installed on the top of the jacket. The top facilities frequently comprise several decks: a drilling deck, a well head/ production deck, and cellar deck and so on. These decks are supported on a gridwork of girders, trusses and columns. The initial section of the deck has legs extending below it with stabbing guides to fit into the piles or jacket legs. The permanent equipment is always pre attached to the decks. Each deck of the platform is lifted on in succesion. After each deck is erected, the remaining equipment for the deck is set.

1.3 Tubular Joints

As mentioned above, most steel offshore structures comprise three dimensional frames composed of cylindrical steel members. These give the best compromise in satisfying the requirements of low drag coeficient, high buoyancy, high strength to weight ratio and equal bending in all directions [Lalani 1987]. The members are connected at their ends forming tubular joints. The tallest of fixed offshore structure with water depth 412m, Bullwinkle in Gulf of Mexico, has been built up from more than 3000 members and over 1000 joints [Anon. 1988]. This shows that the design of tubular joints are a significant part in offshore structure design. Joint design is controlled by static strength or by fatigue strength performance. Other constraints include the properties of available materials, fabrications and inspection criteria.

In general, the joint configuration may be classified into three groups. They are single joints, double joints and complex joints. Single and double joints can be seen in Fig. 1.3. Other joints which are not included in the figure are complex joints [UEG 1985]. The geometric and nondimensional parameters for simple joints can be seen in Fig.1.4 and the basic dimensions which describes simple joints are:

L = chord length
D = chord outside diameter
d = brace outside diameter
T = chord wall thickness
t = brace wall thickness
g = gap (for K, YT and KT joints only)
θ = angle between chord and brace
e = eccentricity
F_y = material yield stress
F_t = material tensile strength

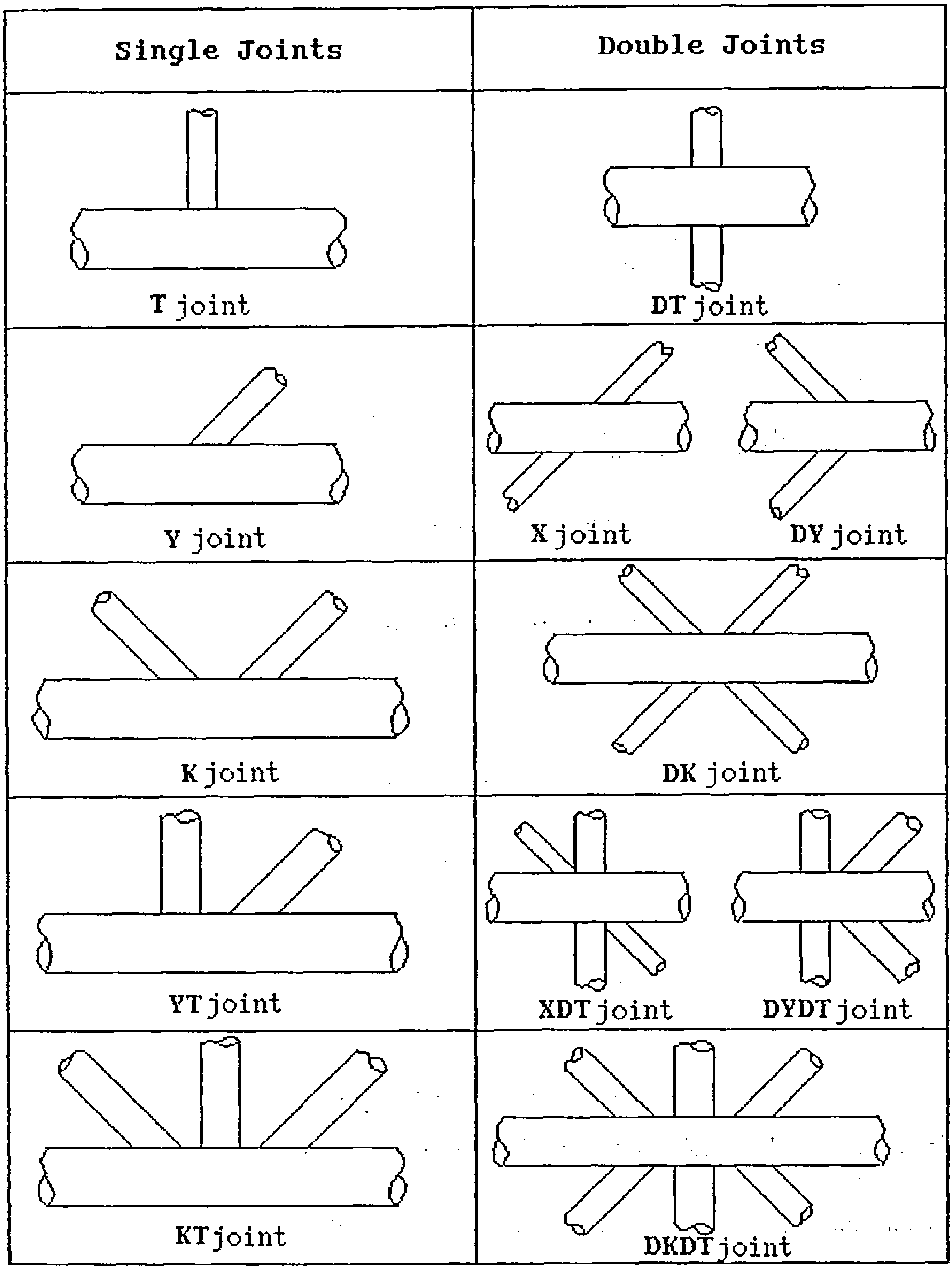

Figure 1.3 : Single and double joint configuration

1.3.1 Tubular Joints Static Strength

Several type of failure mode can occur to the joint under static load. They are:

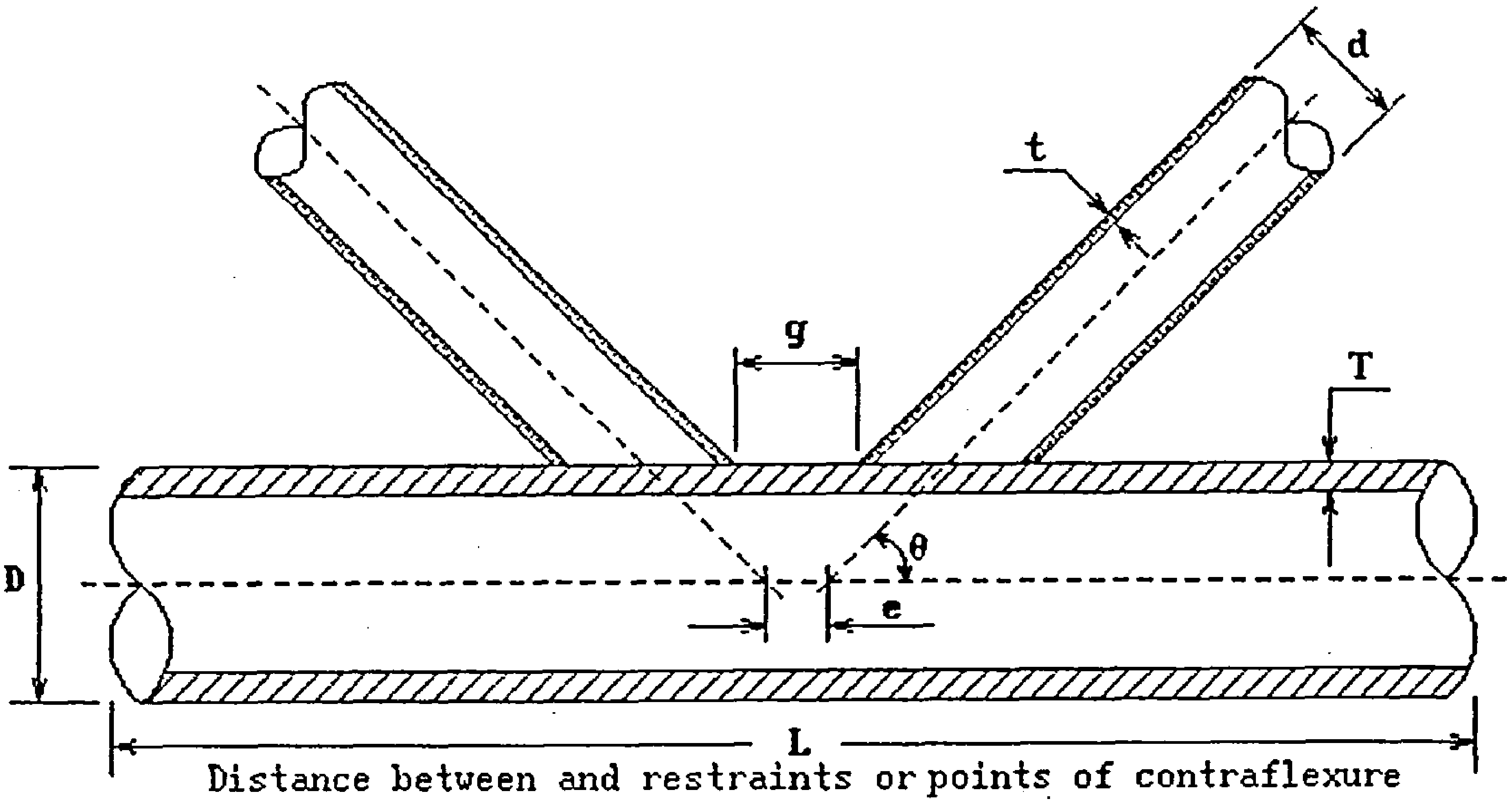

Geometric ratio: $\alpha = \frac{2L}{D}$ $\beta = \frac{d}{D}$ $\gamma = \frac{D}{2T}$ $\tau = \frac{t}{T}$ $\zeta = \frac{g}{D}$

Figure 1.4 : Geometric notation of simple joint

- plastic failure of the chord
- cracking and gross separation of the chord from brace
- cracking of the bracing
- local buckling
- Shear failure of the chord between adjacent bracings
- lammelar tearing of thick chord walls under brace tension loading

The type of failure of a tubular joint under static loading depends on material strength, joint type, loading condition, and geometry of the joints [UEG 1985].

In recent years, a number of reviews and codes for the predictions of the ultimate strength of tubular joints have been published. In the absence of suitable analytical methods, all of those formulae are derived from experimental evidence, based on a 'best fit' to test data points. Most of the formulae in various codes and guidance documents have been derived largely from the same source of information. However no two documents give identical recommendations. This can be understood because of the differences of adopted philosopy, classification, load interaction effects, minimum capacity requirements and safety factors [Lalani 1987]. Futhermore, the lack of data in many practical areas, for instance simple joints with $\beta > 0.8$ [UEG 1985], multiplanar joints, ring stiffened joints, with the result that design codes or the guidance may be not sufficiently accurate and sometimes there is no available guidance for the design of complex joints.

Almost three decade of research in the ultimate strength of tubular joint has been carried out, mostly by experimental testing. However the fundamental issues relating to the ultimate state of tubular joints are still not well understood [Lalani 1987]. Because of the wide range of the joint types, loading condition and the inherent complexity of the joint area, no suitable analytical solution has been developed to predict the ultimate strength of tubular joints [Burdekin 1987], while the design of offshore structures requires an accurate method of prediction. The most feasible way in the near future to understand the behaviour of the ultimate strength of tubular joints is numerical methods, especially the finite element method. The finite element method has developed rapidly during past thirty years and computer systems are now available to assist in this approach.

1.3.2 Finite Element Method In Tubular Joint

In the late sixties, the finite element method was a proven analysis technique that appeared to be ideally suited to the analysis of tubular joints because of its ability to easily model complex geometry, loading and boundary condition. At that time, flat elements were used to analyse tubular joints and a relatively fine mesh was required. To generate the model, a large number of engineering man hours was required. The problem was overcome, by Greste (1970)[as quoted by Cofer *et.al.* 1990] when he introduced a finite element tubular joint analysis integrated with the automatic mesh generator. Futhermore, the finite element method became popular to determine elastic stresses in tubular joints after Ahmad *et.al* [1970] introduced curved shell elements. The research attention was then directed toward validating the finite element method and during the eighties tests parametric studies of the stresses in joints were carried out [Burdekin 1987, Gibstein 1978/1981, Hoffman 1980, Irving 1982, Kuang 1975, Liaw 1976, Visser 1974].

As mentioned above, the analysis of tubular joints using the finite element method quickly became popular, but it was applicable only to the linear elastic model. The development of the nonlinear finite element method and solution techniques procedure to pass the maximum point of ultimate load during eighties gave the possibility of analysing the tubular joints with a nonlinear model. Some work has been done to analyse simple joint and loading [Baba 1984, Cofer 1990,Ebecken 1984, Lalani 1989, Irving 1982, Van Der Valk 1987] In these works, only a few simple joint have been analysed. The detail of those work will be mentioned later in chapter 5 and chapter 6. In the present work, the nonlinear finite element method will be developed to analyse a wide range of tubular joints. The numerical test results will be compared with experimental results.

1.4 Outline Scheme of the Study

The analytical complexities of the problem, rather than lack of interest, have been responsible for the limited number of ultimate load study of tubular joint, particularly when dealing with complex tubular joints and loading conditions. The objectives of this thesis are therefore:

-To develop a nonlinear finite element program for general shell analysis and combine it with automatic incremental loading and iterative solution strategies such as the spherical arc length method to pass the point of the maximum load.

-To develop a simple mesh generator for tubular joints and to analyse a wide range of tubular joints and compare the results with experimental tests.

In chapter two, the degenerate shell finite element method will be developed with six degrees of freedom per node. This six degrees of freedom per node model has the special advantages when dealing with the rotation of tubular joints loaded by in-plane bending moment.

In chapter three, the shell finite element will be developed to include geometric and material nonlinearity. The complete updated Green strain increment will be used to handle geometric nonlinearity of the structure and Von Mises yield criterion will be used to account for material nonlinearity.

In chapter four, the full Newton-Raphson solution technique procedure will be adopted and combined with automatic incremental loading. To pass the maximum point, iterative solution strategies such as the spherical arc length method will be employed.

After developing a simple mesh generator for a tubular joint (presented in appendix A), the nonlinear finite element program will be employed to analyse tubular joints under axial loading conditions in chapter five and in chapter six the numerical results of tubular joints under in-plane bending moment will be compared with experimental results.

In chapter seven, conclusions and recomendations for future work are discussed. Particular emphasis is placed on the application of nonlinear finite element method to the analysis of complex tubular joints.

Chapter II

Shell Finite Element

2.1 Introduction

The development of analysis procedures for shell structures represents one of the most challenging tasks of finite element research. Over the last two decades much effort has been directed towards this task with varying degrees of success. Shell finite elements can be classified as 3-D continuum shells, classical shells and degenerated shells. The skeletal outline of this classification can be seen in Fig. 2.2 [Kanock 1979] and is discussed briefly as follows.

2.1.1 3-D Continuum Elements

The 3-D continuum element can be formed by using the three dimensional field equation. This produces an element which ignores the usual assumptions of most shell problems and it can lead to various difficulties. For instance, along the edge corresponding to the shell thickness, three degree of freedom pernode will produce large stiffens coefficients for relative displacements. This present numerical problems and may lead to ill-condition equations when shell thickness become small compared with the other dimension in the element. Furthermore, economic consideration ussually curtail the usefulness of this element. The large number of nodes across the thickness is required to satisfy the assumption that the normals to the middle surface remain practically straight after deformation [Zienkiewicz 1977].

2.1.2 Classical Shell Elements

The classical shell element is derived by reducing the 3-D field equation to a particular class of shell equation using analytical integration over the thickness while employing shell assumptions. A common assumption is that the rotation of the cross section is simply the slope of the shell. This is true only when the shell is relatively thin and its shear is negligible. As a result normals to the reference surface remain normal. This is the Kirchoff-Love hypothesis and can be illustrated using a one dimensional beam as indicated in Fig. 2.1. This can lead to displacement equations of equilibrium that are a coupled set of two second-order differential equations in-plane and a fourth-order differential equation in the transverse direction of the shell. Therefore, a shell element must be based on C_1 continuity and hence higher order interpolation functions are needed than for shell formulations based on the two other classifications. Nodal variables must include at least three displacements and two derivatives of the transverse displacement. The inplane, membrane interpolation functions are usually of lower order than the transverse, bending, functions. This can create gaps or overlaps between the edges of two nonplanar elements such as fold lines in shells. Many shell elements and shell theories also lack the presence of rigid body modes. although some are reported to perform satisfactorily for linear, infinitesimal displacement analysis [Thompson 1989].

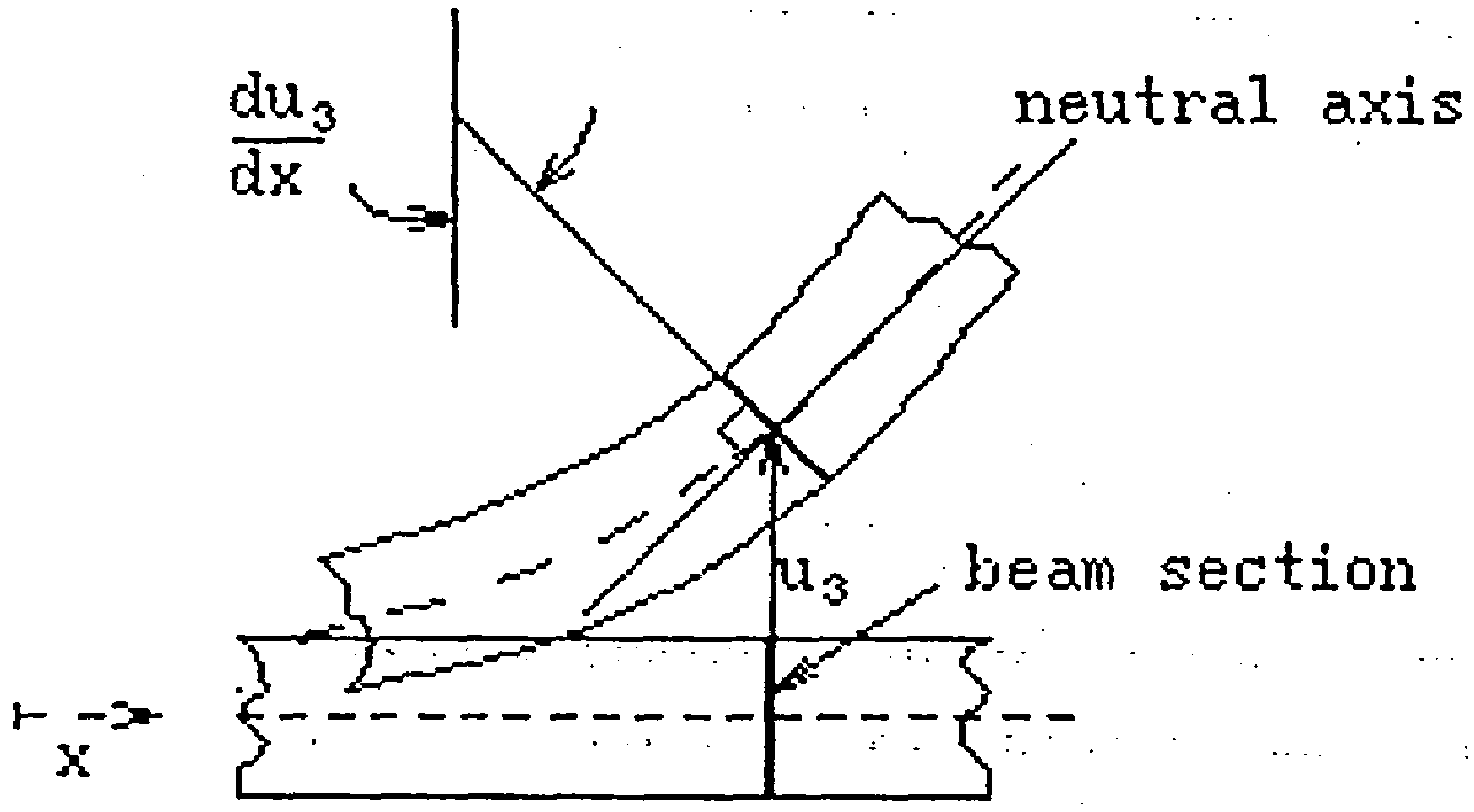

Figure 2.1a : Beam deformation excluding shear effect.

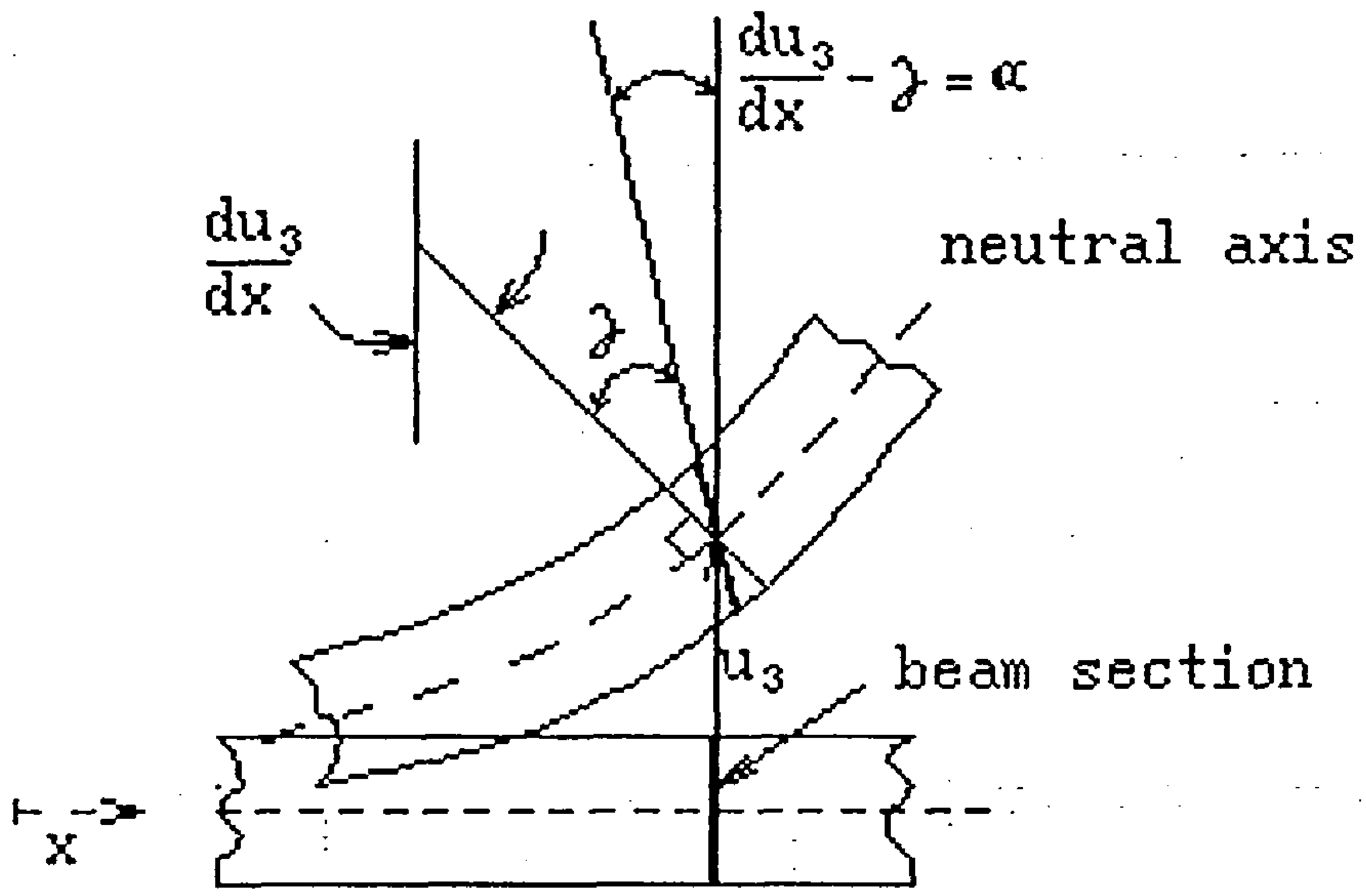

Figure 2.1b : Beam deformation including shear effect.

2.1.3 Degenerate Shell Element

The degeneration concept directly discretizes the 3-D field equations in terms of the mid-surface nodal variables. This procedure was originally introduced by Ahmad *et al.*[1970] for the linear analysis of moderately thick shells. The equilibrium equation with independent rotational and displacement degrees of freedom is employed, in which the three dimensional stress and strain are related to shell behaviour. This permits transverse shear deformation to be taken into account since rotations are not tied to the mid-surface slope. The equilibrium equation is a second order differential equation, therefore, the elements require only a C_0 continuous shape function. Two basic assumptions are adopted in this process. Firstly, it is assumed that even for thick shells, normals to the middle surface remain practically straight after deformation. Secondly, the strain energy corresponding to the stress perpendicular to the middle surface is disregarded; i.e. the stress component normal to the shell midsurface is constrained to be zero in the constitutive equations. The degenerate shell element is adopted in the present work.

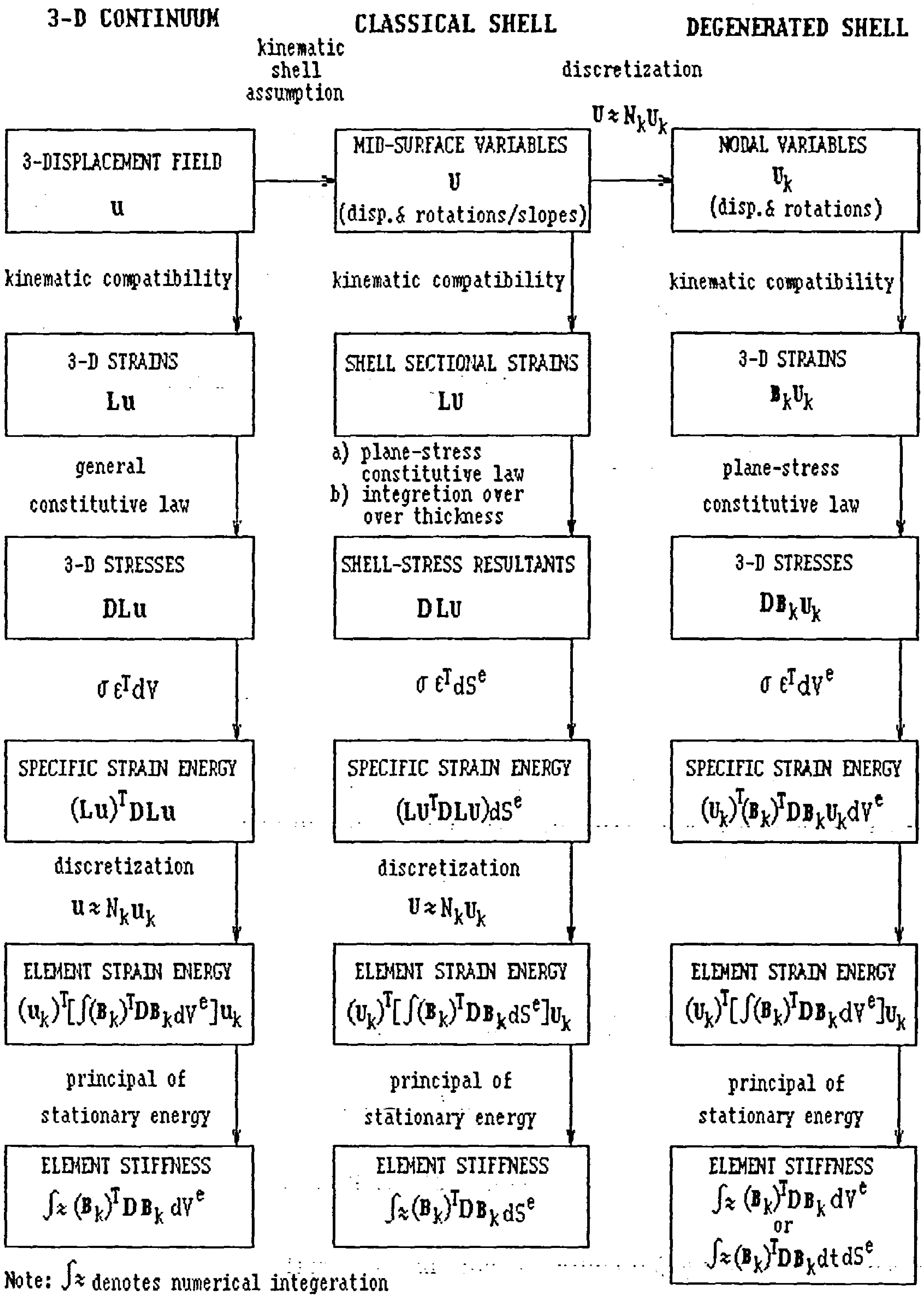

Note: $\int_{\approx}$ denotes numerical integeration

Figure 2.2.: Overview of shell element derivation

2.2 Degenerate Shell Element Formulation

Since the degenerate shell element was introduced by Ahmad, a large amount of work has been done dealing with this shell. The Ahmad implemention of the isoparametric element posseses five degree of freedom. these are the three displacements and two rotations at each nodal point. In this present work six degrees of freedom are specified at each nodal point, corresponding to its three displacements and three rotations. The sixth ('drilling') degree of freedom, is somewhat artificial and is added for completeness using a suitable transformation.

2.2.1 Coordinate System

To formulate degenerate curved shell elements, four different coordinate systems are employed. They are global coordinates, nodal coordinates, curvilinear coordinates and local coordinates (see fig.2.3). They will now be described in turn.

1. Global Coordinate

The global coordinate is a cartesian coordinate system which is freely chosen and defines the structure in space. Fig. 2.3 depicts this system and the notation is used as follows;

$\bar{x}_i$	denotes the base vector of each axes
u_i	denotes the displacement direction
α_i	are the angles of rotation for each axis

where $i = 1,2,3$

2. Curvilinear Coordinate

Here, the curvilinear cordinate ξ, η is on mid-surface of the shell element and ζ is a linear coordinate in the thickness direction (see Fig. 2.3). The element is bounded by planes having constant ξ, η and ζ values of -1 and $+1$. Where ζ is assumed approximately perpendicular to the mid-surface of the element. Eq.(2.9) defines the relation between the curvilinear coordinate and the global coordinates system.

3. Nodal Coordinate

Fig. 2.3 depicts nodal coordinates and variables V_{ik} used at each nodal point k. The vector V_{3k} is the normal thickness vector at nodal point k and can be constructed using the following procedure.

$$V_{3k} = \bar{V}'_{3k} \times t \tag{2.1}$$

where t is the shell thickness at node k and the unit vector V_{3k} can be obtained as

$$\bar{V}_{3k} = \frac{\bar{V}'_{3k} \times t}{|\bar{V}'_{3k} \times t|} \tag{2.2}$$

$\bar{V}'_{3k}$ is the normal to the mid surface and is defined as follows

$$\bar{V}'_{3k} = \frac{x_{i,\xi} \times x_{i,\eta}}{|x_{i,\xi} \times x_{i,\eta}|} \tag{2.3}$$

where

$$x_{i,\xi} = \begin{bmatrix} \frac{\partial x_1}{\partial \xi} \\ \frac{\partial x_2}{\partial \xi} \\ \frac{\partial x_3}{\partial \xi} \end{bmatrix}$$

$$x_{i,\eta} = \begin{bmatrix} \frac{\partial x_1}{\partial \eta} \\ \frac{\partial x_2}{\partial \eta} \\ \frac{\partial x_3}{\partial \eta} \end{bmatrix}$$

To define the other vector (V_{1k}; V_{2k}), some assumptions must be introduced. There is no unique way to define the directions of vectors V_{1k} and V_{2k}. Here, two methods will be adopted. First, it is assumed that vector V_{2k} is parallel to the $x_2 x_3$ plane and perpendicular to V_{3k} . This implies that

$$V_{2k}^{x} = 0$$

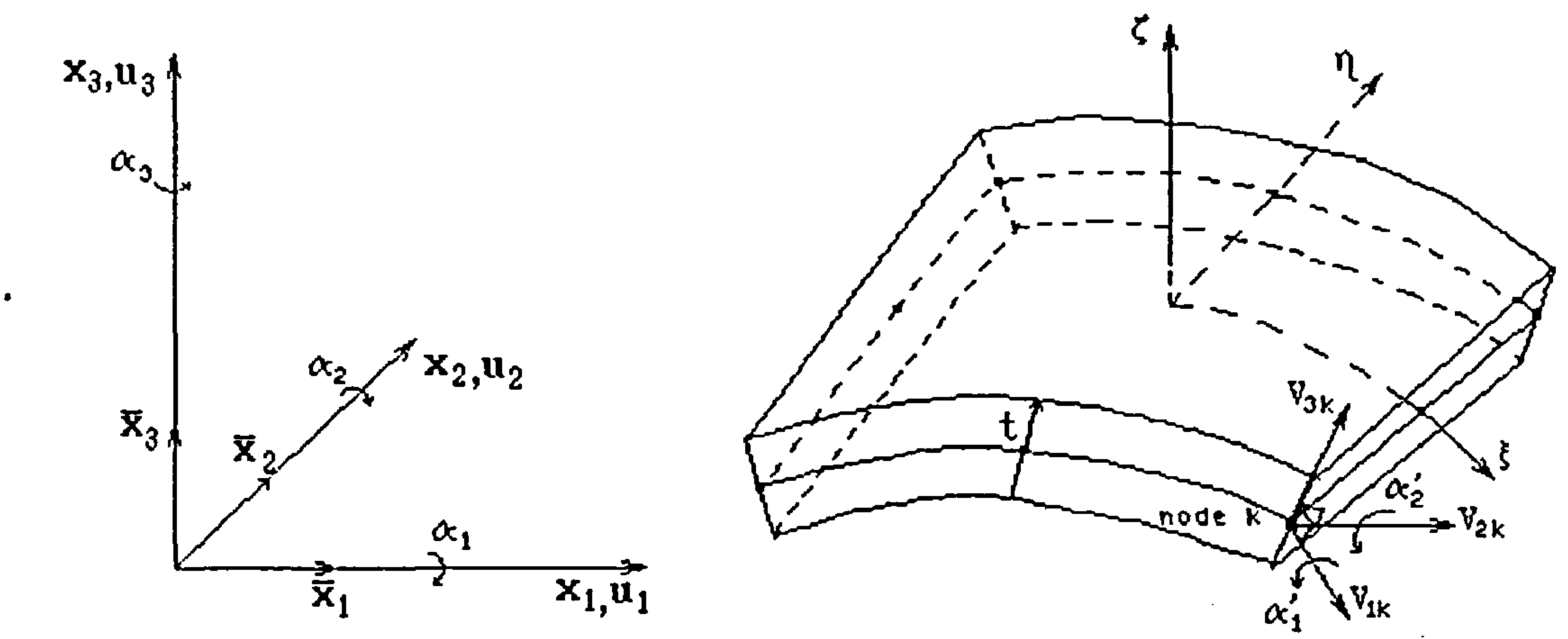

global coordinate system

nodal coordinate system
at node k

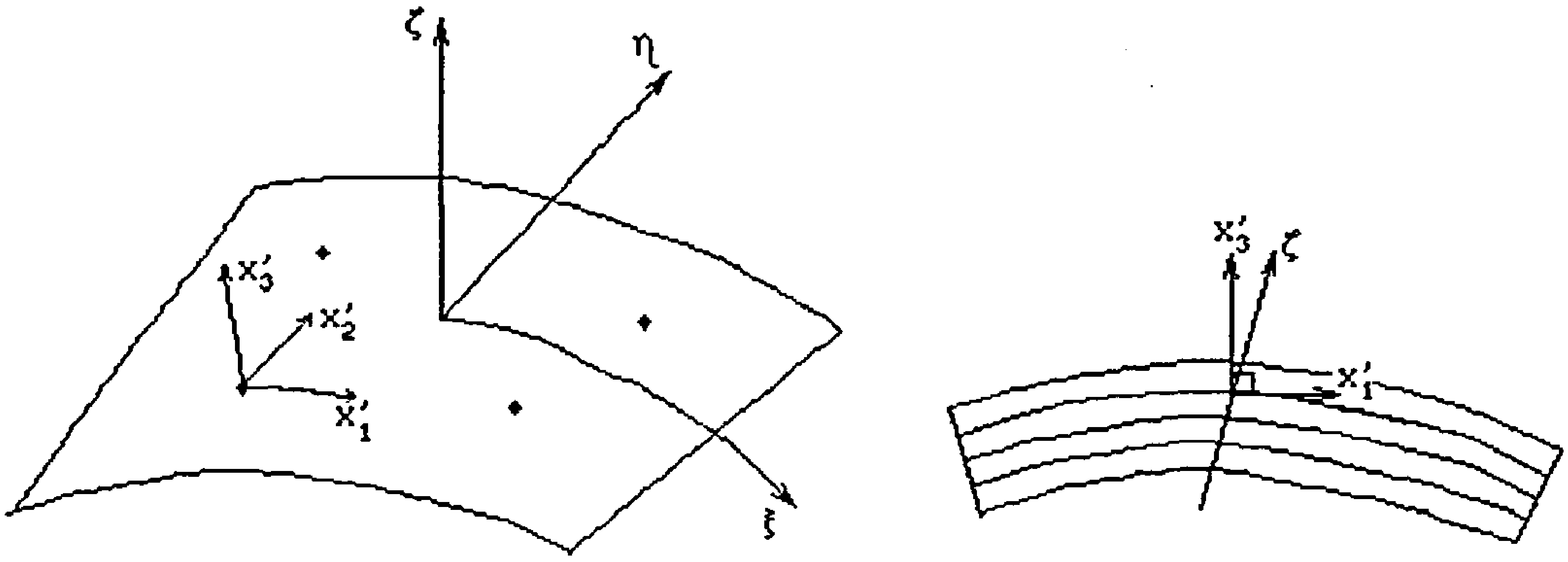

surface ζ = constant

surface η = constant

local coordinate system

Figure 2.3 : Coordinate systems

$$V_{2k}^{y} = V_{3k}^{z}$$

$$V_{2k}^{z} = -V_{3k}^{y} \tag{2.4a}$$

if V_{3k} is parallel to the x_1 direction, this gives

$$V_{3k}^{y} = 0$$

$$V_{3k}^{z} = 0$$

$$V_{2k}^{y} = V_{3k}^{x} \tag{2.4b}$$

Superscripts x, y, z denote projection to the global coordinates x_1, x_2, x_3. The second assumption is that the normal vector V_{3k} is orthogonal to the tangent vector of η axes at the centre of element, this gives

$$V_{2k} = V_{3k} \times x_{i,\eta(0,0)} \tag{2.5a}$$

and the unit vector V_{2k} is

$$\bar{V}_{2k} = \frac{V_{3k} \times x_{i,\eta(0,0)}}{|V_{3k} \times x_{i,\eta(0,0)}|} \tag{2.5b}$$

The direction of the vector V_{1k} can now be obtained from the cross product of vector V_{2k} and V_{3k}, as

$$V_{1k} = V_{2k} \times V_{3k} \tag{2.6a}$$

and the unit vector V_{1k} is

$$\bar{V}_{1k} = \frac{V_{2k} \times V_{3k}}{|V_{2k} \times V_{3k}|} \tag{2.6b}$$

The direction cosine θ which relates the transformations between the nodal and global coordinate system is defined by,

$$[\theta_k] = [\bar{V}_{1k}, \bar{V}_{2k}, \bar{V}_{3k}] \tag{2.7}$$

or

$$[\theta_k] = \begin{bmatrix} \bar{V}_1^x & \bar{V}_1^y & \bar{V}_1^z \\ \bar{V}_2^x & \bar{V}_2^y & \bar{V}_2^z \\ \bar{V}_3^x & \bar{V}_3^y & \bar{V}_3^z \end{bmatrix} = \begin{bmatrix} \theta_{11} & \theta_{12} & \theta_{13} \\ \theta_{21} & \theta_{22} & \theta_{23} \\ \theta_{31} & \theta_{32} & \theta_{33} \end{bmatrix} \tag{2.7a}$$

where $\bar{V}_1, \bar{V}_2$ and $\bar{V}_3$ are unit vectors in the direction of V_1, V_2 and V_3 axes respectively.

4. Local Coordinate

The local coordinate is the cartesian coordinate system defined at Gauss sampling points where the stress and strain are to be calculated. Fig. 2.3 depicts this system and the notation used is x'_1, x'_2, x'_3. The local coordinate system can be obtained by interpolating the nodal coordinate as;

$$x'_i = \sum_{k=1}^{n} N_{k(\xi,\eta)} V_i \tag{2.8a}$$

As usual, the unit vector can be defined as follows

$$\bar{x}'_i = \frac{x'_i}{|x'_i|} \tag{2.8b}$$

Eq.(2.8b) defines direction cosines which gives the transformation between local coordinates and global coordinate. Eq.(2.8b) can be written as;

$$\varphi = \bar{x}'_i = \begin{bmatrix} \bar{x}'^x_1 & \bar{x}'^y_1 & \bar{x}'^z_1 \\ \bar{x}'^x_2 & \bar{x}'^y_2 & \bar{x}'^z_2 \\ \bar{x}'^x_3 & \bar{x}'^y_3 & \bar{x}'^z_3 \end{bmatrix} = \begin{bmatrix} \varphi_{11} & \varphi_{12} & \varphi_{13} \\ \varphi_{21} & \varphi_{22} & \varphi_{23} \\ \varphi_{31} & \varphi_{32} & \varphi_{33} \end{bmatrix} \tag{2.8c}$$

The local coordinates can also be defined in a similar way as the nodal coordinate system, but the ξ and η value are measured with reference to the Gauss sampling points.

2.2.2 Geometry and Displacement Field

A general shell element, with a total of n nodes on the midsurface, can be defined by curvilinear coordinates. Geometric interpretation is given in Fig. 2.3 and Fig. 2.4, which feature a non dimensional thickness coordinate. As the thickness of the shell element is defined in the direction of ζ, the normal to the mid surface, the position of any point in the element can be defined as follows;

$$x_{i(\xi,\eta,\zeta)} = \sum_{k=1}^{n} N_k(x_{ik} + \frac{1}{2}\zeta t \bar{V}_{3k}) \tag{2.9}$$

where

x_{ik} = the coordinate of the midsurface at node k

t = thickness

n = total number of nodes per element

$\bar{V}_{3k}$ = the unit normal vector at node k

The quadratic serendipity interpolation functions N_k are C_0 continuous, taking a value of unity at node k and zero at all other nodes and are given [Zienkiewicz 1977] by

corner nodes

$$N_k = \frac{1}{4}(\xi + \xi\xi_k)(1 + \eta\eta_k)(\xi\xi_k + \eta\eta_k - 1)$$

midside nodes

$$\xi_k = 0, \qquad N_k = \frac{1}{2}(1 - \xi^2)(1 + \eta\eta_k)$$

$$\eta_k = 0, \qquad N_k = \frac{1}{2}(1 + \xi\xi_k)(1 - \eta^2) \tag{2.10}$$

where ξ_k and η_k are the ξ and η coordinate of the kth node respectively. This interpolation function is implemented in this present study.

Taking into consideration the shell assumption that normals to the middle surface remain practically straight after deformation even for thick shells, the displacement field can be described by six degrees of freedom; three displacements at mid surface and three rotations. The element displacement field can be expressed by

$$u_{i(\xi,\eta,\zeta)} = \sum_{k=1}^{n} N_k\{u_{ik} + U_{k\alpha}\} \tag{2.11}$$

Where u_{ik} is the nodal displacement vector on the midsurface, and $U_{k\alpha}$ is the relative nodal displacement vector produce by a normal rotation at node k (see Fig. 2.4). The vector $U_{k\alpha}$ is to be expressed in terms of two rotation vector inplane and drilling rotation vectors, α_{ik}, about each of global axes. Considering Fig. 2.4

the nodal displacements produced by normal rotations are

$$\delta_{ik(\zeta)} = \frac{1}{2}\zeta t \begin{bmatrix} \alpha_2' \\ -\alpha_1' \\ 0 \end{bmatrix} \tag{2.12}$$

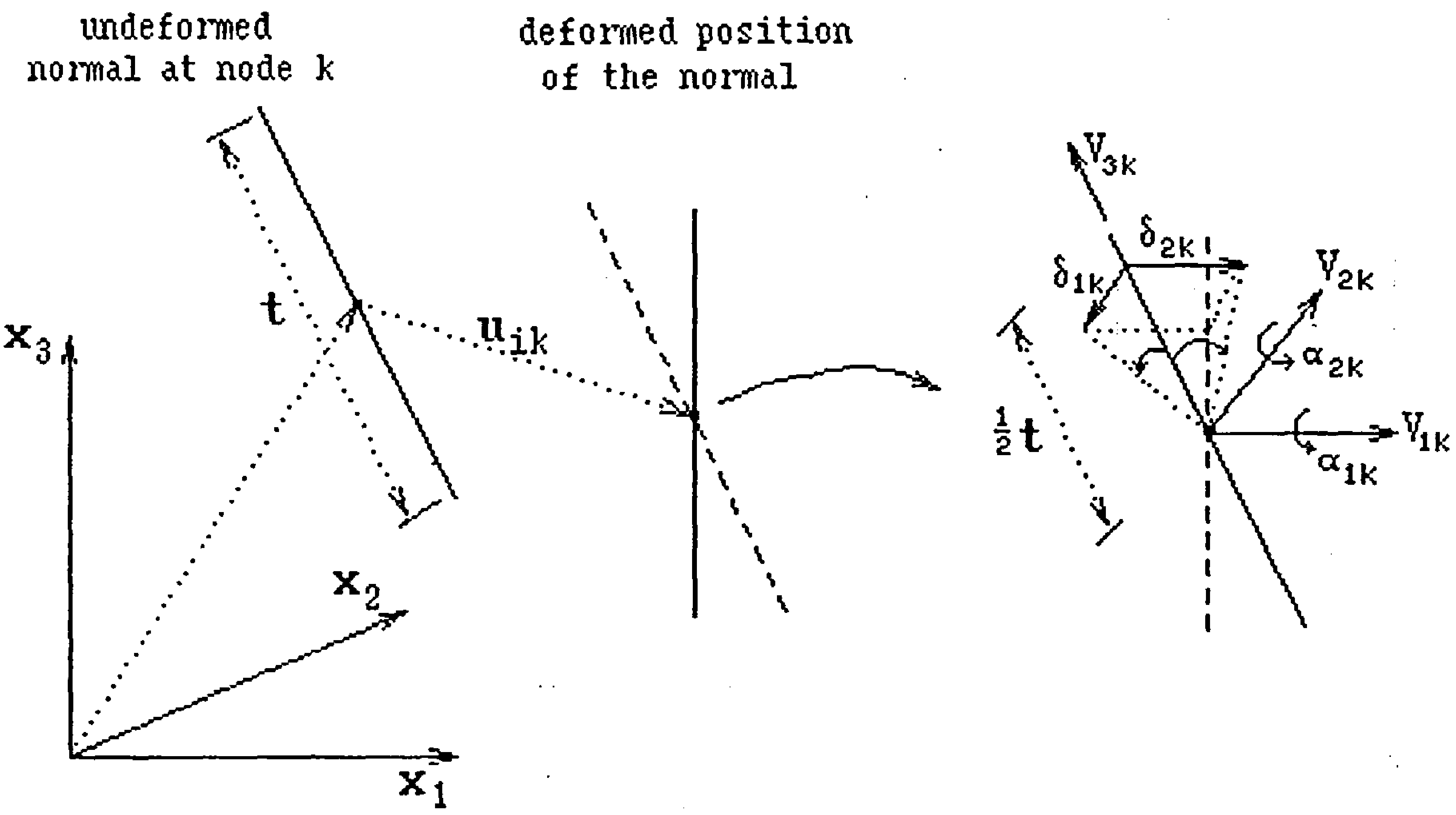

Figure 2.4 : Displacements of a point on the normal at node k

For infinitesimal rotations, the usual transformation from δ_{ik} to $U_{k\alpha}$ and α'_k to α_{ik}, in view of eq.(2.12) leads to

$$U_{k\alpha} = \frac{1}{2}t\zeta\Phi^k\alpha_{ik} \tag{2.13a}$$

where

$$\Phi_k = \begin{bmatrix} 0 & \theta^k_{33} & -\theta^k_{23} \\ -\theta^k_{33} & 0 & \theta^k_{13} \\ \theta^k_{23} & -\theta^k_{13} & 0 \end{bmatrix}$$

$$[\alpha_i]^T = (\alpha_1, \alpha_2, \alpha_3)$$

where θ_{ij} are defined in eq.(2.7a). On substituting eq.(2.13a) into eq.(2.11) we obtain the expression for the displacement vector at any point in the shell element in terms of nodal variables.

$$u_i = \sum_{k=1}^{n} N_k\{u_{ik} + \frac{1}{2}\zeta t\Phi^k \alpha_{ik}\} \tag{2.14}$$

2.2.3 Strain Displacement Relationship

In order to deal more easily with the shell assumption of zero normal stress in the x'_3 direction ($\sigma'_z = 0$), the strain component should be defined in terms of the local coordinate system. At any point in the shell element, the local strain components are

$$\mathrm{e}' = \begin{bmatrix} \epsilon'_{x'_1x'_1} \\ \epsilon'_{x'_2x'_2} \\ \epsilon'_{x'_3x'_3} \\ \epsilon'_{x'_1x'_2} \\ \epsilon'_{x'_2x'_3} \\ \epsilon'_{x'_3x'_1} \end{bmatrix} = \begin{bmatrix} \frac{\partial u'_1}{\partial x'_1} \\ \frac{\partial u'_2}{\partial x'_2} \\ \frac{\partial u'_3}{\partial x'_3} \\ \frac{\partial u'_1}{\partial x'_2} + \frac{\partial u'_2}{\partial x'_1} \\ \frac{\partial u'_2}{\partial x'_3} + \frac{\partial u'_3}{\partial x'_2} \\ \frac{\partial u'_1}{\partial x'_3} + \frac{\partial u'_3}{\partial x'_1} \end{bmatrix} \tag{2.15}$$

where u'_1, u'_2 and u'_3 are displacement components in the local coordinate system. Using the matrix transformation eq.(2.8c), the local derivatives can be obtained as follows;

$$\begin{bmatrix} \frac{\partial u'_1}{\partial x'_1} & \frac{\partial u'_2}{\partial x'_1} & \frac{\partial u'_3}{\partial x'_1} \\ \frac{\partial u'_1}{\partial x'_2} & \frac{\partial u'_2}{\partial x'_2} & \frac{\partial u'_3}{\partial x'_2} \\ \frac{\partial u'_1}{\partial x'_3} & \frac{\partial u'_2}{\partial x'_3} & \frac{\partial u'_3}{\partial x'_3} \end{bmatrix} = \varphi^T \begin{bmatrix} \frac{\partial u_1}{\partial x_1} & \frac{\partial u_2}{\partial x_1} & \frac{\partial u_3}{\partial x_1} \\ \frac{\partial u_1}{\partial x_2} & \frac{\partial u_2}{\partial x_2} & \frac{\partial u_3}{\partial x_2} \\ \frac{\partial u_1}{\partial x_3} & \frac{\partial u_2}{\partial x_3} & \frac{\partial u_3}{\partial x_3} \end{bmatrix} \varphi \tag{2.16}$$

The displacement derivatives corresponding to the global coordinate may be obtained numerically through the Jacobian matrix transformation.

$$\begin{bmatrix} \frac{\partial u_1}{\partial x_1} & \frac{\partial u_2}{\partial x_1} & \frac{\partial u_3}{\partial x_1} \\ \frac{\partial u_1}{\partial x_2} & \frac{\partial u_2}{\partial x_2} & \frac{\partial u_3}{\partial x_2} \\ \frac{\partial u_1}{\partial x_3} & \frac{\partial u_2}{\partial x_3} & \frac{\partial u_3}{\partial x_3} \end{bmatrix} = [\mathrm{J}]^{-1} \begin{bmatrix} \frac{\partial u_1}{\partial \xi} & \frac{\partial u_2}{\partial \xi} & \frac{\partial u_3}{\partial \xi} \\ \frac{\partial u_1}{\partial \eta} & \frac{\partial u_2}{\partial \eta} & \frac{\partial u_3}{\partial \eta} \\ \frac{\partial u_1}{\partial \zeta} & \frac{\partial u_2}{\partial \zeta} & \frac{\partial u_3}{\partial \zeta} \end{bmatrix} \tag{2.17}$$

The Jacobian matrix **J** contains the derivative of x_i with respect to the curvilinear coordinates ξ, η, ζ. Using eq.(2.19), the Jacobian matrix can be obtained as;

$$[\mathrm{J}] = \begin{bmatrix} \frac{\partial x_1}{\partial \xi} & \frac{\partial x_2}{\partial \xi} & \frac{\partial x_3}{\partial \xi} \\ \frac{\partial x_1}{\partial \eta} & \frac{\partial x_2}{\partial \eta} & \frac{\partial x_3}{\partial \eta} \\ \frac{\partial x_1}{\partial \zeta} & \frac{\partial x_2}{\partial \zeta} & \frac{\partial x_3}{\partial \zeta} \end{bmatrix} \tag{2.18}$$

The geometric and displacement derivatives with respect to curvilinear coordinates can be expressed as;

$$x_{i,\xi} = \sum_{k=1}^{n} N_{k,\xi}\{x_{ik} + \frac{1}{2}\zeta t \bar{V}_{3k}\}$$

$$x_{i,\eta} = \sum_{k=1}^{n} N_{k,\eta}\{x_{ik} + \frac{1}{2}\zeta t \bar{V}_{3k}\}$$

$$x_{i,\zeta} = \sum_{k=1}^{n} \frac{1}{2} N_k t \bar{V}_{3k} \tag{2.19a}$$

and

$$u_{i,\xi} = \sum_{k=1}^{n} N_{k,\xi}\{u_{ik} + \frac{1}{2}\zeta t \Phi^k \alpha_{ik}\}$$

$$u_{i,\eta} = \sum_{k=1}^{n} N_{k,\eta}\{u_{ik} + \frac{1}{2}\zeta t \Phi^k \alpha_{ik}\}$$

$$u_{i,\zeta} = \sum_{k=1}^{n} \frac{1}{2} t \Phi^k \alpha_{ik} \tag{19b}$$

the symbol $(.)_{,*}$ defines derivative with respect to the variable $*$. The Jacobian matrix eq.(2.18) can be written as

$$\mathbf{J} = \mathbf{J}^0 + \zeta \mathbf{R} \tag{2.20}$$

where $\mathbf{J}^0$ is the Jacobian associated with the midsurface of the shell and $\mathbf{R}$ is a matrix describing the curvature of the mid surface. $\mathbf{R}$ is given by

$$\mathbf{R} = \begin{bmatrix} \frac{1}{2} N_{k,\xi} t V_{3k} \\ \frac{1}{2} N_{k,\eta} t V_{3k} \\ 0 \end{bmatrix} \tag{2.21}$$

In order to obtain the Jacobian matrix, $\mathbf{J}$, some workers [Ahmad 1970, Kanock 1979, Parisch 1981, Thompson 1989, Zienkiewicz 1971, etc] take the constant value $\zeta = 0$. This is the usual assumption made when using explicit integration and is embodied in Love's first approximation in classical shell theory. However with such a simplification, the resulting linear and nonlinear curvature expressions do not in general satisfy rigid body rotation requirements. Hence the standard form of explicit integration ($\zeta = 0$) is inadequate for linear shell analysis [Milford 1986].

Considering the effect of ζ in explicit integration, Belytschko [1989], Crisfield [1986] and Milford [1986] use an approximation to obtain the inverse of the Jacoban matrix. The result is that there is no straining under rigid body rotations[Milford 1986]. In this present work, the effect of ζ is considered by implicit integration. Implicit integration can be adopted in layered shell analysis and this is presented later in section 2.3. Layer analysis is necessary to take account of the variation of stress through the thickness of the shell when it is used to analyse material nonlinearity.

Using the inverse of the Jacobian matrix the displacement derivative can be written as

$$\frac{\partial u_i}{\partial x_j} = \sum_{k=1}^{n} \{\Theta_{jk} u_{ik} + o_{jk} \Phi_k \alpha_k\} \tag{2.22a}$$

where

$$\Theta_{jk} = I_{j,1} N_{k,\xi} + I_{j,2} N_{k,\eta} \tag{2.22b}$$

and

$$\phi_{jk} = \frac{1}{2} t(\zeta \Theta_{jk} + I_{j,3} N_k) \tag{2.22c}$$

and the $\{I_{i,j}\}$ are the component of the inverse of the Jacobian matrix given by

$$\mathbf{J}^{-1} = \begin{bmatrix} I_{11} & I_{12} & I_{13} \\ I_{21} & I_{22} & I_{23} \\ I_{31} & I_{32} & I_{33} \end{bmatrix} \tag{2.23}$$

By using eq.(2.22) the strain displacement matrix B of a shell element can be constructed. The details of the displacement derivative of eq.(2.22) will be presented in section(2.2.5). The rows in the matrix correspond to all six global strain components defined by the global vector $\{\mathrm{e}\}^T$ given by

$$\{\mathrm{e}\}^T = \{\epsilon_{x_1 x_1}, \epsilon_{x_2 x_2}, \epsilon_{x_3 x_3}, \epsilon_{x_1 x_2}, \epsilon_{x_2 x_3}, \epsilon_{x_3 x_3}\} \tag{2.24}$$

The strain matrix B relates the global strain vector $\{\mathrm{e}\}^T$ to the nodal variables $U \equiv [u, \alpha]^T$ such that

$$\{\mathrm{e}\}^T = \sum_{k=1}^{n} B_k U_k \tag{2.25}$$

As an alternative, we can employ the local strain as indicated by eq.(2.16) and eq.(2.15). The relation between local strain $\{\mathrm{e}'\}^T$ and the nodal variables $\delta \equiv [u, \alpha]^T$ can be expressed as

$$\{\mathrm{e}'\}^T = \sum_{k=1}^{n} B'_k U_k \tag{2.26}$$

where B' is the local strain displacement matrix.

2.2.4 Stress-Strain Relationship

The stress-strain relationship in local coordinate system can be written in tensor notation as follows

$$\sigma'_{ij} = C'_{ijkl}\mathrm{e}'_{kl} \tag{2.27}$$

where σ'_{ij} and e'_{kl} are the stress and strain tensors and C'_{ijkl} is the tensor elastic constant. For an isotropic material, this has the explicit form [Bathe 1982,Chen 1988]

$$C'_{ijkl} = \lambda\delta_{ij}\delta_{kl} + \mu\delta_{ik}\delta_{jl} + \mu\delta_{il}\delta_{jl} \tag{2.28}$$

where λ and μ are the Lamé constants and δ_{ij} is the Kronecker delta defined by

$$\delta_{ij} = \begin{cases} 1 & \text{if } i = j \\ 0 & \text{if } i \neq j \end{cases}$$

The stress-strain tensor, eq.(2.27), can be represented in matrix form as

$$\sigma' = C''\mathrm{e}' \tag{2.29}$$

where

$$\{\sigma'\}^T = \left[\sigma'_{x_1x_1}, \sigma'_{x_2x_2}, \sigma'_{x_3x_3}, \sigma'_{x_1x_2}, \sigma'_{x_2x_3}, \sigma'_{x_3x_1}\right] \tag{2.30}$$

and e' is the local strain as indicated by eq.(2.15). To satisfy the shell assumption that the normal stress is zero, the constitutive equation must be modified. The third row in C' , must be zero so that $\sigma'_{x_3x_3} = 0$ and column three is zero to decouple all stress from $e'_{x_3x_3}$. The elastic constant C' can be written in the following form.

$$\left[C'\right] = \frac{E}{1-\nu^2} \begin{bmatrix} 1 & \nu & 0 & 0 & 0 & 0 \\ & 1 & 0 & 0 & 0 & 0 \\ & & 0 & 0 & 0 & 0 \\ & & & \frac{1-\nu}{2} & 0 & 0 \\ & & & & \frac{1-\nu}{2k} & 0 \\ & & & symm & & \frac{1-\nu}{2k} \end{bmatrix} \tag{2.31}$$

where E and ν are Young's modulus of elasticity and Poisson's ratio respectively. k a is shear correction factor which is usually to be taken 1.2 [Ahmad 1970]. This is because the true distribution of shear stress across the thickness of the shell is parabolic, rather than constant.

In order to obtain the appropriate constitutive equation for the global coordinate, the tensor transformation T must be applied which relates the stress and strain between global and local systems.

$$\{\sigma\} = [T]\{\sigma'\} \tag{2.32}$$

and

$$\{e'\} = [T]^T\{e\} \tag{2.33}$$

Subtituting eq.(2.33) into eq.(2.29) and subtituting the result into eq.(2.32), we will obtain the transformation of the tensor elastic constant.

$$\{\sigma'\} = \left[C'\right][T]^T\{e\} \tag{2.31}$$

$$\{\sigma\} = [T]\left[C'\right][T]^T\{e\} \tag{2.35}$$

$$[C] = [T]\left[C'\right][T]^T \tag{2.36}$$

The elements of T are obtained from the direction cosines of the local axis measured in global coordinate axes and is given by [Bathe 1982].

$$[T] = \begin{bmatrix} \varphi_{11}^2 & \varphi_{21}^2 & \varphi_{31}^2 & \varphi_{11}\varphi_{21} & \varphi_{21}\varphi_{31} & \varphi_{31}\varphi_{11} \\ \varphi_{12}^2 & \varphi_{22}^2 & \varphi_{32}^2 & \varphi_{12}\varphi_{22} & \varphi_{22}\varphi_{32} & \varphi_{32}\varphi_{12} \\ \varphi_{13}^2 & \varphi_{23}^2 & \varphi_{33}^2 & \varphi_{13}\varphi_{23} & \varphi_{23}\varphi_{33} & \varphi_{33}\varphi_{13} \\ 2\varphi_{11}\varphi_{12} & 2\varphi_{21}\varphi_{22} & 2\varphi_{31}\varphi_{32} & \varphi_{11}\varphi_{22}+\varphi_{11}\varphi_{21} & \varphi_{21}\varphi_{32}+\varphi_{22}\varphi_{31} & \varphi_{31}\varphi_{12}+\varphi_{32}\varphi_{11} \\ 2\varphi_{12}\varphi_{13} & 2\varphi_{22}\varphi_{23} & 2\varphi_{32}\varphi_{33} & \varphi_{12}\varphi_{23}+\varphi_{13}\varphi_{22} & \varphi_{22}\varphi_{23}+\varphi_{23}\varphi_{32} & \varphi_{32}\varphi_{13}+\varphi_{33}\varphi_{12} \\ 2\varphi_{13}\varphi_{11} & 2\varphi_{23}\varphi_{21} & 2\varphi_{33}\varphi_{31} & \varphi_{13}\varphi_{21}+\varphi_{11}\varphi_{23} & \varphi_{23}\varphi_{31}+\varphi_{21}\varphi_{33} & \varphi_{33}\varphi_{11}+\varphi_{31}\varphi_{13} \end{bmatrix} \tag{2.37}$$

where φ_{ij} is defined in equation (2.8c).

2.2.5 Derivation of Element Stiffness

As usual, the standard form of element stiffness matrix can be written as follows [Zienkiewicz 1977].

$$\mathbf{K} = \int_V B^T C B dV \tag{2.38}$$

Substituting eq.(3.36) into eq.(3.38), yields

$$\mathbf{K} = \int_V B^T T C' T^T B dV$$

$$\mathbf{K} = \int_V B'^T C' B' dV \tag{2.39}$$

If we use equation (2.38) we do not need to transfer the global strain derivatives into local strain derivatives (see eq.(2.16)). Equation (2.38) has satisfied the assumptions of shell analysis. On the other hand by using eq.(2.39) we do not need to transfer the elastic constants from local to global coordinate systems. Both eq(2.38) and (2.39) must give the same result and can be expressed in the curvilinear coordinate system as;

$$\mathbf{K} = \int_{-1}^{1}\int_{-1}^{1}\int_{-1}^{1} B^T C B |\mathbf{J}| \; d\xi d\eta d\zeta \tag{2.40}$$

or

$$\mathbf{K} = \int_{-1}^{1}\int_{-1}^{1}\int_{-1}^{1} B'^T C' B' |\mathbf{J}| \; d\xi d\eta d\zeta \tag{2.41}$$

- Contribution of displacement derivative

$$\begin{aligned}\frac{\partial u_1}{\partial x_1} = \sum_{k=1}^{n} [& \{I_{11}N_{k,\xi} + I_{12}N_{k,\eta}\} u_1 \\ & \{\frac{1}{2}t(\zeta I_{11}N_{k,\xi}\theta_{33} + \zeta I_{12}N_{k,\eta}\theta_{33} + I_{13}N_k\theta_{33})\}\alpha_2 \\ & \{\frac{1}{2}t(-\zeta I_{11}N_{k,\xi}\theta_{23} - \zeta I_{12}N_{k,\eta}\theta_{23} - I_{13}N_k\theta_{23})\}\alpha_3]\end{aligned}$$

$$\begin{aligned}\frac{\partial u_2}{\partial x_1} = \sum_{k=1}^{n} [& \{I_{11}N_{k,\xi} + I_{12}N_{k,\eta}\} u_2 \\ & \{\frac{1}{2}t(-\zeta I_{11}N_{k,\xi}\theta_{33} - \zeta I_{12}N_{k,\eta}\theta_{33} - I_{13}N_k\theta_{33})\}\alpha_1 \\ & \{\frac{1}{2}t(\zeta I_{11}N_{k,\xi}\theta_{13} + \zeta I_{12}N_{k,\eta}\theta_{13} + I_{13}N_k\theta_{13})\}\alpha_3]\end{aligned}$$

$$\begin{aligned}\frac{\partial u_3}{\partial x_1} = \sum_{k=1}^{n} [& \{I_{11}N_{k,\xi} + I_{12}N_{k,\eta}\} u_3 \\ & \{\frac{1}{2}t(\zeta I_{11}N_{k,\xi}\theta_{23} + \zeta I_{12}N_{k,\eta}\theta_{23} + I_13N_k\theta_{23})\}\alpha_1 \\ & \{\frac{1}{2}t(-\zeta I_{11}N_{k,\xi}\theta_{13} - \zeta I_{12}N_{k,\eta}\theta_{13} - I_{13}N_k\theta_{13})\}\alpha_2]\end{aligned}$$

$$\begin{aligned}\frac{\partial u_1}{\partial x_2} = \sum_{k=1}^{n} [& \{I_{21}N_{k,\xi} + I_{22}N_{k,\eta}\} u_1 \\ & \{\frac{1}{2}t(\zeta I_{21}N_{k,\xi}\theta_{33} + \zeta I_{22}N_{k,\eta}\theta_{33} + I_{23}N_k\theta_{33})\}\alpha_2 \\ & \{\frac{1}{2}t(-\zeta I_{21}N_{k,\xi}\theta_{23} - \zeta I_{22}N_{k,\eta}\theta_{23} - I_{23}N_k\theta_{23})\}\alpha_3]\end{aligned}$$

$$\begin{aligned}\frac{\partial u_2}{\partial x_2} = \sum_{k=1}^{n} [& \{I_{21}N_{k,\xi} + I_{22}N_{k,\eta}\} u_2 \\ & \{\frac{1}{2}t(-\zeta I_{21}N_{k,\xi}\theta_{33} - \zeta I_{22}N_{k,\eta}\theta_{33} - I_{23}N_k\theta_{33})\}\alpha_1 \\ & \{\frac{1}{2}t(\zeta I_{21}N_{k,\xi}\theta_{13} + \zeta I_{22}N_{k,\eta}\theta_{13} + I_{23}N_k\theta_{13})\}\alpha_3]\end{aligned}$$

$$\frac{\partial u_3}{\partial x_2} = \sum_{k=1}^{n}[\{I_{21}N_{k,\xi} + I_{22}N_{k,\eta}\}u_3$$

$$\{\frac{1}{2}t(\zeta I_{21}N_{k,\xi}\theta_{23} + \zeta I_{22}N_{k,\eta}\theta_{23} + I_{23}N_k\theta_{23})\}\alpha_1$$

$$\{\frac{1}{2}t(-\zeta I_{21}N_{k,\xi}\theta_{13} - \zeta I_{22}N_{k,\eta}\theta_{13} - I_{23}N_k\theta_{13})\}\alpha_2]$$

$$\frac{\partial u_1}{\partial x_3} = \sum_{k=1}^{n}[\{I_{31}N_{k,\xi} + I_{32}N_{k,\eta}\}u_3$$

$$\{\frac{1}{2}t(\zeta I_{31}N_{k,\xi}\theta_{33} + \zeta I_{32}N_{k,\eta}\theta_{33} + I_{33}N_k\theta_{33})\}\alpha_2$$

$$\{\frac{1}{2}t(-\zeta I_{31}N_{k,\xi}\theta_{23} - \zeta I_{32}N_{k,\eta}\theta_{23} - I_{33}N_k\theta_{23})\}\alpha_3]$$

$$\frac{\partial u_2}{\partial x_3} = \sum_{k=1}^{n}[\{I_{31}N_{k,\xi} + I_{32}N_{k,\eta}\}u_3$$

$$\{\frac{1}{2}t(-\zeta I_{31}N_{k,\xi}\theta_{33} - \zeta I_{32}N_{k,\eta}\theta_{33} - I_{33}N_k\theta_{33})\}\alpha_1$$

$$\{\frac{1}{2}t(\zeta I_{31}N_{k,\xi}\theta_{13} + \zeta I_{32}N_{k,\eta}\theta_{13} + I_{33}N_k\theta_{13})\}\alpha_3]$$

$$\frac{\partial u_3}{\partial x_3} = \sum_{k=1}^{n}[\{I_{31}N_{k,\xi} + I_{32}N_{k,\eta}\}u_3$$

$$\{\frac{1}{2}t(\zeta I_{31}N_{k,\xi}\theta_{23} + \zeta I_{32}N_{k,\eta}\theta_{23} + I_{33}N_k\theta_{23})\}\alpha_1$$

$$\{\frac{1}{2}t(-\zeta I_{31}N_{k,\xi}\theta_{13} - \zeta I_{32}N_{k,\eta}\theta_{13} - I_{33}N_k\theta_{13})\}\alpha_2]$$

2.3 Numerical Integration

In the shell plane (surface $\zeta = 0$) the normal (full) integration rule consists of $m \times m$ Gauss point where m is the number of nodes along each element side. However, when degenerate shell elements are fully integerated, they exhibit shear and membrane locking in the thin shell limit and this can affect the majority of applications. This shear locking was first identified in the late sixties [Zienkiewicz 1971]. Zienkiewicz retained the transverse shear energy but used a reduction in integration in order to evaluate it, for quadratic and cubic isoparametric and serendipity elements. For the lower order elements, reduced integration appears to be absolutely essential for good behaviour in thin shell applications; for higher order elements significants improvements in accuracy are attained with reduced integration. However, reduced integration often suffers from the drawback that it may lead to the occurance of non zero energy deformation mode, in addition to rigid modes. Therefore the assembled stiffness matrix for a system of underintegrated elements may be singular [Thompson 1989]. Whether or not the assembled stiffness matrix is singular depends on the boundary conditions [Cook 1981]. As a natural extension, selective integration can be adopted to eliminate locking [Hinton 1984, Huang 1986]. Other methods to eliminate locking have been proposed by Stolarski [1982] and Belytschko [1985] and are based on some form of stress (or strain) projection.

In the through thickness direction, where a linear variation of strain is assumed, two Gauss points are sufficient to capture the bending behaviour in linear material problems [Hinton 1984]. High order Gaussian quadrature has been suggested for nonlinear material problem by Cormeau[1978]. Burgoyne and Crisfield [1990] have tested the overall performance of the numerical procedures that relate to the integration of stresses through the thickness of plates and shells when there are discontinuities in stress. The conclusion is that Gauss integration should be used, if integration is always required over the same range, and that as high an order formula as possible should be used rather than making repeated use of simpler formulas. However, simple and general procedures to discretize and integrate through the thickness are adopted in the so-called 'layer model', shown in Figure 2.5.

For through shell thickness integration with ξ and η kept constant, the stiffness matrix can be written as follows :

$$K = \int_{-1}^{1} k(\zeta) d\zeta \tag{2.42}$$

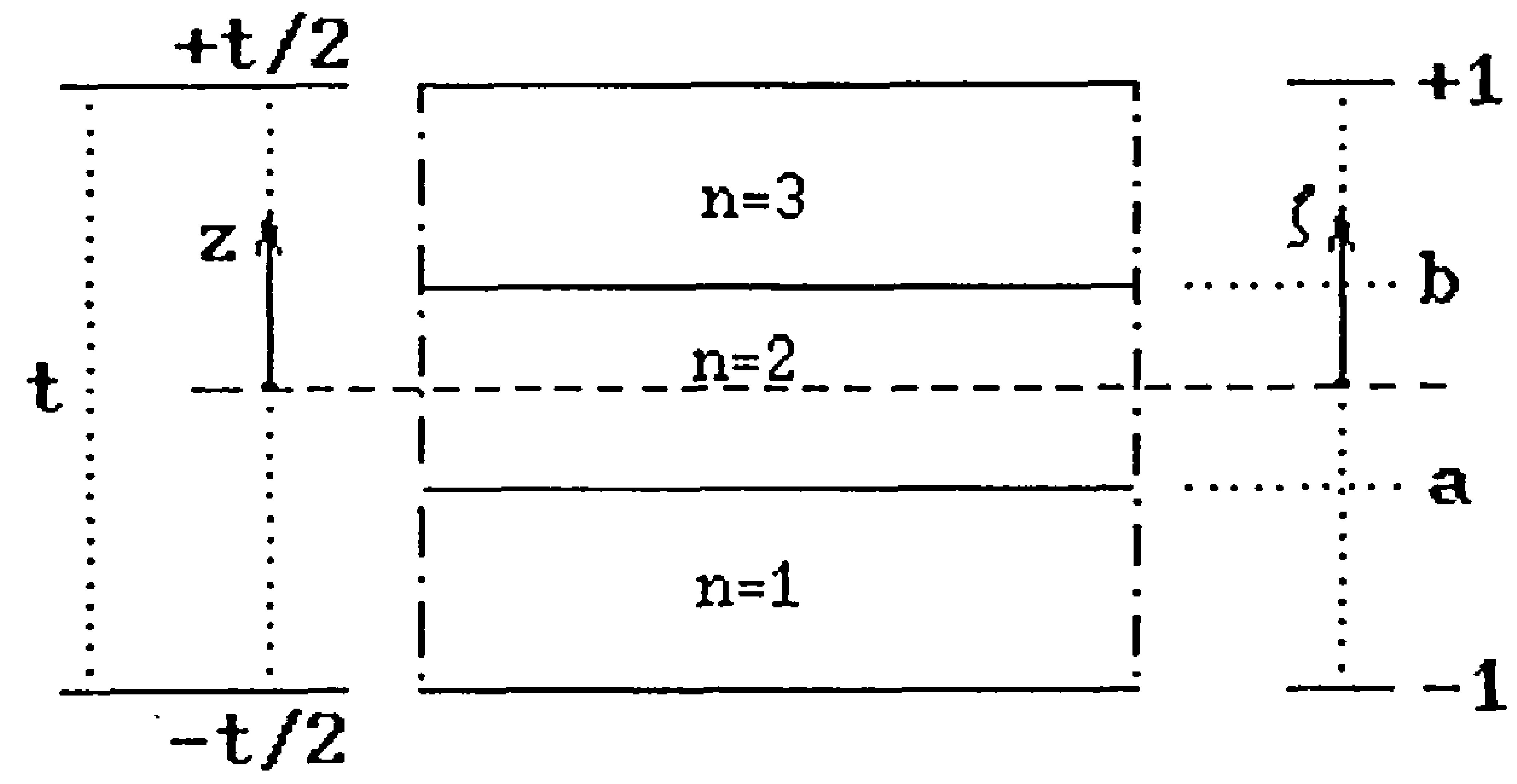

Figure 2.5 : Layered model

Using n layers (see Fig. 2.5), in this case 3 layers, eq.(2.42) can be written as

$$K = \int_{-1}^{a} k(\zeta)d\zeta + \int_{a}^{b} k(\zeta)d\zeta + \int_{b}^{1} k(\zeta)d\zeta \qquad (2.43)$$

If R_i is the abscissca of a Gauss sampling point and W_i is the weight for the interval -1 to $+1$, the corresponding abscissca of the Gauss sampling point, r_i, and weight w_i for the interval a to b in the second layer are [Bathe 1982]

$$r_i = \frac{a+b}{2} + \frac{b-a}{2} \times R_i \qquad (2.44)$$

and

$$w_i = \frac{b-a}{2} \times W_i \qquad (2.45)$$

Two point Gauss integration for each layer is adopted in present work. Using the above formulation, arbitrary numbers of layers can be dealt with. This process of integration in the thickness direction is computationally more expensive, but is more appropriate for variable thickness problems in which the variation of the local system of axes, and the variation of the Jacobian matrix through the shell thickness must be taken into account as was discussed in section 2.2.3.

2.4 Torsional Effect

The local stiffness corresponding to the drilling rotation is a common problem of the shell or plate which employs six degrees of freedom per node. This problem can be seen when a facet shell element is used to approximate a curved surface [Kanock 1979]. Here the convergence is spoiled by the weakly restrained torsional mode after the mesh reaches some state of refinement. The reason is that the resistance to the torsional rotation at node k comes directly from the coupling of the α_k nonplanar elements surrounding node k and when the finite element mesh is refined the angles of the kinks between these elments tend towards 2π and the coupling effect is reduced. This weak coupling only generates a minute amount of stiffness for the torsional rotation. Therefore, any slight disturbance in the generalized load corresponding to this degree of freedom can amplify the torsional mode by an unrealistic amount, which affects the global solution.

In a degenerated shell, the rotation of the normal and midsurface displacement field are independent. The idea then is to derive an additional constraint between the torsional rotation of the normal α_3' and the rotation of the midsurface, $\frac{1}{2}(\frac{\partial u'_2}{\partial x'_1} - \frac{\partial u'_1}{\partial x'_2})$, which is illustrated in Fig. 2.6.

It can be seen from Fig. 2.6a, that the deviation of associated rotation, α_2', from mid-surface slope, $\frac{\partial u'_3}{\partial x'_1}$), is governed by the transverse shear strain energy. This relation is given in eq.(2.46a). Similarly.the deviation of the torsional rotation of the normal from that of the midsurface (see Fig. 2.6b), is assumed to have governing strain energy [Kanok 1979] given in equation 2.46b.

$$\pi_t = k_t G t \int_s [\alpha'_3 - \frac{1}{2}\{\frac{\partial u'_2}{\partial x'_1} - \frac{\partial u'_1}{\partial x'_2}\}]^2 dA \qquad (2.46b)$$

k_t is a parameter such that $k_t G t$ is large relative to the factor Et^3 which appears in the bending strain energy. Equation 2.46b will play the role of a penalty function and results in the desired constraint.

$$\alpha'_3 \equiv \frac{1}{2}\left[\frac{\partial u'_2}{\partial x'_1} - \frac{\partial u'_1}{\partial x'_2}\right] \qquad (2.47)$$

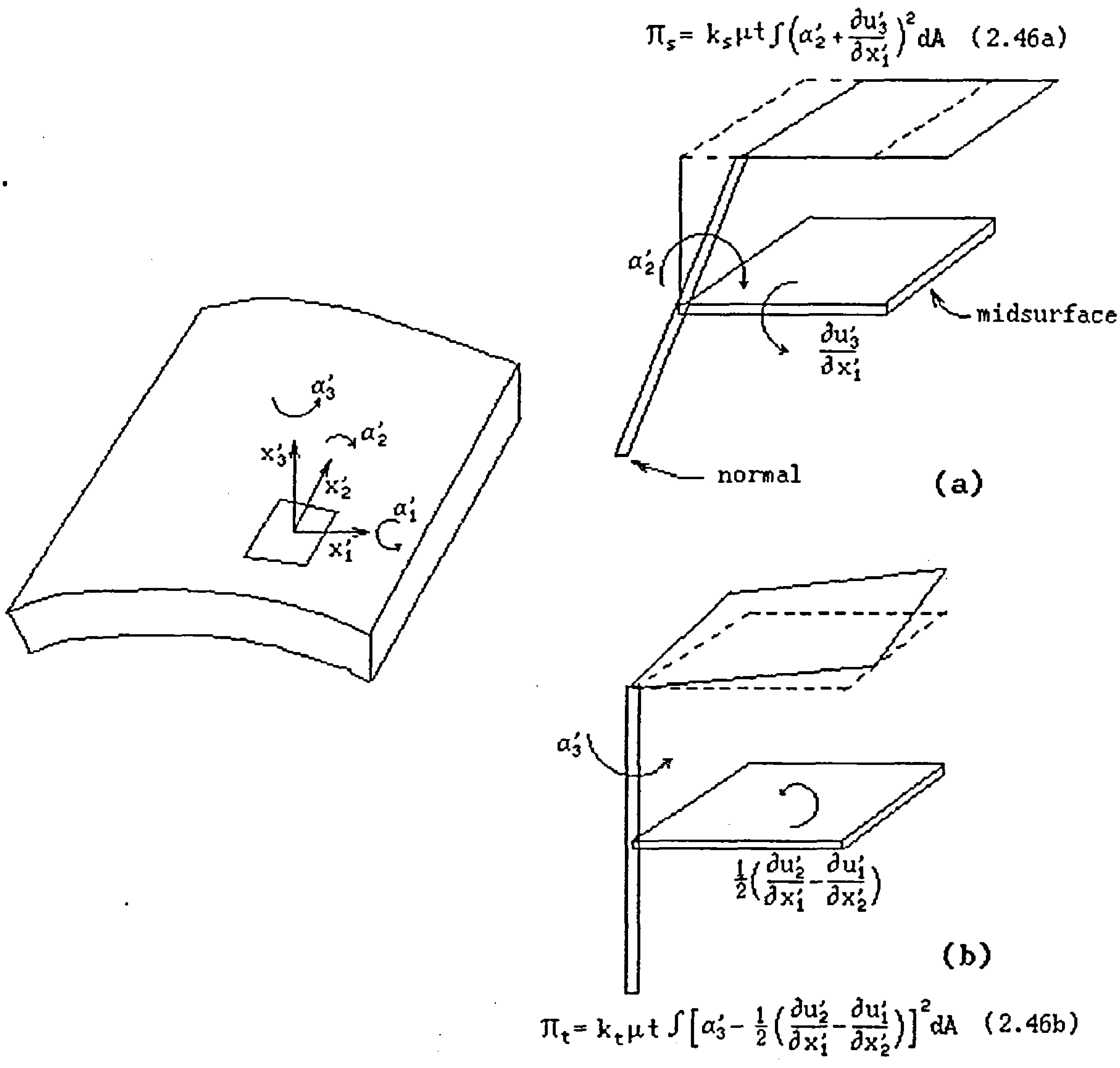

Figure 2.6 : Penalty function for transverse shear and torsion at the Gauss point.

The component of the penalty function can be expressed in the terms of the global strain derivatives as :

$$\frac{\partial u'_2}{\partial x'_1} = \sum_{m=1}^{3} \sum_{p=1}^{3} \varphi_{m,1} \varphi_{p,2} u_{p,x_m} \tag{2.48}$$

$$\frac{\partial u'_1}{\partial x'_2} = \sum_{m=1}^{3} \sum_{p=1}^{3} \varphi_{m,2} \varphi_{p,1} u_{p,X_m} \tag{2.49}$$

$$\alpha'_3 = N_k \left[\theta_{13} \quad \theta_{23} \quad \theta_{33}\right] \{\alpha_k\}$$

$$\alpha'_3 = N_k \mathbf{k}\{\alpha_k\} \tag{2.50}$$

For n nodes in a shell element and using eq.(2.48) to eq.(2.49) the strains produced from the derivation of the torsional rotation from the rotation of the mid surface may be given by :

$$\begin{aligned} \alpha'_3 - \frac{1}{2}\{\frac{\partial u'_2}{\partial x'_1} - \frac{\partial u'_1}{\partial x'_2}\} = \sum_{k=1}^{n} \sum_{m=1}^{3} \{ -\frac{1}{2}[\varphi_{m,2} - \varphi_{k,1}] \\ [\Theta_{km}\{u_k\} + \phi_{km}\Phi_k\{\alpha_k\}] + N_k\{\mathbf{k}\}^T\{\alpha_k\}\} \end{aligned} \tag{2.51}$$

If we look at eq.(2.46a) and eq.(2.46b), the two penalty factors k_t and k_s should be of the same order of magnitude. Kanok[1979] employed a value of $k_t = 10$ in his faceted shell element and indicated that the converged solution is insensitive to k_t, as long as k_t is large enough (> 0.1) to sufficiently restrain the troublesome torsional modes. Thompson [1989] has studied the effect of k_t in this degenerated curved shell element and he found that penalty function for the inplane rotation performed satisfactorily using $k_t = 10$.

A popular approach in the shell formulation using six global degree of freedom per node is to incorporate a fictitious torsional spring. This may be added either locally at the element level or in some pseudo-normal direction defined at each node [Bathe 1981]. It has been suggested that the stiffness corresponding to this in-plane rotation should be set equal to 10^{-4} times the smallest bending stiffness of the element [Kardestuncer 1987], which is implemented in this present work.

2.5 Numerical Examples

The purpose of this section is to demonstrate the numerical performance of the element compared with other workers results or analytic solution. A good shell element must have the ability to handle inextensional bending mode deformation, membrane states of strain and rigid body motion without strain. Presented in this section are the analyses of five test problems, which are outlined below.

Example 1. Pinched Cylinder

The first problem is a pinched cylinder with rigid diaphragms at the two ends in Fig. 2.7. This problem is very popular for testing a shell element and exhibits two main features in terms of deformation behaviour of structures. These are in extensional bending and membrane response around the point load. Structural symmetry is exploited and only one eighth of the shell is modelled.

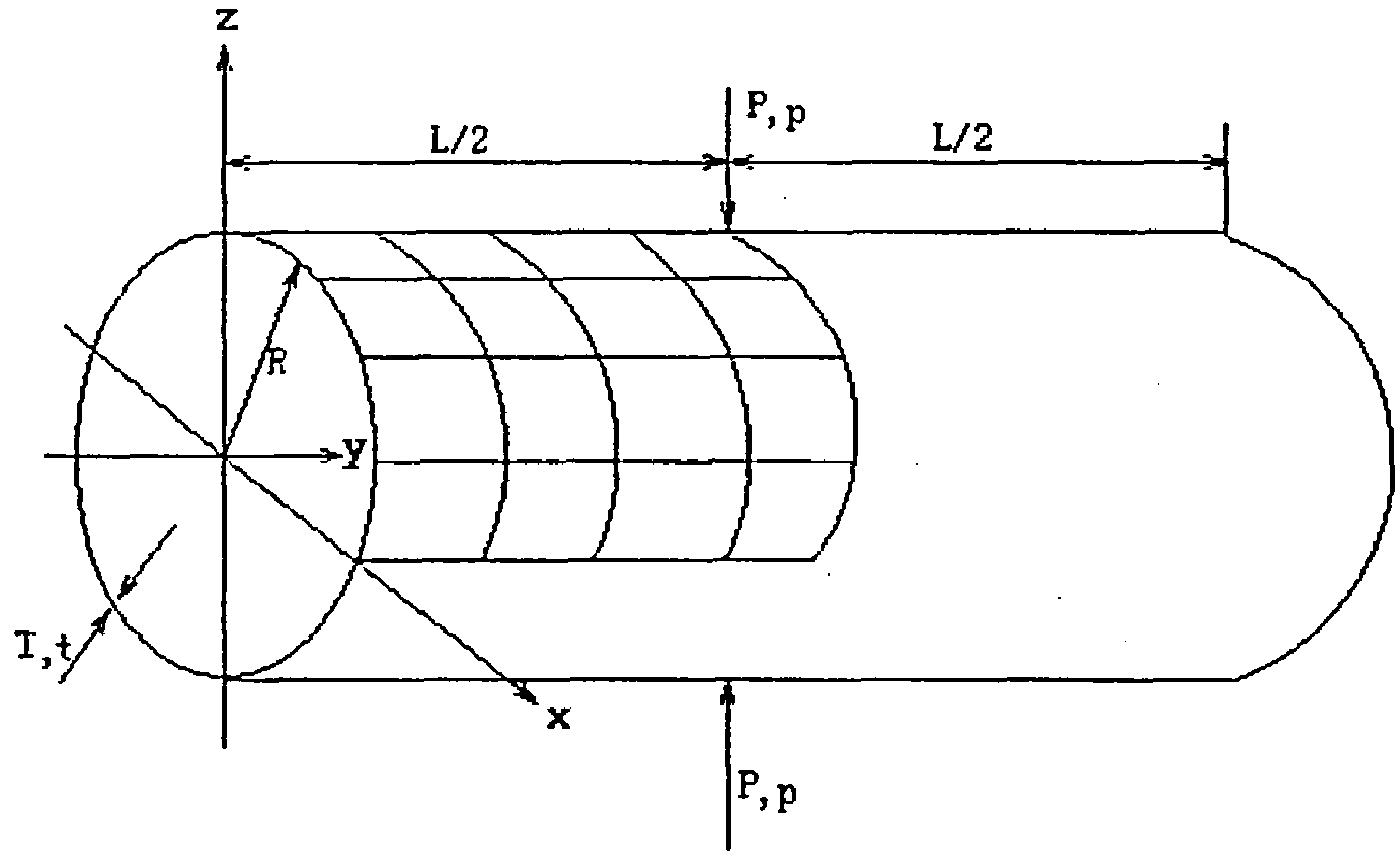

$R = 4.935$ inches
$L = 10.35$ inches
$E = 10.5\ 10^6\ \mathrm{lb/in}^2$
$T = 0.094$ inches
$t = 0.01548$ inches
$P = 100$ lb (for T)
$p = 0.1$ lb (for t)
$\nu = 0.3125$

Figure 2.7 : The pinched cylinder test problem

This problem also demonstrates the accuracy and convergence of the shell by means of various meshes. Thick and fairly thin shells are employed in this problem. Tables 2.1a-b and Fig. 2.8a-b show the normalized values with respect to the analytic solution. It shows that the present shell element performs very well compared to other elements found in the literature.

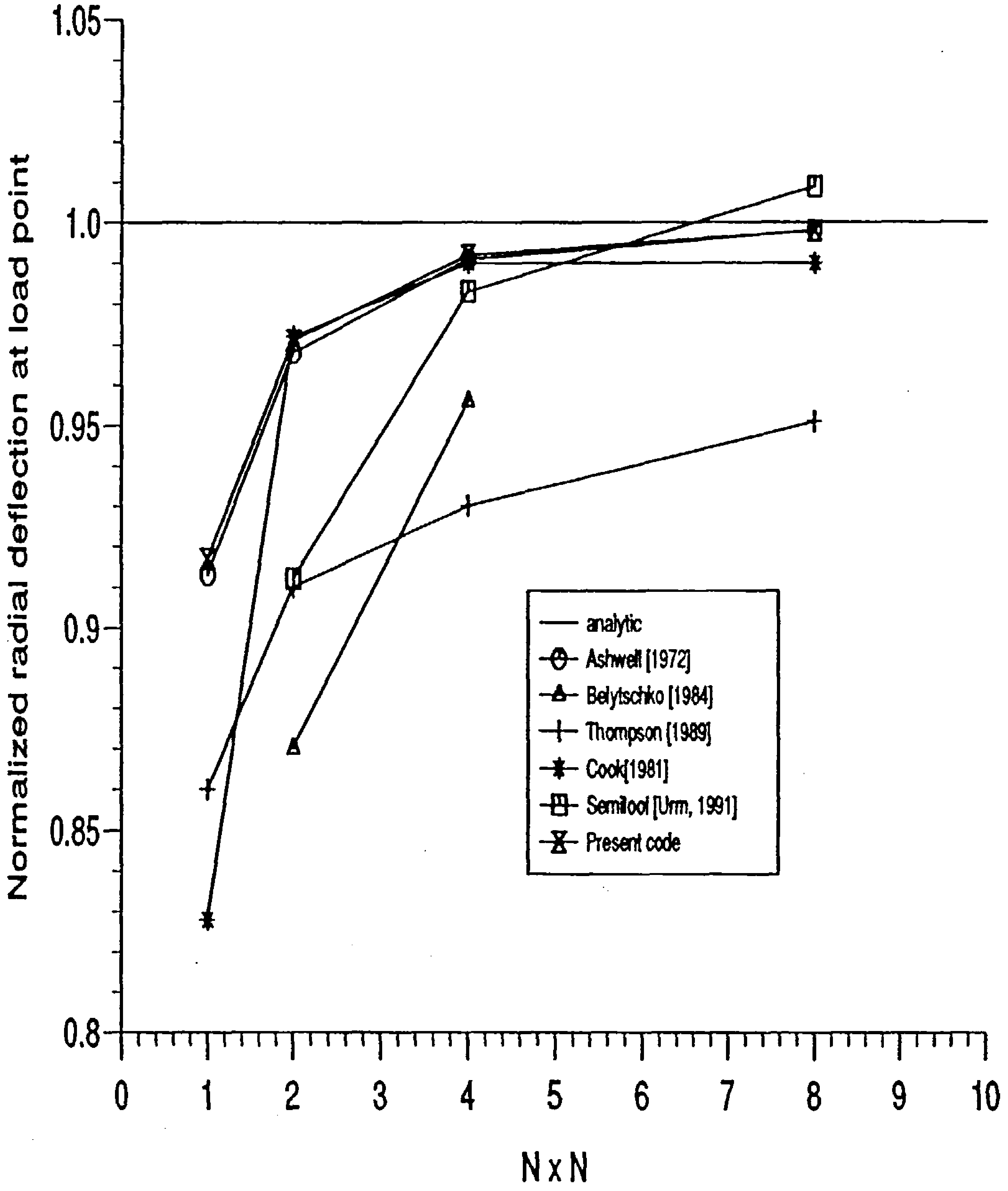

Figure 2.8a : A comparison of convergence of pinched cylinder with thick shell. t=0.094

T = 0.094 inches: deflection at load point= 0.1139 inches [Cantin, 1970]

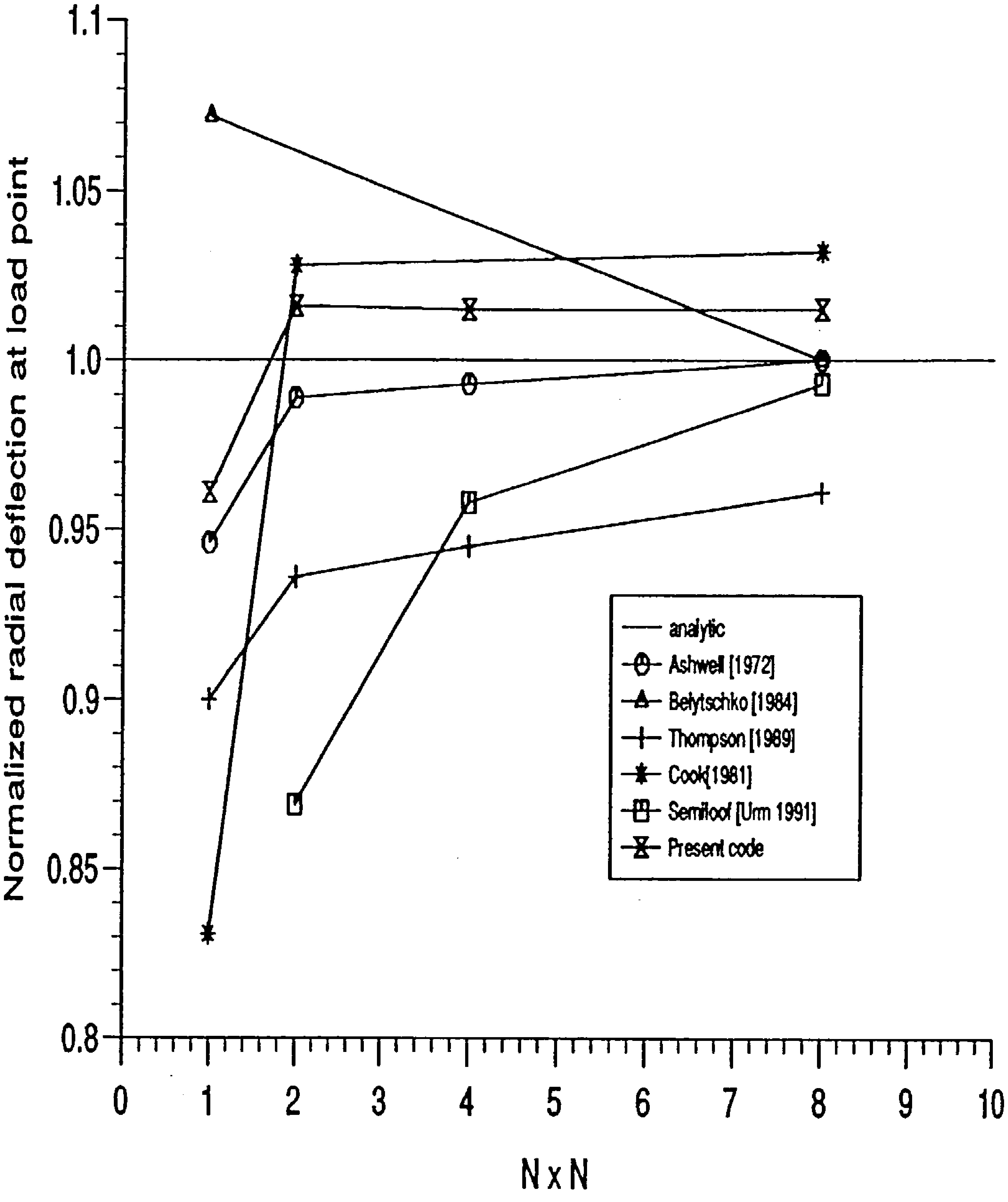

Figure 2.8b : A comparison of convergence of pinched cylinder
with thin shell, t=0.01548

t = 0.01548 inches: deflection at load point= 0.0241 inches [Ashwell 1972]

mesh	Ashwell (1972)	Belytschko (1984)	Thompson (1989)	Cook (1981)	Semiloof (Urm 1991)	Present code
1 x 1	0.913	-	0.86	0.828	-	0.917
2 x 2	0.968	0.87	0.91	0.972	0.912	0.971
4 x 4	0.991	0.956	0.93	0.99	0.983	0.992
8 x 8	0.998	-	0.951	0.99	1.009	0.998

Table 2.1 — Normalized deflection of pinched cylinder with thick shell

mesh	Ashwell (1972)	Belytschko (1984)	Thompson (1989)	Cook (1981)	Semiloof (Urm 1991)	Present code
1 x 1	0.946	1.072	0.90	0.831	-	0.912
2 x 2	0.989	-	0.936	1.028	0.869	1.016
4 x 4	0.993	-	0.945	-	0.958	1.015
8 x 8	1.0	1.0	0.961	1.032	0.993	1.015

Table 2.2 — Normalized deflection of pinched cylinder with thin shell

Example 2. Cylindrical Roof

As proposed by MacNeal [1985], the cylindrical roof is used to demonstrate the performance of the shell. This problem is often referred to as the Scordelis-Lo cylindrical roof. The cylindrical roof is subjected to a gravity load and has prescribed rigid diaphgrams at the two ends (see Fig. 2.9). Both membrane and bending response are equally essential in this problem. Various meshes are used to demonstrate the accuracy and convergence of shell element. Fig. 2.10a and Fig. 2.10b show the vertical deflection at the middle of the shell and the axial deflection at the support. The convergence rate is fairly rapid as the mesh density is increased. In fact, the solution of the one shell element model is already close to the analytic solution.

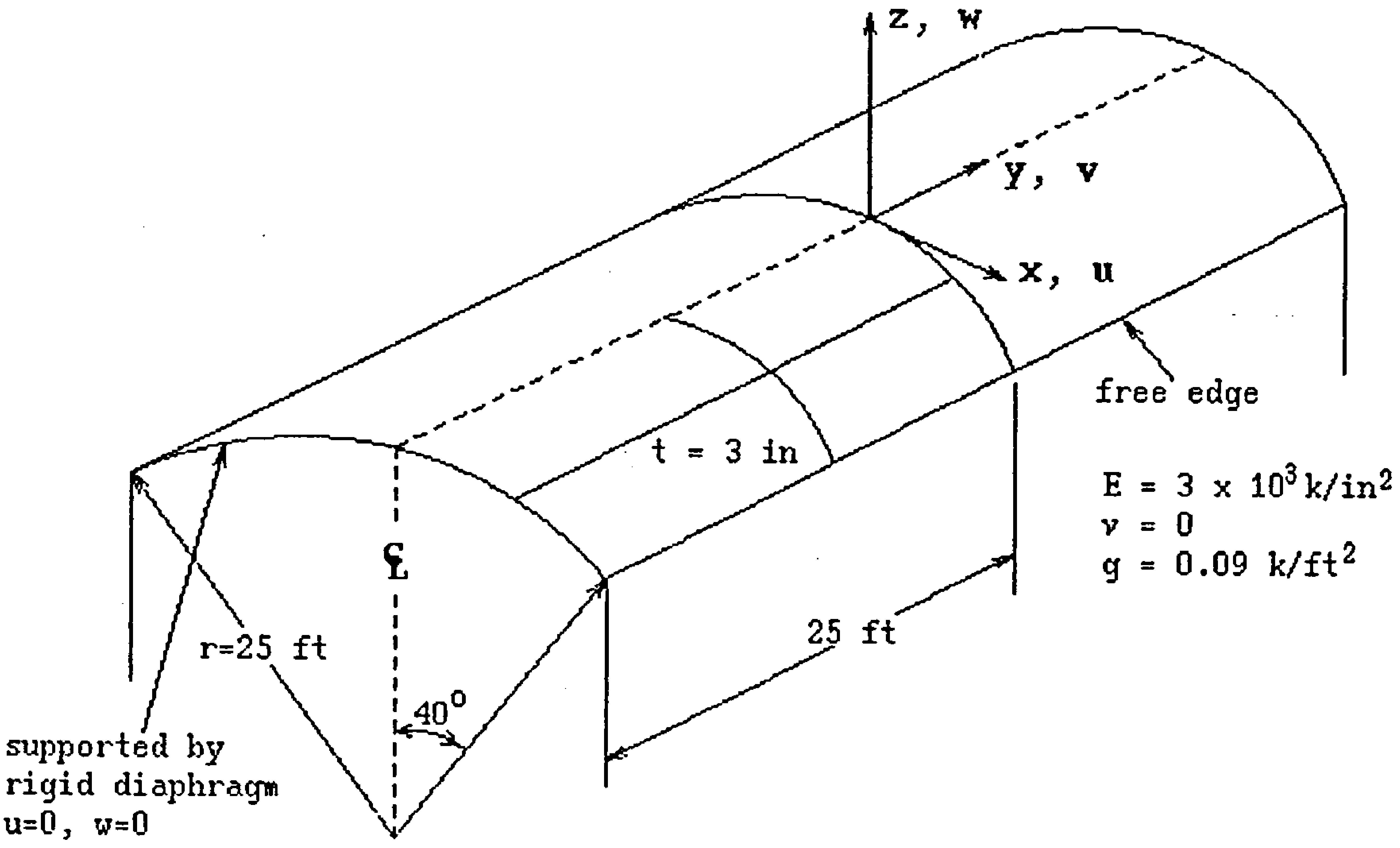

Figure 2.9 : Cylindrical roof test problem

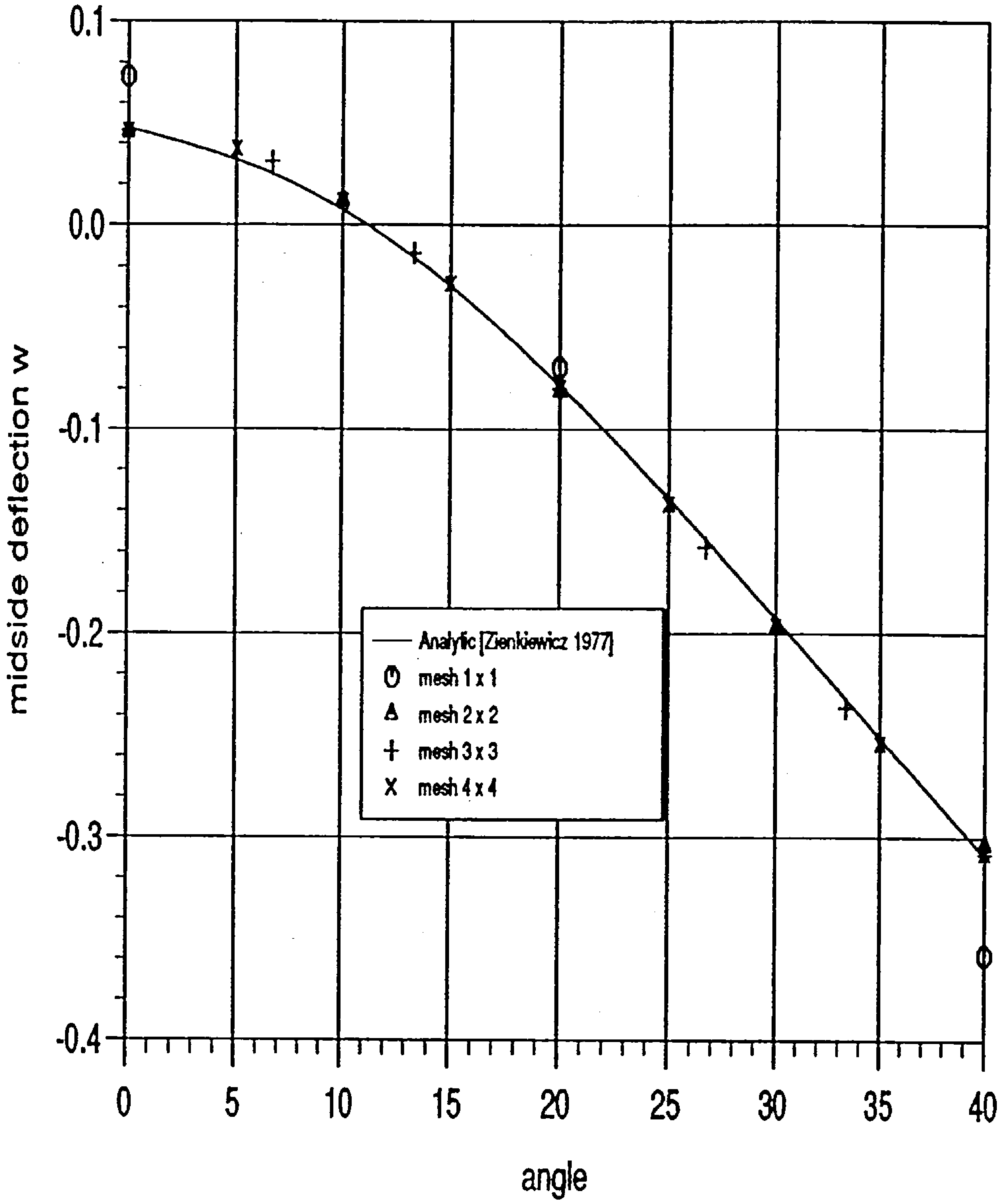

Figure 2.10a : Vertical deflection at midle of the shell of cylindrical roof test problem

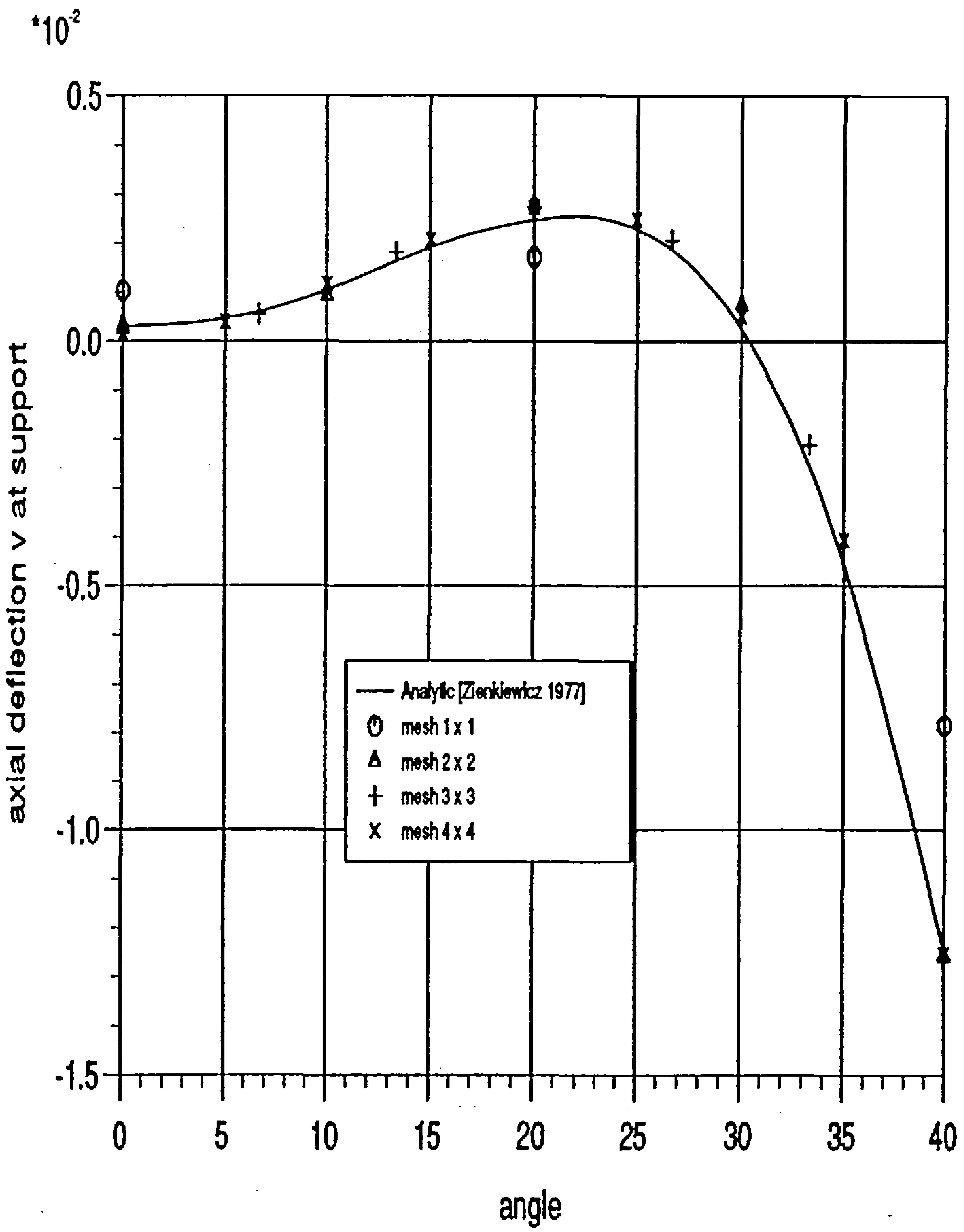

Figure 2.10b : Axial deflection at the support of cylindrical roof test problem

Example 3. A spherical Cap

Fig. 2.11 shows the geometry and the meshes used for a spherical cap subjected to a uniform external pressure. This is a good example for demonstrating the element's ability in representing doubly curved deep shell action, with an inextensional bending mode with almost no membrane strain. On the whole the results for the radial deflection along the arch of the cap, as shown Fig. 2.12, are in satisfactory agreement with the exact solution [Zienkiwiecz 1989] with such a

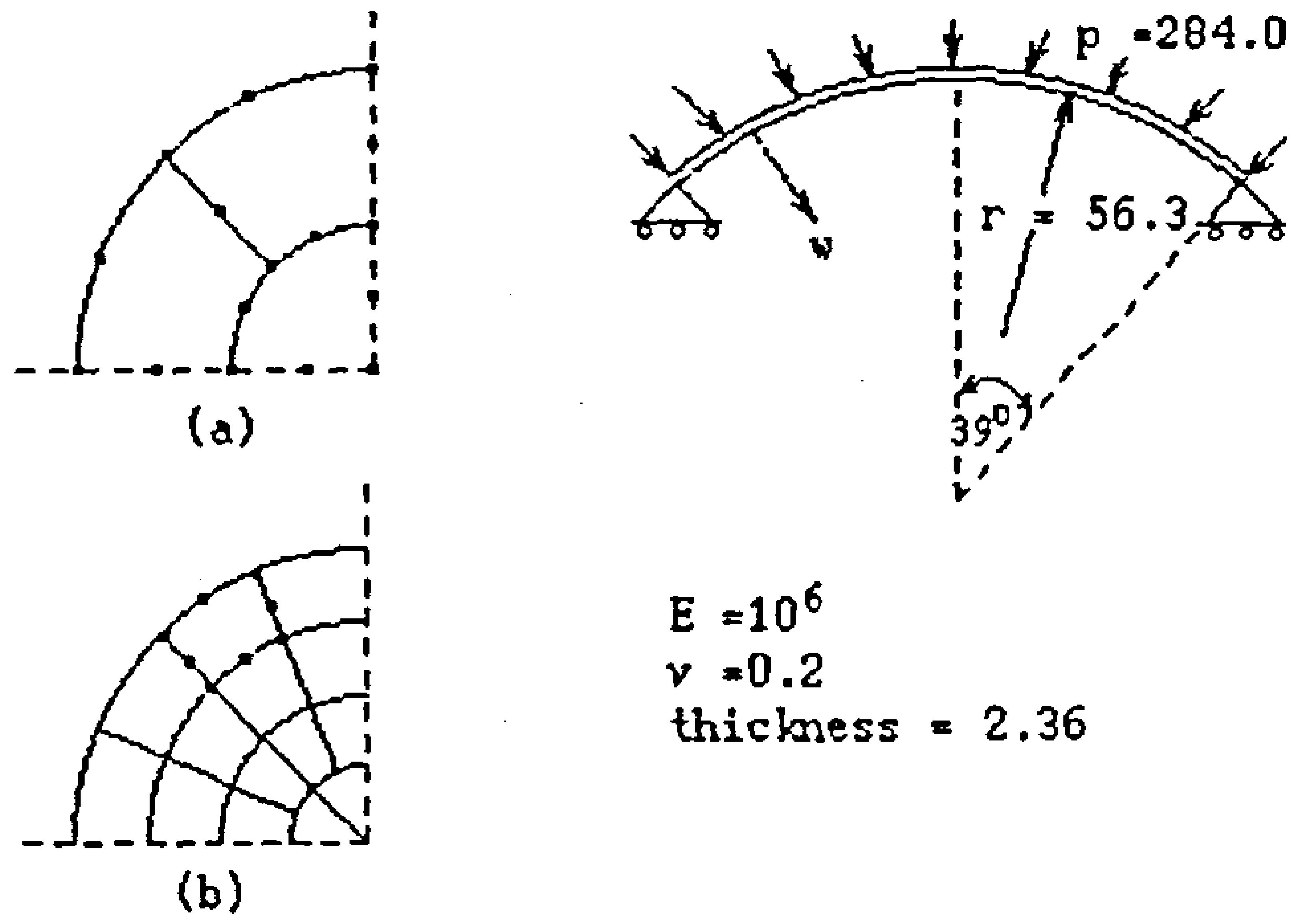

Figure 2.11 : Geometry and meshes of spherical cap test problem

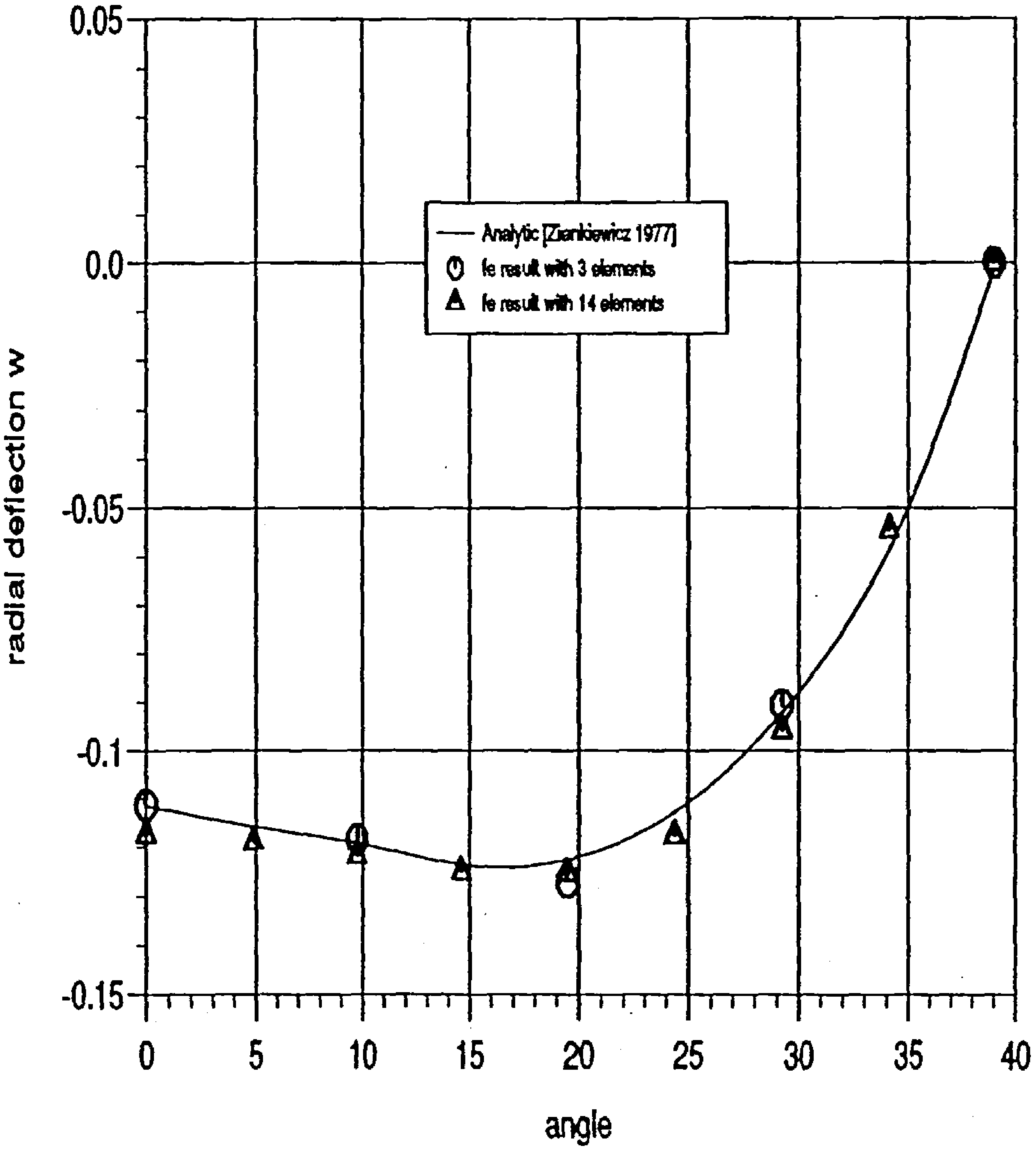

Figure 2.12 : Radial displacement on a spherical cap under uniform pressure

coarse mesh.

Example 4. Hemispherical Shell

As proposed by MacNeal [1985], hemispherical shell under a point load on the quadrant is analysed. Fig. 2.13 shows the detailed geometry. By symmetry, only one eighth of the sphere was modelled by various refined meshes. This is also a good example for demonstrating the element's ability in representing doubly curved deep shell action, an inextensional bending mode with almost no strains and rigid body rotation. Fig. 2.14 shows the convergence curves for normalized displacement in the direction of applied load against N, where N is the number of elements along one edge. As the number of elements increased, reasonable results were obtained by the present analysis.

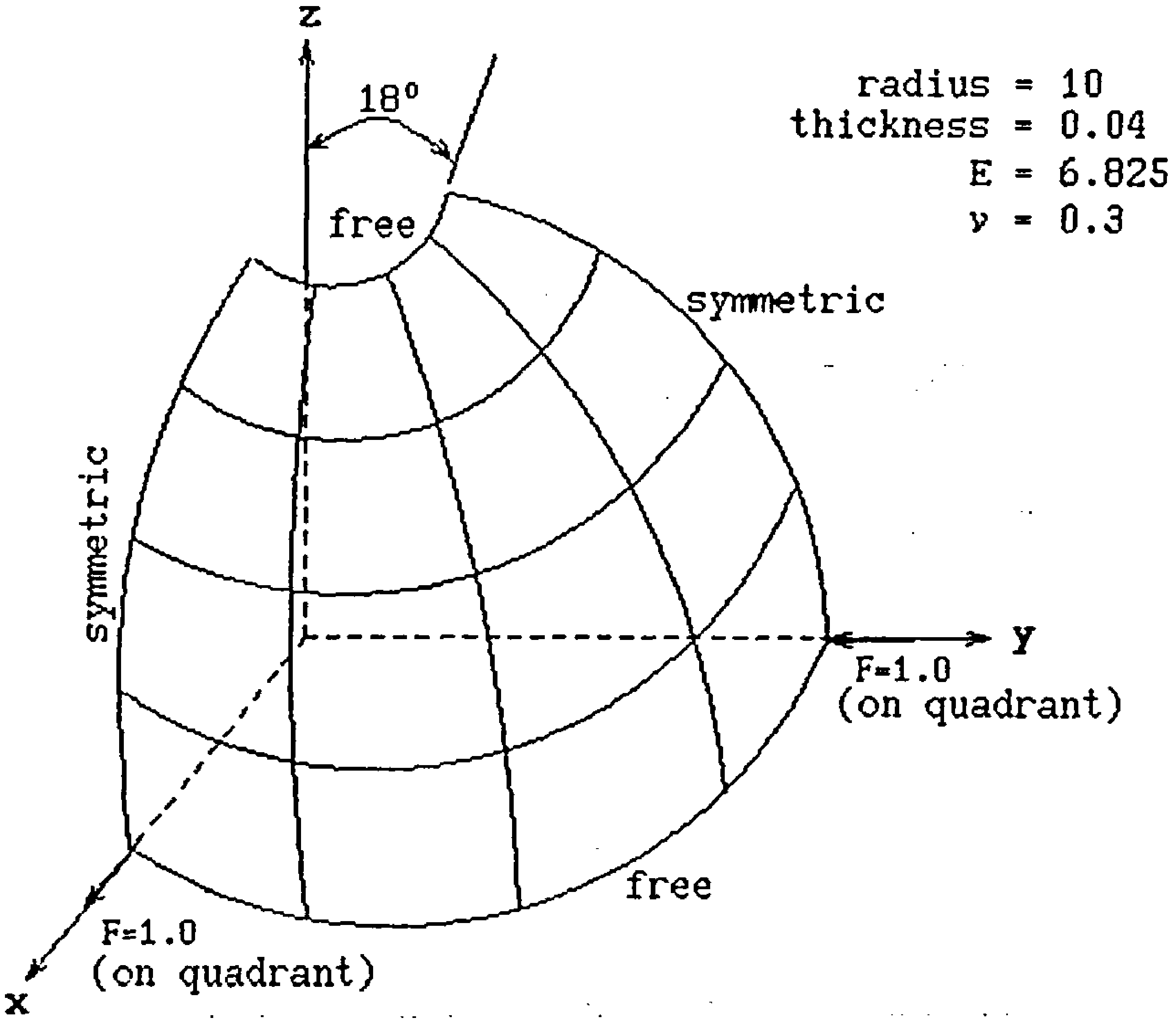

Figure 2.13 : One eighth of a hemi-spherical shell

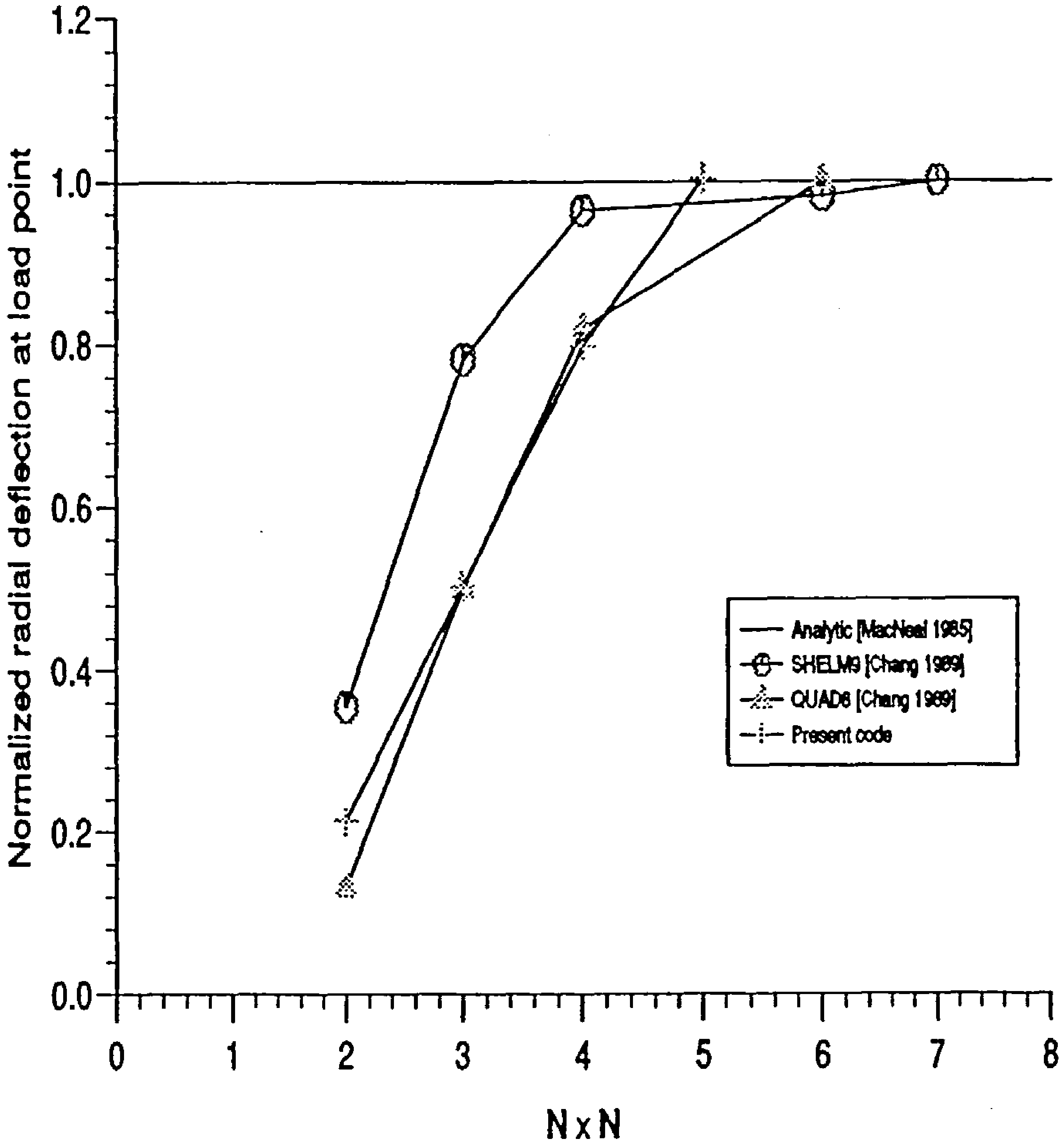

Figure 2.14 : The convergence curve of normalized displacement of hemispherical shell

Example 5. Cantilever Cylindrical Beam

A cantilever cylinder beam under tip loading was analysed. Fig. 2.15 shows the geometry of the cylinder beam. The purpose of this example is to demonstrate the abilty of shell element with respect to rigid body rotation by using implicit thickness integration in the Jacobian matrix as discussed in section 2.2.3. Different material properties are applied at the tip of the cylinder beam. Fig. 2.16 shows that straining under rigid body rotations strain occurred for the shell element without thickness integration when different material properties are applied on the tip of the beam.

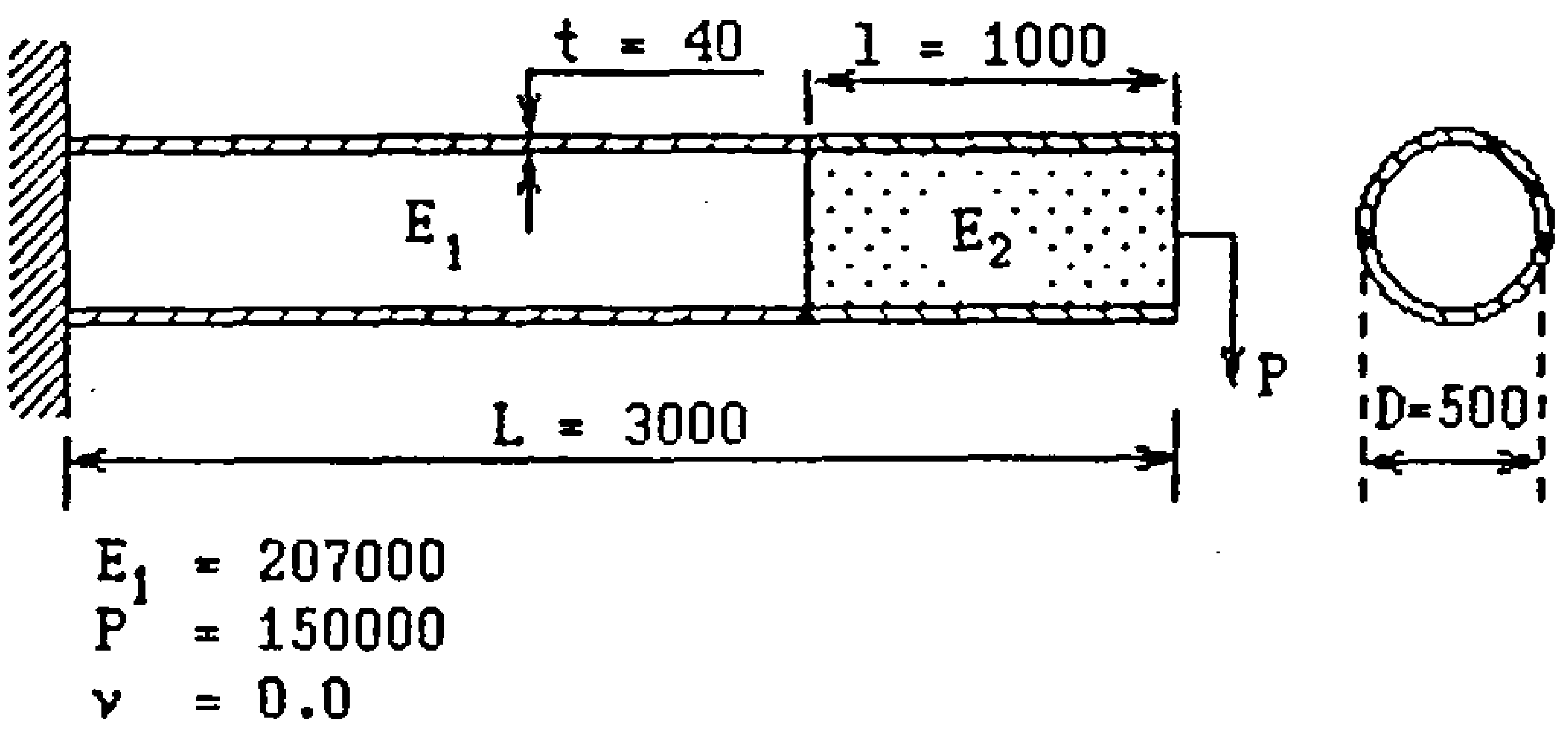

Figure 2.15 : A cantilever cylinder beam

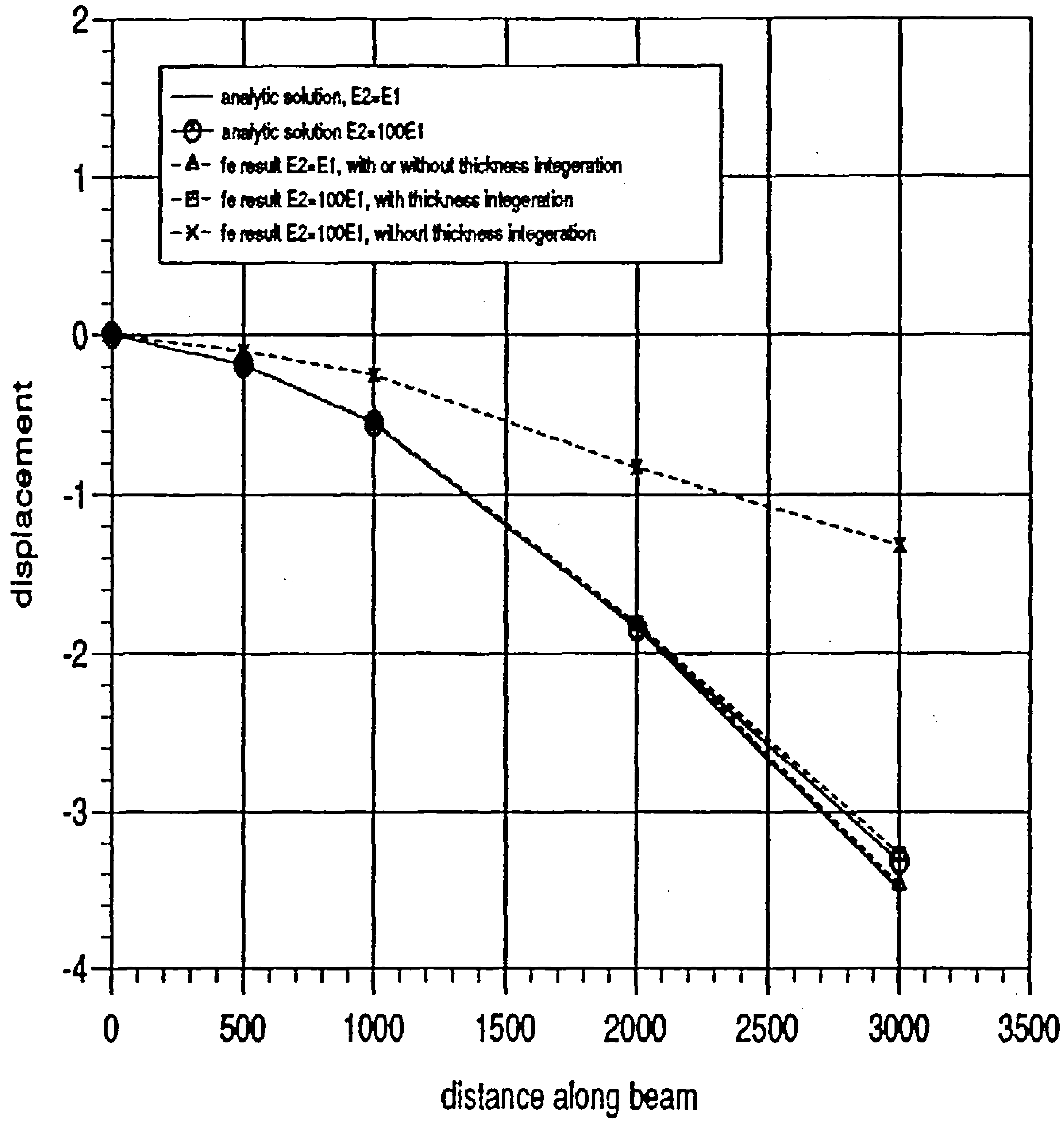

Figure 2.16 : A cantilever cylinder beam deflection

2.6 Summary

Several benchmark tests have been employed in the present shell element formulation and results show that the shell element performs resonable well. The formulation of local and nodal coordinates has the advantage that the present formulation does not require the upper and bottom surface coordinates. This advantage leads to the simpler coding of the mesh generator. Six degree of freedom is advantageous when used to analyse folded shell structures.

The layer intgration through the thickness of the element avoids the restrain of rigid body rotation and takes into account variation of the stress which are important in the analysis of the material nonlinerity. However, the layer analysis requires large CPU time.

Chapter III

Geometrically and Materially Nonlinear Analysis of Shell Finite Element

3.1 General Formulation of Nonlinear Finite Element

If a problem is geometrically nonlinear this implies that the displacements are so large that small displacement theory is no longer valid, while material nonlinearity means that the material behaviour is no longer limited to the elastic region [Washizu 1985]. The formulation of geometrically nonlinear and materially nonlinear problems may use small strain or large strain. In the case of large strain analysis, special relationship between stress and strain have to be introduced [Crisfield 1991, Zienkiewicz 1991]. Moreover the definitions of stress and strain are no longer unique. To formulate a nonlinear problem, incremental theories must be be employed. Various formulations have been used in practice, for example the Eulerian formulation, the Lagrangian formulation and the corotational formulation, and some results have been obtained for nonlinear analysis invoking large displacement and large strain Bathe[1980], Crisfield[1991], Hibbit[1970], Zienkiewicz[1991]. Here, the total Lagrangian and the update Lagrangian formulation will be adopted, and we now define them.

The total Lagrangian formulation is also referred to as the Lagrangian formulation. In this solution scheme all static and kinematic variables are referred to the initial configuration. The updated Lagrangian formulation is based on the same procedures that are used in total Lagrangian formulation, but in the solution all static and kinematic variables are referred to the configuration at the previous state, state t, and as the name suggests, the configuration is regularly updated. To formulate the total and updated Lagrangian, the Green and updated Green strain increment tensors must be employed.

3.1.1 Green and Updated Green Strain Increment

The loading path of a solid body problem can be approximated by linearization into a number of equlibrium states ${}^0\Omega$, ${}^t\Omega$, ${}^{t+\Delta t}\Omega$, ${}^{2t}\Omega$, where ${}^0\Omega$ and ${}^{2t}\Omega$ are the initial and the final states of deformation and the other states are arbitrary intermediate states. Here, the analysis of the body motion is referred to a stationary cartesian coordinate system as displayed in Fig. 3.1. To develop a solution strategy, it is assumed that the solution for stresses, strains and displacements, together with the loading history have been obtained up to the previous equilibrium state ${}^t\Omega$. Then the solution processes for the next step require the equilibrium position corresponding to ${}^{t+\Delta t}\Omega$. This process can be approached by using the stress and strain result at ${}^t\Omega$, and the process is repeated until the complete final solution path has been obtained.

To formulate the incremental strain, we shall refer to Fig. 3.1. The coordinates of point ${}^0P$ in the body at state 0 are ${}^0x_1$, ${}^0x_2$, ${}^0x_3$ and at state t the coordinates of point ${}^tP$ are ${}^tx_1$, ${}^tx_2$, ${}^tx_3$ and at state $t + \Delta t$ the coordinates of point ${}^{t+\Delta t}P$ are ${}^{t+\Delta t}x_1$, ${}^{t+\Delta t}x_2$, ${}^{t+\Delta t}x_3$. The left superscript denotes the configuration of the body. The displacement at the state t is denoted by ${}^tu_i$ and the displacement at state $t + \Delta t$ is denoted by ${}^{t+\Delta t}u_i$ or the incremental displacement from state ${}^t\Omega$ to state ${}^{t+\Delta t}\Omega$ is denoted by Δu_i. Where $i = 1,2,3$.

Using the notation of Fig. 3.1, the vector position of point ${}^0P$, ${}^tP$, and ${}^{t+\Delta t}P$ in cartesian coordinates can be written as follows:

$$\begin{aligned}
{}^0r &= {}^0x_i v_i \\
{}^tr &= {}^tx_i v_i = {}^0r + U = ({}^0x_i + {}^tu_i)v_i \\
{}^{t+\Delta t}r &= {}^{t+\Delta t}x_i v_i = {}^0r + U + \Delta U \\
{}^{t+\Delta t}r &= {}^tx_i + \Delta u_i v_i = ({}^0x_i + {}^tu_i + \Delta u_i)v_i
\end{aligned} \tag{3.1}$$

where $\{v_1, v_2, v_3\}$ is the base vector of the cartesian coordinate system.

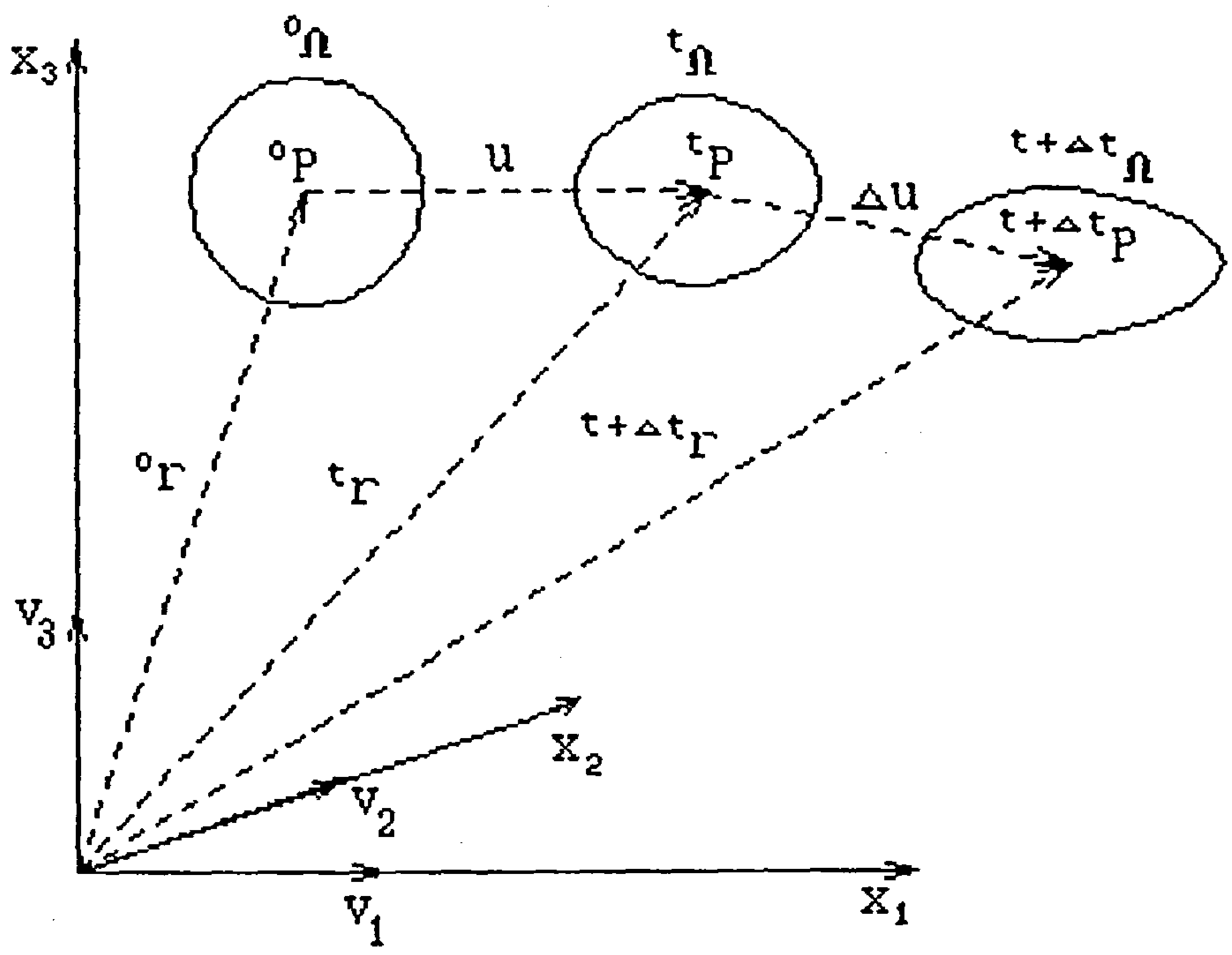

Figure 3.1 : The equilibrium of moving body.

During the motion of the body, the Green strain tensor at state $^t\Omega$ can be written as follows:

$$2E_{ij} = {}^t r_{,i} \cdot {}^t r_{,j} - {}^0 r_{,i} \cdot {}^0 r_{,j}$$

$$2E_{ij} = u_{i,j} + u_{j,i} + u_{k,i}u_{k,j} \tag{3.2}$$

and at state $^{t+\Delta t}\Omega$ the Green strain tensor can be written as follows:

$$2(E_{ij} + \varepsilon_{ij}) = {}^{t+\Delta t} r_{,i} \cdot {}^{t+\Delta t} r_{,j} - {}^0 r_{,i} \cdot {}^0 r_{,j} \tag{3.3}$$

where $(*)_{,i} = \frac{\partial(*)}{\partial^0 x_j}$. On substituting eq.(3.2) into eq.(3.3), the strain increment ε_{ij} can be written as:

$$2\varepsilon_{ij} = {}^{t+\Delta t} r_{,i} \cdot {}^{t+\Delta t} r_{,j} - {}^t r_{,j} \cdot {}^t r_{,i}$$

$$2\varepsilon_{ij} = (\delta_{kj} + u_{k,j})\Delta u_{k,i} + (\delta_{ki} + u_{k,i})\Delta u_{k,j} + \Delta u_{k,i}\Delta u_{k,j}$$

$$2\varepsilon_{ij} = (\delta_{kj} + \frac{\partial u_k}{\partial^0 x_j})\frac{\Delta u_k}{\partial^0 x_i} + (\delta_{ki} + \frac{\partial u_k}{\partial^0 x_i})\frac{\Delta u_k}{\partial^0 x_j} + \frac{\partial u_k}{\partial^0 x_i}\frac{\partial u_k}{\partial^0 x_j} \quad (3.4)$$

ε_{ij} is called the Green strain increment tensor. If ${}^t\Omega$ is taken as an initial strain increment tensor, another definition of strain increment may be adopted. Denoting the strain increment by ε^*_{ij}, we may write it as:

$$2\varepsilon^*_{ij} = \frac{\partial^{t+\Delta t} r}{\partial^t x_i} \cdot \frac{\partial^{t+\Delta t} r}{\partial^t x_j} - \frac{\partial^t r}{\partial^t x_i} \cdot \frac{\partial^t r}{\partial^t x_j}$$

$$2\varepsilon^*_{ij} = \frac{\partial \Delta u_i}{\partial^t x_j} + \frac{\partial \Delta u_j}{\partial^t x_i} + \frac{\partial \Delta u_k}{\partial^t x_i}\frac{\partial \Delta u_k}{\partial^t x_j} \quad (3.5)$$

The strain increment ε^*_{ij} is called the updated Green strain increment tensor. Using the Jacobian transformation laws, the relation between ε_{ij} and ε^*_{ij} can be expressed as follows.

$$\varepsilon_{ij} = \frac{\partial^t x_m}{\partial^0 x_i}\frac{\partial^t x_n}{\partial^0 x_j}\varepsilon^*_{mn}$$

$$\varepsilon^*_{ij} = \frac{\partial^0 x_m}{\partial^t x_i}\frac{\partial^0 x_n}{\partial^t x_j}\varepsilon_{mn} \quad (3.6)$$

If ε_{ij} and ε^*_{ij} are linearized with respect to u_k, eq.(3.4) and eq.(3.5) may be written as follows:

$$2e_{ij} = (\delta_{kj} + u_{k,j})\Delta u_{k,i} + (\delta_{ki} + u_{k,i})\Delta u_{k,j}$$

$$2e^*_{ij} = \frac{\partial \Delta u_i}{\partial^t x_j} + \frac{\partial \Delta u_j}{\partial^t x_i} \quad (3.7)$$

3.1.2 Total and Updated Langrangian Formulation

Let the stress be denoted by σ_{ij} and the strain denoted by E_{ij}. The principle of virtual work can be formulated in general form as follows:

$$\int_V \sigma_{ij}\delta E_{ij} dV = \delta w \quad (3.8)$$

where δw is the variation of virtual work. Considering the definition of total Lagrangian given previously, eq.(3.8) at state ${}^{t+\Delta t}\Omega$ can be expressed in more detail.

$$\int_V [(\sigma_{ij} + \Delta\sigma_{ij})\delta(E_{ij} + \varepsilon_{ij}) - (F_i^b + \Delta F_i^b)\delta\Delta u_i] d^0V$$

$$- \int_A (F_i^s + \Delta F_i^s)\delta\Delta u_i d^0A = 0 \tag{3.9}$$

where variations are taken with respect to Δu_i. The Green strain tensor is defined by eq.(3.3) and $(\sigma_{ij} + \Delta\sigma_{ij})$ is the Kirchoff stress tensor. The body forces F_i^b and surface forces F_i^s are defined per unit volume and per unit area respectively at $^0\Omega$. ΔF_i^s is incremental surface force. On substituting eq.(3.3) into eq.(3.9) and neglecting displacement product terms of higher order, we obtain:

$$\int_V [(\Delta\sigma_{ij}\delta e_{ij} + \sigma_{ij}\delta\frac{1}{2}(u_{k,i}u_{k,j}) - \Delta F_i^b \delta u_i] d^0V - \int_A \Delta F_i^s d^0A$$

$$- \int_V [\sigma_{ij}\delta e_{ij} - F_i^b \delta\Delta u_i] d^0V - \int_A F^s \delta\Delta u_i d^0A = 0 \tag{3.10}$$

If it is assumed that $^t\Omega$ state is in equilibrium, then the terms

$$\int_V [\sigma_{ij}\delta e_{ij} - F_i^b \delta\Delta u_i] d^0V - \int_A F^s \delta\Delta u_i d^0A \tag{3.11}$$

will vanish and we obtain the principle of virtual work for the total Lagrangian method as follows:

$$\int_V [(\Delta\sigma_{ij}\delta e_{ij} + \sigma_{ij}\delta\frac{1}{2}(\Delta u_{k,i}\Delta u_{k,j}) - \Delta F_i^b \delta u_i] d^0V - \int_A \Delta F_i^s d^0A = 0 \tag{3.12}$$

where ϵ_{ij} is the linear strain defined by eq.(3.7).

For the updated Lagrangian formulation, the principle of virtual work at the state $^{t+\Delta t}\Omega$ may be expressed by:

$$\int_V [(\sigma_{ij}^E + \Delta\sigma_{ij}^*)\delta\varepsilon_{ij}^* - (F_i^b + \Delta F_i^b)\delta\Delta u_i] d^tV - \int_A (F_i^s + \Delta F_i^s) d^tA = 0 \tag{3.13}$$

where the variations are taken with respect to Δu_i. The updated Green strain tensor ε^*_{ij} is defined in eq.(3.5). σ^E_{ij} is the Euler stress tensor and $\Delta\sigma^*_{ij}$ is the updated Kirchoff stress. The body forces F^b_i and the surface forces F^s_i are defined per unit volume and per unit area respectively at ${}^t\Omega$. On subtituting eq.(3.5) into eq.(3.13) we obtain:

$$\int_V [\Delta\sigma^*_{ij}\delta\epsilon^*_{ij} + \frac{1}{2}\sigma^E_{ij}\delta(\frac{\partial\Delta u_k}{\partial x_i}\frac{\partial\Delta u_k}{\partial x_j}) - \Delta F^b_i\delta\Delta u_i]d^tV - \int_A \Delta F^s_i\delta\Delta u_i d^tA$$

$$-\int_V [\sigma^E_{ij}\delta\epsilon^*_{ij} - F^b_i\delta\Delta u_i]d^tV - \int_A F^b_i\delta\Delta u_i d^tA = 0 \qquad (3.14)$$

If it is assumed that ${}^t\Omega$ is an equilibrium state then the term

$$-\int_V [\sigma^E_{ij}\delta\epsilon^*_{ij} - F^b_i\delta\Delta u_i]d^tV - \int_A F^s_i\delta\Delta u_i d^tA = 0 \qquad (3.15)$$

will vanish in which case we can obtain the updated Lagrangian principle of virtual work statement as follows:

$$\int_V [\Delta\sigma^*_{ij}\delta\epsilon^*_{ij} + \frac{1}{2}\sigma_{ij}\delta(\frac{\partial\Delta u_k}{\partial x_i}\frac{\partial\Delta u_k}{\delta x_j}) - \Delta F^b_i\delta\Delta u_i]d^tV - \int_A \Delta F^s_i\delta\Delta u_i d^tA = 0 \quad (3.16)$$

where e^*_{ij} is a linear Green strain tensor for updated Lagrangian strain which is given in eq.(3.7). The formulations of total Lagrangian eq.(3.12) and updated Lagrangian eq.(3.16) can now be implemented for the nonlinear shell finite element.

3.2 Nonlinear Shell Finite Element Analysis

The geometric and displacement field which is formulated in shell finite element will be adopted to develop nonlinear shell finite element. Using eq.(2.9), the coordinate at any point in an element of any configuration can be written as:

$${}^tx(\xi,\eta,\zeta) = \sum_{k=1}^{n} N^k(\xi,\eta)[{}^tx^k_i + 0.5\zeta\,{}^tV_{3k}] \qquad (3.17a)$$

where the left superscript denotes the configuration of the element. The displacement field at any point and the incremental displacement field can be written using eq.(2.11) as:

$$ {}^t u(\xi,\eta,\zeta) = \sum_{k=1}^{n} N^k(\xi,\eta)\{{}^t u_i^k + \frac{1}{2}\zeta t \Phi^k \alpha_i^k\} \tag{3.17b} $$

and

$$ \Delta u(\xi,\eta,\zeta) = \sum_{k=1}^{n} N^k(\xi,\eta)\{\Delta u_i^k + \frac{1}{2}\zeta t \Phi^k \alpha_i^k\} \tag{3.17c} $$

The displacement derivatives of any configuration and the displacement increment with respect to the global coordinate system can be obtained using eq.(2.22). Then the derivative of displacement at any configuration and the displacement increment respect to the local coordinate system may be obtained using eq.(2.16). For the next presentation, all the derivatives displacement are in the local coordinate system.

3.2.1 Stress-strain Relationship of Nonlinear Shell

The stress field ${}^{t+\Delta t}\sigma_{ij}$ always refers to the state ${}^t\Omega$ and it has to satisfy the yield criteria in nonlinear material analysis. For the total Lagrangian formulation Kirchoff stress tensor is applied to eq.(3.10 & 3.12) and for the Updated Lagrangian formulation the updated Kirchoff stress tensor or Jaumann stress tensor may be applied. Both formulations should give the same result, Bathe [1982]. Referring to equation 3.9 and 3.13 the stress at state ${}^{t+\Delta t}\Omega$

$$ {}^{t+\Delta t}\sigma_{ij} = \sigma_{ij} + \Delta\sigma_{ij} \tag{3.18a} $$

for Kirchoff stress and

$$ {}^{t+\Delta t}\sigma^*_{ij} = \sigma^E_{ij} + \Delta\sigma^*_{ij} \tag{3.18b} $$

for Updated Kirchoff stress. σ^E_{ij} is Euler stress tensor.For the next state ${}^{t+2\Delta t}\Omega$, the Kirchoff stress may be applied directly to total Lagrangian formulation because the measurements are taken with respect to the initial configuration. Before applying the updated Lagrangian formulation, the updated Kirchoff stresses need to be transformed to the ${}^{t+\Delta t}\Omega$ configuration, and it is then called the Euler stress σ^E_{ij} or Cauchy stress [Washizu 1982]. The transformation law between $\sigma^E_{ij} + \Delta\sigma^*_{ij}$ and $\sigma^E_{ij} + \Delta\sigma^E_{ij}$ may be written as follows:

$$\sigma^E_{ij} + \Delta\sigma^E_{ij} = \frac{1}{|D^{t+\Delta t}|}\frac{\partial^{t+\Delta t}x_i}{\partial^t x_k}\frac{\partial^{t+\Delta t}x_j}{\partial^t x_l}(\sigma^E_{kl} + \Delta\sigma^*_{kl}) \qquad (3.19a)$$

where $|D^{t+\Delta t}|$ is a determinant which can be obtained as follows :

$$|D^{t+\Delta t}| = \frac{\partial({}^{t+\Delta t}x_1, {}^{t+\Delta t}x_2, {}^{t+\Delta t}x_3)}{\partial({}^t x_1, {}^t x_2, {}^t x_3)} \qquad (3.19b)$$

The incremental Kirchoff stress and the updated Kirchoff stress may be defined using the constitutive equation as follows:

$$\Delta\sigma_{ij} = C_{ijkl}\Delta\epsilon_{ij} \qquad (3.20a)$$

and

$$\Delta\sigma^*_{ij} = C_{ijkl}\Delta\epsilon^*_{ij} \qquad (3.20b)$$

where $\Delta\epsilon_{ij}$ is the Green strain increment tensor and $\Delta\epsilon^*_{ij}$ is the updated Green strain increment tensor which are defined in eq.(3.7). C_{ijkl} is the elastic properties tensor which is given in eq.(2.28). For shell analysis, as usual, the elastic properties may be employed in the two dimensional forms as indicated in eq.(2.31) and can be rewritten as :

$$\left[\mathrm{C}'\right] = \frac{E}{1-\nu^2}\begin{bmatrix} 1 & \nu & 0 & 0 & 0 & 0 \\ & 1 & 0 & 0 & 0 & 0 \\ & & 0 & 0 & 0 & 0 \\ & & & \frac{1-\nu}{2} & 0 & 0 \\ & & & & \frac{1-\nu}{2k} & 0 \\ & symm. & & & & \frac{1-\nu}{2k} \end{bmatrix} \qquad (2.31)$$

where E and ν are Young's modulus and Poisson's ratio respectively and k is shear correction factor. For elasto-plastic analysis, the material properties must include the effect of past loading history and details of nonlinear material analysis will be discussed in section (3.3). Using eq.(2.31) the stress strain relation can be written as follows:

$$\Delta\sigma^{c} = \mathbf{C}'\mathbf{e} \tag{3.21a}$$

for incremental Kirchoff stress and

$$\Delta\sigma^{*} = \mathbf{C}'\Delta\mathbf{e}^{*} \tag{3.21b}$$

for incremental updated Kirchoff stress, where the stress is now in a vector form as:

$$[\Delta\sigma]^{T} = \{\Delta\sigma_{x}, \Delta\sigma_{y}, \Delta\sigma_{z}, \Delta\sigma_{xy}, \Delta\sigma_{yz}, \Delta\sigma_{xz}\} \tag{3.22a}$$

and

$$[\Delta\sigma^{*}]^{T} = \{\Delta\sigma^{*}_{x}, \Delta\sigma^{*}_{y}, \Delta\sigma^{*}_{z}, \Delta\sigma^{*}_{xy}, \Delta\sigma^{*}_{yz}, \Delta\sigma^{*}_{xz}\} \tag{3.22b}$$

The Green strain increment in vector form may be constructed from eq.(3.7) as follows:

$$\mathbf{e} = \begin{bmatrix} \epsilon_x \\ \epsilon_y \\ \epsilon_z \\ \epsilon_{xy} \\ \epsilon_{yz} \\ \epsilon_{xz} \end{bmatrix} = \begin{bmatrix} \frac{\partial \Delta u'_1}{\partial^0 x'_1} \\ \frac{\partial \Delta u'_2}{\partial^0 x'_2} \\ \frac{\partial \Delta u'_3}{\partial^0 x'_3} \\ \frac{\partial \Delta u'_1}{\partial^0 x'_2} + \frac{\partial \Delta u'_2}{\partial^0 x'_1} \\ \frac{\partial \Delta u'_2}{\partial^0 x'_3} + \frac{\partial \Delta u'_3}{\partial^0 x'_2} \\ \frac{\partial \Delta u'_1}{\partial^0 x'_3} + \frac{\partial \Delta u'_3}{\partial^0 x'_1} \end{bmatrix} +$$

$$\frac{1}{2}\begin{bmatrix} \frac{\partial u'_1}{\partial^0 x'_1}\frac{\partial \Delta u'_1}{\partial^0 x'_1} + \frac{\partial u'_2}{\partial^0 x'_1}\frac{\partial \Delta u'_2}{\partial^0 x'_1} + \frac{\partial u'_3}{\partial^0 x'_1}\frac{\partial \Delta u'_3}{\partial^0 x'_1} \\ \frac{\partial u'_1}{\partial^0 x'_2}\frac{\partial \Delta u'_1}{\partial^0 x'_2} + \frac{\partial u'_2}{\partial^0 x'_2}\frac{\partial \Delta u'_2}{\partial^0 x'_2} + \frac{\partial u'_3}{\partial^0 x'_2}\frac{\partial \Delta u'_3}{\partial^0 x'_2} \\ \frac{\partial u'_1}{\partial^0 x'_3}\frac{\partial \Delta u'_1}{\partial^0 x'_3} + \frac{\partial u'_2}{\partial^0 x'_3}\frac{\partial \Delta u'_2}{\partial^0 x'_3} + \frac{\partial u'_3}{\partial^0 x'_3}\frac{\partial \Delta u'_3}{\partial^0 x'_3} \\ \frac{\partial u'_1}{\partial^0 x'_2}\frac{\partial \Delta u'_1}{\partial^0 x'_1} + \frac{\partial u'_1}{\partial^0 x'_1}\frac{\partial \Delta u'_1}{\partial^0 x'_2} + \frac{\partial u'_2}{\partial^0 x'_2}\frac{\partial \Delta u'_2}{\partial^0 x'_1} + \frac{\partial u'_2}{\partial^0 x'_1}\frac{\partial \Delta u_2}{\partial^0 x'_2} + \frac{\partial u'_3}{\partial^0 x'_2}\frac{\partial \Delta u'_3}{\partial^0 x'_1} + \frac{\partial u'_3}{\partial^0 x'_1}\frac{\partial \Delta u'_3}{\partial^0 x'_2} \\ \frac{\partial u'_1}{\partial^0 x'_3}\frac{\partial \Delta u'_1}{\partial^0 x'_2} + \frac{\partial u'_1}{\partial^0 x'_2}\frac{\partial \Delta u'_1}{\partial^0 x'_3} + \frac{\partial u'_2}{\partial^0 x'_3}\frac{\partial \Delta u'_2}{\partial^0 x'_2} + \frac{\partial u'_2}{\partial^0 x'_2}\frac{\partial \Delta u'_2}{\partial^0 x'_3} + \frac{\partial u'_3}{\partial^0 x'_3}\frac{\partial \Delta u'_3}{\partial^0 x'_2} + \frac{\partial u'_3}{\partial^0 x'_2}\frac{\partial \Delta u'_3}{\partial^0 x'_3} \\ \frac{\partial u'_1}{\partial^0 x'_3}\frac{\partial \Delta u'_1}{\partial^0 x'_1} + \frac{\partial u'_1}{\partial^0 x'_1}\frac{\partial \Delta u'_1}{\partial^0 x'_3} + \frac{\partial u'_2}{\partial^0 x'_3}\frac{\partial \Delta u'_2}{\partial^0 x'_1} + \frac{\partial u'_2}{\partial^0 x'_1}\frac{\partial \Delta u'_2}{\partial^0 x'_3} + \frac{\partial u'_3}{\partial^0 x'_3}\frac{\partial \Delta u'_3}{\partial^0 x'_1} + \frac{\partial u'_3}{\partial^0 x'_1}\frac{\partial \Delta u'_3}{\partial^0 x'_3} \end{bmatrix} \tag{3.23}$$

where the right superscript denotes the local system coordinate. $\Delta u'_i$ is increment displacement, and u'_i is the previous displament at ${}^{t}\Omega$. From eq.(3.7), the updated

Green strain increment tensor in vector form as follows:

$$\mathbf{e} = \begin{bmatrix} \epsilon_x^* \\ \epsilon_y^* \\ \epsilon_z^* \\ \epsilon_{xy}^* \\ \epsilon_{yz}^* \\ \epsilon_{xz}^* \end{bmatrix} = \begin{bmatrix} \frac{\partial \Delta u_1'}{\partial^t x_1'} \\ \frac{\partial \Delta u_2'}{\partial^t x_2'} \\ \frac{\partial \Delta u_3'}{\partial^t x_3'} \\ \frac{\partial \Delta u_1'}{\partial^t x_2'} + \frac{\partial \Delta u_2'}{\partial^t x_1'} \\ \frac{\partial \Delta u_2'}{\partial^t x_3'} + \frac{\partial \Delta u_3'}{\partial^t x_2'} \\ \frac{\partial \Delta u_1'}{\partial^t x_3'} + \frac{\partial \Delta u_3'}{\partial^t x_1'} \end{bmatrix} \tag{3.24}$$

It can be seen from eq.(3.24) that the updated Green strain increment is measured with respect to the ${}^t\Omega$ state configuration and there is no explicit previous displacement to define the increment of strain.

3.2.2 Stiffness Matrix of Total Lagrangian

The principle of virtual work for the total Lagrangian formulation in eq.(3.10) may be written as follows:

$$\int_V [(\Delta\sigma_{ij}\delta\epsilon_{ij} + \sigma_{ij}\delta\frac{1}{2}(\Delta u'_{k,i}\Delta u'_{k,j})]d^0V - \Delta R_{ext} = \varphi \tag{3.26}$$

where $\Delta R_{ext} = \int_V F_i^b \delta\Delta u_i d^0V + \int_A \Delta F_i^s d^0A$, which is in practice called the external work increment. φ is called the residual work, which should be zero if the increment state is in equilibrium, as mentioned before, and may be written as :

$$\varphi = \int_V [\sigma_{ij}\delta\epsilon_{ij} - F_i^b \delta\Delta u_i]d^0V - \int_A F_i^s d^0A \tag{3.27}$$

As indicated in eq.(3.20) and eq.(3.23) the material properties C'_{ijkl} and the Green strain tensor may be written in two dimensional form and vector form respectively. The Green strain increment eq.(3.23) may be separated into two terms as follows:

$$\mathbf{e} = \mathbf{e}_l + \mathbf{e}_{nl} \tag{3.28}$$

where e_l is the first term and e_{nl} is the second term of the right hand side of eq.(3.23). The incremental strain e_l can be written using the element shape function as:

$$\mathbf{e}_l = \mathbf{B}_0 \Delta \mathbf{U} \tag{3.29}$$

where $\mathbf{B}_0$ is the strain matrix of linear term of Green strain and ΔU are the vector incremental displacements $(\Delta u'_1, \Delta u'_2, \Delta u'_3)$ and rotations $(\Delta\alpha'_1, \Delta\alpha'_2, \Delta\alpha'_3)$ in terms of local coordinate. The second term of eq.(3.28), $\mathbf{e}_{nl}$ may be written in the the following matrix form:

$$\mathbf{e}_{nl} = \frac{1}{2}\begin{bmatrix} \frac{\partial u'_1}{\partial^0 x'_1} & \frac{\partial u'_2}{\partial^0 x'_1} & \frac{\partial u'_3}{\partial^0 x'_1} & 0 & 0 & 0 & 0 & 0 & 0 \\ 0 & 0 & 0 & \frac{\partial u'_1}{\partial^0 x'_2} & \frac{\partial u'_2}{\partial^0 x'_2} & \frac{\partial u'_3}{\partial^0 x'_2} & 0 & 0 & 0 \\ 0 & 0 & 0 & 0 & 0 & 0 & \frac{\partial u'_1}{\partial^0 x'_3} & \frac{\partial u'_2}{\partial^0 x'_3} & \frac{\partial u'_1}{\partial^0 x'_3} \\ \frac{\partial u'_1}{\partial^0 x'_2} & \frac{\partial u'_2}{\partial^0 x'_2} & \frac{\partial u'_3}{\partial^0 x'_2} & \frac{\partial u'_1}{\partial^0 x'_1} & \frac{\partial u'_2}{\partial^0 x'_1} & \frac{\partial u'_3}{\partial^0 x'_1} & 0 & 0 & 0 \\ 0 & 0 & 0 & \frac{\partial u'_1}{\partial^0 x'_3} & \frac{\partial u'_2}{\partial^0 x'_3} & \frac{\partial u'_1}{\partial^0 x'_3} & \frac{\partial u'_1}{\partial^0 x'_2} & \frac{\partial u'_2}{\partial^0 x'_2} & \frac{\partial u'_3}{\partial^0 x'_2} \\ \frac{\partial u'_1}{\partial^0 x'_3} & \frac{\partial u'_2}{\partial^0 x'_3} & \frac{\partial u'_1}{\partial^0 x'_3} & 0 & 0 & 0 & \frac{\partial u'_1}{\partial^0 x'_1} & \frac{\partial u'_2}{\partial^0 x'_1} & \frac{\partial u'_3}{\partial^0 x'_1} \end{bmatrix} \begin{bmatrix} \frac{\partial \Delta u'_1}{\partial^0 x'_1} \\ \frac{\partial \Delta u'_2}{\partial^0 x'_1} \\ \frac{\partial \Delta u'_3}{\partial^0 x'_1} \\ \frac{\partial \Delta u'_1}{\partial^0 x'_2} \\ \frac{\partial \Delta u'_2}{\partial^0 x'_2} \\ \frac{\partial \Delta u'_3}{\partial^0 x'_2} \\ \frac{\partial \Delta u'_1}{\partial^0 x'_3} \\ \frac{\partial \Delta u'_2}{\partial^0 x'_3} \\ \frac{\partial \Delta u'_3}{\partial^0 x'_3} \end{bmatrix}$$

$$= \frac{1}{2} A\gamma \tag{3.30a}$$

where A is the matrix related to the previous displacement and γ is the column vector related to the incremnt of displacement. Taking the variation of eq. 3.30a, we obtain :

$$d\mathbf{e}_{nl} = \frac{1}{2} dA\gamma + \frac{1}{2} A d\gamma = AG\Delta U \tag{3.30b}$$

The variation of strain $d\mathbf{e}_{nl}$, may be written in terms of the shape functions as follows:

$$d\mathbf{e}_{nl} = \mathbf{B}_l \Delta \mathbf{U} \tag{3.31}$$

where $\mathbf{B}_l$ is the strain matrix of nonlinear term of green strain. The complete Green strain increment in terms of the shape functions is now:

$$\mathbf{B} = (\mathbf{B}_0 + \mathbf{B}_l)\Delta \mathbf{U} \tag{3.32}$$

Referring to eq.(3.26), the first term of the left hand side may be written in terms of the stiffness matrix using eq.(3.20) and (3.32) as follows:

$$\mathbf{K} = \int_V (\mathbf{B}_0 + \mathbf{B}_l)^T \mathbf{C}' (\mathbf{B}_0 + \mathbf{B}_l) d^0V$$

or

$$\mathbf{K} = \mathbf{K}_0 + \mathbf{K}_l$$

where

$$\mathbf{K}_0 = \int_V \mathbf{B}_0^T \mathbf{C}' \mathbf{B}_0 d^0V$$

and

$$\mathbf{K}_l = \int_V (\mathbf{B}_0^T \mathbf{C}' \mathbf{B}_l + \mathbf{B}_l^T \mathbf{C}' \mathbf{B}_l + \mathbf{B}_l^T \mathbf{C}' \mathbf{B}_0) d^0V \tag{3.33}$$

in which $\mathbf{K}_0$ represents the usual small displacement stiffness matrix and $\mathbf{K}_l$ is sometimes known as the initial displacement stiffness matrix [Zienkiewicz 1991].

The second term of left handside eq.(3.26) can be written in two dimensional form as follows:

$$\mathbf{K}_s = \int_V \mathbf{G}^T \mathbf{S} \mathbf{G} d^0V \tag{3.34}$$

where matrix $\mathbf{G}$ has the same form as eq.(3.30) and matrix $\mathbf{S}$ may be written as:

$$\mathbf{S} = \begin{bmatrix} \sigma_{11}\mathbf{I}_3 & & symm. \\ \sigma_{12}\mathbf{I}_3 & \sigma_{22}\mathbf{I}_3 & \\ \sigma_{13}\mathbf{I}_3 & \sigma_{23}\mathbf{I}_3 & \sigma_{33}\mathbf{I}_3 \end{bmatrix}$$

$$\mathbf{I}_3 = \begin{bmatrix} 1 & 0 & 0 \\ 0 & 1 & 0 \\ 0 & 0 & 1 \end{bmatrix} \tag{3.35}$$

and $\mathbf{K}_s$ is called the initial stress stiffness matrix. By summing eq.(3.33) and (3.34) the total stiffness matrix for the total Lagrangian formulation may be written as:

$$\mathbf{K}_t = \mathbf{K}_0 + \mathbf{K}_l + \mathbf{K}_s \tag{3.36}$$

$\mathbf{K}_t$ is usually called the *tangent stiffness matrix*. To obtain the stiffness matrix in global coordinate system, procedure in section 2.2.5 must be adopted.

3.2.3 Stiffness Matrix of Updated Lagrangian

The principle of virtual work for the updated Lagrangian in eq.(3.16) may be rewritten as the following:

$$\int_V [C'_{ijkl}\epsilon^*_{ij}\delta\epsilon^*ij + \frac{1}{2}\sigma_{ij}\frac{\partial\Delta u'_k}{\partial^t x'_i}\frac{\partial\Delta u'_k}{\partial^t x'_j}]d^tV - \Delta R_{ext} = \varphi \qquad (3.37)$$

where the external work increment

$$\Delta R_{ext} = \int_V F^b_i\delta\Delta u_i d^tV + \int_A \Delta F^s_i\delta\Delta u_i d^tA \qquad (3.38)$$

and the residual work, φ, should be zero if the state is in equlibrium. φ may be written in complete form as:

$$\varphi = \int_V [\sigma^E_{ij}\delta c^*_{ij} - F^b_i\delta\Delta u_i]d^tV - \int_A F^s_i\delta\Delta u_i d^tA \qquad (3.39)$$

Using eq.(3.23) and (3.24), the material properties C'_{ijkl} and the updated Green strain increment may be written in two dimensional form and vector form respectively. The updated Green strain increment, eq.(3.24), can be written as follows:

$$\mathbf{e}^* = \mathbf{B}\Delta\mathbf{U} \qquad (3.40)$$

where $\mathbf{B}$ is strain matrix which refers to the t configuration. Referring to eq.(3.37), the first term of left hand side could be written in term of stiffness matrix using eq.(3.10) and (3.20) as:

$$\mathbf{K} = \int_V \mathbf{B}^T\mathbf{C}'\mathbf{B}d^tV \qquad (3.41)$$

The second term of the left hand side of eq.(3.37) $\int_V \sigma_{ij}\frac{1}{2}(\Delta u_{k,i}\Delta u_{k,j})d^tV$ is a similar expression to eq.(3.34), but the stress is the Cauchy stress and refers to the

t configuration as follows:

$$\mathbf{K}_s = \int_V \mathbf{G}^{*T}\mathbf{S}^*\mathbf{G}^* d^tV \tag{3.42}$$

where

$$\mathbf{S}^* = \begin{bmatrix} \sigma_{11}^E\mathbf{I}_3 & & symm. \\ \sigma_{12}^E\mathbf{I}_3 & \sigma_{22}^E\mathbf{I}_3 & \\ \sigma_{13}^E\mathbf{I}_3 & \sigma_{23}^E\mathbf{I}_3 & \sigma_{33}^E\mathbf{I}_3 \end{bmatrix}$$

$$I_3 = \begin{bmatrix} 1 & 0 & 0 \\ 0 & 1 & 0 \\ 0 & 0 & 1 \end{bmatrix}$$

and

$$\mathbf{G}^*\Delta\mathbf{U} = \begin{bmatrix} \frac{\partial\Delta u_1^t}{\partial^t x_1} \\ \frac{\partial\Delta u_2^t}{\partial^t x_1} \\ \frac{\partial\Delta u_3^t}{\partial^t x_1} \\ \frac{\partial\Delta u_1^t}{\partial^t x_2} \\ \frac{\partial\Delta u_2^t}{\partial^t x_2} \\ \frac{\partial\Delta u_3^t}{\partial^t x_2} \\ \frac{\partial\Delta u_1^t}{\partial^t x_3} \\ \frac{\partial\Delta u_2^t}{\partial^t x_3} \\ \frac{\partial\Delta u_3^t}{\partial^t x_3} \end{bmatrix}$$

The complete stiffness matrix for updated Lagrangian formulation method may be formed by summing eq.(3.41) and (3.42) as:

$$\mathbf{K}_t = \mathbf{K} + \mathbf{K}_s \tag{3.43}$$

As with with the total Lagrangian formulation, to obtain the stiffness matrix in global coordinate system, the procedure described in section 2.2.5 must be adopted. Comparing with the total Lagrangian stiffness matrix, the updated Lagrangian stiffness is relatively simpler due to there being no nonlinear part in the strain formulation and there is no explicit previous displacement in the stiffness matrix formulation. However, the configuration must be updated at each increment step.

In the present work, the updated Lagrangian will be implemented. The numerical results are presented in section 4.6.

3.3 Elasto-Plastic Analysis

In elastic analysis, the total stress may be calculated from total strain as given by eq.(2.27) whereas in plastic analysis eq.(2.27) is unavailable because the material properties change for different level of stress. So, a criterion is needed to indicate that the stress level has reached a plastic condition. This criterion is called the *yield criterion*. There is no unique relationship between stress and strain components in the plastic region, because the stress depends not only on the final state of strain, but also on the loading history. For this reason, the stress strain relation which is presented at section 3.2.1 has to be replaced by the relations between the increment of the stress and strain in the development of plasticity. This is called the flow theory of plasticity [Washizu 1982].

3.3.1 The Flow Rule

During any increment of stress in plastic analysis, the changes of strain are assumed to be separated into elastic and plastic components so that :

$$d\epsilon_{ij} = (d\epsilon_{ij})_e + (d\epsilon_{ij})_p \qquad (3.44)$$

The first term of the right hand side, $(d\epsilon_{ij})_e$, is the elastic strain increment and the second term of the right hand side, $(d\epsilon_{ij})_p$, is the plastic increment strain. The elastic strain increment is related to the stress increment by eq.(2.27). Stress terms can be decomposed into their deviatoric and hydrostatic stress components as:

$$(d\epsilon_{ij})_e = \frac{d\sigma'_{ij}}{2G} + \frac{(1-2\nu)}{E}\delta_{ij}d\sigma_{kk} \qquad (3.45)$$

where

$$\sigma'_{ij} = \sigma_{ij} - \frac{1}{2}\delta_{ij}\sigma_{kk}$$

and

$$G = \frac{E}{2(1+\nu)}$$

E is Young's modulus of elasticity, ν the Poisson ratio and G is the shear modulus. The relation between plastic strain increment and the stress increment can be written using the assumption that the plastic strain increment is proportional to the stress gradient of the plastic potential $Q(\sigma,\kappa)$, so that:

$$(d\epsilon_{ij})_p = d\lambda \frac{\partial Q}{\partial \sigma_{ij}} \tag{3.46}$$

where $d\lambda$ is the plastic strain-rate multiplier. An important case is the simplest case when the yield function, $f(\sigma,\kappa)$, and plastic potential function, $Q(\sigma,\kappa)$, coincide, thus:

$$(d\epsilon_{ij})_p = d\lambda \frac{\partial f}{\partial \sigma_{ij}} \tag{3.47}$$

Equation(3.47) is called associated flow rule and is also called the normality condition because $\partial f/\partial \sigma_{ij}$ is a vector directed normal to the yield surface. When the plastic flow occur, the stresses must remain on the yield surface. This condition may be written as,

$$f(\sigma,\kappa) = 0 \tag{3.48}$$

The yield condition can be vizualized as a surface in n dimension stress space (Fig. 3.2) with the position of the surface dependent on the instantenous value of parameter κ.

Experimental observations indicate that this normality condition is an acceptable assumption for metals [Chen 1988, Hinton 1980] in relationship between the plastic strain increment and stress increment. When the Von Mises yield criterion (section 3.2.2) is used, eq.(3.47) is known as the Prandtl-Reuss equation. On subtituting eq.(3.47) and (3.45) into eq.(3.44), the complete relationship between strain and stress for elasto-plastic deformation may be written as:

$$(d\epsilon_{ij})_t = \frac{d\sigma'_{ij}}{2G} + \frac{(1-2\mu)}{E}\delta_{ij} d\sigma_{kk} + d\lambda \frac{\partial f}{\partial \sigma_{ij}} \tag{3.49}$$

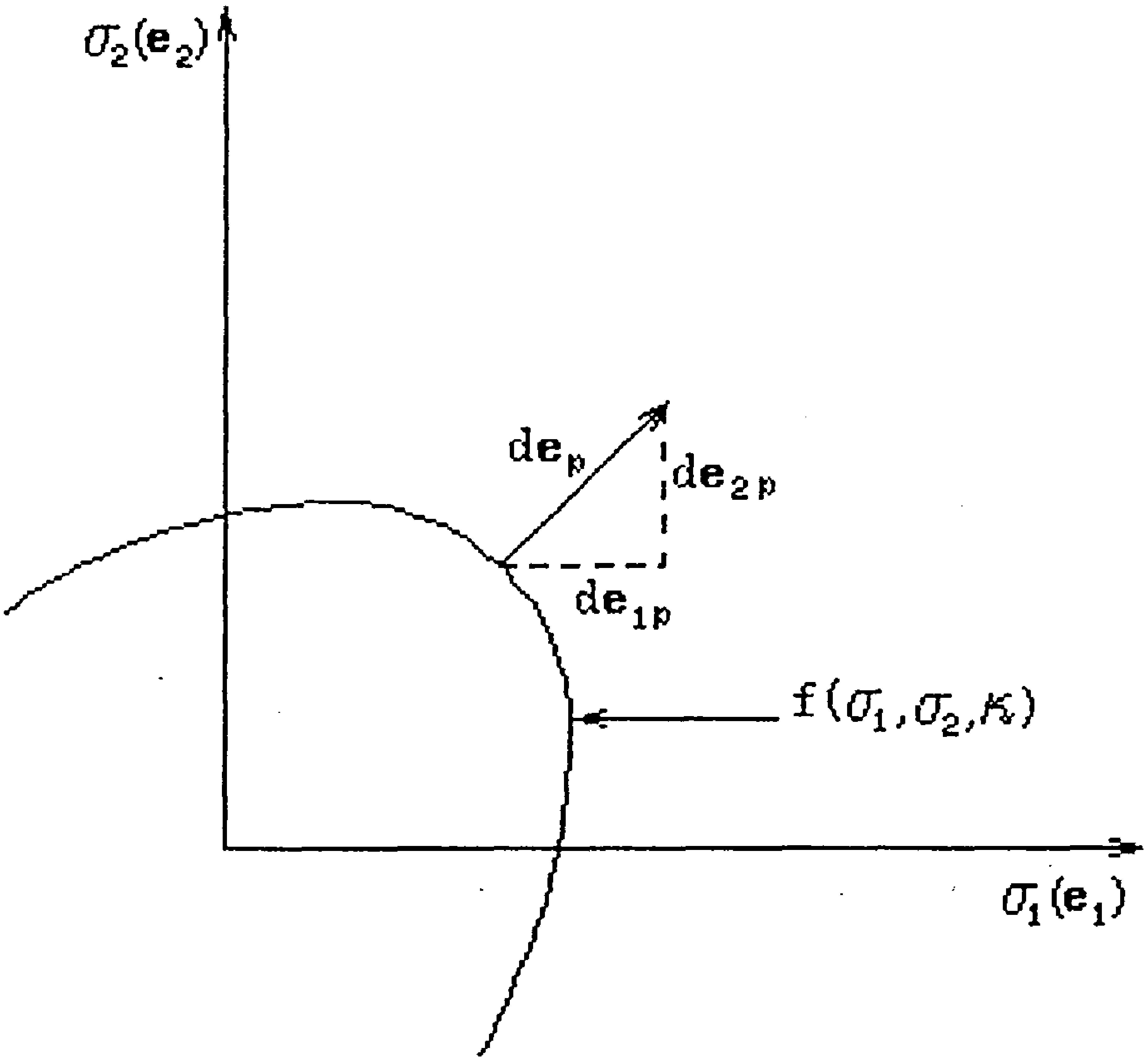

Figure 3.2 : Yield surface in two dimensonal stress with κ constant.

3.3.2 The Von Mises Yield Criterion

There are some yield criteria which may be adopted to determine the stress level at which plastic deformation commences for instance Tresca, Von Mises, Mohr-Coulomb and Drucker-Prager etc. The Tresca and Von Mises yield criteria is the most suitable yield critria for metal [Chen 1988]. The Von Mises yield criterion is used to analysize metal plasticity. Von Mises suggested that yielding occurs when J_2 reaches a critical value of

$$f(J_2) = J_2 - K(\kappa)^2 = 0 \tag{3.50}$$

The term K is a function of the hardening parameter κ and J_2 is the second deviatoric stress invariant. J_2 can be written as:

$$J_2 = \frac{1}{2}[\sigma'^2_{11} + \sigma'^2_{22} + \sigma'^2_{33}] + \sigma'^2_{12} + \sigma'^2_{23} + \sigma'^2_{31} \tag{3.51}$$

or in terms of principle stresses

$$f(J_2) = (\sigma_1 - \sigma_2)^2 + (\sigma_2 - \sigma_3)^2 + (\sigma_3 - \sigma_1)^2 - 6K(\kappa)^2 = 0 \qquad (3.52)$$

The yield criterion eq.(3.51) may be written in terms of effective stress or equivalent $\bar{\sigma}$ stress as follows:

$$\bar{\sigma} = \sqrt{3}(J_2)^{\frac{1}{2}} = \sqrt{3}K$$

or

$$f(J_2) = \bar{\sigma} - \sqrt{3}(J_2)^{\frac{1}{2}} = \bar{\sigma} - \sqrt{3}K = 0 \qquad (3.53)$$

In a uniaxial tension test, yielding will occur when $\sigma_1 = \sigma_0, \sigma_2 = \sigma_3 = 0$. On substituting these values into eq.(3.53) one finds

$$K = \frac{\sigma_0}{\sqrt{3}} \qquad (3.54)$$

where σ_0 is the yield stress in uniaxial tension test. From eq.(3.53) the yield criterion may be written as follows:

$$f(J_2) = \bar{\sigma} - \sigma_0 = \sqrt{3}(J_2)^{\frac{1}{2}} - \sigma_0 = 0 \qquad (3.53)$$

3.3.3 Matrix Formulation

The flow rule and yield criterion mentioned in section(3.41) and (3.42) will now be converted to matrix form. The stress and strain without subscript in the following formulation are in the vector form, for example equation 3.22, 3.23 and 3.24, and the material properties are in two dimensional form as in eq.2.31. The strain in equation 3.44 may be written as:

$$(de)_\epsilon = de - (de)_p \qquad (3.56)$$

where the plastic strain increment $(de)_p$ is formulated in equation 3.47 and de is the total strain increment and de_e is the elastic strain. Using equation 3.47 and 3.56, the elastic strain changes may be obtained as follows;

$$(de)_e = de - d\lambda\frac{\partial f}{\partial \sigma} \tag{3.57}$$

or

$$(de)_e = de - d\lambda \mathrm{a} \tag{3.58}$$

Where $\mathrm{a} = \partial f/\partial\sigma$, is the flow vector. Using equation 3.56, the stress changes may be written as

$$\Delta\sigma = \mathrm{C}'[de - (de)_p]$$

$$\Delta\sigma = \mathrm{C}'[de - d\lambda \mathrm{a}] \tag{3.59}$$

where C' is the matrix of elastic properties as indicated in equation 2.31. For plastic flow to occur, the stresses must remain on the yield surface (see eq. 3.48) and if the hardening parameter assumed to be zero, the plastic flow rate may be written as

$$df = \frac{\partial f^T}{\partial \sigma}\Delta\sigma \tag{3.60}$$

Fig. 3.3 describes the situation of eq.(3.60) and shows that the instantaneous change of stresses $\Delta\sigma$ is directed tangentially to the surface. The stresses are orthogonal to the vector a. The strain rate multiplier $d\lambda$ may be obtained using equation 3.59 and 3.60. Equation 3.59 is premultiplied by the flow vector a^T as follows

$$\mathrm{a}^T\Delta\sigma = \mathrm{a}^T\mathrm{C}'de - \mathrm{a}^T\mathrm{C}'d\lambda\mathrm{a} \tag{3.61}$$

and using equation 3.60 $d\lambda$ may be written as

$$d\lambda = \frac{\mathrm{a}^T C'' de}{\mathrm{a}^T\mathrm{C}'\mathrm{a}} \tag{3.62}$$

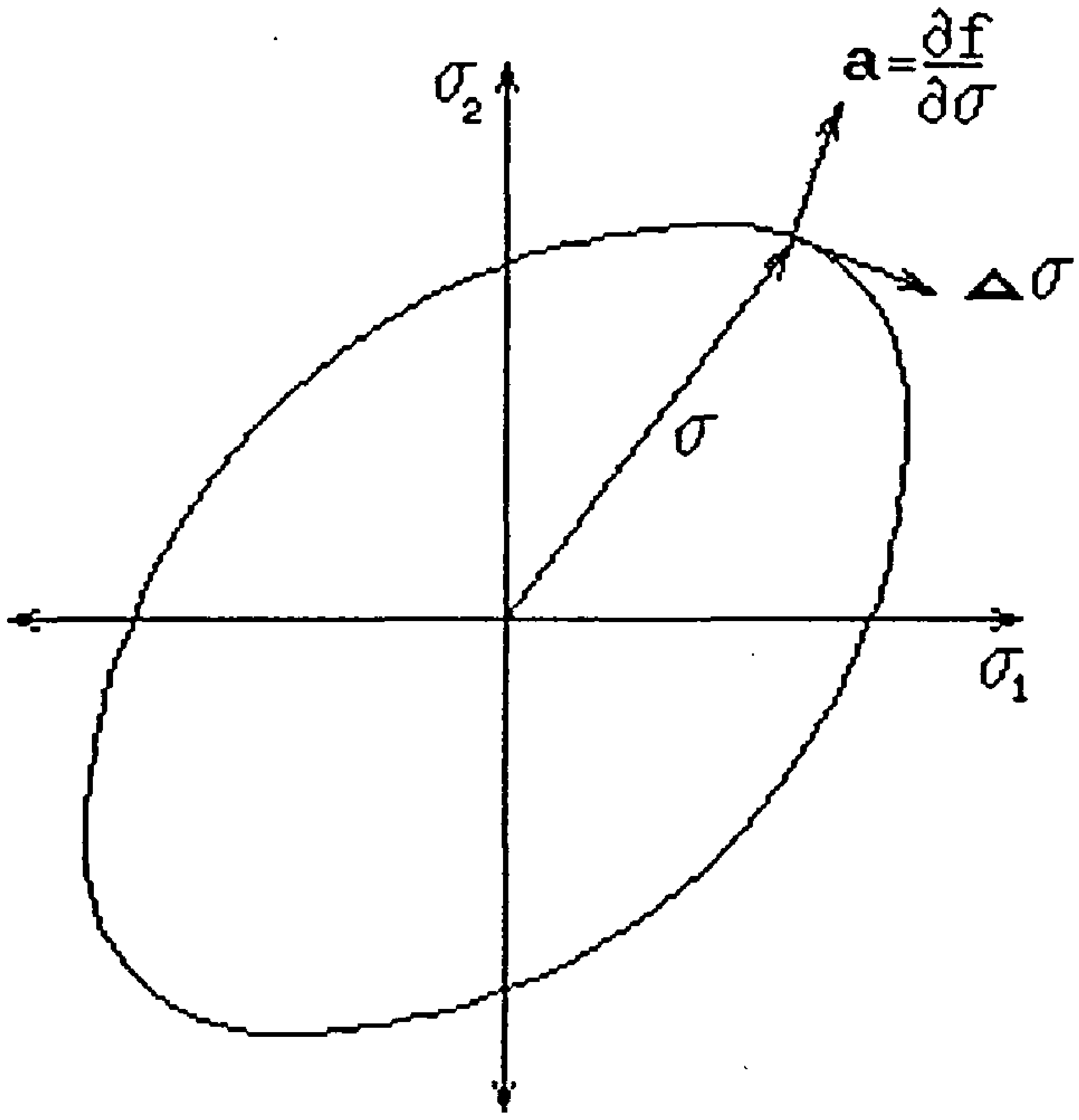

Figure 3.3 : The normality condition on the yield surface in two dimensional stress.

Consequently, substituting eq. 3.62 into eq. 3.59 gives

$$\Delta\sigma = \mathrm{C}'[d\mathrm{e} - \frac{\mathrm{a}^T\mathrm{C}'d\mathrm{ea}}{\mathrm{a}^T\mathrm{C}'\mathrm{a}}]$$

$$\Delta\sigma = [\mathrm{C}' - \frac{\mathrm{d}_d\mathrm{d}_d^T}{\mathrm{d}_d^T\mathrm{a}}]d\mathrm{e} \tag{3.63}$$

where d_d is $\mathrm{C}'\mathrm{a}$ and equation 3.63 may be written in simple form as

$$\Delta\sigma = \mathrm{C}'_{ep}d\mathrm{e} \tag{3.64}$$

where C'_{ep} is the tangent modulus matrix which is not only a function of E and ν but also a function of the current stress σ.

In order to calculate the C'_{ep} matrix, the flow vector **a** should be written in a form suitable for numerical computation. Using the Von Mises yield criterion, the flow vector **a** may be written as

$$\mathbf{a}^T = \frac{\partial f}{\partial \sigma} = \frac{\partial(\bar{\sigma} - \sigma_0)}{\partial \sigma} = \frac{\partial(\sqrt{3}J_2^{\frac{1}{2}} - \sigma_0)}{\partial \sigma}$$

$$\mathbf{a}^T = \sqrt{3}\mathbf{a}_1^T \tag{3.65}$$

where

$$\mathbf{a}_1^T = \frac{\partial \sqrt{3}J_2^{\frac{1}{2}}}{\partial \sigma}$$

$$\mathbf{a}_1^T = \frac{1}{2(J_2)^{\frac{1}{2}}}(\sigma'_{11}, \sigma'_{22}, \sigma'_{33}, 2\sigma'_{21}, 2\sigma'_{23}, 2\sigma'_{31})$$

and σ' is a deviatoric stress.

3.3.4 Strain Hardening

After the initial yield point has been reached, the stress-strain curve continues to rise although the slope become less steep until the it falls to zero as failure occurs. Then the yield stress will not increase with further straining. The phenomenon of a material being able to withstand a greater stress after plastic deformation is known as strain hardening or work hardening, in the sense that the material gets stronger the more it is strained or worked [Chen 1988].

Using eq.(3.55), the strain hardening can be evaluated by changing the fixed uniaxial yield stress σ_0 to a variable stress, $\sigma_0(\epsilon_{ps})$, so that

$$f = \bar{\sigma} - \sigma_0(\epsilon_{ps}) \tag{3.66}$$

where ϵ_{ps} is the equivalent plastic strain and may be written as the accumulated equivalent plastic strain rate as follows

$$\epsilon_{ps} = \sum d\epsilon_{ps} = \int d\epsilon_{ps} \tag{3.67}$$

The equivalent plastic strain rates can be obtained as follows

$$d\epsilon_{ps} = \sqrt{\frac{2}{3}}[(d\mathbf{e})_p(d\mathbf{e})_p]^{\frac{1}{2}} \tag{3.68}$$

For uniaxial tension σ_x, $d\epsilon_{px} = d\epsilon_{pz} = -\frac{1}{2}d\epsilon_{px}$ since plastic straining is assumed to be incompressible and Poisson's ratio is then effectively 0.5. Using that condition, the plastic strain rate $d\epsilon_{ps} = d\epsilon_{px}$ and $\bar{\sigma} = \sigma_o = \sigma_x$. The relation between σ_0 and ϵ_{ps} can be taken from uniaxial stress/plastic strain relationship and using Fig. 3.4 the strain hardening is defined as follows:

$$H' = \frac{\partial \sigma_0}{\partial \epsilon_{ps}} = \frac{\partial \sigma_x}{\partial \epsilon_{px}} = \frac{E_T}{1 - \frac{E_T}{E}} \quad 3.69)$$

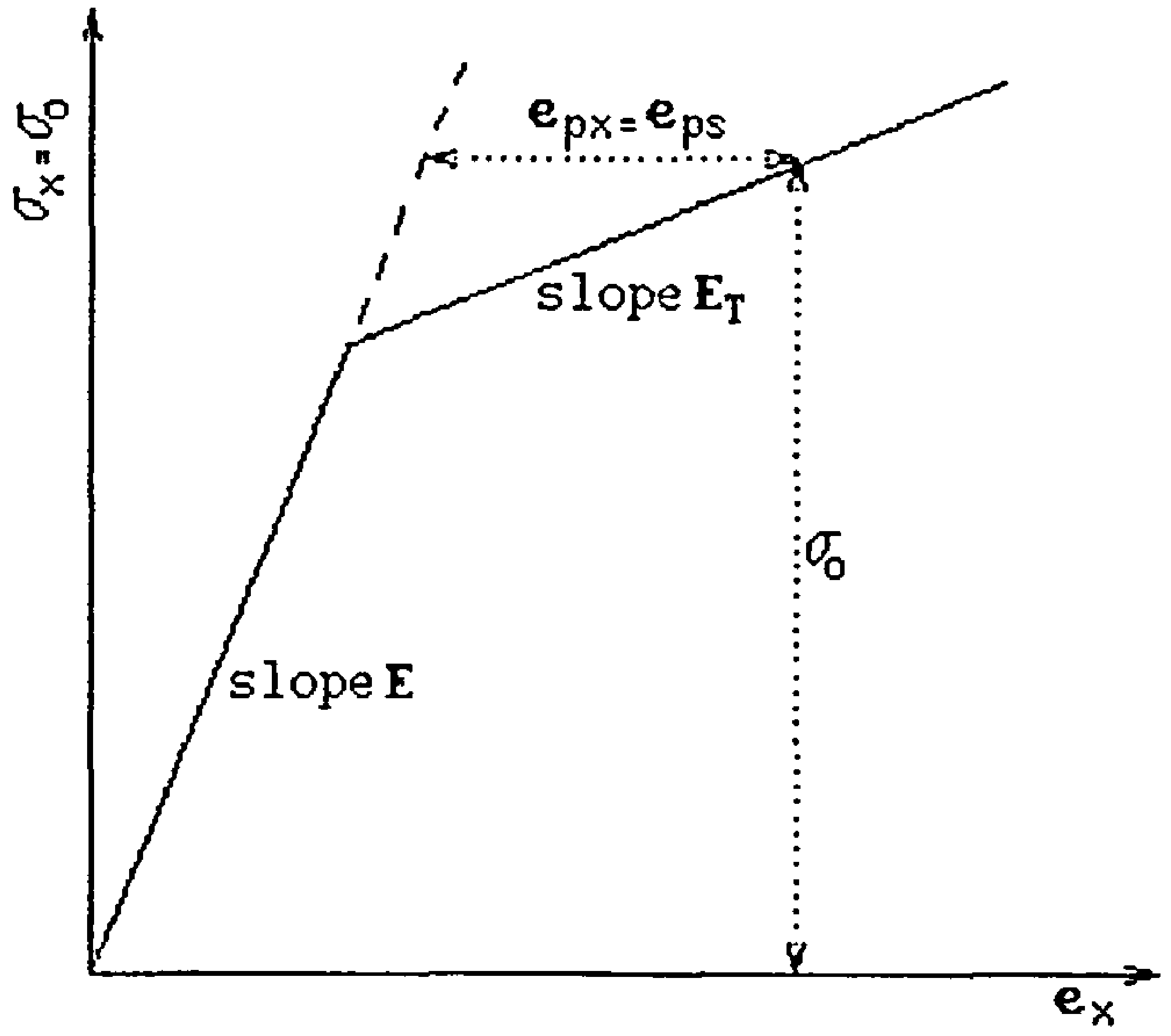

Figure 3.4 : Uniaxial stress-strain relationship with linear hardening.

Similarly to eq.(3.60), if the hardening parameter is not zero, the plastic flow rate may be written using eq. 3.48 as follows

$$df = \frac{\partial f}{\partial \sigma}\Delta\sigma + \frac{\partial f}{\partial \sigma_0}\frac{\partial \sigma_0}{\partial \epsilon_{ps}}d\epsilon_{ps} = a^T\Delta\sigma - H'd\epsilon_{ps} = 0 \quad (3.70)$$

On substituting equation 3.47 into equation 3.68, the equivalent plastic strain rate may be written as :

$$d\epsilon_{ps} = B(\sigma)d\lambda \quad (3.71)$$

For the Von Mises yield criterion $B(\sigma) = 1$. Equation 3.70 and 3.71 gives

$$df = \mathbf{a}^T \Delta\sigma - H'Bd\lambda = \mathbf{a}^T \Delta\sigma - A'd\lambda \tag{3.72}$$

where A' is constant for a linear hardening parameter.

The rate multiplier eq.(3.62) now can be modified by introducing the hardening parameter. Premultiplying eq.(3.59) by flow vector **a** and subtituting eq.(3.72) give

$$d\lambda = \frac{\mathbf{a}^T \mathbf{C}' d\mathbf{e}}{\mathbf{a}\mathbf{C}'\mathbf{a} + A'} \tag{3.73}$$

and eq.(3.63) can be replaced by

$$\Delta\sigma = [\mathbf{C}' - \frac{\mathbf{d}_d \mathbf{d}_d^T}{\mathbf{d}_d^T \mathbf{C}'\mathbf{a} + A'}]d\mathbf{e}$$

or

$$\Delta\sigma = \mathbf{C}'_{\epsilon p} d\epsilon$$

and

$$C'_{\epsilon p} = C' - \frac{\mathbf{d}_d \mathbf{d}_d^T}{\mathbf{d}_d^T \mathbf{C}'\mathbf{a} + A'} \tag{3.74}$$

Here the tangent modulus matrix, $\mathbf{C}'_{\epsilon p}$, is not only a function of E, ν and current stress σ, but also a function of hardening parameter H'.

3.3.5 Integrating the Rate of the Equation

During a load increment where the elastic stress exceeds that permitted by the yield criterion, plastic deformation must occur. When the load increment is very small which gives small stress and strain, the tangential formula or foward Euler method can be effectively applied. However, when the strain and stress are not small, this method can lead to some error. Methods to minimize this error will be discussed later. Before using the tangential predictor, the crossing point at the yield surface should be known. This will now be defined.

- **Crossing The Yield surface**

To obtain the crossing point at the yield surface, point A in Fig. 3.6a, a simple scaling formula has been proposed by Hinton [1980] using uniaxial stress-strain graph. Using Fig. 3.5, the simple scaling α may be written as,

$$\alpha = \frac{\sigma_r - \sigma_0}{\sigma_r - \sigma_{r-1}} \tag{3.75}$$

and the remaining stress may be written as

$$\Delta\sigma = \alpha\Delta\sigma_r \tag{3.76}$$

Where σ_0 is the uniaxial yield stress. σ_{r-1} is the previous stress and σ_r is the total increment of stress. For n dimensional stress analysis, the equivalent stress may be used as follows:

$$\alpha = \frac{\bar{\sigma}_r - \sigma_0}{\bar{\sigma}^r - \bar{\sigma}_{r-1}} \tag{3.77}$$

Before using eq.(3.77), the yield constant, σ_0, has to be updated due to the hardening as $\sigma_0 = \sigma_0 + \epsilon_{ps} A'$, where ϵ_{ps} is the equivalent plastic strain and A' is the hardening parameter. From eq.(3.77), it can be seen that, if plastic condition has occurred the ratio α wll be equal to 1. Another formulation to define the crossing point on yield surface, has been proposed by Bicanic [1989] based on $f(\sigma) = 0$ and this give a quadratic equation.

- **Standard Predictor**

The standard predictor [Hinton 1980] which is the Euler Foward procedure is implemented in the present work. Using eq.(3.59), the incremental stress may be rewritten as;

$$\Delta\sigma = \mathrm{C}'d\mathrm{e} - d\lambda\mathrm{C}'\mathrm{a} \tag{3.78}$$

It can be seen from Fig. 3.6b, that after reaching the yield surface (point A), the elastic incremental stress is $\alpha\Delta\sigma$. In relation to Fig. 3.6b

$$\sigma_c = \sigma_a + \alpha\Delta\sigma_r - d\lambda\mathrm{C}'\mathrm{a} \tag{3.79}$$

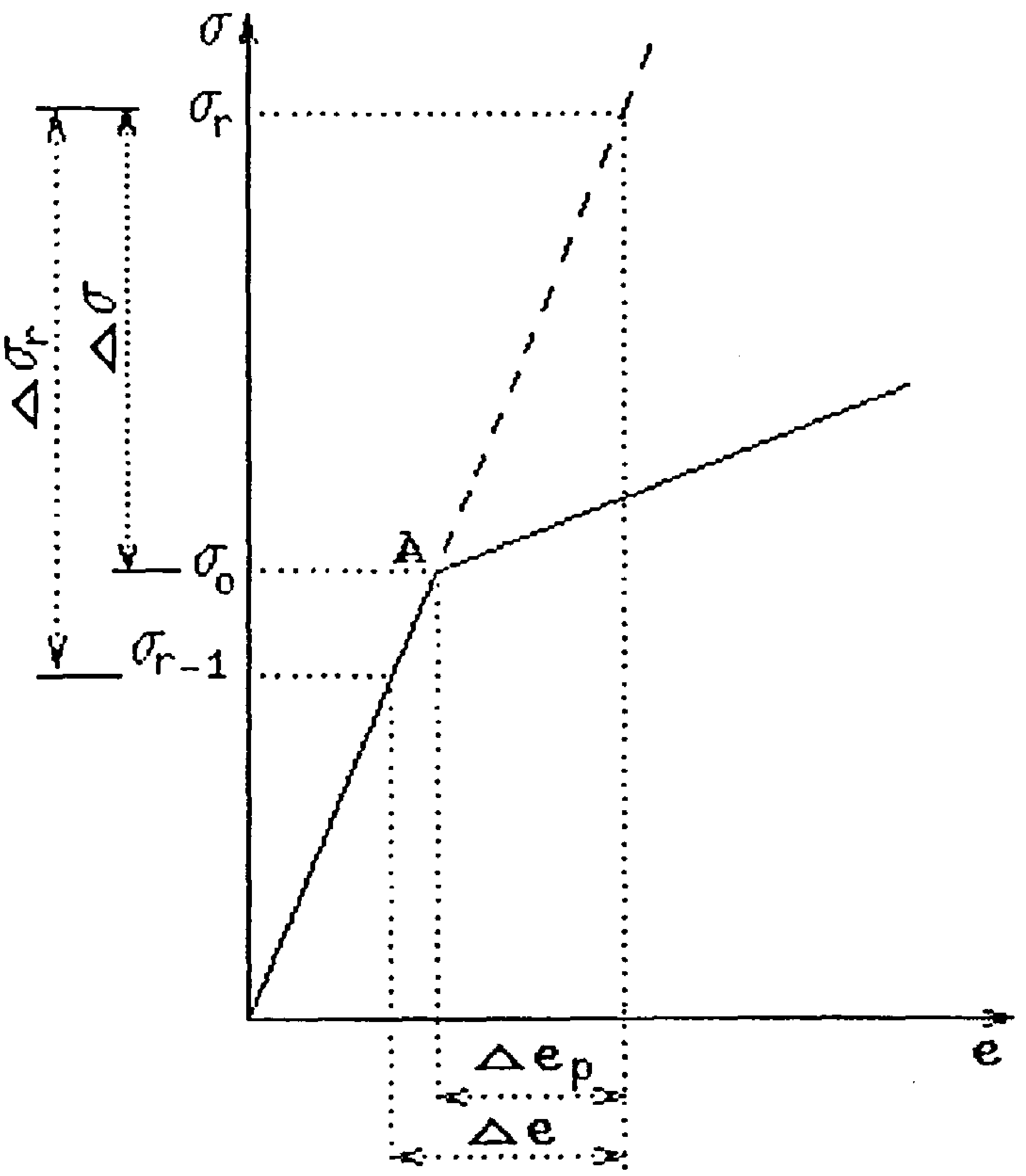

Figure 3.5 : Incremental stress and strain in uniaxial elasto plastic.

and equation 3.79 can be viewed as the elastic step from point A to B followed by a plastic return to point A. However, since the tangential predictor or Euler Foward method gives some error [Crisfield 1991, Hinton 1980], the stress does not lie in yield surface but it only reaches point C. To minimize the error, a subincremental method can be used. Another predictor, which is recently often used, is the backward Euler method [Crisfield 1991, Matthies 1989]. The foward Euler method use the normal at point A, backward Euler method use the normal at the elastic trial point B.

- **Subincrement Method**

The error introduced by the tangential predictor will accumulate if it is not reduced. To minimize that error, the return to the yield surface method [Ortiz 1985] can be used with simply scaled stresses. Instead of using an artificial return

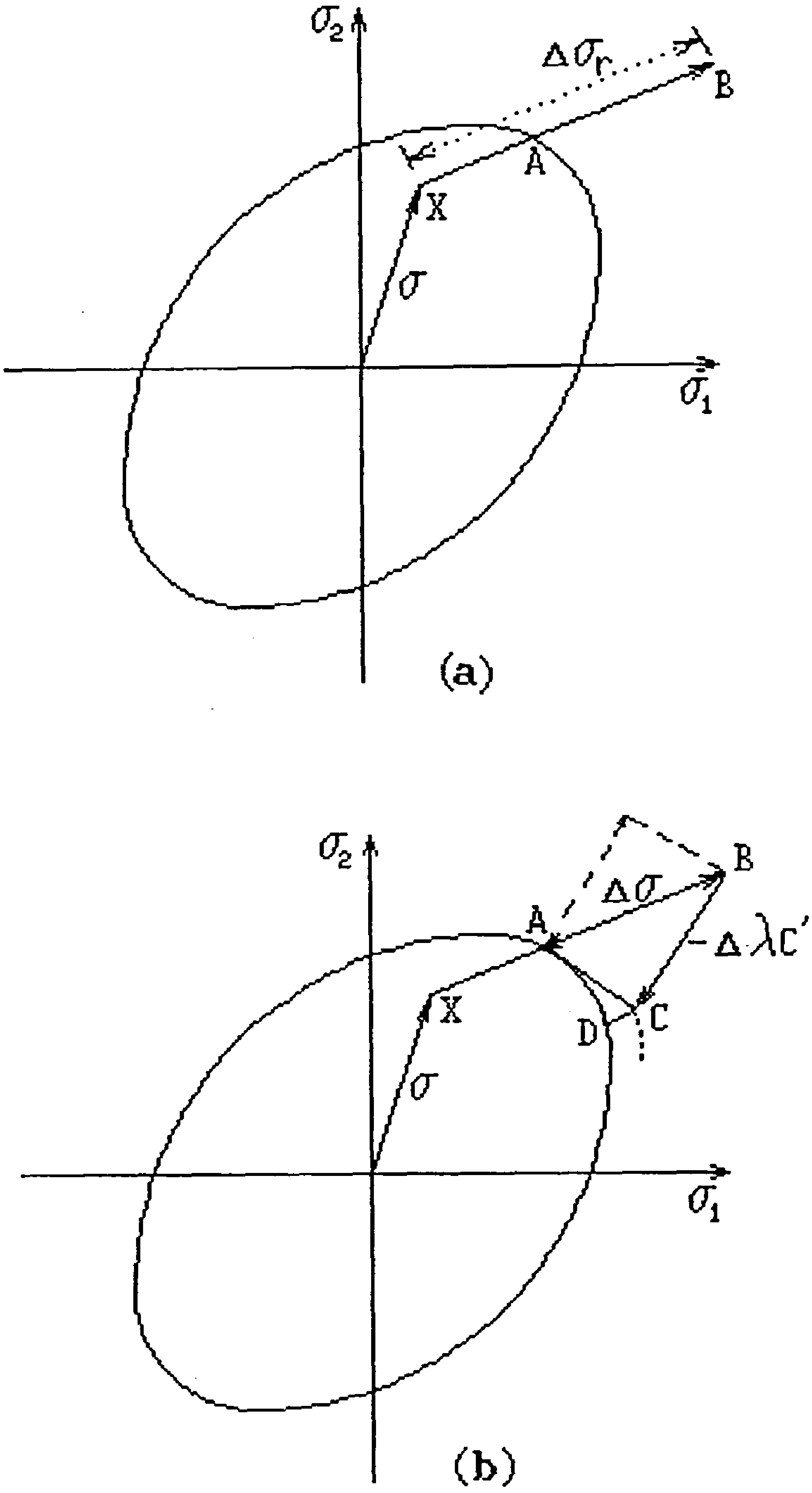

Figure 3.6 : The foward-Euler method in two dimensional stress;
a. stress increment, b. moving tangentially from A to C.

to the yield surface, the subincremental method may be used [Nyssen 1980, Sloan 1987]. Nyssen proposed the technique of dividing the incremental strain $d\mathrm{e}$ into a certain number of steps m. Each substep has strain increment $d\mathrm{e}/m$ and stress increment $\Delta\sigma = \mathbf{C}'_{ep}(\sigma)d\mathrm{e}/m$ where the tangent modulus matrix $\mathbf{C}'_{ep}$ is dependent on the previous substep stress. Hinton [1980] proposed the technique of dividing the incremental stress, $\Delta\sigma$, into a certain number of steps. This is different from substep strain increment, because the tangent modulus matrix $\mathbf{C}'_{ep}$ is dependent on the previous increment stress.

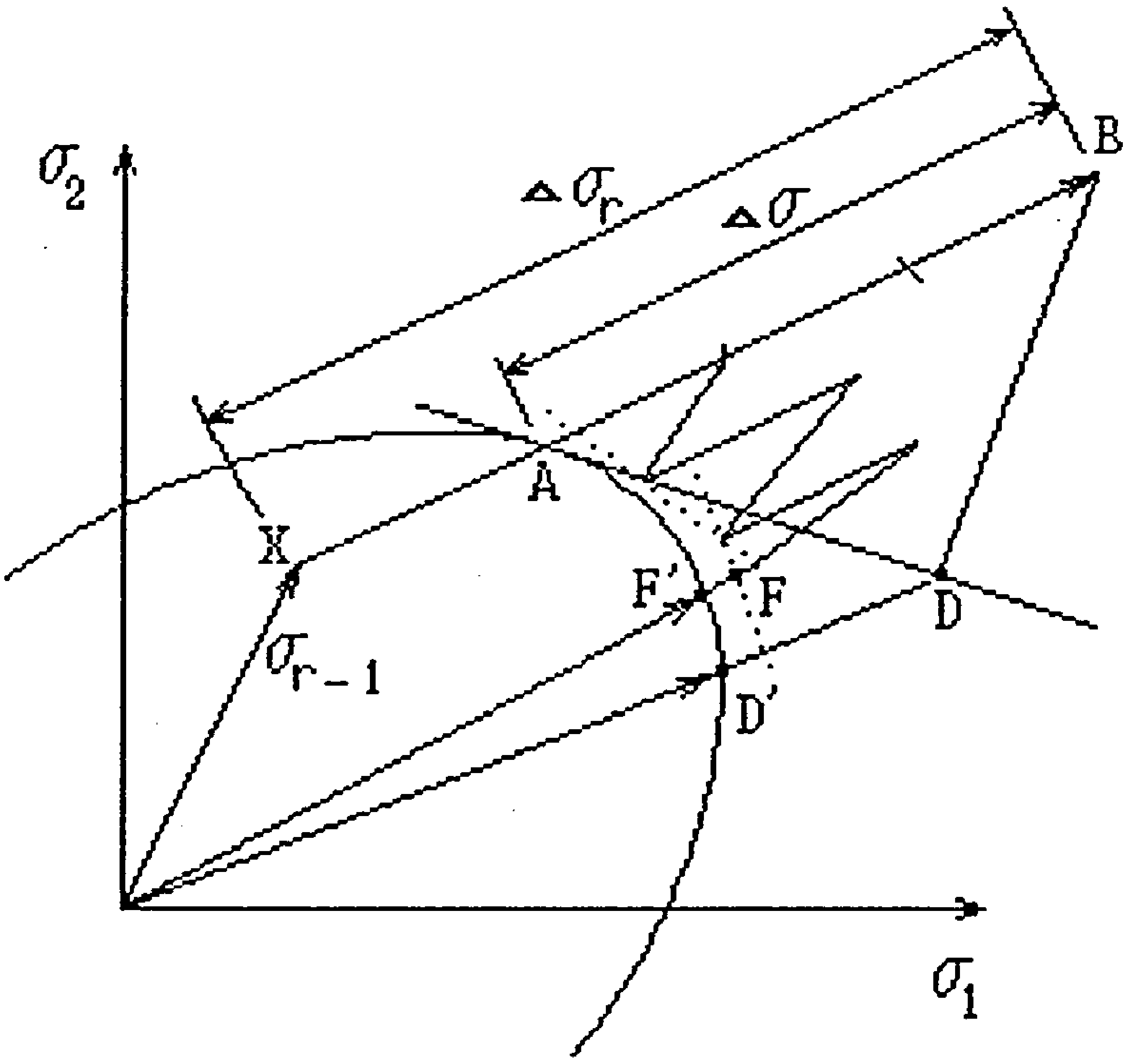

Figure 3.7 : Subincrement of stress for reducing stress point to yield surface.

It can be seen from Fig. 3.7 that the final stress point D does not coincide with the yield surface. The point D can be reduced to the yield surface by simply scaling σ_r as follows. If the point D lies on the yield surface, the value of effective stress $\bar{\sigma}_r$ due to σ_r should be same as $\sigma_0 = \sigma_0 + A'\epsilon_{ps}$. Where σ_0 is the uniaxial yield stress, A' is the hardening parameter and ϵ_{ps} is effective strain. Then the simple scaling can be given as:

$$\sigma^r = \sigma^r\left[\frac{\sigma_0 + A'\epsilon_{ps}}{\bar{\sigma}^r}\right] \tag{3.80}$$

Without using the subincrement stress and applying equation 3.80 the stress point D will return to point D'. Greater accuracy may be achieved by dividing $\Delta\sigma$ into a certain number m of steps. From Fig. 3.7, it can be seen, that the $\Delta\sigma$ is divided into 3 parts. After using the foward Euler method for the three subincrement stress, the stress point now is F. Using simple scaling equation 3.80, the stress point F can be reduced to the final stress point F'. There is a sigficant difference between point D' and F'. The greater number of step is applied, the greater accuracy obtained. Hinton proposed that the appropriate number of steps could be estimated as follows:

$$m = [\frac{\bar{\sigma}^r - \bar{\sigma}_0}{\sigma_0}]8 + 1 \qquad (3.81)$$

and this is implemented in the present work.

Chapter IV

Finite Element Solution Procedure

4.1 Linear solution

The most effective direct solution techniques currently used are basically applications of the method of Gauss elimination. Their effectiveness in finite element analysis depends on the specific properties of the finite element stiffness matrix namely symmetry, positive definitness and bandedness [Bathe 1982]. The simultaneous linear equations of structural finite element can be written as :

$$Ku = F \tag{4.1}$$

where K is the system stiffness matrix, u is the displacement vector and F is the load vector of the finite element system. The stiffness matrix may be decomposed as follows:

$$K = LDL^T \tag{4.2}$$

where L is the lower triangular matrix and D is diagonal matrix. For a detailed theory of LDL^T decomposition, referred to Bathe (1982). In this present work, a profile matrix solver with built in constraint facility, based on LDL^T decomposition, is used to solve the simultaneous linear equations. The details of a profile matrix solver are given by Bettess [1986].

4.2 Nonlinear Solution Procedures

Numerous papers and books have been published [Hinton 1980, Bathe 1982, Zienkiewicz 1991, Crisfield 1991] in recent years concerning the application of nonlinear solution procedures of the finite element method to nonlinear problems. The aim of all these works is to find a solution technique which is stable, accurate and inexpensive. The difficulties are problem dependent and so solution schemes which are ideal for certain classes of problem may be useless for others. The engineer must use his experience to decide upon the solution strategy required. In this present work, a combination of incremental and iterative procedures is employed to obtain a solution to the equilibrium equation.

As mentioned in chapter 3, the incremental theory is implemented to formulate the nonlinear finite element problem. Each problem may be considered as a linear step. The loads and displacements are accumulated from each solution step. This incremental solution procedure can be expressed as :

$$F_n + \Delta F_n = F_n + (\frac{dF_n}{du})\Delta u_n \tag{4.3}$$

where the increment displacement, Δu_n, is given by

$$\Delta u_n = (\frac{dF_n}{du})^{-1}\Delta F_n \tag{4.4}$$

ΔF_n is the incremental applied load and subscript n denotes the number of the increment. $(dF/du)_n^{-1}$ is the tangent stiffness matrix, K_T, of the finite element formulation. The tangent stiffness matrix, K_T, is calculated at the beginning of each increment. Following each load increment, the displacement and load are accumulated as:

$$u_{n+1} = u_n + \Delta u_n$$

$$F_{n+1} = F_n + \Delta F_n \tag{4.5}$$

Using purely incremental procedure, equilibrium is not satisfied in each increment step [Crisfield 1991] and the solution tends to diverge from the true solution path. But an improvement may be obtained in this increment technique by applying the residual :

$$g_n = F_n - Fi_n \tag{4.6}$$

where g_n is the vector of out-balance forces, Fi is the internal force and subscript n denotes the number of the increment. This residual force is added to the next loading increment.

To improve the accuracy of the solution. iterative strategies may be used in combination with incremental techniques. One well known iterative strategy is the Newton-Raphson [NR] method. A truncated Taylor expansion may be used to express the Newton-Raphson iterative procedure as:

$$g_{n+1} \cong g_n + (\frac{dg_n}{du})\delta u_n + \frac{1}{2}(\frac{d^2 g_n}{du^2})\delta u^2 \qquad (4.7)$$

To obtain a better approximation, the third term on the right hand side that is the high order term of eq.(4.7) is neglected [Hinton 1980, Crisfield 1991]. Using the previous solution, as an initial estimation, provided that $g_n(u_n) \neq 0$, and setting $g_{n+1} = 0$ we obtain:

$$\delta u_n = -(\frac{dg_n}{du})^{-1} g_n(u_n) \qquad (4.8)$$

Here, $(dg_n/du)^{-1}$ is the tangent stiffness matrix, K_T, in the finite element formulation. The new estimate for u is

$$u_{n+1} = u_n + \delta u_n \qquad (4.9)$$

This solution may be used in the following iteration as:

$$\delta u_{n+1} = -(\frac{dg_{n+1}}{du})^{-1} g_{n+1}(u_{n+1}) \qquad (4.10)$$

Eq.(4.10) is repeated using the latest solution until a convergence criterion is satisfied. Eq.(4.10) denotes that the tangent stiffness matrix is evaluated in each iteration. The Newton-Raphson method can be interpreted as in Fig. 4.1 for one load increment.

The updating of the stiffness matrix after each iteration can be avoided by keeping the same stiffness matrix during the iteration in an increment. This technique

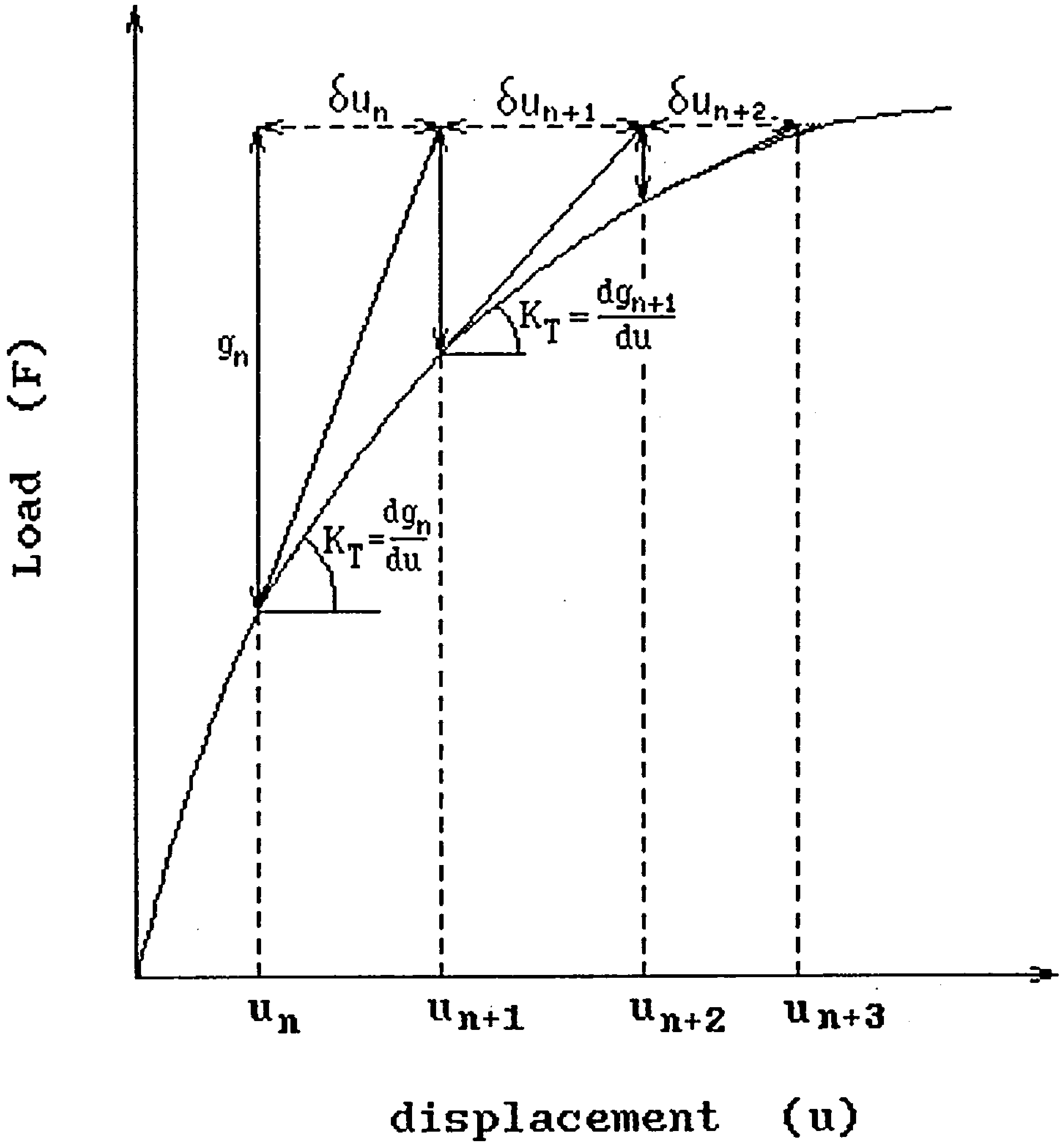

Fig. 4.1 : The Newton-Raphson Iteration Scheme.

is called modified Newton-Rapshon [MNR] method and has a slower convergence rate than the Newton-Rapshon method, but involves less work in each increment.

4.3 Convergence Criteria

To terminate an iterative procedure, a convergence criterion must be applied. For nonlinear finite element analysis, convergence criteria can be classified into force criteria, displacement criteria, stress criteria and combinations of them

[Bergan 1972, Crisfield 1991]. Usually the *lp* norm [Kreyszig 1988] :

$$\|x\|_p = (|x_1|^p + |x_2|^p + ... + |x_n|^p)^{\frac{1}{p}} \tag{4.11}$$

where $p \geq 1$, may be imposed as a convergence criteria. In practice, one usually takes $p = 1$ or 2 and a third norm, $\|x\|_\infty$, that is

$$\|x\|_1 = (|x_1| + ... + |x_n|) \tag{4.12}$$

is called the l_1 norm.

$$\|x\|_2 = (|x_1|^2 + ... + |x_n|^2)^{\frac{1}{2}} \tag{4.13}$$

is called Euclidean or l_2 norm.

$$\|x\|_\infty = max|x_j| \tag{4.14}$$

is called l_∞ norm or maximum norm. The Euclidean norm is used most often.

A force convergence criterion can be defined as follows;

$$\|g\|_p < \beta_d\|q_e\|_p \tag{4.15}$$

where g is the out-of-balance force and q_e is the external force or sometimes the reaction force. The constant β_d is given as a scaling value. Another force criterion, involves some scaling [Crisfield 1991], so that

$$\|gS\|_p < \beta_d\|q_eS\|_p \tag{4.16}$$

where S is the scaling factor. Crisfield use $S = C^{-1}$, where C is a diagonal matrix containing the leading diagonal terms from the tangent stiffness matrix at the beginning of the increment.

Based on displacement, the convergence criterion can be written as

$$\|\delta u\|_p < \beta_d\|u\|_p \tag{4.17}$$

where δu is the iterative displacement and u the accumulated displacement. The combination of displacement and force can be introduced as a convergence criterion which gives an energy-based criterion.

$$\|\delta u^T g|_p < \beta_d\|u^T q_e\| \tag{4.18}$$

In the present work, the force and displacement criteria are adopted. The Euclidean norm or $p = 2$ is employed in eq.(4.15) and (4.16). Both of them are implemented and convergence is achieved if one of them is satisfied.

4.4 Automatic Load Increment

Once the solution has converged, a new load increment must be chosen. The choice of increment size is important. If the load increment is too big the number of iterations will increase, and the convergence will be slow. On the other hand, too small an increment will increase computation time due to more converged states than strictly necessary being calculated and an increase in the number of incremental steps.

A number of methods for controlling the increment size have been published. Automatic incremental strategies can be divided into three groups. The first is based on the ratio of the desired number of iteration and the number of the previous iteration, the second is based on the current stiffness parameter and the last is based on a parabolic approximation to the load-deflection response [Murray *et al.* 1990]. Murray found that load incrementation based on the ratio of the desired iteration and the previous iteration is more effective than other schemes in his work on geometrically nonlinear finite element analysis of plane frames and arches.

The load incrementation strategy based on the ratio of J_d/J_{n-1} (where J_d is the desired number of iteration and J_{n-1} is the number of iterations in the previous increment step) can be combined with some steering parameter such as a load parameter, a selected displacement component, arc length and the external work-done. In the present work, the load incrementation based on J_d/J_{n-1} combined with arc length and load parameter is used.

To develop the load incrementation based on J_d/J_{n-1} combined with arc length, we let the new arc length Δl_n be defined based on the old arc length and the number of iteration given [Crisfield 1991],

$$\Delta l_n = \Delta l_{n-1}(\frac{J_d}{J_{n-1}})^\gamma \tag{4.19}$$

where Δl_{n-1} is the old arc length and the definition of arc length is presented in section(4.5.1) in eq.(4.32). The new load increment load factor, $\Delta\lambda_n$, is set to:

$$\Delta\lambda_n = \Delta\lambda_{n-1}(\frac{J_d}{J_{n-1}})^\gamma \tag{4.20}$$

where $\Delta\lambda_{n-1}$ is the previous load increment factor. The number of iterations desired should be supplied by the user. The initial load increment factor is usually given and eq.(4.20) may be used to calculate the new load increment factor. On substituting eq.(4.19) into (4.20), the new load increment factor is

$$\Delta\lambda_n = \Delta\lambda_{n-1}(\frac{\Delta l_n}{\Delta l_{n-1}})^\gamma \tag{4.21}$$

in which the exponent γ typically lies in the range 0.5 to 1.0 [Murray 1990]. The maximum load increment factor and possibly the minimum load increment load factor should be provided to avoid the cutting of increment size (section 4.5.1) because otherwise an imaginary root can occur, especially in the arc length method (section 4.5.1).

4.5 Iterative solution Strategy

The iterative solution strategy is intended to enable solution algorithms to pass maximum or minimum limit points, which are found in all nonlinear finite element problems. In nonlinear problems, it is always connected with singularities that occur somewhere along the solution path. These singularities are better known as critical points. Their classification into limit points is well known [Riks 1979]. Fig. 4.2a illustrate the load/deflection curve involving limit point B with snap through. Without an iterative solution strategy, the final convergence will fail in the neighbourhood of limit point B, that is point A, or may be possible to move directly to point D in some cases.

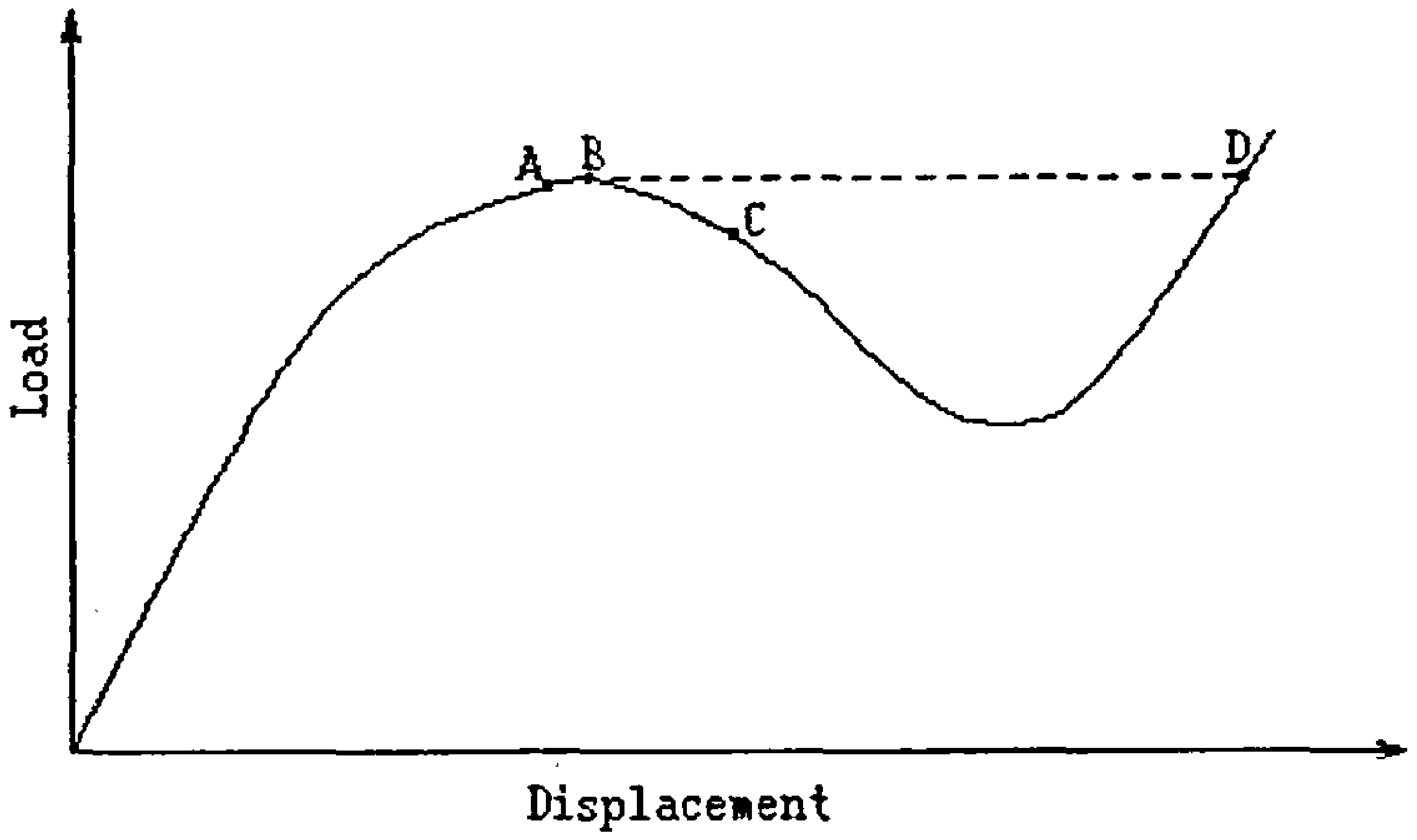

Fig. 4.2a : Load/deflection curve of snap-through.

In the present work, the need for an iterative solution strategy can be illustrated using a load/deflection curve of an elastic perfectly plastic material with limit point B (see Fig. 4.2b). Without an iterative solution strategy, the final convergence of the nonlinear equilibrium path just reaches point A, just before point B. On the other hand, by means of iterative solution strategy the nonlinear equilibrium path can pass easily from limit point B to point C.

Several methods have been developed e.g.: iteration at constant displacement, iteration at constant arc-length, iteration at constant external work, iteration at minimum unbalanced displacement norm, iteration at minimum unbalanced force

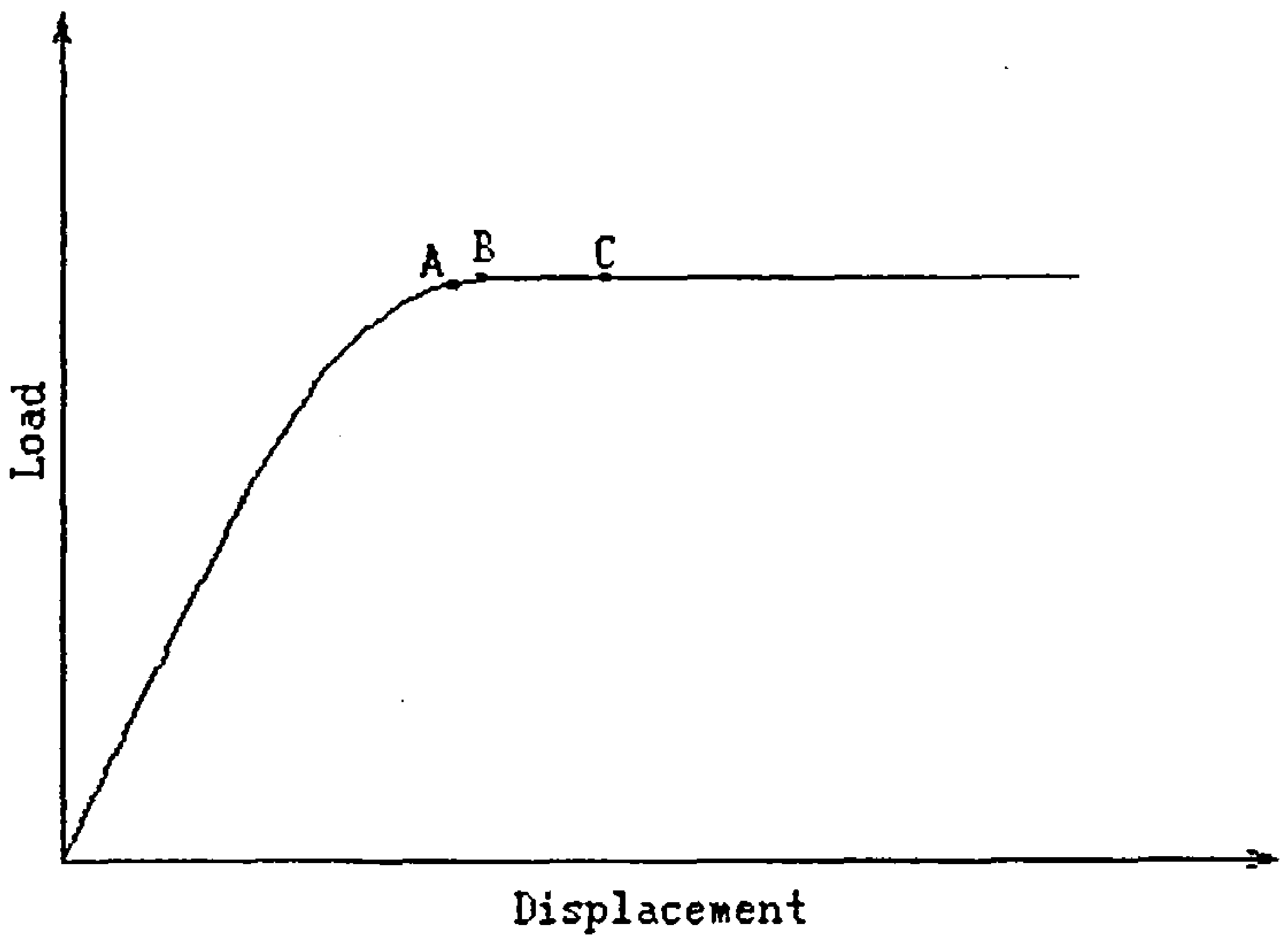

Fig. 4.2b : Load/deflection curve of elastic perfectly plastic.

and iteration at a constant weighted response [Murray *et al.* 1990], for such problems.

Murray found in his work on the geometrically nonlinear finite element analysis of plane frames and arches, that three of the above methods, namely iteration at constant arc length, iteration at minimum unbalanced displacement norm and iteration at constant weighted response, exhibit virtually identical performance and are the most successful general purpose iteration techniques. None of these three methods appears to require suppression of equilibrium iterations in the neighbourhood of load and displacement limit points. In this present work, iteration at constant arc length method is implemented. This method will be described in detail in the next section.

4.5.1 Constant Arc Length Method

Originally the arc length method was proposed by Riks [1979] and Wempner [1971]. Riks used the normal tangent rather than circular path (see Fig. 4.3a) but this method sometimes fails [Crisfield 1981, Murray 1990]. The arc length method then is modified by Crisfield [1981, 1982, 1986, 1991] as follows.

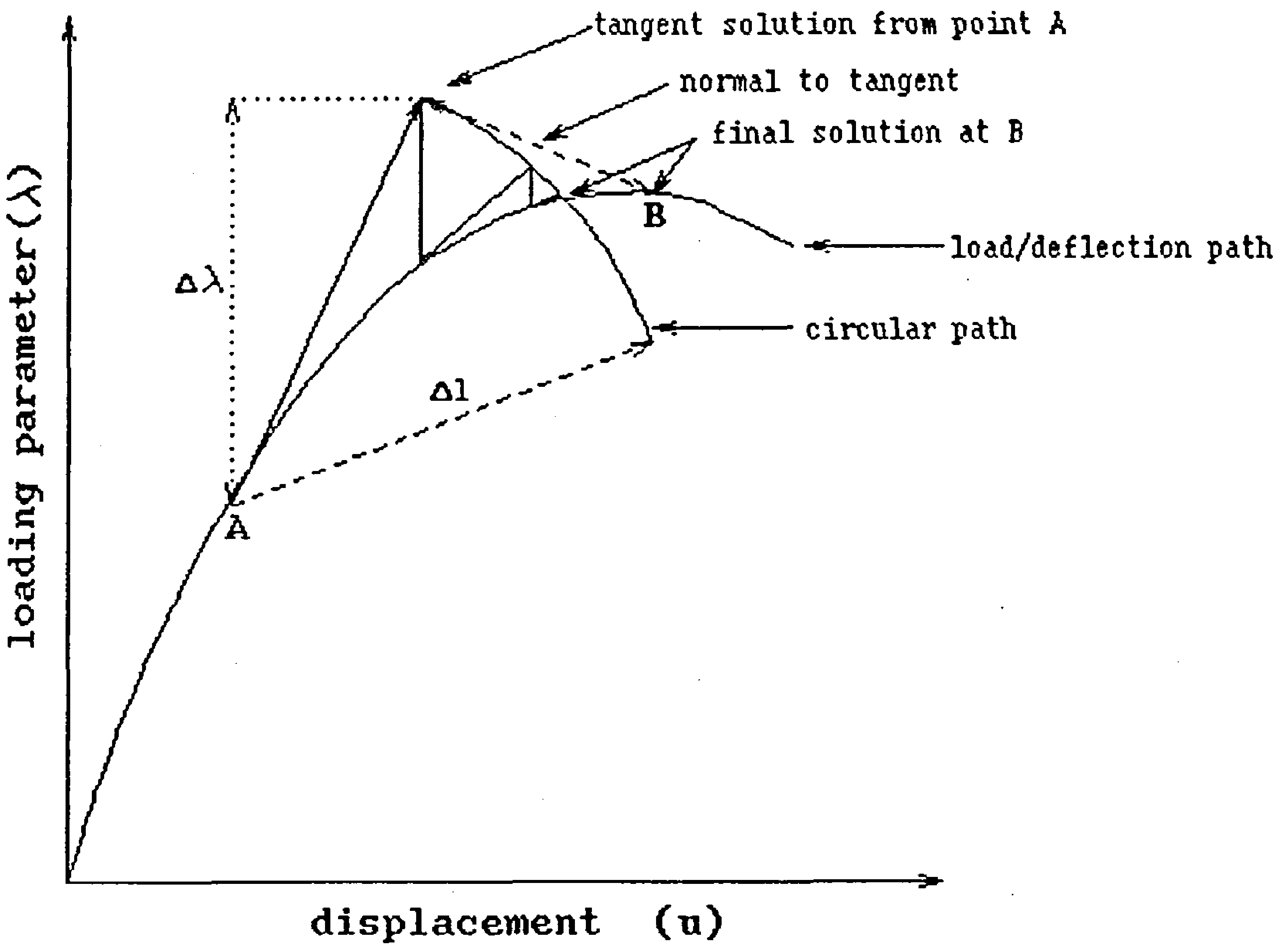

Fig. 4.3a: Risk method [Crisfield 1981]

For a given load level $\Delta\lambda$ it is desired to satisfy the equilibrium equation

$$g(u,\lambda) = F_i(u) - \Delta\lambda F_{ef} = 0 \tag{4.22}$$

where F_i is the internal force as a function of the displacements u, F_{ef} is a fixed load vector and $\Delta\lambda$ is the loading factor. In the previous section, the incremental loading factor is obtained at the beginning of each increment and without iterative strategy is kept constant at each iteration. The purpose of iterative strategy, in this case constant arc length, is to find the intersection during iteration between the path true solution given by eq.(4.22) and the constant arc length given by the load parameter $\Delta\lambda$ at the beginning of increment (see Fig. 4.3b) The load parameter $\Delta\lambda$ may be changed at each iteration in order to obtain the intersection. Using Fig. 4.3b the constant arc length can be defined as

$$l = \int dl \tag{4.23a}$$

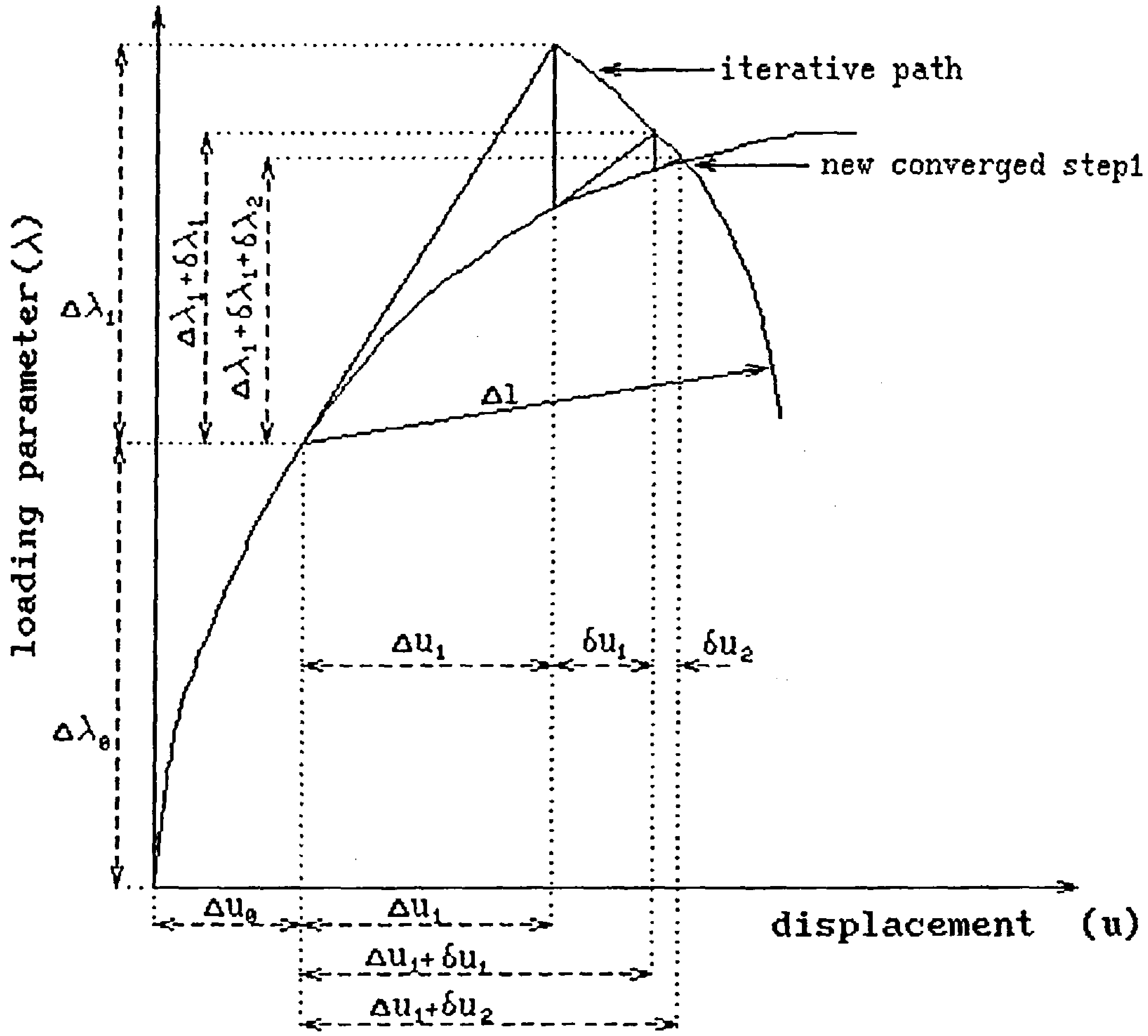

Fig. 4.3b: spherical arc length method.

where

$$dl = \sqrt{du^T du + d\lambda^2 \varphi^2 F_{\epsilon f}^T F_{\epsilon f}} \tag{4.23b}$$

The parameter φ is the scaling parameter between the load and displacement terms [Crisfield 1991]. Eq.(4.23b) may be written as follows

$$dl^2 = du^T du + d\lambda^2 \varphi^2 F_{\epsilon f}^T F_{\epsilon f} \tag{4.24a}$$

If the above equation is written in an incremental form and all terms moved to the left hand side we have

$$a = (\Delta u^T \Delta u + \Delta\lambda^2 \varphi^2 F_{\epsilon f}^T F_{\epsilon f}) - \Delta l^2 = 0 \tag{4.24b}$$

where Δl is the constant arc length of the desired intersection. Using truncated Taylor series eq.(4.22) and (4.24b) may be written as

$$g_n = g_o + \frac{\partial g}{\partial u}\delta u + \frac{\partial g}{\partial \lambda}\delta\lambda = g_o + K_t\delta u - F_{\epsilon f}\delta\lambda = 0 \tag{4.25}$$

and

$$a_n = a_o + 2\Delta u^T\delta u + 2\Delta\lambda\delta\lambda\varphi^2 F_{\epsilon f}^T F_{\epsilon f} = 0 \tag{4.26}$$

Where subscript $_o$ means old and $_n$ means new. The unknown value δu and $\delta\lambda$ can be obtained the following equations

$$\begin{pmatrix} \delta u \\ \delta\lambda \end{pmatrix} = -\begin{bmatrix} K_T & -F_{\epsilon f} \\ 2\lambda u^T & 2\Delta\lambda\varphi^2 F_{\epsilon f}^T F_{\epsilon f} \end{bmatrix}^{-1} \begin{bmatrix} g_o \\ a_o \end{bmatrix} \tag{4.27}$$

and the new increment load factor can be written as

$$\Delta\lambda_n = \Delta\lambda_o + \delta\lambda \tag{4.28}$$

However, the stiffness matrix in eq.(4.27) is neither symmetric nor banded. Instead of solving eq.(4.27), one may use eq.(4.25) as

$$g_o + K_T\delta u - F_{\epsilon f}\delta\lambda = 0$$

$$\delta u = -K_T^{-1}(g_o(\Delta u_o, \lambda_o) - \delta\lambda F_{\epsilon f}) \tag{4.29a}$$

Equation (4.29a) can be explicitly rewritten as follows

$$\delta u = \bar{\delta u} + \delta\lambda\delta u_{\epsilon f} \tag{4.29b}$$

where $\delta u_{\epsilon f} = K_T^{-1}F_{\epsilon f}$, is the displacement vector corresponding to the fixed load vector $F_{\epsilon f}$. Using equation (4.29b) the displacement increment can be written as

$$\Delta u_n = \Delta u_o + \delta u = \Delta u_o + \bar{\delta u} + \delta\lambda\delta u_{\epsilon f} \tag{4.30}$$

Considering eq.(4.30), $\delta\lambda$ is the only unknown variable and it can be calculated using eq.(4.24b) and (4.30). Since arc length is constant, eq.(4.24b) can be expressed as

$$\Delta u_o^T \Delta u_o + \Delta\lambda_o \varphi^2 F_{\epsilon f}^T F_{\epsilon f} = \Delta u_n^T \Delta u_n + \Delta\lambda_o \varphi^2 F_{\epsilon f}^T F_{\epsilon f} = \Delta l^2 \tag{4.31}$$

On substituting eq(4.30) into eq.(4.31), the unknown $\delta\lambda$ can be obtained and gives a quadratic equation

$$A\delta\lambda^2 + B\delta\lambda + C = 0 \tag{4.32}$$

where

$$A = \delta u_{\epsilon f}^T \delta u_{\epsilon f} + \varphi^2 F_{\epsilon f}^T F_{\epsilon f}$$

$$B = 2\delta u_{\epsilon f}(\Delta u + \bar{\delta} u) + 2\Delta\lambda_o \varphi^2 F_{\epsilon f}^T F_{\epsilon f}$$

$$C = (\Delta u_o + \bar{\delta} u)(\Delta u_o + \bar{\delta} u) - \Delta l^2 + \Delta\lambda_o^2 F_{\epsilon f}^T F_{\epsilon f}$$

Instead of applying eq.(4.24) numerical experience has shown that it is preferable to neglect the term involving the parameter φ [Crisfield 1981], then eq.(4.24) may be replaced by

$$a = (\Delta u^T \Delta u^T) - \Delta l^2 = 0 \tag{4.33}$$

and using eq.(4.33), eq.(4.32) may be written as

$$A\delta\lambda^2 + B\delta\lambda + C = 0 \tag{4.34}$$

where

$$A = \delta u_{\epsilon f}^T \delta u_{\epsilon f}$$

$$B = 2\delta u_{\epsilon f}(\Delta u + \bar{\delta} u)$$

$$C = (\Delta u_o + \bar{\delta} u)(\Delta u_o + \bar{\delta} u) - \Delta l^2$$

Ramm (as quoted by Crisfield (1991)] also independently concluded that for practical problems the parameter φ had little effect and suggested setting φ equal to zero. As a result, eq.(4.33) and (4.34) should be considered as cylindrical rather than spherical.

Denote the two roots of equation (4.34) $\delta\lambda_1$ and $\delta\lambda_2$. The correct choice is the one which avoids 'doubling back' on the load-deflection response, that is the solution with which gives the minimum angle between Δu_o and Δu_n and this angle is the maximum cosine of

$$\cos\theta = \frac{\Delta u_o^T \Delta u_n}{\Delta l^2} = \Delta u_o^T \frac{(\Delta u_o + \Delta\delta\bar{u})}{\Delta l^2} + \delta\lambda \frac{\Delta u_o^T \delta u_{\epsilon f}}{\Delta l^2} \qquad (4.35)$$

Being a quadratic equation, eq.(4.34) will have imaginary root, if $B^2 - 4AC$ is less than zero. This problem can appear if the initial load increment is too large [Crisfield 1981] and the structure exhibits multiple instability directions at a point [Meek 1989]. If the imaginary root appears, it is necessary to cut the load incremental size. A simple strategy can be used as follows [Crisfield 1991]

$$\frac{\Delta\lambda_n}{\Delta\lambda_o} \text{or} \frac{\Delta l_n}{\Delta l_o} = \frac{\beta_d}{\beta_o} \geq 0.1 \quad \text{and} \quad \leq 0.5 \qquad (4.36)$$

where β_o is the convergence factor and β_d is the given desired convergence factor (see section 4.3). This strategy can also be implemented when the convergence of the structural equilibrium iteration is not achieved within the specified number of iterations.

- **Initial Predictor**

If the constant arc length method is employed with the modified Newton-Raphson method, an initial predictor must be adopted to compute the tangent displacement $\Delta u_{\epsilon f_p}$. This is due to the fact that K_T does not change during each iteration [Crisfield 1991]. We rewrite the tangent displacement solution as

$$\Delta u_{\epsilon f} = K_T^{-1} F_{\epsilon f} \qquad (4.37)$$

If the initial predictor is denoted by $\Delta\lambda_p$ then the tangent displacement is given by

$$\Delta u_{cfp} = \Delta\lambda_p K_T^{-1} F_{cf} = \Delta\lambda_p \Delta u_{cf} \tag{4.38}$$

where K_T is the tangent stiffness matrix at the beginning of an increment. Substituting eq.(4.37) into (4.31) with $\varphi = 0$ gives

$$(\Delta\lambda_p \Delta u_{\epsilon f})^T (\Delta\lambda_p \Delta u_{\epsilon f}) - \Delta l^2 = 0$$

$$\Delta\lambda_p^2 \Delta u_{\epsilon f}^T \Delta u_{cf} - \Delta l^2 = 0$$

$$\Delta\lambda_p = \pm \frac{\Delta l}{\sqrt{\Delta u_{\epsilon f}^T \Delta u_{\epsilon f}}} \tag{4.39}$$

where Δl is the given increment. In eq(4.39) the sign of the initial load can be positive or negative. It is important to choose the correct sign. It is proposed that the sign of $\Delta\lambda_p$ should follow that in the previous increment unless the determinant of the tangent stiffness matrix changes sign. When Gaussian elimination without row or column interchanges is employed, a row reduced upper triangular matrix is obtained. Then the determinant of the tangent stiffness matrix can be readily obtained as the product of all the diagonal terms of this matrix. This determinant can have a very large value may exceed computer's capacity. To avoid this problem and since only the sign is needed, every product of diagonal terms is divided by its absolute value.

The constant arc length can be used from the beginning of the first incremental loading or after a certain degree of nonlinearity is reached. Since the constant arc length is needed to pass the limit point, the arc length method, in the present work, is used after reaching a certain degree of nonlinearity. Then the automatic incremental load factor (section 4.4) is replaced by on initial load predictor even if the full Newton-Raphson method is employed. The advantages of using the initial predictor after reaching a certain degree of nonlinearity is that a change of sign of incremental loading shows the turning of the load-deflection direction. The constant arc length, Δl, in eq(4.39) is given

$$\Delta l = \Delta\lambda_o \Delta l_o \tag{4.40}$$

where $\Delta\lambda_o$ is the previous load increment factor and Δl_o is the previous constant arc length. As in the automatic load increment factor method, the constant arc length must be given an upper and lower bound. In this present work the bounds are

$$\Delta l_{min} \leq \Delta l \leq \Delta l_{max}$$

$$\Delta l_{min} = 0.01\Delta\lambda_o$$

$$\Delta l_{max} = 2.0\Delta\lambda_o \tag{4.41}$$

To switch the constant iterative method to the arc length method, some measure of the degree of nonlinearity is needed. The current stiffness parameter originally introduced by Bergan [1978] can be used as such a measure. The stiffness of the system means the relation between a load increment and the corresponding displacement as

$$k' = \frac{\Delta F}{\Delta u} \tag{4.42}$$

ΔF and Δu can be made scalar by multiplying both by Δu [Crisfield 1991, Bergan 1982]

$$k = \frac{\Delta u^T \Delta F}{\Delta u^T \Delta u} = \frac{F_{\epsilon f} \Delta u_{\epsilon f}}{u_{\epsilon f}^T u_{\epsilon f}} \tag{4.43}$$

The stiffness parameter k_s, can then be obtained by simply scaling the current k value by the initial k_o value

$$k_s = \frac{k}{k_o} \tag{4.44}$$

It can be seen from eq.(4.44) that if k_s is equal to 1, there is no change of the current stiffness and the value k_s is equal to zero at the limit point. To switch the constant iteration solution to a constant arc length procedure, the desired current stiffness can be introduced as follows

$$|1 - k_s| \geq k_d \tag{4.45}$$

where k_d is the desired current stiffness parameter and must be equal to or less than 1.0.

4.6 Numerical Examples

The purpose of this section is to demonstrate the numerical performance of the nonlinear shell finite element in comparison with other numerical solutions and analytical solutions. Examples which consist of seven nonlinear problems are presented in this section. All the numerical examples employed the solution technique which has been described above, with a convergence criterion of 1.2% or less.

Example 1. Circular Plate with Uniform Load

The first example is a circular plate. Only geometric nonlinearity is considered. The analytical solution can be found in Timoshenko [1959]. The plate is clamped around the edge and a quarter model is used. Fig. 4.4 shows the geometry of problem. Two types of meshes are used to analyse the problem. First, twelve elements are employed using large load increments. Fig. 4.5a shows that the proposed element gives reasonable result. Futhermore by applying smaller loading increments, the convergence rate is greatly increased. Second, thirty two elements are employed. As the first case, large and small load increments are applied. Fig. 4.5b shows that the convergence rate is greatly increased by using smaller load increments. Comparing Fig. 4.5a and Fig. 4.5b show that the solution accuracy is not much influenced by the number of elements used. Both figures show that the convergence rate is largely increased by using small load increments.

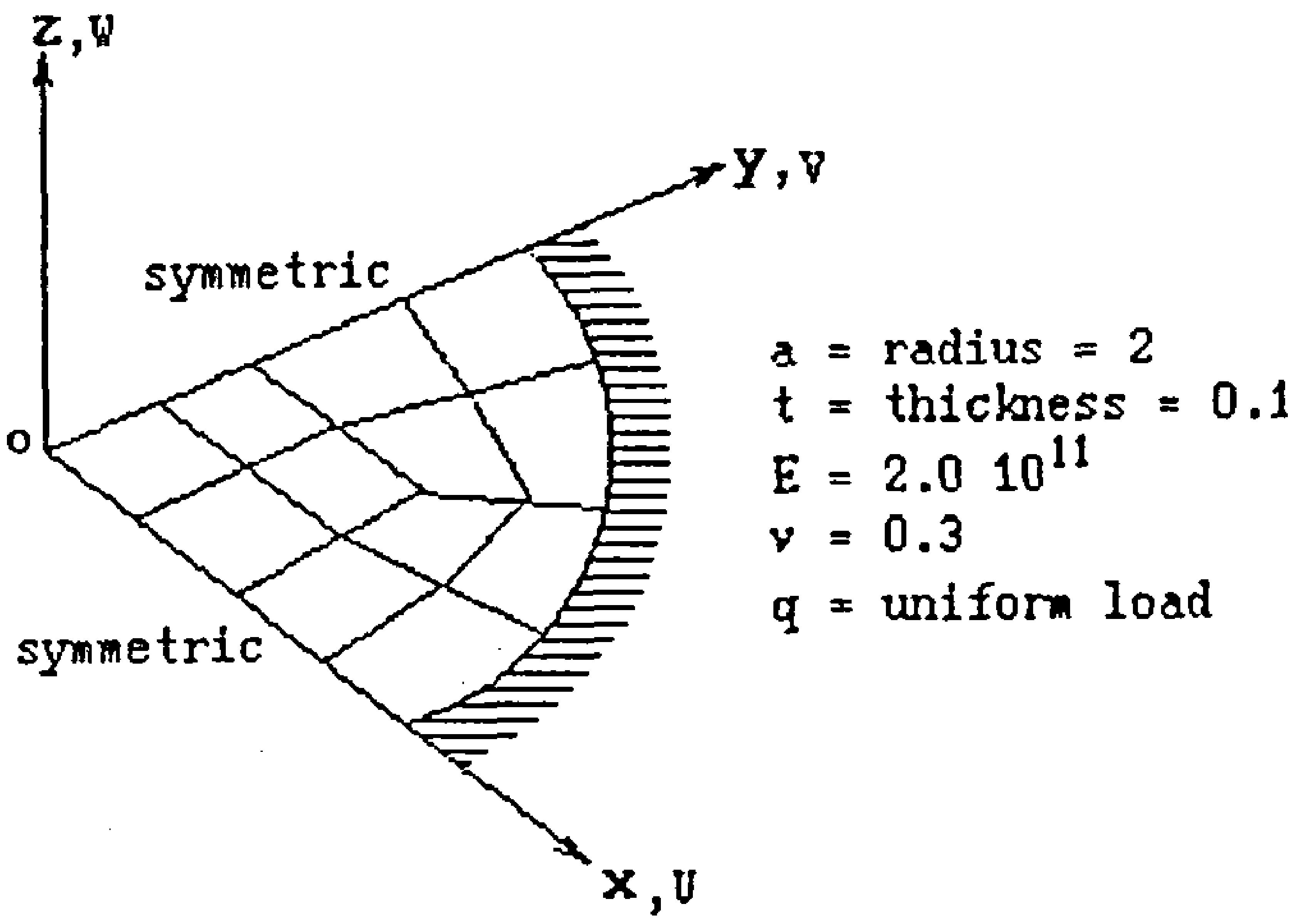

Fig. 4.4 : A quarter model of circular plate.

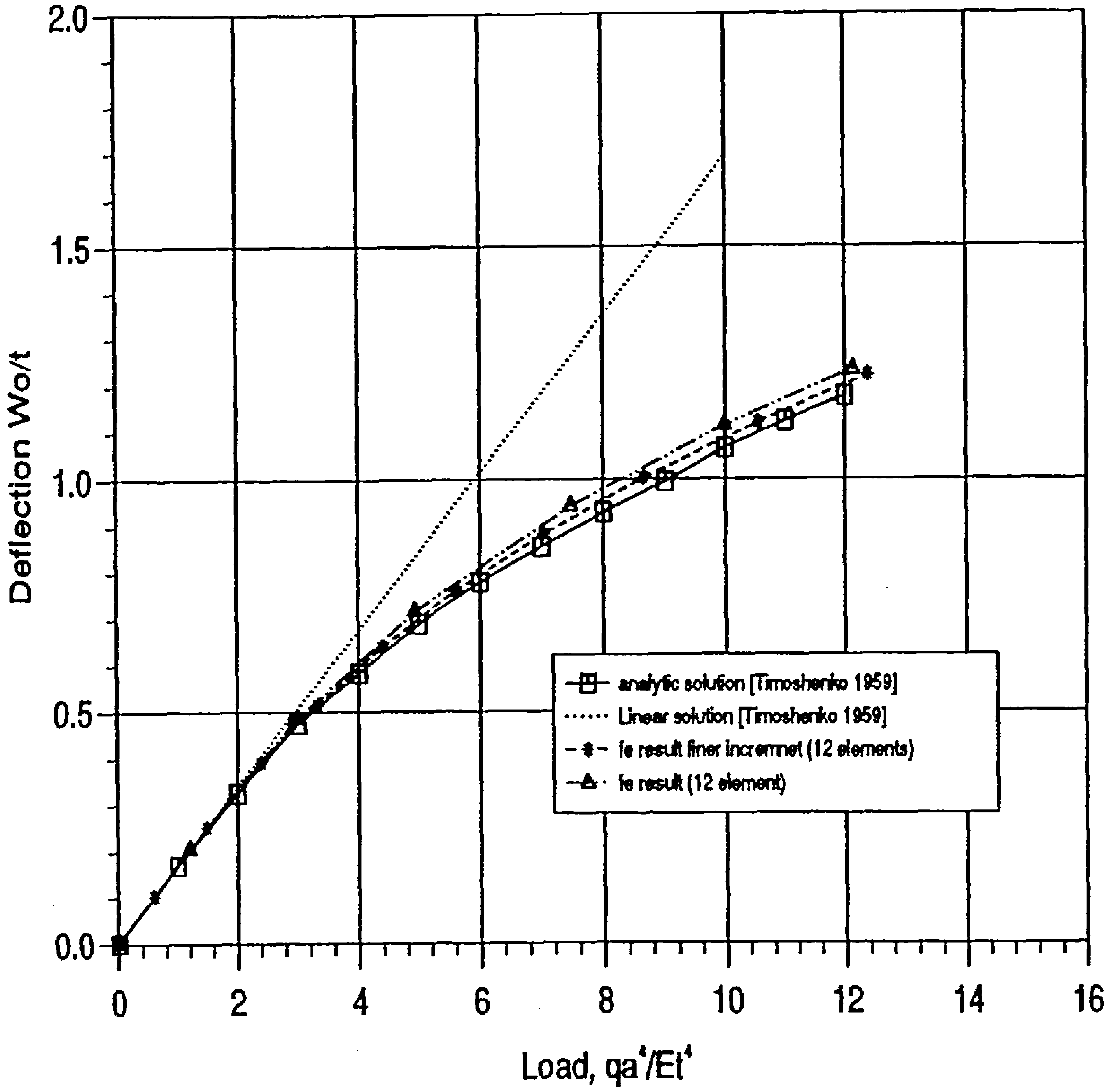

Fig. 4.5a : Centre displacement of circular plate under uniform load with 12 element.

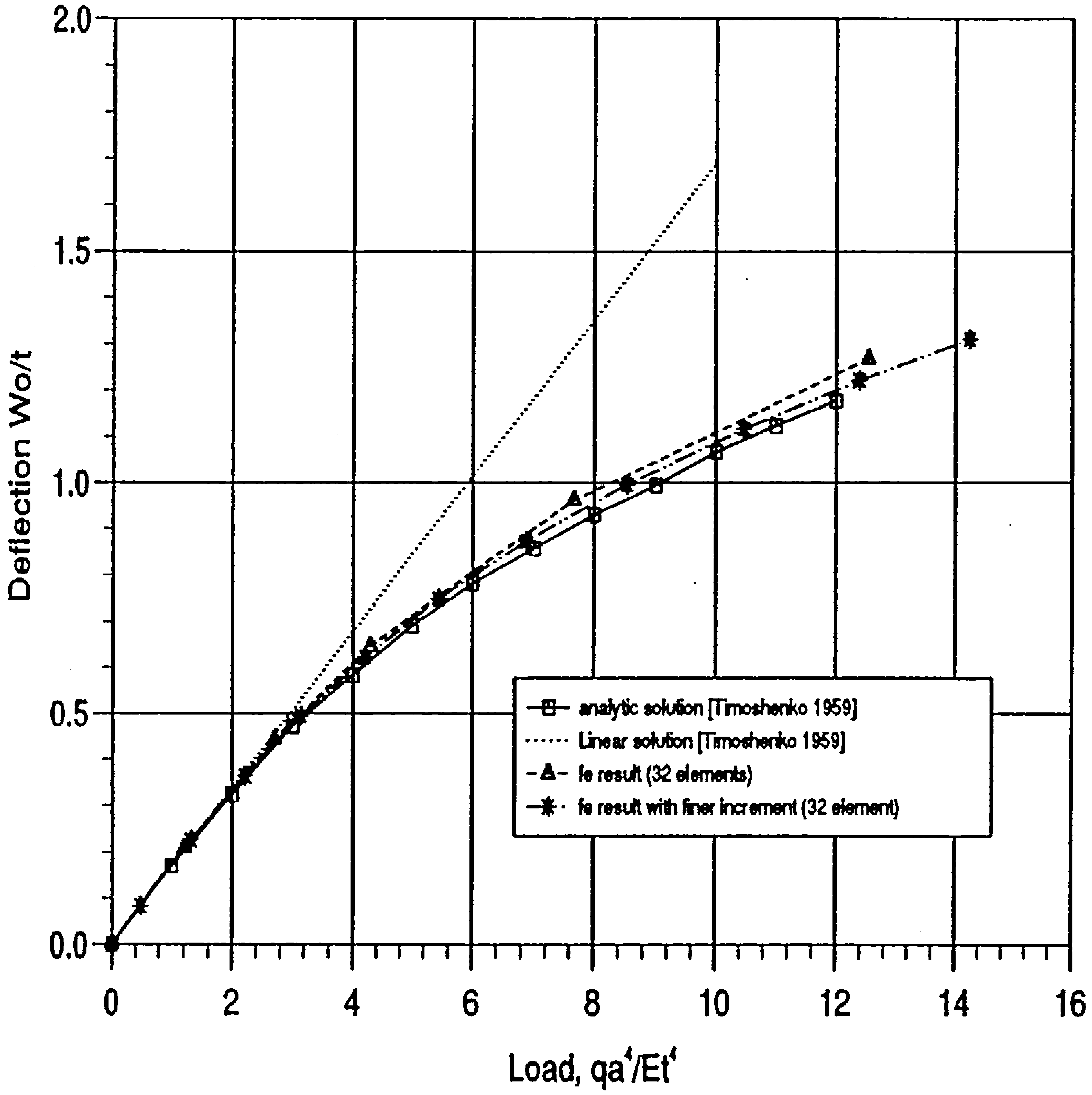

Fig. 4.5b : Centre displacement of circular plate under uniform load with 32 element.

Example 2. Cantilever Beam Subjected to End Loading.

This simple problem, shown in Fig. 4.6, has been analysed by a number of workers [Parisch 1981, Milford 1986, Saleeb 1990]. The analytic solution was given by Parisch [1981]. Three types of nonlinear problems are considered as follows.

First, the problem is analysed as a perfectly plastic material with small displacements using twenty two element with ten layers per element. Using constant load increments i.e without the iterative strategy solution, the finite element solution can not pass the maximum point. The solution diverged when the load neared the ultimate load (see Fig. 4.7a). By using the iterative strategy solution, the finite element method can pass the maximum point easily. The maximum load obtained by the finite element method is 6% higher than the analytical solution. The difference is due to the fact that the integration point are not on the surface of the element, hence the plasticity is delayed.

Second, geometric nonlinerity is considered. Fig. 4.7b shows that finite element solution gives a reasonable result. Here, the analytical solution assumes that the stretching of the beam neglible in comparison with the bending deformation [Parisch 1981].

Third, geometric and material nonlinearity problems are both considered together. Like the first case, twenty two elements with ten layers per element are used. Fig. 4.7c shows that good agreement with the analytic solution is obtained by the finite element solution.

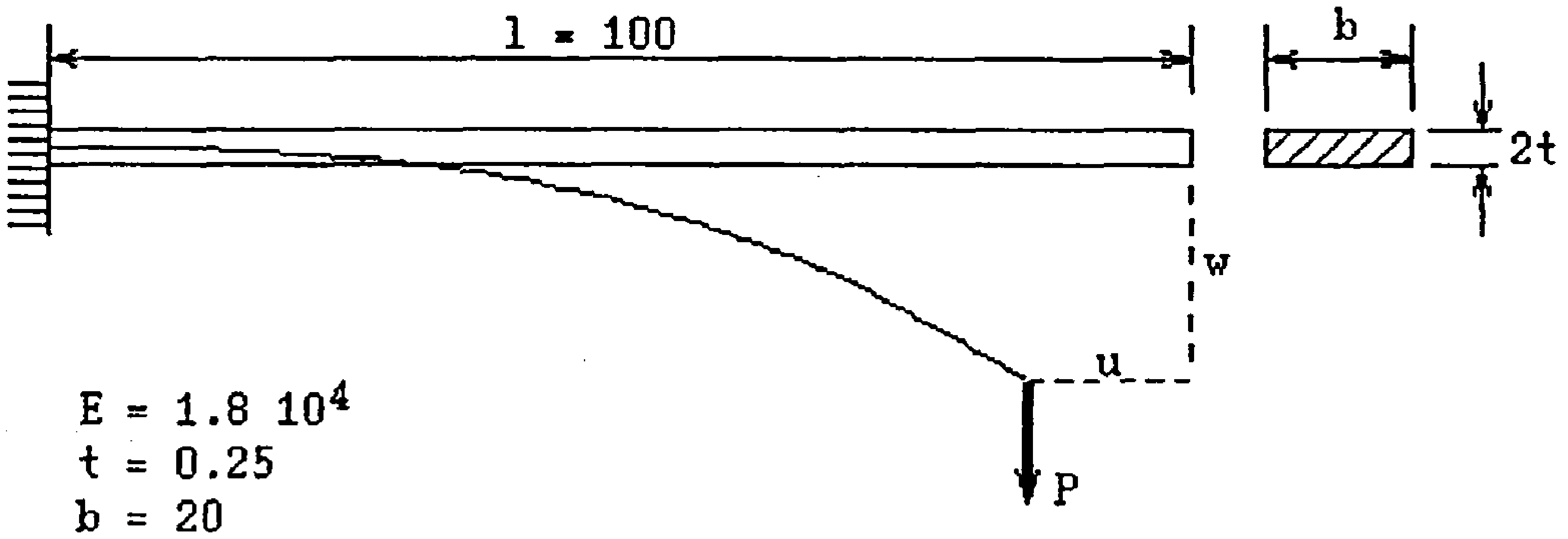

$E = 1.8\ 10^4$

$t = 0.25$

$b = 20$

$\sigma_y = 40$ (yield stress)

$P_y = 1/3$ (yield load-linear solution)

$$k_p = -\frac{\sigma_y l}{Et} = -\frac{8}{9}$$

$$k_e = \frac{l^2 P}{D}$$

D = bending rigidity

Fig. 4.6 : Cantilever beam with end load.

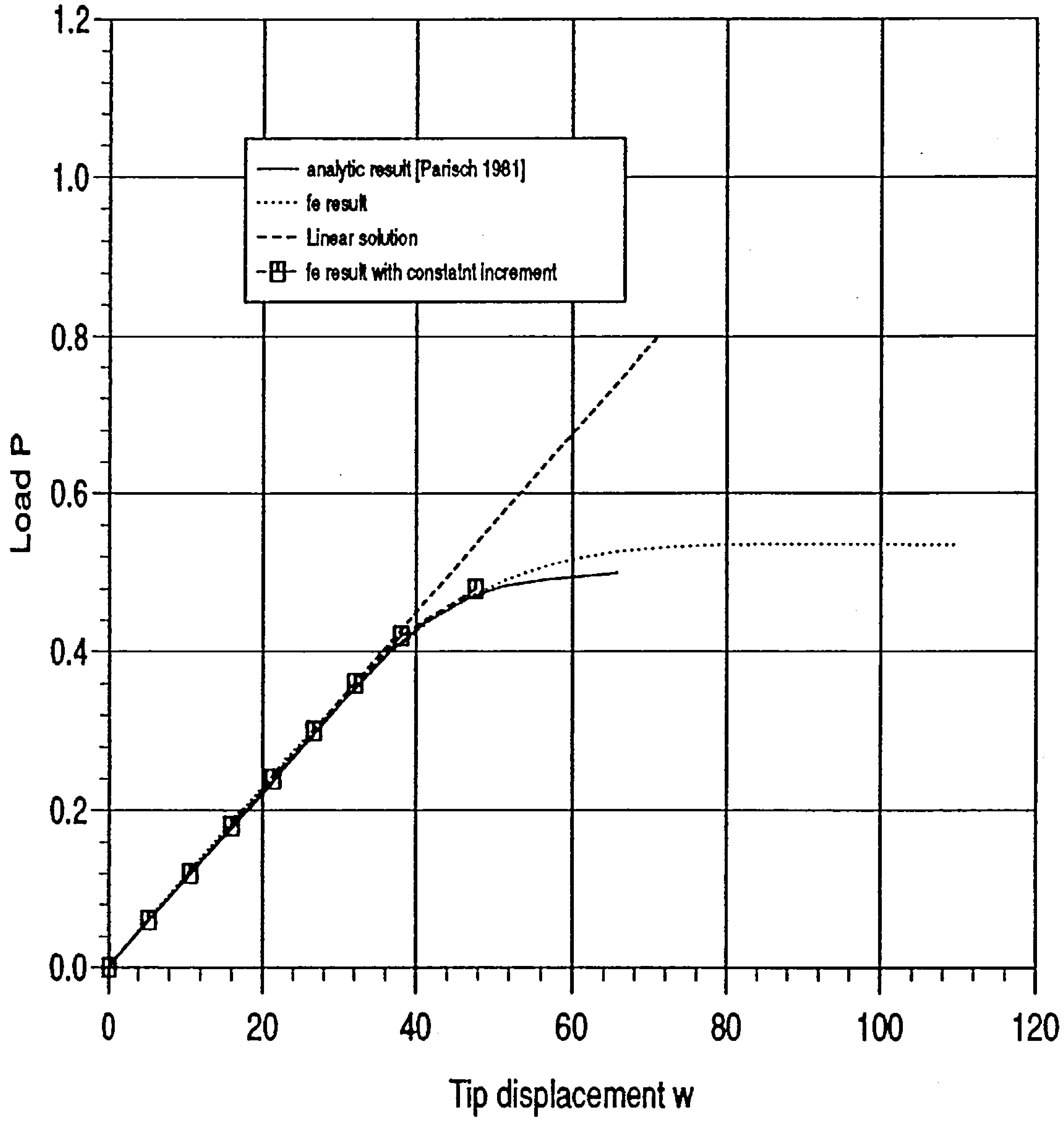

Fig. 4.7a : Tip displacement of cantilever beam: elastic-perfectly plastic problem.

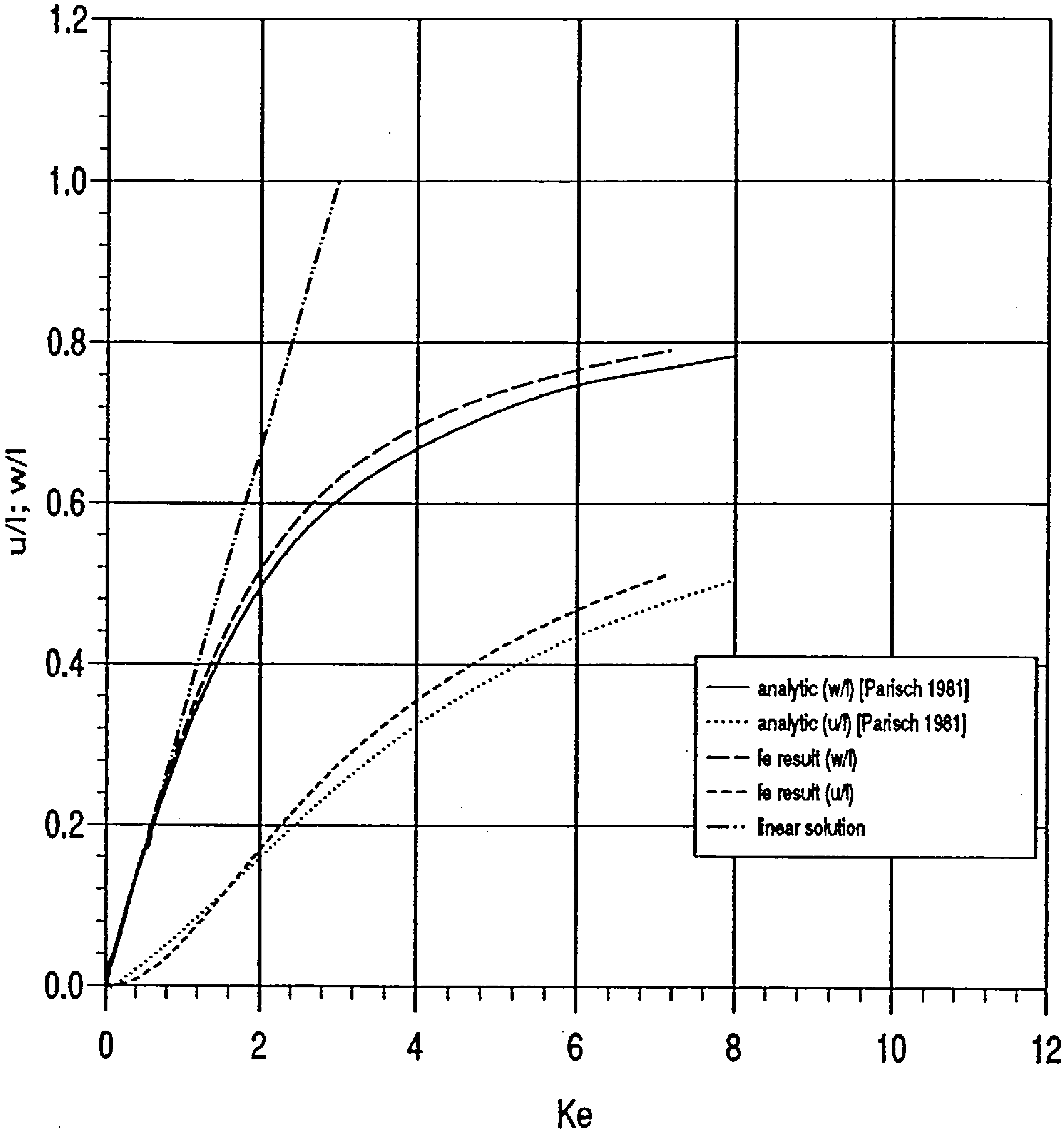

Fig. 4.7b : Tip displacement of cantilever beam; geometric nonlinearity problem.

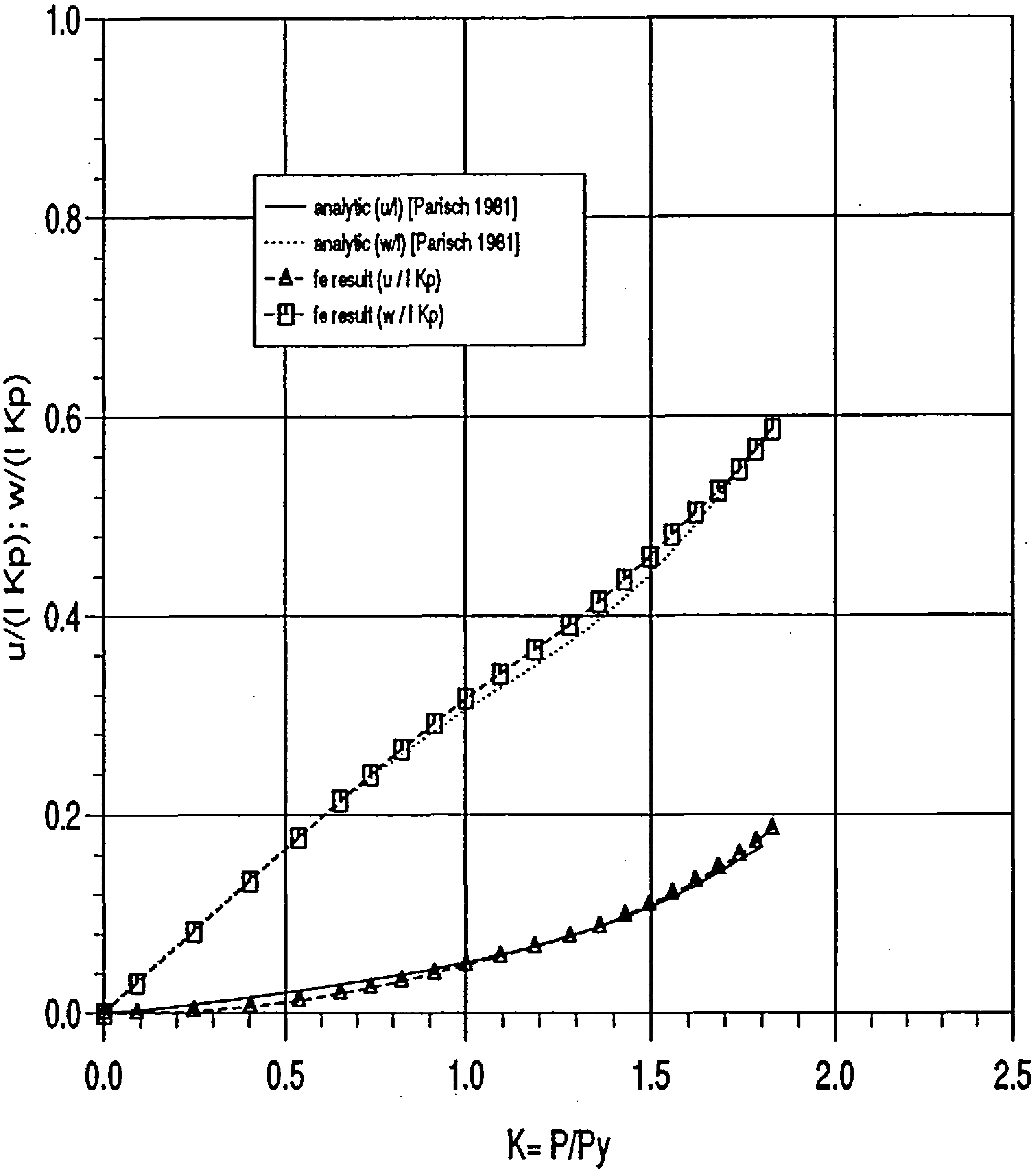

Fig. 4.7c : Tip displacement of cantilever beam; geometric and material nonlinearity problem.

Example 3. Large Displacement Analysis of Hinged Cylindrical Shell

Fig. 4.8 shows the geometry of a hinged cylindrical shell subjected to a point load at its centre. The present code gives reasonable results compare to other workers' results (see Fig. 4.9). A high solution accuracy with 3 to 5 iterations per load increment was noticed for a relative error of 0.75%.

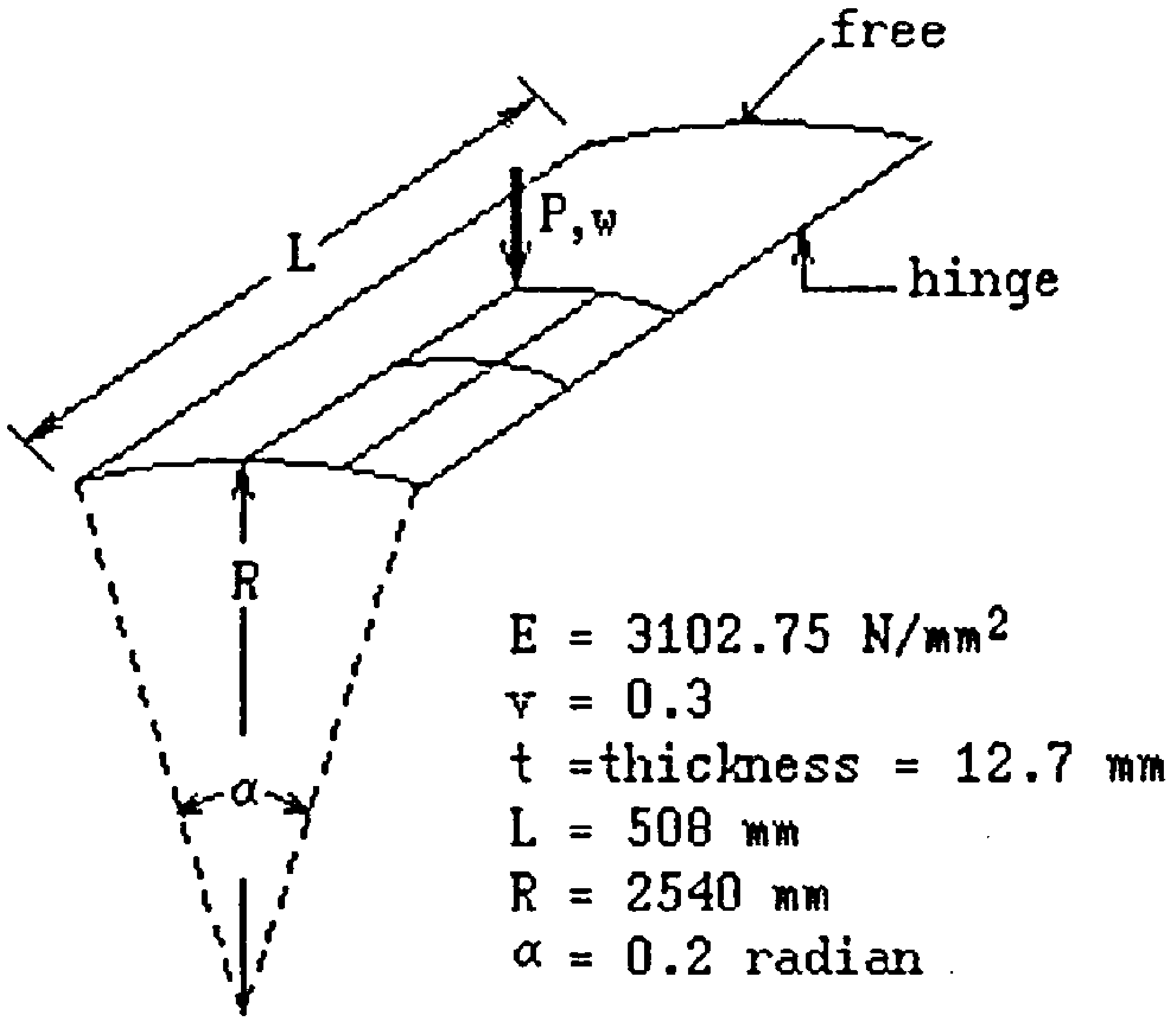

Fig. 4.8 : Hinged cylindrical shell.

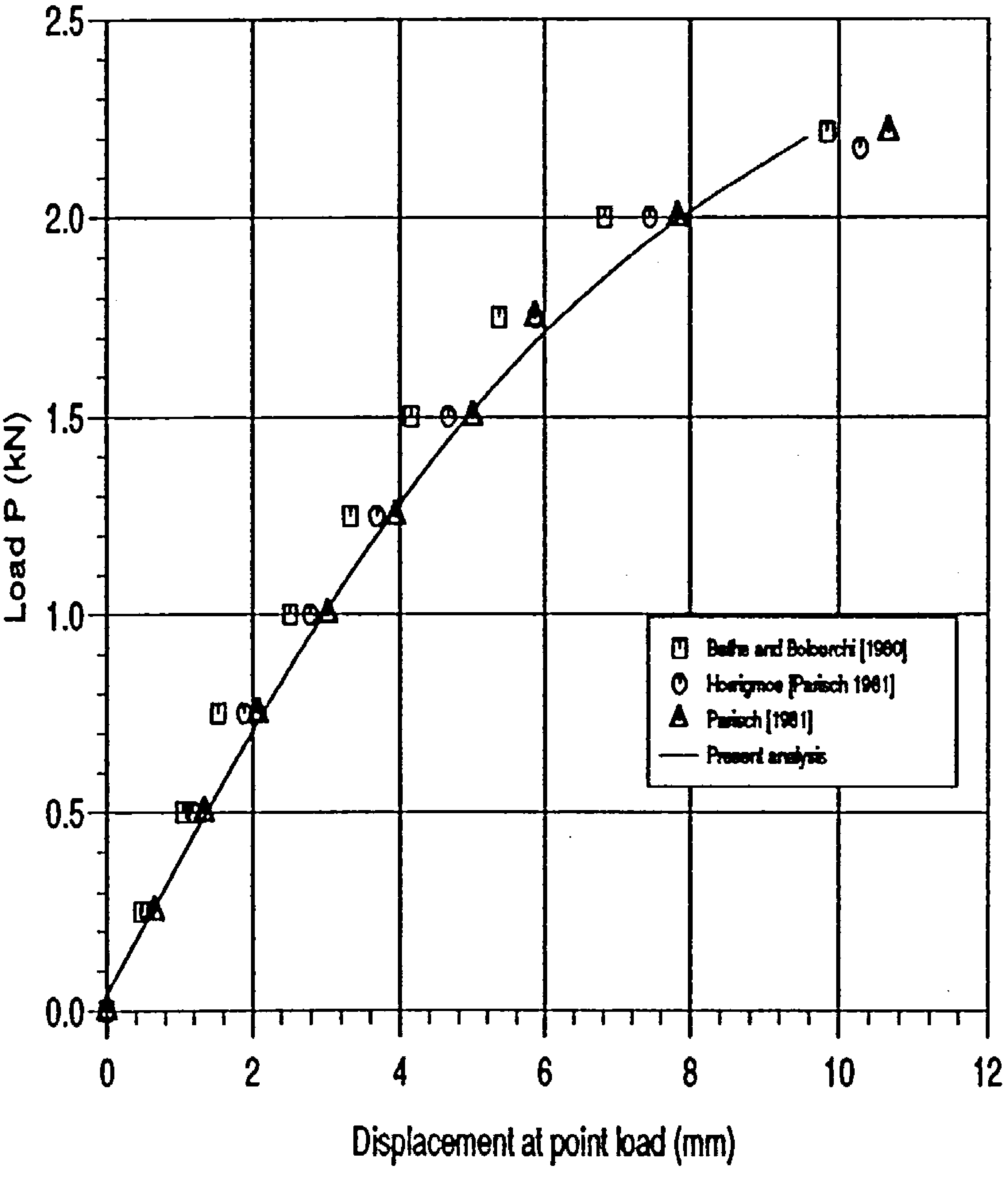

Fig. 4.9 : Centre displacement of hinged cylindrical shell.

Example 4. Cylindrical Roof under Gravity Loading

Fig. 4.10 shows the geometry of a cylindrical roof. It is assumed that the straight longitudinal edges are free and the two circular edges are supported by diaphragms. One quarter of the shell is analysed using a 2x2 mesh and three layers are employed per element. Two problems are considered as follows.

First, the elastic-perfectly plastic problem is analysed. As shown in Fig. 4.11a, good agreement with Hinton's [1984] result is obtained by the present code. More flexible results are given by Yang [1985] and Dupuis [1971]. However, all load displacement curves have approximately the same ultimate load.

Second, the shell is analysed including the effects of geometric nonlinearity. The same finite element modeling and number of layers are used. The result of middle edge displacement against gravity load is plotted in Fig. 4.11b. Again, good agreement with Hinton's [1984] result is obtained by the present code.

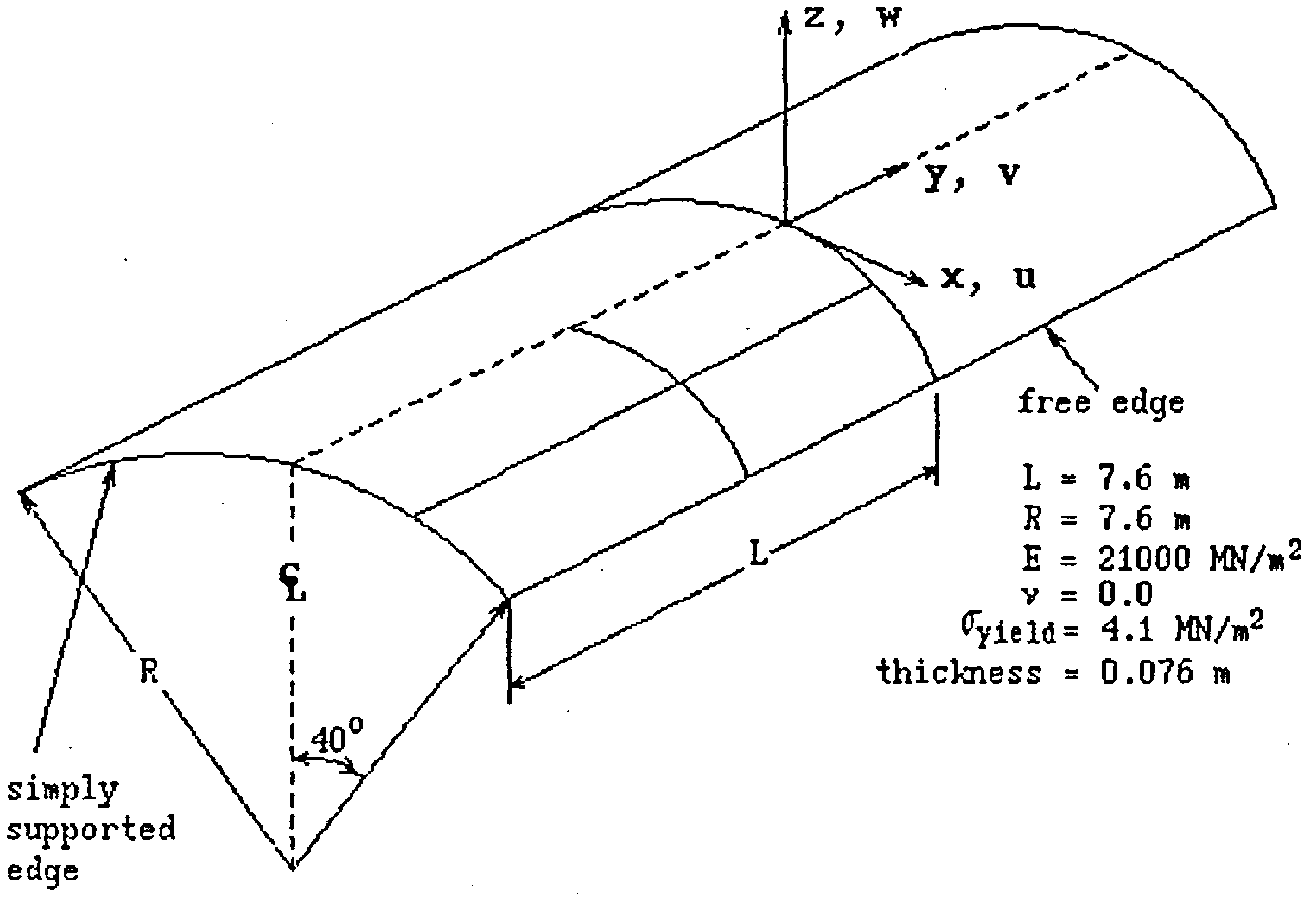

Fig. 4.10 : Cylindrical roof model.

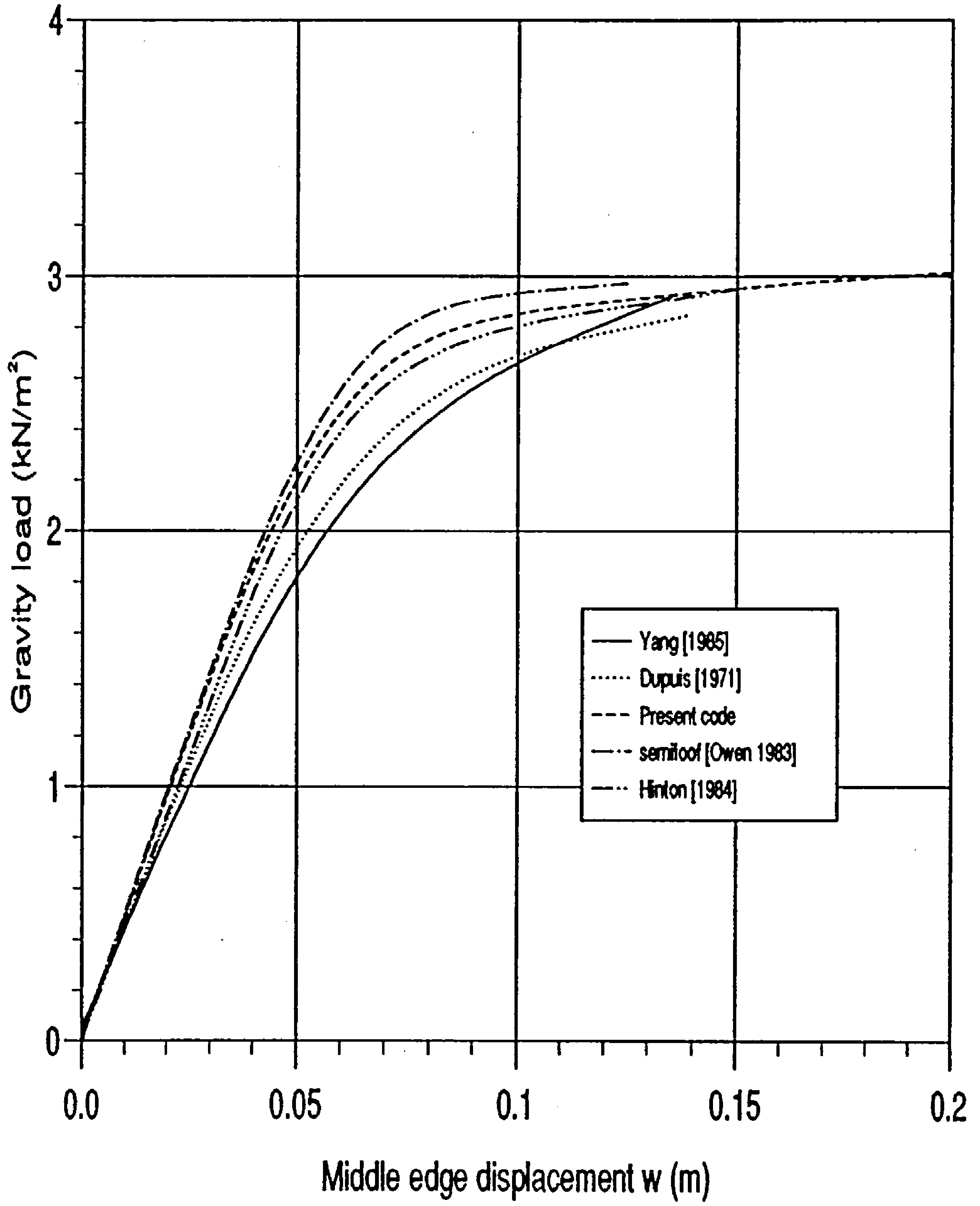

Fig: 4.11a : Elastic perfectly plastic analysis of cylindrical roof.

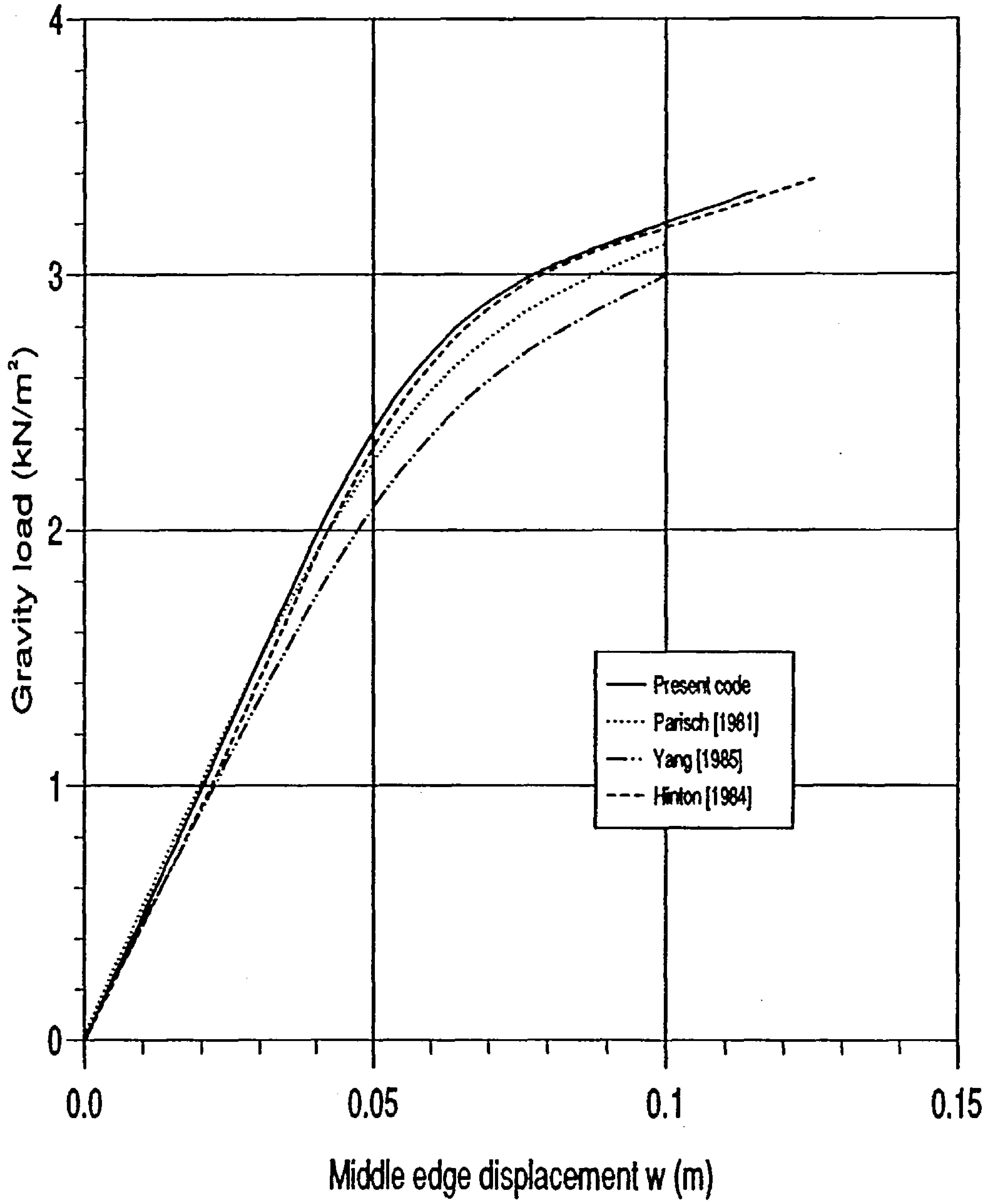

Fig. 4.11b : Geometric and material nonlinearity analysis of cylindrical roof.

4.7 Summary

The present section is the summary of chapter 3 and 4. The present non-linear shell finite element has been tested against several numerical results and analytic solutions and performs reasonable well. The update Lagrangian avoids the big housekeeping overhead which is required in the total Lagrangian formulation. However, the update Lagrangian formulation requires more computer time to update the configuration in each increment. Multilayer element give a better solution in elasto-plastic analysis than a single layer element. An elasto-plastic material model with linear isotropic hardening can be used in the future for multilinear hardening analysis.

The automatic incremental load requires an experienced user in nonlinear analysis to give the initial loading and the number of the desired iteration. The smaller the initial load and the bigger the number of desired iteration, the better is the solution. However, these require large computation time to reach the ultimate load. The arc length method adopted in the solution strategy, performs very well in passing the maximum point in given numerical examples.

Chapter V

Axial Loading in T, Y, and DT Joints

5.1 Introduction

Typical tubular joint configurations has been considered in chapter 1. In the present chapter, the ultimate strenght of **T**. **Y**, and **DT** joints will be calculated using finite element and the results will be compared with experimental test results, especially those using axial loading. A review of numerical work on the ultimate strength of tubular joints is given below.

Using semiloof thin shell elements, Irving[1982] analysed the collapse of **T** joints loaded in compression. Both material and geometric nonlinearities were included using the total Lagrangian method. Irving employed the Von Mises yield criterion relevant for elasto-plastic analysis and also considered isotropic strain hardening and used multilayer shell finite elements.

In 1984, Baba *et al.* analysed three different type of stiffened **DT** joint, these are double ring, single vertical and double vertical stiffened joints (see Fig. 5.1). He used an isoparametric thick shell finite element and employed perfect plastic analysis and small strain displacement analysis. In the same year, Ebecken *et al.* published similar work in which they analysed **DT** joint under axial loading in a study concerned with the applicability of the finite element method to the analysis of tubular joints. Ebecken *et al.*[1987] continued this work by adding large displacement analysis where **T** and **DT** joints under axial loading were analysed using flat shell and superparametric shell elements.

Van Der Valk [1988] extensively analysed **T** joints under tension and compression loads. He used the computer program MARC and his methods of analysis include eight node thin shell elements which disregard transverse shear, the Von

Mises yield criterion for elasto-plasticity, and isotropic multilinear strain hardening. The solution strategy employed is the full Newton Raphson method and he adopted displacement control using the automatic increment based on arc length method. Van Der Valk then compared the experimental and numerical test results of two **T** joints and based on these comparisons, an extensive study of the parameters controlling **T** joint behaviour under axial loading was made using 45 numerical models.

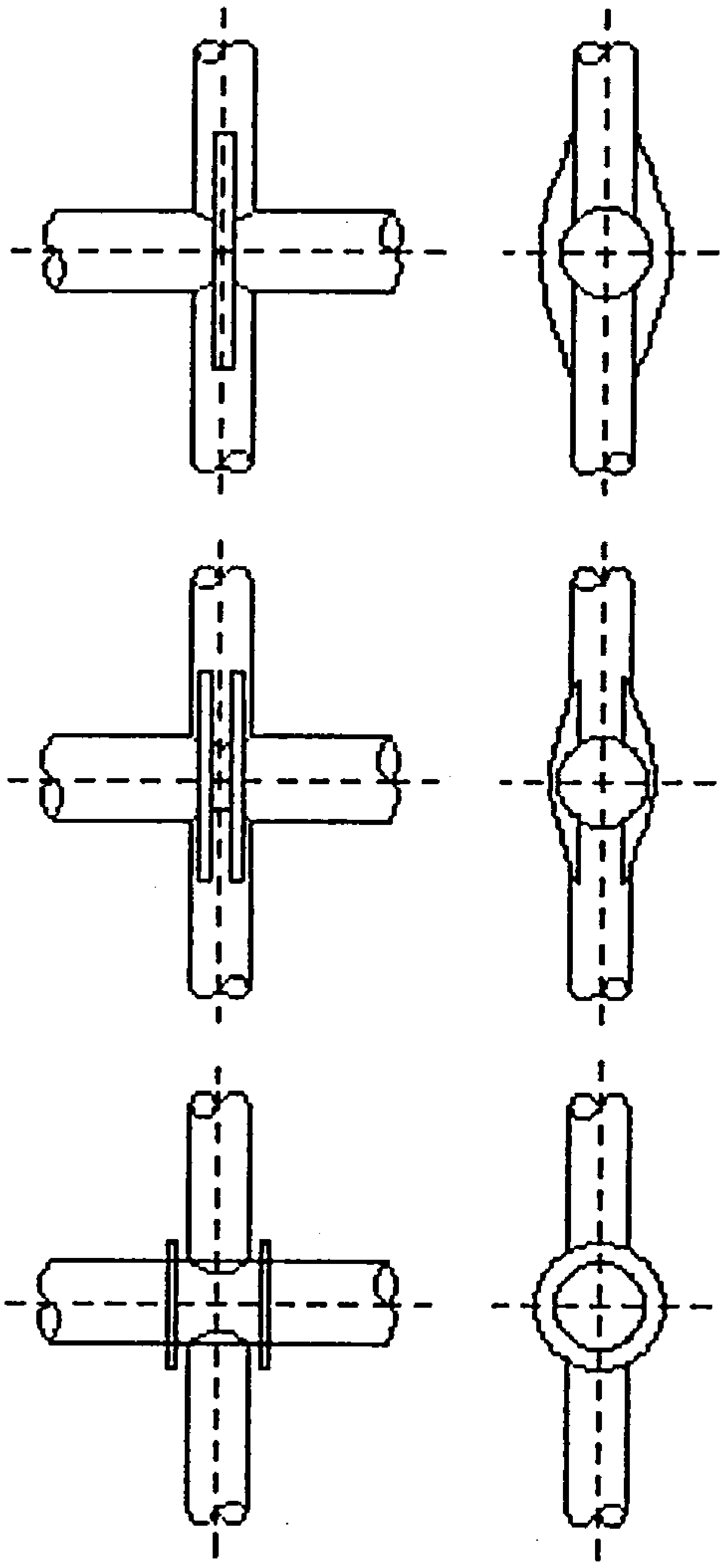

Figure 5.1 : Three different type of stiffened of DT joints.

The most recent work in this field is by Lalani *et.al* [1989] and Cofer *et.al* [1990]. The computer program FINAS, which will be futher mentioned in section 5.5.4, was used to compare numerical and experimental tests for **T**, **DT**, and **K** joints with axial and balance axial loading.

In considering the influence of cylindrical intersections and welding upon tubular joints, Cofer *et.al*[1990] used three types of element when modelling tubular joints. Cofer analysed two configurations of tubular joints; the **T** joints with tensile loading and **DT** joints with compressive loading and balanced axial and inplane bending moment loading.

In the present work, the experimental data used was supplied by Wimpey Offshore [1989] using large scale specimens. This data was chosen because it avoids scale effects and because it is the only available data which describes in detail the test arrangements and the procedures. The numerical results and experimental data for **DT** joints, as used by Cofer and Lalani, is also considered.

5.2 Experimental Studies of Tubular Joints

The experimental study of **T** and **Y** joints with compression loading, and **Y** and **K** joints with inplane bending moments was undertaken by Wimpey Offshore [1989], using large scale tubular joints. The chord and brace members for all the specimens were fabricated using one seam welded BS 4360 Grade 43A steel plate, with a minimum yield stress of $240N/mm^2$. The chord and brace flanges were fabricated from BS 4360 Grade 43A forged steel rings.

Experiments on a **DT** joint with compression load were carried out by Boone *et al.* (as quoted by Lalani *et al.* [1989] and Cofer *et. al* [1990].). The test specimen was fabricated from AD-5LX Grade X-42 welded pipe line with a yield stress of $321.2N/mm^2$.

The dimensions of the specimen and the material properties are presented in Table 5.1-3 for axial loading and Table 6.1-2 for inplane bending moments. No material hardening parameter is available and so in this study, it is assumed to vary from 0% to 20% of the value of Young Modulus and is taken to be bilinear hardening. The hardening is taken to be zero when the stress reaches ultimate value (see Fig. 5.2). Experimental results were available for the deflection at the top of the brace under the load and the point where yield first occurred in

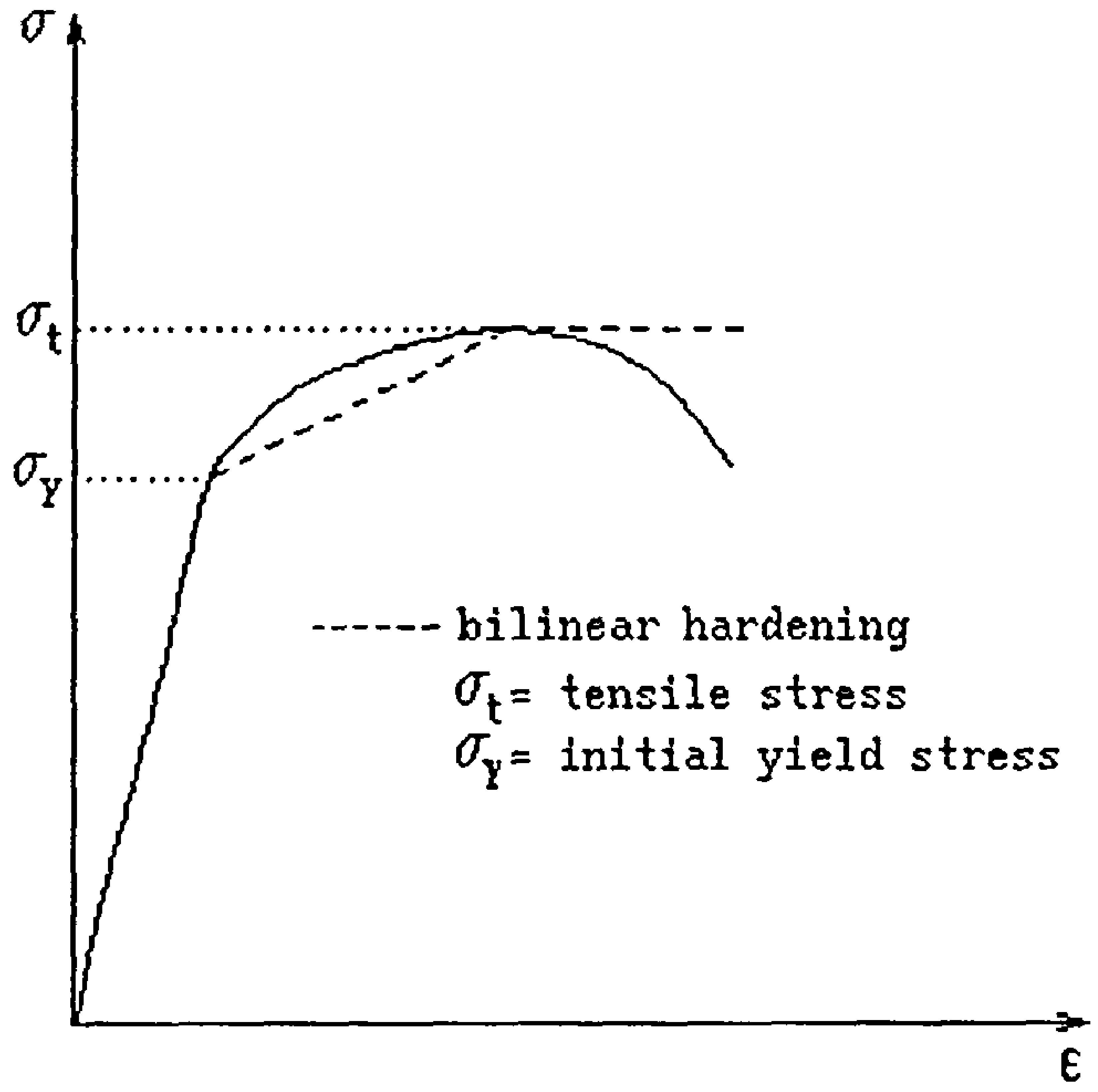

Figure 5.2 : Stress strain curve and bilinear hardening.

the structure. As reported by Wimpey Offshore, an axial compression load was applied to the brace joint in this arrangement. Pilgrim jacks were placed on the brace top hat and reacted against the rig through ball seating (see Fig. 5.20). Details of the loading procedure can be found in Wimpey Offshore [1989] report.

Model	D	d	T	t	L	l	β	γ	Fy (N/mm^2)		Ft (N/mm^2)	
	(mm)	(mm)	(mm)	(mm)	(mm)	(mm)			chord	brace	chord	brace
T1	508	406	12.5	12.5	1575	1000	0.8	20.32	339	344	500	496
T2	508	508	12.5	12.5	1575	760	1.0	20.32	334	312	476	445
T3	508	406	8.0	8.0	1575	1175	0.8	31.75	307	306	444	442
T4	508	508	8.0	8.0	1575	760	0.8	31.75	322	380	447	510

Table 5.1 — Geometrical and material properties of T joints

Model	D	d	T	t	L	l	θ	β	γ	Fy (N/mm^2)		Ft (N/mm^2)	
	(mm)	(mm)	(mm)	(mm)	(mm)	(mm)				chord	brace	chord	brace
Y1	508	406	12.5	12.5	1575	1000	45^0	0.8	20.32	340	380	483	518
Y2	508	406	8.0	8.0	1575	1000	45^0	0.8	31.75	312	370	427	484
Y3	508	508	8.0	8.0	1575	1000	45^0	1.0	31.75	276	288	419	422

Table 5.2 — Geometrical and material properties of Y joints

Model	D	d	T	t	L	l	β	γ	Fy (N/mm^2)		Ft (N/mm^2)	
	(mm)	(mm)	(mm)	(mm)	(mm)	(mm)			chord	brace	chord	brace
DT	406	273	7.9	7.9	3556	-	0.67	25.7	321	-	-	-

Table 5.3 — Geometrical and material properties DT joints

5.3 Simplification in the Numerical Models

To analyse a tubular joint using the finite element method, a mesh generator is necessary. Here, a simple mesh generator is developed for symmetric joints. The mesh generator theory is presented in Appendix A. Structural symmetries are exploited. Only half of **T**, **Y** and **K** joints need to be modelled and only a quarter of **DT** joints (see Fig. 5.13-15). The midsurface dimension is used on the modelling. Each element consists of two layers which means than four Gauss points are employed through the thickness.

The test arrangement is shown in Fig. 5.20. The gap between the pinned connection and the attachment flanges are added to the length of the chord in the model. The effect of flanges is modelled by adjusting the stiffness of the additional length which will effectively behave as a rigid link. The stiffness is adjusted by using a higher Young's modulus in the range of 100 to 1000 times the true Young's modulus. As shown in Fig. 5.16, the displacements of the middle nodes marked A and B are fixed but they are free to rotate. Because of the method of attachment, the Young's modulus at the top of the brace is given a higher value than that of the brace itself. However, this technique can be replaced by fixing the displacement (u, v) at the top of the brace **DT** and **T** joints. Uniform distributed force is applied axially to the brace around the top of brace (see Fig. 5.16).

5.4 T joint with Compressive Load

As mentioned before, four sets of experimental results for **T** joints are compared with the numerical results.

5.4.1 Model T1

Model T1 is used as a base case study to examine the hardening parameter and the mesh density. Four different hardening parameters are applied and the total mesh density equals 122 elements (Fig. 5.13a). The hardening parameter is taken between 0% to 20% Young's modulus (E). Excellent results are obtained when the hardening parameter is given as 20%E, but other numerical tests also give reasonable results (see Fig. 5.3a). Table 5.4 shows that the differencies of ultimate load for four hardening parameters is in the range 0% to 20%. Based on these numerical tests, the density of elements is increaesed with the hardening parameter as 15% and 20% E and the total element equals to 182 (Fig. 5.13b). Excellent results are obtained by the present analysis. As indicated in Table 5.4, the ultimate load from the numerical analysis using a finer mesh is slightly higher, by 1.3%, than the experimental result. Fig. 5.3b shows the load displacement curve.

It can be seen from Fig. 5.3a, that the numerical displacement in the elastic range is smaller than the displacement results from the experimental test, which in this case shows that the numerical model is more rigid than the experimental specimen. This difference could be accounted for by the finite stiffness of the physical test frame. First yielding in the numerical test is found at the chord saddle positions at a load of 976kN (59% ultimate load) while in the experimental test the first yielding was recorded at the chord saddle position at load 760kN (47% ultimate load).

Case	hardening parameter (%E)	ultimate load (kN)	differences (%)
Experiment	-	1633	-
FE coarse mesh	0	1428	-12.6
FE coarse mesh	5	1450	-11.2
FE coarse mesh	10	1550	-5.1
FE coarse mesh	15	1586	-2.9
FE coarse mesh	20	1608	-1.6
FE finer mesh	15	1636	0.2
FE finer mesh	20	1654	1.3

Table 5.4 — Model T1 result compare with experiment

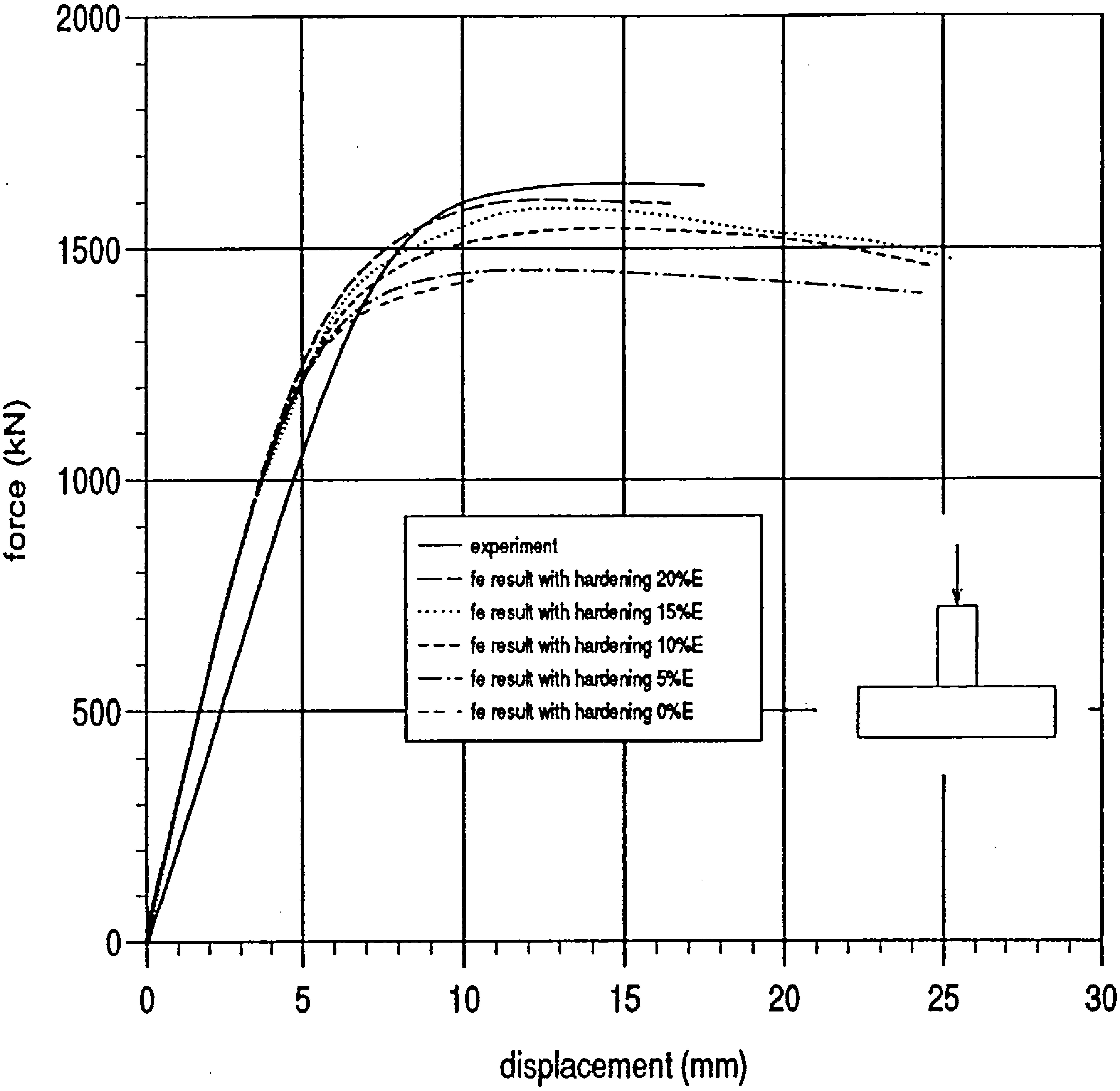

Figure 5.3a : Load-displacement curve of model T1.

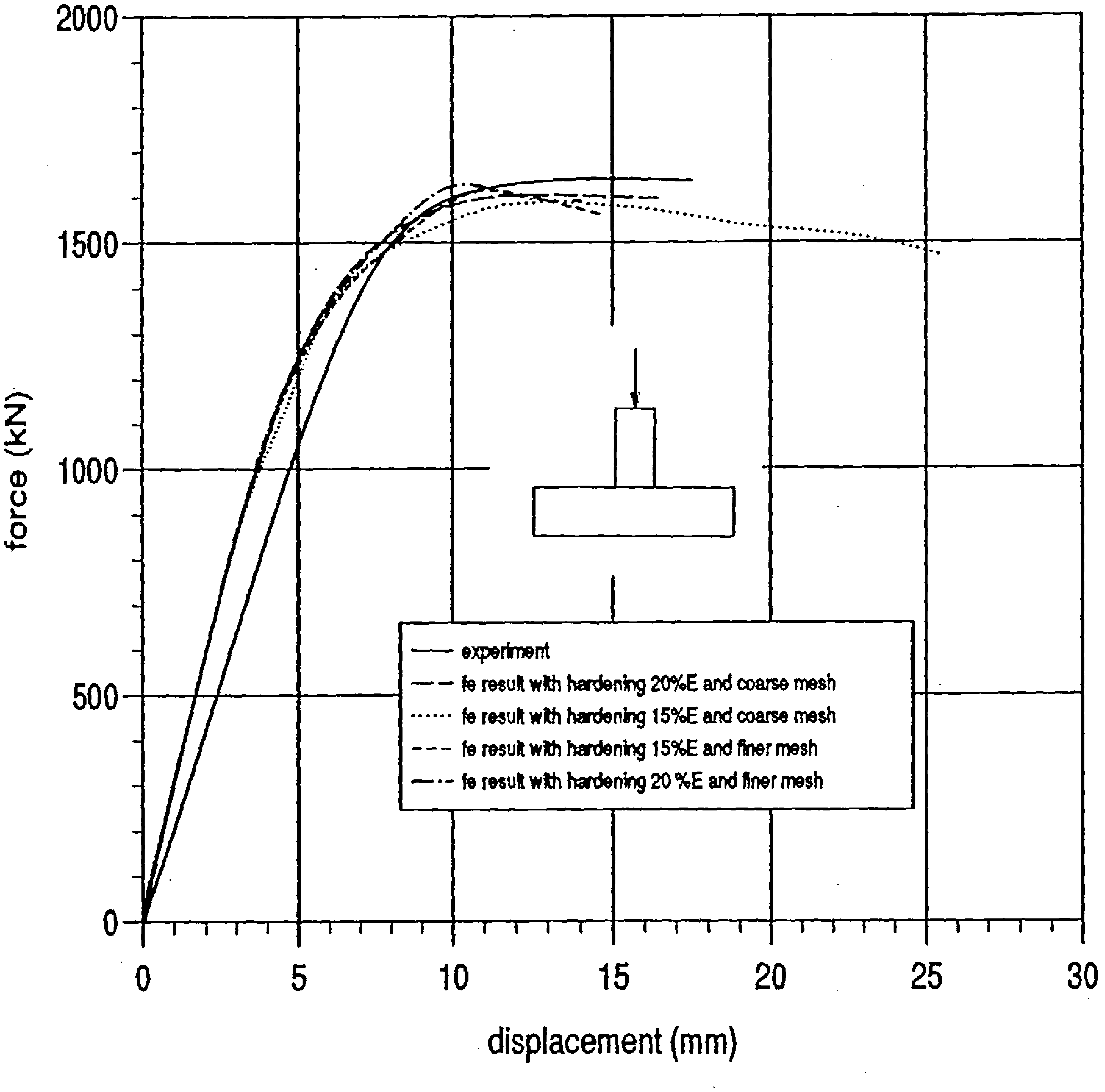

Figure 5.3b : Load-displacement curve of model T1 with finer mesh.

5.4.2 Model T2

As shown in Table 5.1, the dimension of the chord diameter is the same as the brace diameter that is, $\beta = 1$. As with Model T1, this numerical model is more rigid than the experimental specimen. Two numerical tests model are carried out. The first model has 122 elements and the second model has 150 elements. Both models give similar results (see Fig. 5.4). It was reported in the experimental tests that yielding was initiated at the crown positions at 1360kN (58% ultimate load) and at the chord saddle position yielding was initiated at 1650 kN.

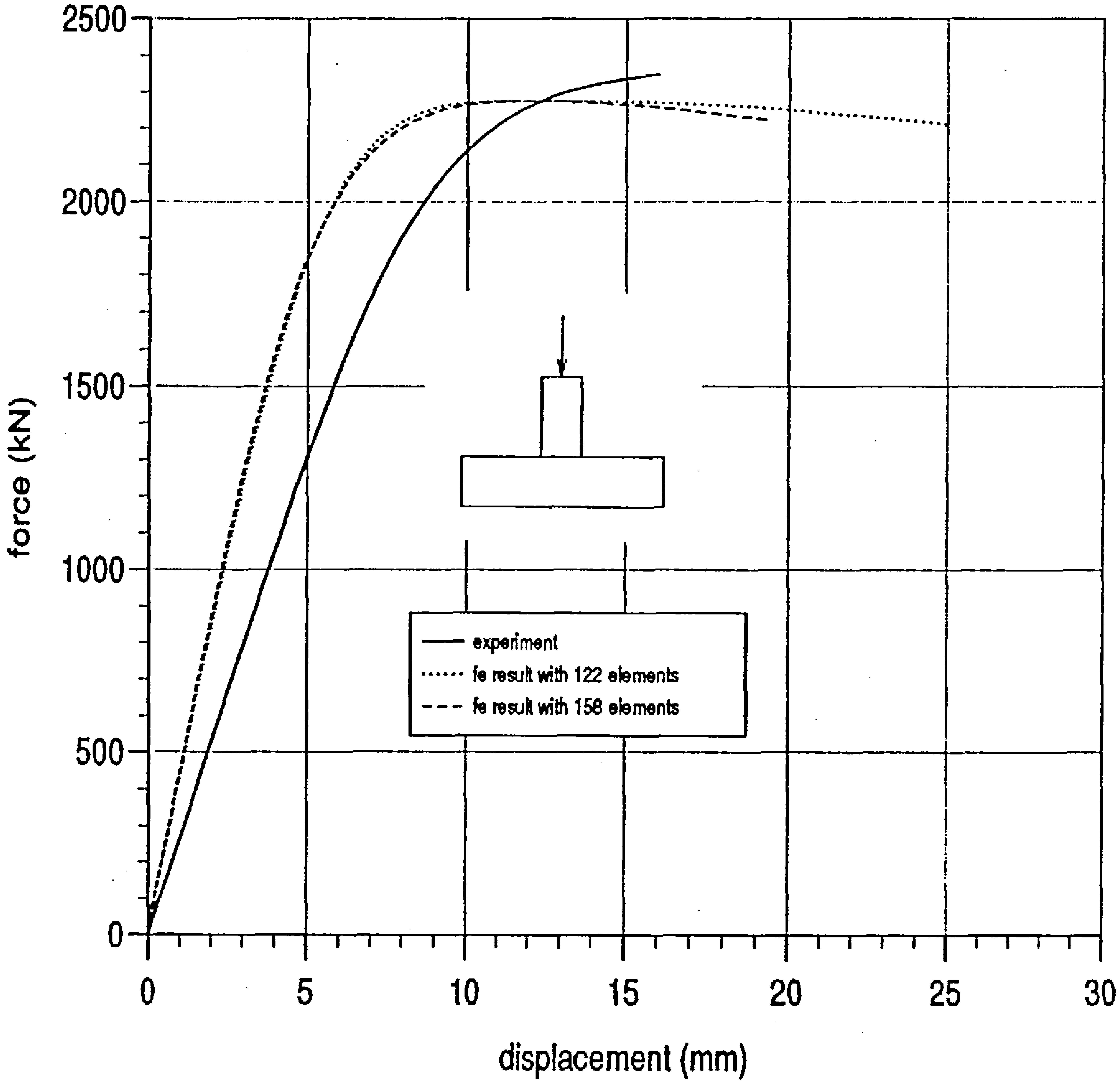

Figure 5.4 : Load-displacement curve of model T2.

First yielding in the numerical test occurred at the chord saddle position, at the crown position and at the crown position of the plug when the applied load increment was 1680kN (72% ultimate load). There is small load difference at first yield between the experiment and numerical test at the crown position. The specimen failed at 2328kN, while the model attained an ultimate load 2273kN. The difference is −2.4% as shown in Table 5.5.

5.4.3 Model T3

Like in models T1 and T2, 122 elements are employed in model T3. It can be seen from Fig. 5.5, that the displacement in the numerical model is much greater than in the experimental model. It is suspected that the measurements taken in the experiments for specimen T3 are not accurate. This suspicion can be justified as follows. From Table 5.1 it can be seen that the specimens T1 and T3 have the same chord length, diameter of brace and chord. The brace of specimen T3 is slightly longer than the brace of specimen T1, but the length of the brace does not have much influence on the strength of T joint when a compressive load is applied. Specimen T1 is thicker than specimen T3, thus it may be concluded that specimen T1 is stiffer than specimen T3 and it is also reported that in both specimens, experimental test failures occur due to plastic collapse. However, the displacement of specimen T1 is always bigger than the displacement of specimen T3 at the same load level. Because of this, the result from specimen T3 are suspect. There is a possibility that a mistake has made in reading the displacement from the chart. If the displacement reading is multiplied by two, the agreement with the numerical result is very good[1].

In the experiment, yielding was first detected at the chord saddle position with a load of 296kN (44% ultimate load). Yielding at the crown position was recorded at 357kN. In the numerical model, the first yield was found at the chord saddle and the crown at a load of 558kN (81% ultimate load). However, the difference

---

[1] This discrepancy has been pointed out to Wimpey and their comments invited, but no reply has been received to our letter.

between the ultimate loads for the experiment (674kN) and the numerical test (637kN) shows small differences, as shown in Table 5.3.

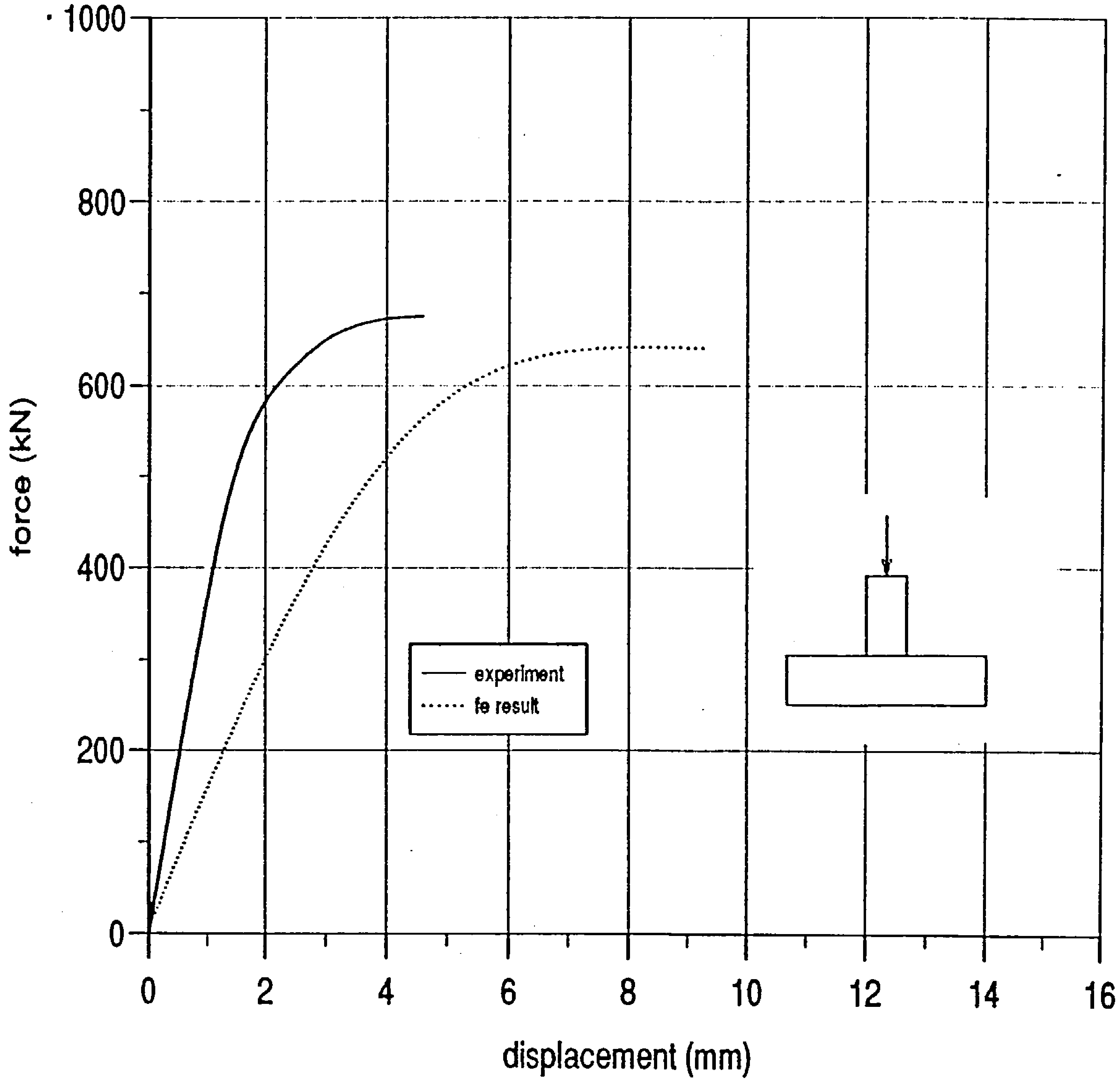

Figure 5.5 : Load-displacement curve model T3.

5.4.4 Model T4

Like in models T1 and T2, this numerical model with 122 element is stiffer than the experimental specimen. The first yield was recorded at the chord crown position at a load of 550kN in the experimental test. Yielding was found at the chord saddle at a load of 660kN and at 870kN the plastic deformation of chord wall extended to the toe of the entire periphery of the joint. In the numerical result of model T4, the first yield was obtained at the chord saddle position when the load level reached 778.9kN. Yield was found in upper surface of the chord crown position at a load of 890.5kN. The maximum load capacity, 1193kN, is slightly higher than the maximum load (1190kN) experimental test. The curved load displacement is presented in Fig. 5.6.

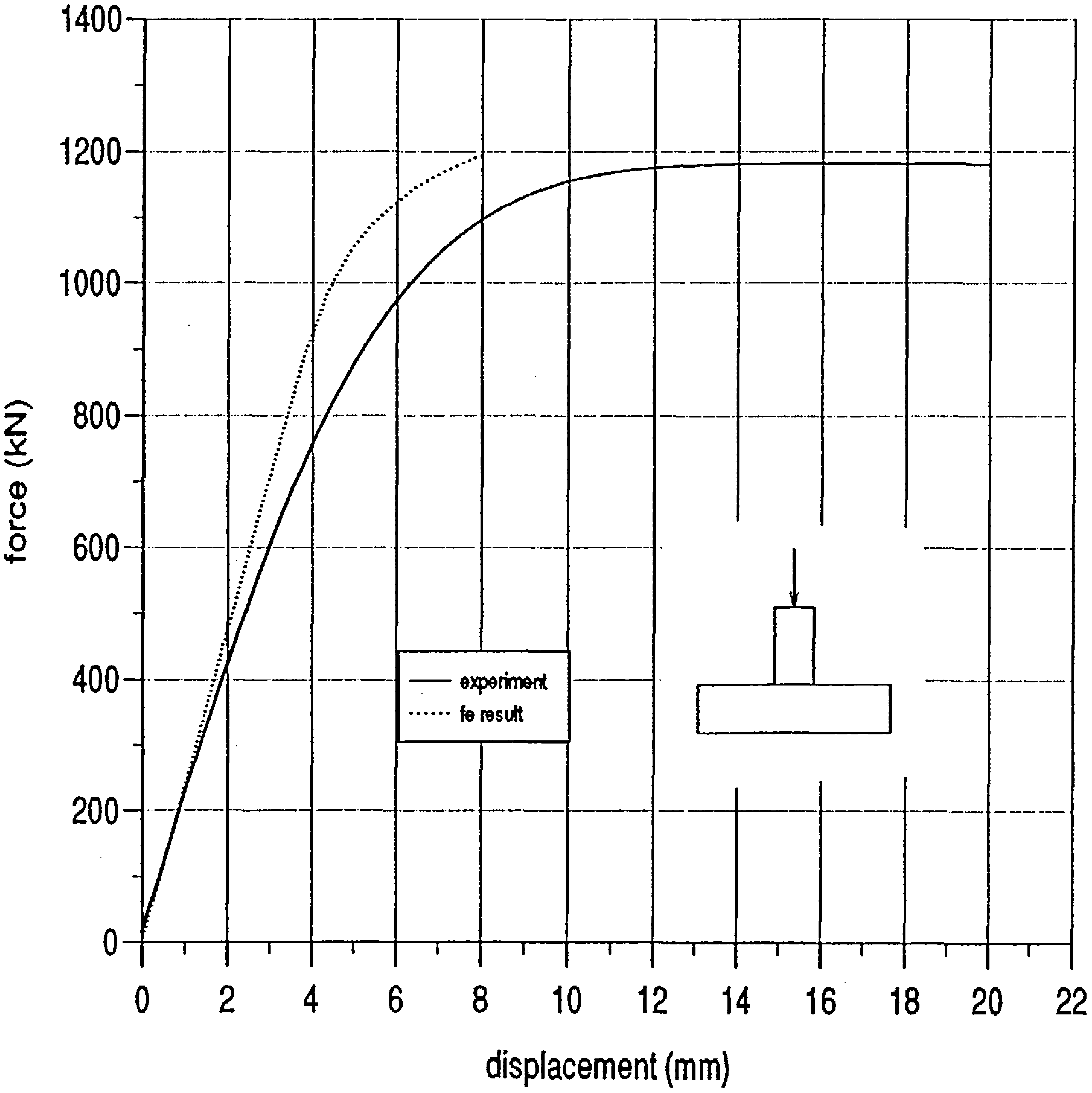

Figure 5.6 : Load-displacement curve model T4.

Model	Experiment result (kN)	Numerical result (kN)	difference %
T1	1633	1636	0.02
T2	2328	2273	-2.4
T3	671	637	-5.5
T4	1180	1194	1.2

Table 5.5 — Ultimate load numerical and experimental test of T joints

5.5 Y joint with compressive Load

Three set of experiment test are compared with numerical tests. It is expected that Y joints will behave in a manner similar to T joints. As mentioned previously, the material properties for the top 50 mm of brace are higher than those of the brace itself. The axial displacement of the numerical test is obtained from the resultant displacement of the brace.

5.5.1 Model Y1

From zero load up to approximately 57% of the ultimate load, the load displacement curve of the numerical test is linearly elastic, see Fig. 5.7. At the same load level, the numerical displacement curve is always larger than the experimental displacement. It shows that the experimental specimen Y1 is stiffer than the numerical model.

At a load of 1344kN, the first yield occurred at the chord crown and saddle position in the numerical test. The plastic deformation of the chord wall extended around the cylindrical intersection with a load of 1632kN. In the experimental test, first yield was detected at the chord saddle position at 1100kN. At 1600kN yielding occurred at the crown toe position. In the numerical test, the maximum load reached 2466kN while in experimental test the maximum loading capacity was recorded as 2346kN load level. As shown in Table 5.6, the differences of maximum load between experimental and numerical test is only 5.2%

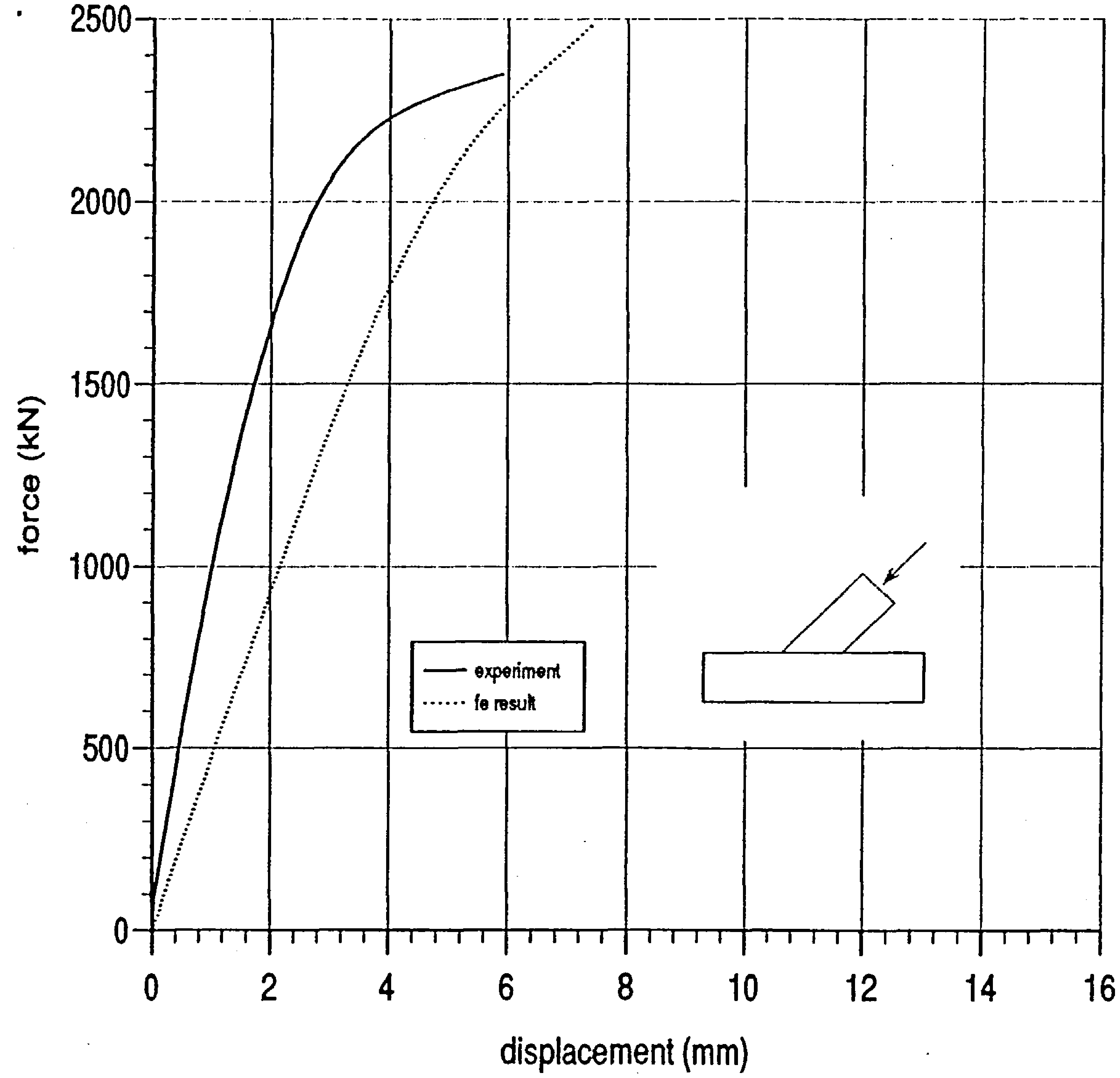

Figure 5.7 : Load-displacement curve of model Y1.

5.5.2 Model Y2

As shown in Fig. 5.8, the numerical test displacement result is close to the experimental result. Yielding was first detected at the chord saddle and crown positions in the numerical model result at a load of 744kN. At the next load increment, 872.35kN, the yielding starts to spread around the joint. In the experimental results, the first yielding load is lower than in the numerical test result. The yielding was first detected at the chord saddle position at 490kN. At 800kN, the plastic deformation of chord wall extended from the two saddles toward the crown toe position. The load increment in the numerical model reached 990kN and stopped since the iterative procedure could not converge. This implies that the loading path of the structure reaches a critical point which is known as ultimate point load. Slightly lower failure loads occurred in the experiment at 985kN.

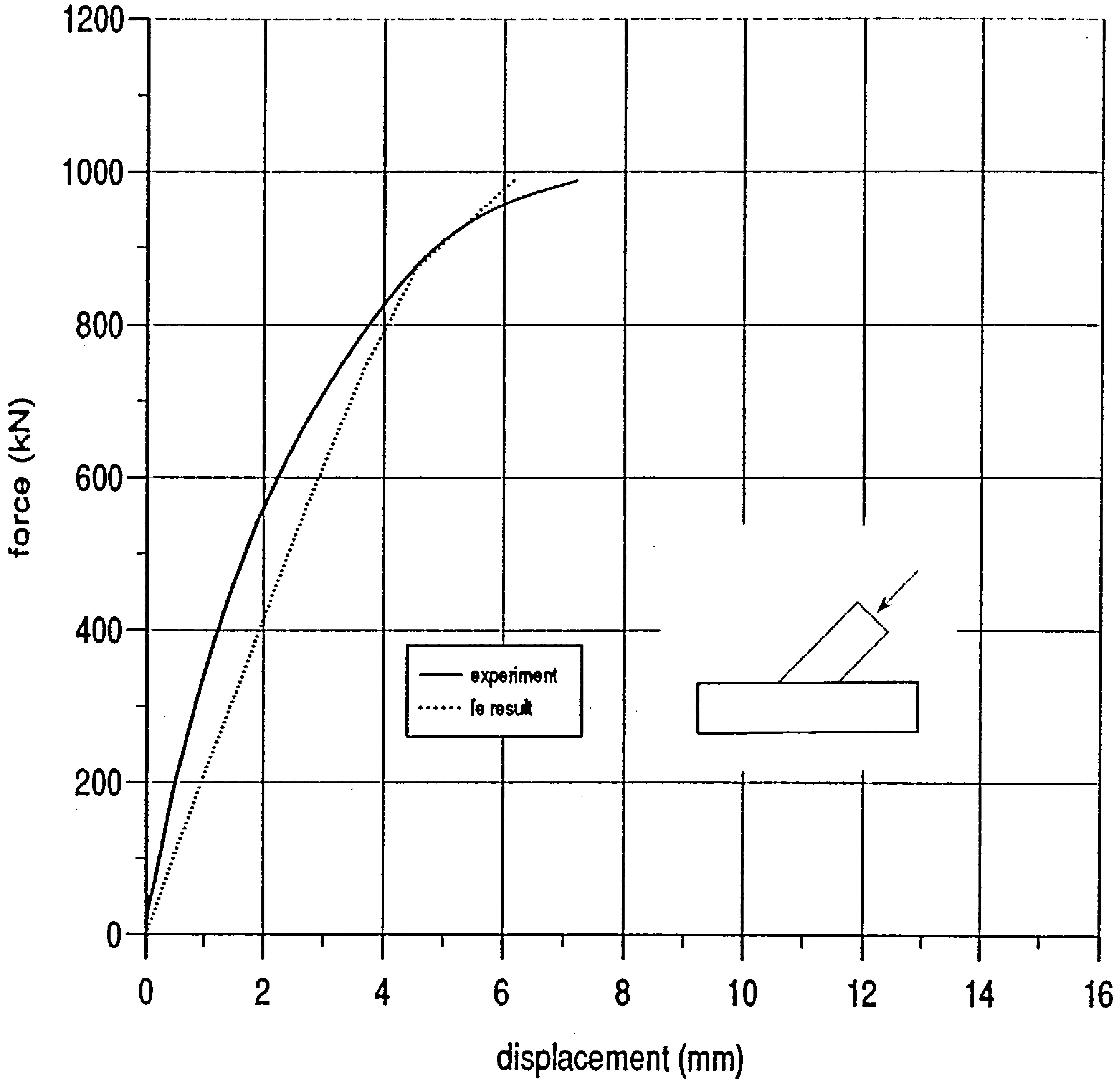

Figure 5.8 : Load-displacement curve of model Y2.

5.5.3 Model Y3

The behaviour is similar to that of model Y2 obtained from numerical tests. Fig. 5.9 shows the load displacement curve. The numerical test displacement is close to the experimental result. However, the numerical displacement result is smaller than the experimental result, when the load is close to the ultimate load.

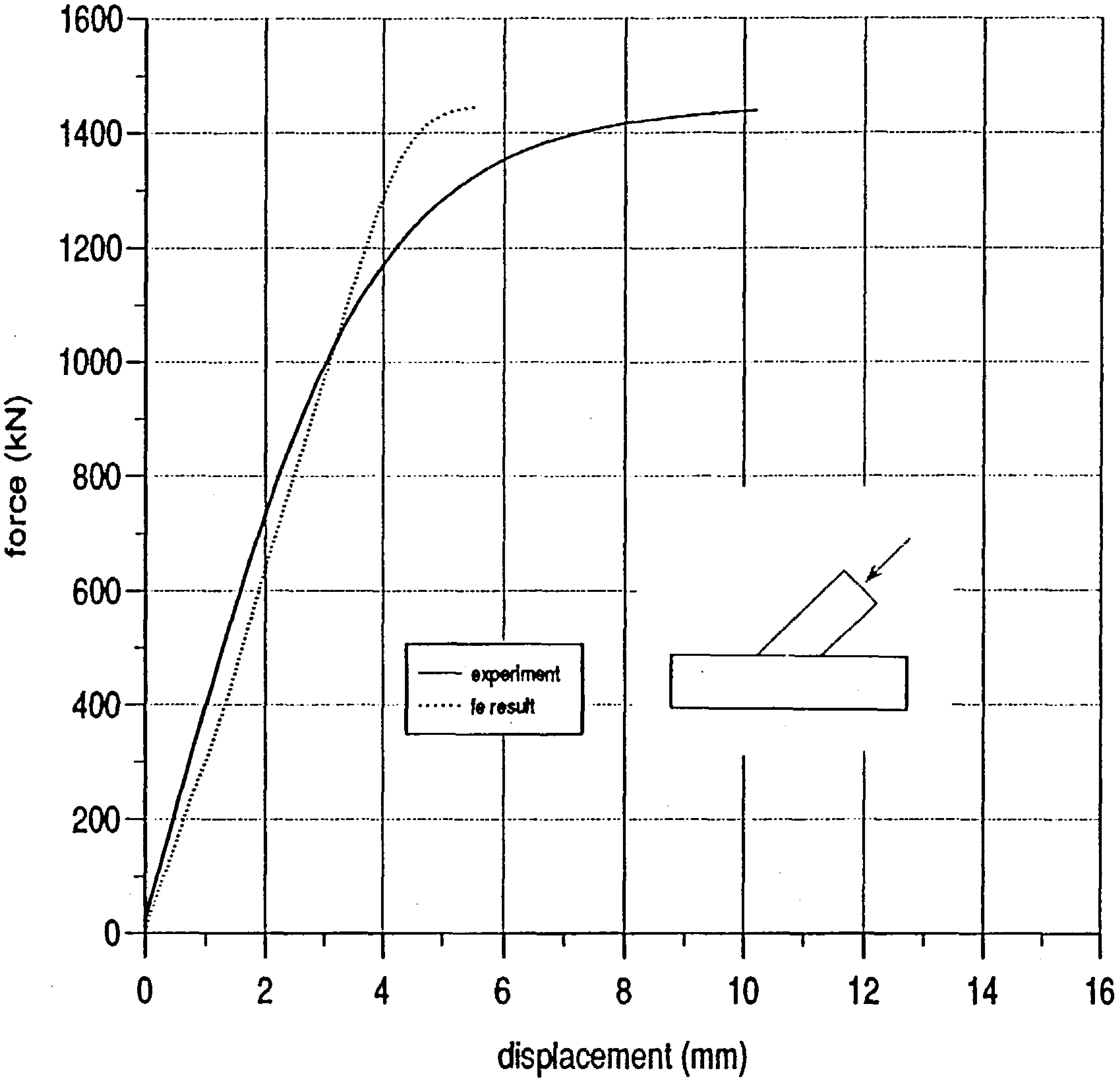

Figure 5.9 : Load-displacement curve of model Y3.

Yielding first occurs in the chord crown and saddle positions at 1165.44kN in the numerical test. At a load of 750kN, yielding was detected at the chord crown position in the experimental analysis. At 1130kN plastic deformation of the chord wall extended from chord saddle to crown position. The specimen failed at 1435kN while the numerical model reached a load of 1439.38kN and stopped since the iterative procedure could not converge.

Model	Experiment result (kN)	Numerical result (kN)	difference %
Y1	2346	2466	5.1
Y2	985	990	0.5
Y3	1435	1439	0.3

Table 5.6 — Ultimate load numerical and experimental test of Y joints

5.5.4 DT Joint with Compressive Load

An experimental test of a **DT** joint will be compared with its corresponding numerical test. Some numerical test results for **DT** joints from Cofer *et al.* [1990] and Lalani *et al.* [1989] will also be compared. The load displacement curve is shown in Fig. 5.11.

The most critical area of tubular joints occurs at the line intersection between cylinders. Due to this, Cofer *et al.* [1990] developed a finite element program TUBJNT. This program takes into account the intersection and welding effect, see Fig. 5.10. To capture the three dimensional stress distribution at the shell intersection, Cofer used a twenty node, isoparametric, brick element at the intersection of the tubular joint. To model the weld profile, Cofer used fifteen node, isoparametric, solid wedge elements. Cofer employed solid shell elements as a transition between brick element and shell element (see Fig. 5.10). The TUBJNT program takes into account elasto plastic behaviour with isotropic hardening. Finite deflections and rotations were considered in the updated Lagrangian approach. The modified Newton-Raphson method with a scalar accelerator to speed convergence was employed. One eighth of a **DT** joint with a total of 216 element was used to analyse the ultimate strength.

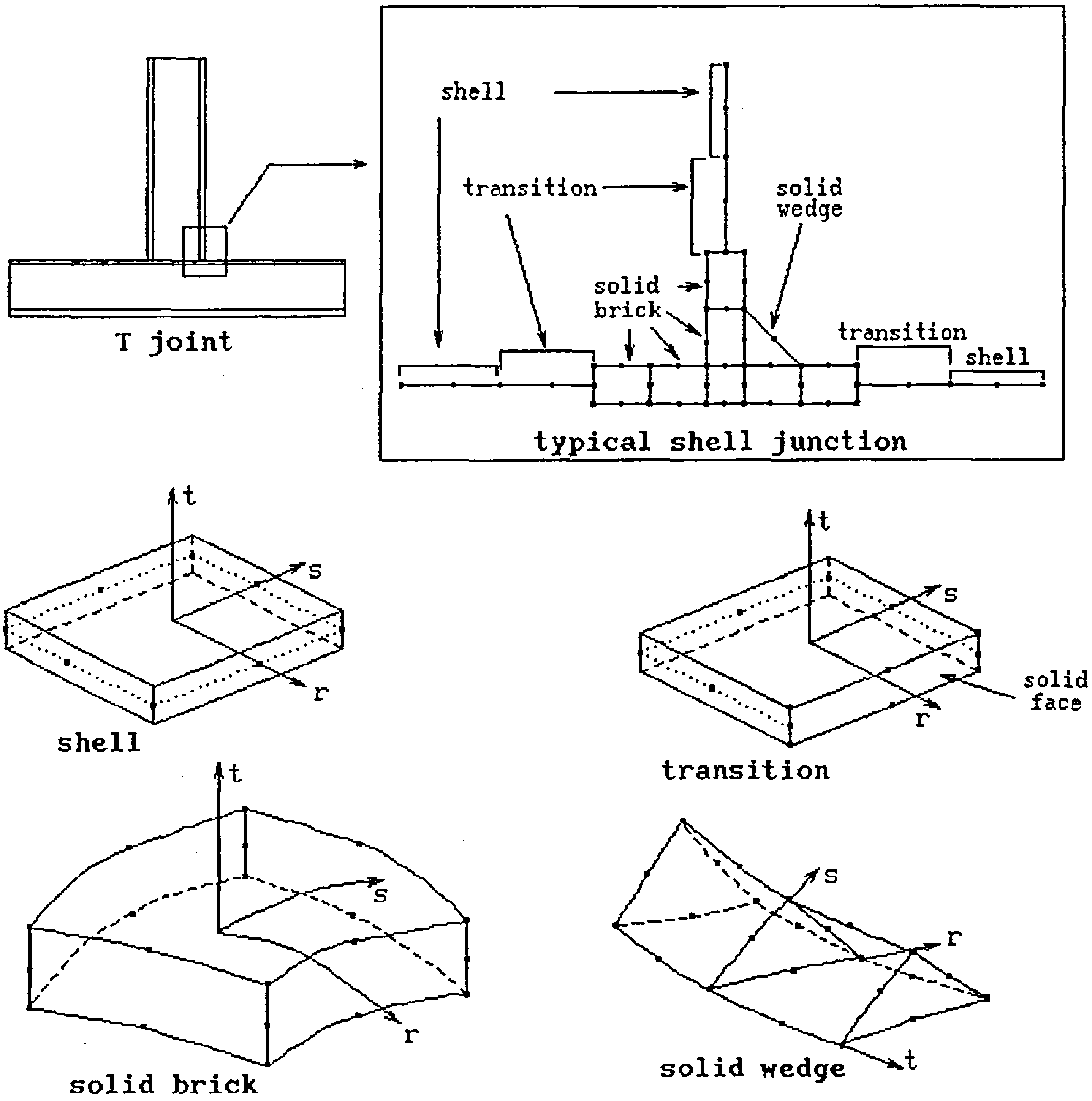

Figure 5.10 : Model of Typical Shell Junction and Element Type.

Another numerical test was done by Lalani *et al.* [1989] using FINAS, a finite element program which was developed at Imperial College, University of London. As reported by Lalani *et al.*, the material laws include elastic, elasto plastic based on single layer yield criterion and elasto plastic with multilayer solutions with integration in the transverse direction. The nonlinear solution strategies employ Newton-Raphson, Modified Newton-Raphson or the KT01 method (the latter reforms the tangent stiffness matrix at the beginning of each load step and after the first iteration). To cross the limit points and to select the appropriate load increment size automatically, three methods are available in FINAS program. One of them is well known as the spherical arc length method. The others were displacement control of a charesteristic displacement component when solution approaches a limit point (load control is also available) and automatic selection of constraint equation (displacement variable) with the most rapid change in displacement, to focus on the critical and weakest structural componenet. The elements used were doubly curved eight node isoparametric shell element with six degrees of freedom per node. The elements are based on a non-linear strain displacement relation and include large displacement/rotation effects. To analyse the **DT** joint, Lalani *et al.* employed of one eighth of the joint with a total of approximately 146 elements.

It can be seen from Fig. 5.11, that not all the numerical displacements compared well with the displacement from the experimental test at peak load. Lalani *et al.* and Cofer *et al.* reported that the differences between numerical and experimental displacement may be attributed to additional deflection from movement of the load frame. This conclusion was also mentioned by Irving [1982] in his work.

There is no available data for the first yield in experimental and other numerical tests. In the current numerical test, the yielding was first recorded at the saddle position in the middle of the chord at a load of 177.1kN. Ward [1988] also analysed this **DT** joint and reported that the yield was initiated from the saddle point. At 217.33kN, yield occurred between the chord crown and the saddle position near the cylinder intersection. Ultimate load capacity reached 351kN in the experimental test. Good comparison of ultimate load was obtained by Cofer at a load of 343kN, and Lalani *et al.* using multilayer elements with a fine mesh obtained an ultimate load of approximately 341.74kN. As in the Cofer and Lalani results, the present numerical test reached a maximum load at 344.9kN using a fine mesh. Excellent results were obtained from the FINAS program using Ivanov's single layer yield criterion at a load of approximately 354.4kN for a fine mesh. When the element density was reduced by 30%, the displacement was slightly lower than the fine mesh result. This behaviour also occurred in the FINAS result. Using a coarse mesh, the present numerical test reaches an ultimate load at 336.66kN which is lower than the fine mesh ultimate load. On the other hand, FINAS obtained a higher value of the ultimate load when the density of elements was reduced (see Fig. 5.12). Considering the total elements used, the present numerical model is less dense than the other numerical models. It can be seen that if a similar model of a DT joint is used, the present numerical model will use only 89 elements. The differences in the ultimate load between numerical and experimental tests can be seen in Table 5.7.

Case	Ultimate Load (kN)	difference %
Experiment	351	-
FE multilayer [Lalani *et al.* 1989]	342	-2.6
FE Ivanov's single layer [Lalani *et al.* 1989]	354	1.0
FE [Cofer *et al.* 1990]	343	-2.3
Present analysis	345	-1.7

Table 5.7 — Ultimate load numerical and experimental test of DT joint

5.6 Discussion

Four sets of numerical results for T joint show that most of numerical displacements give reasonable comparisons to the experimental result. The load displacement curves prediction show that the finite element model is usually stiffer than physical model but that the shape of load displacement curves are generally well predicted by the finite element model.

Most of the first yield load of numerical tests are higher than those of experimental tests. This is to be expected, as will be discussed in section 6.6. However,

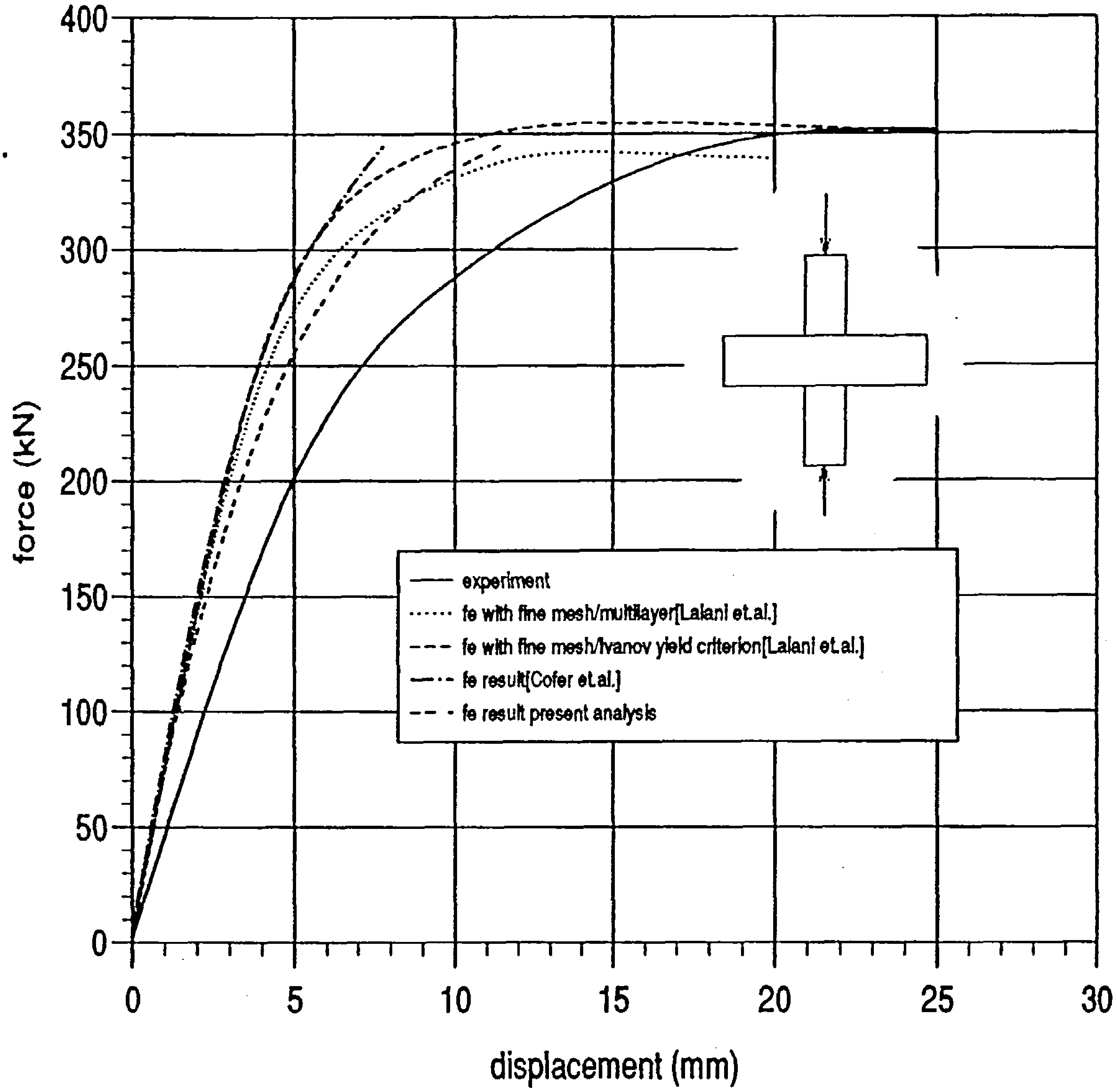

Figure 5.11 : Load-displacement curve of model DT joint using fine mesh.

the spread of plasticity of the numerical tests of T joints model behaves broadly the same as the experimental tests. Both numerical and experimental tests demonstrated plastic collapse. The ultimate load in numerical tests give reasonable results in comparison with the experimental results. The differences from the experiment range between −5.5% and 1.2% as indicated Table 5.5. The average of ultimate load differences is −2.1%.

Generally, the numerical results for the displacement of Y joints is reasonably good compared to the experiment results. The load displacement curves show that

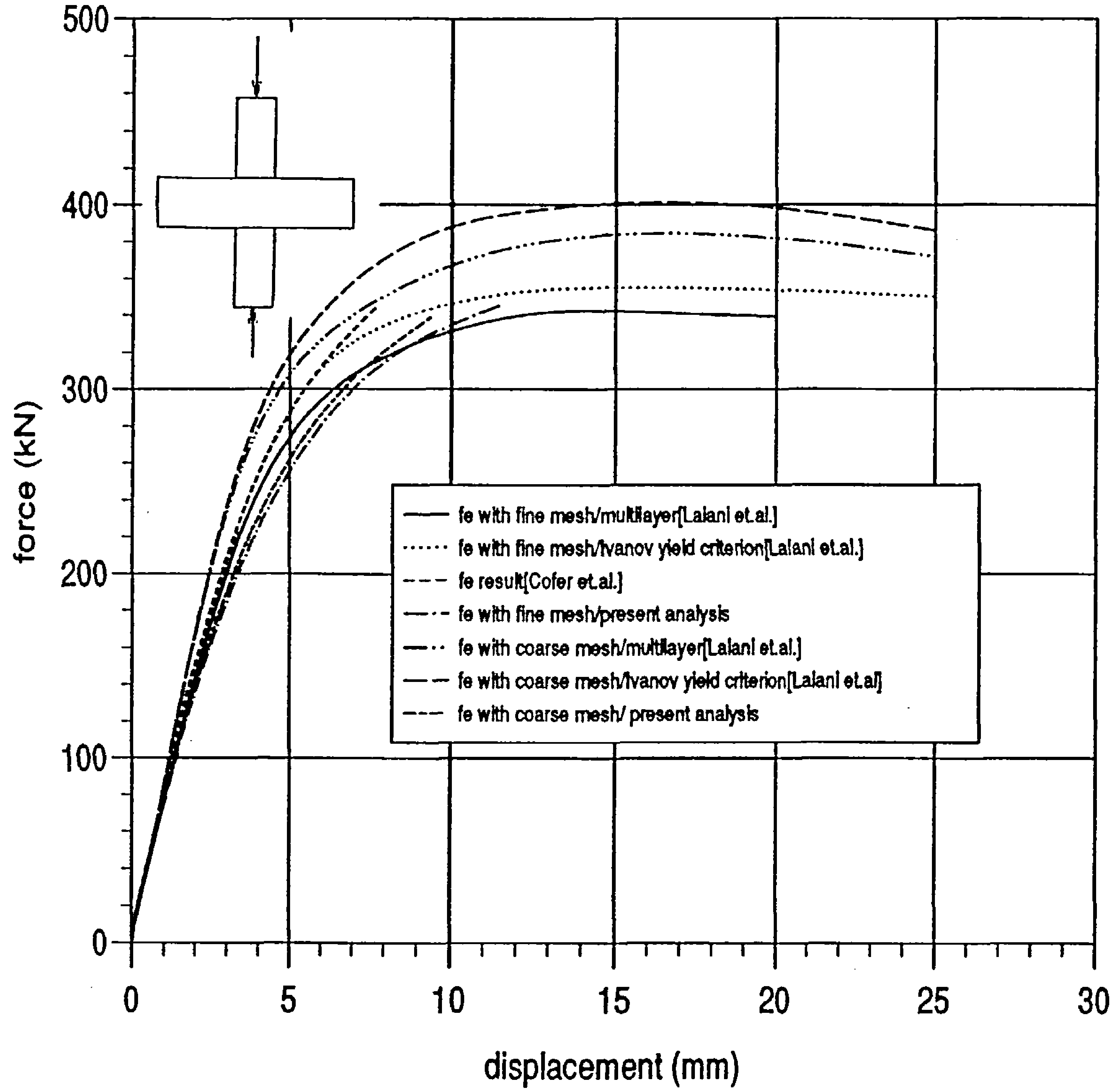

Figure 5.12 : Load-displacement curve of model DT joint using fine and coarse mesh.

the physical model is usually stiffer than the numerical model. The first yield load of numerical tests are always higher than that of the experimental tests. However, the initial yielding zone of the numerical tests has the same location as in the experimental tests. Both numerical and experimental tests demonstrated plastic collapse behaviour. An excellent comparison on the ultimate load is obtained between the numerical and experimental tests with range 0.3% and 5.1% as indicated Table 5.6.

As mentioned before, not all of the numerical results for the displacement of

DT joints compare well with displacement from the experimental tests. However, compared to the ultimate load of the experimental tests, the numerical tests ultimate load give excellent results. The range of differences is between −2.6% and 1.0% as indicated Table 5.7. It can be seen from load displacement curve for the DT joint (Fig. 5.11) that the effect of including the weld profile elements on the global plastic collapse load is not too significant. That figure also shows that the stiffness of numerical models is increased by using the weld profile elements.

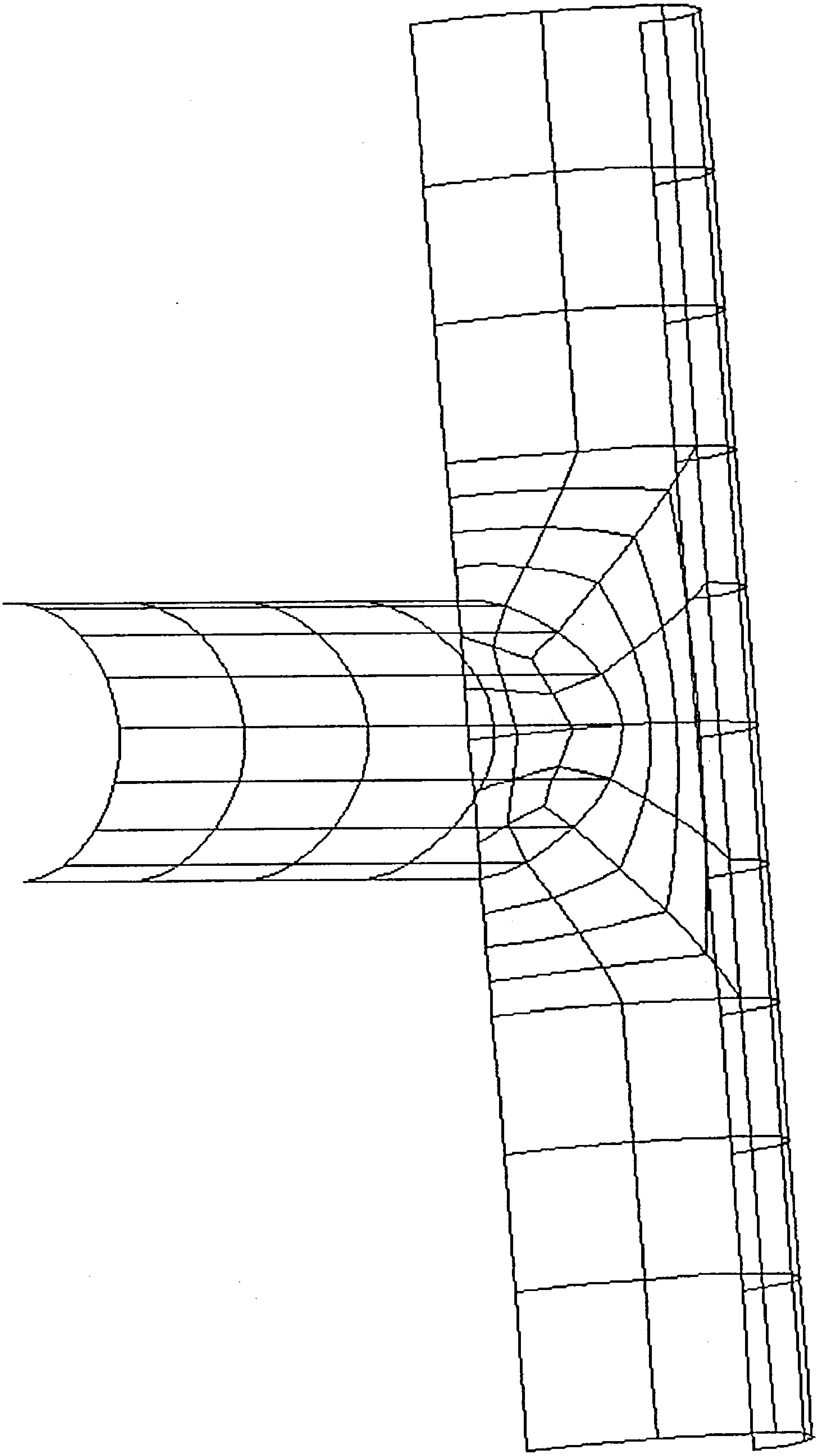

Figure 5.13a T joint mesh with total of 122 elements

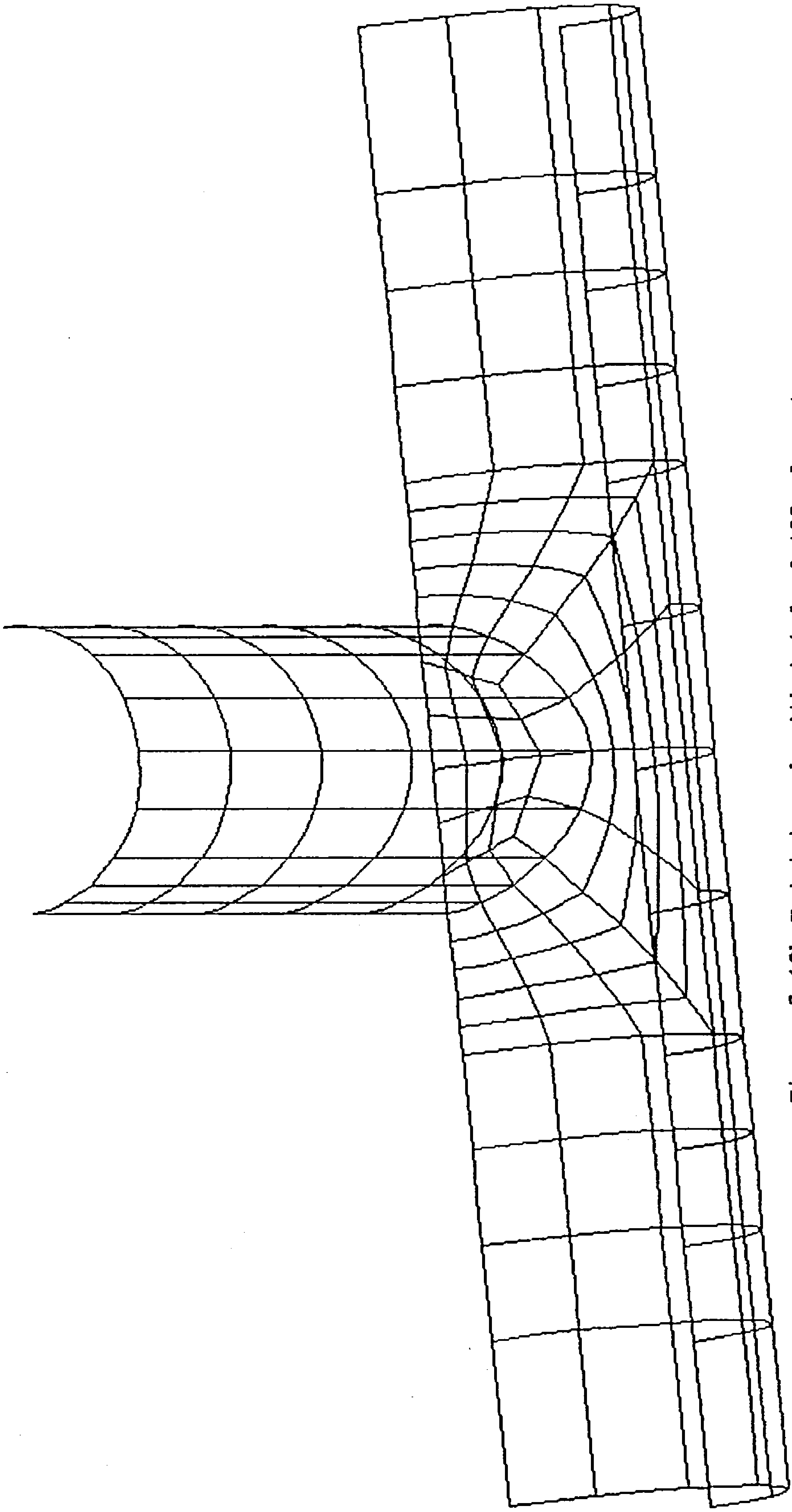

Figure 5.13b T joint mesh with total of 182 elements

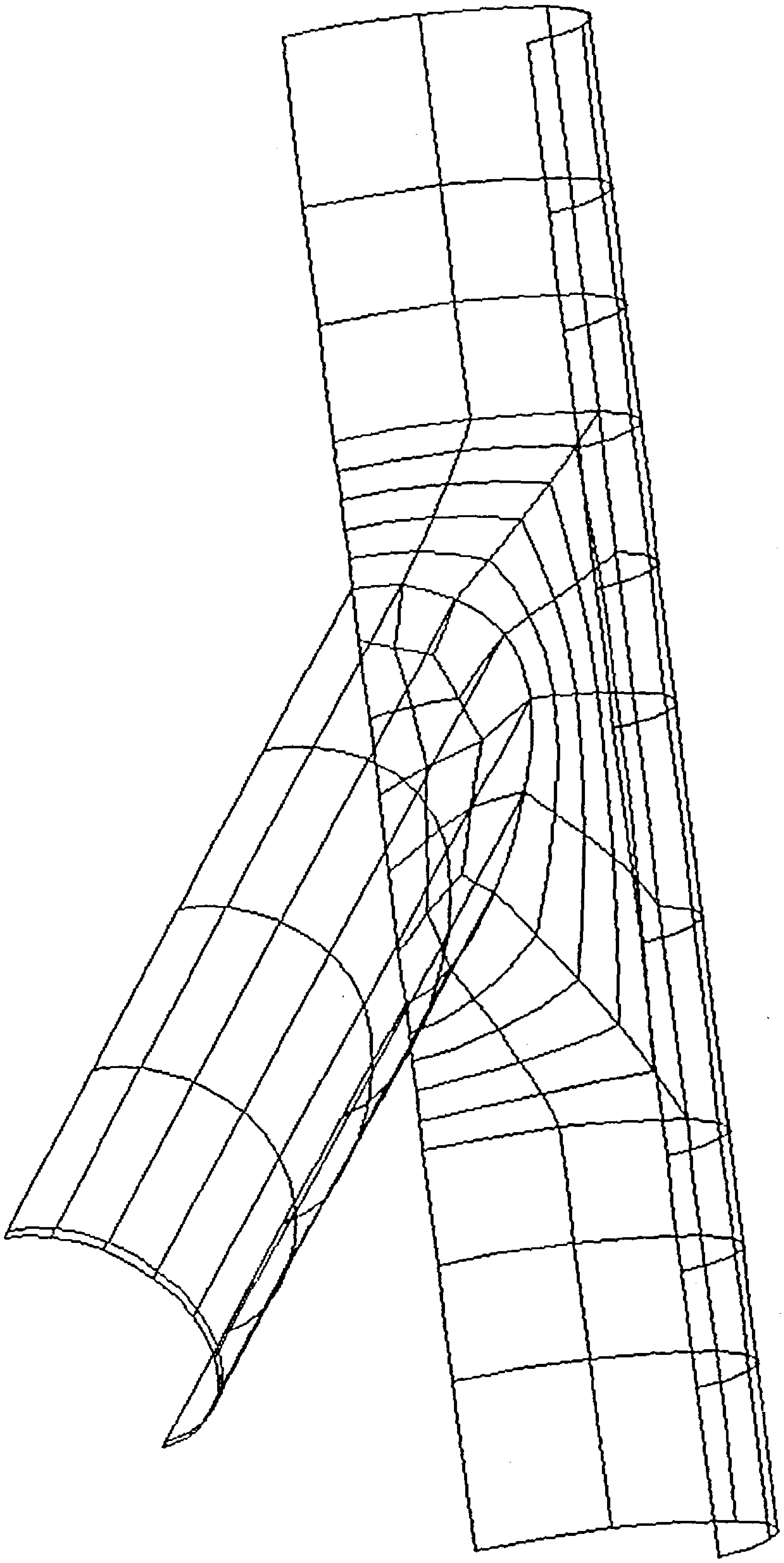

Figure 5.14 Y joint mesh

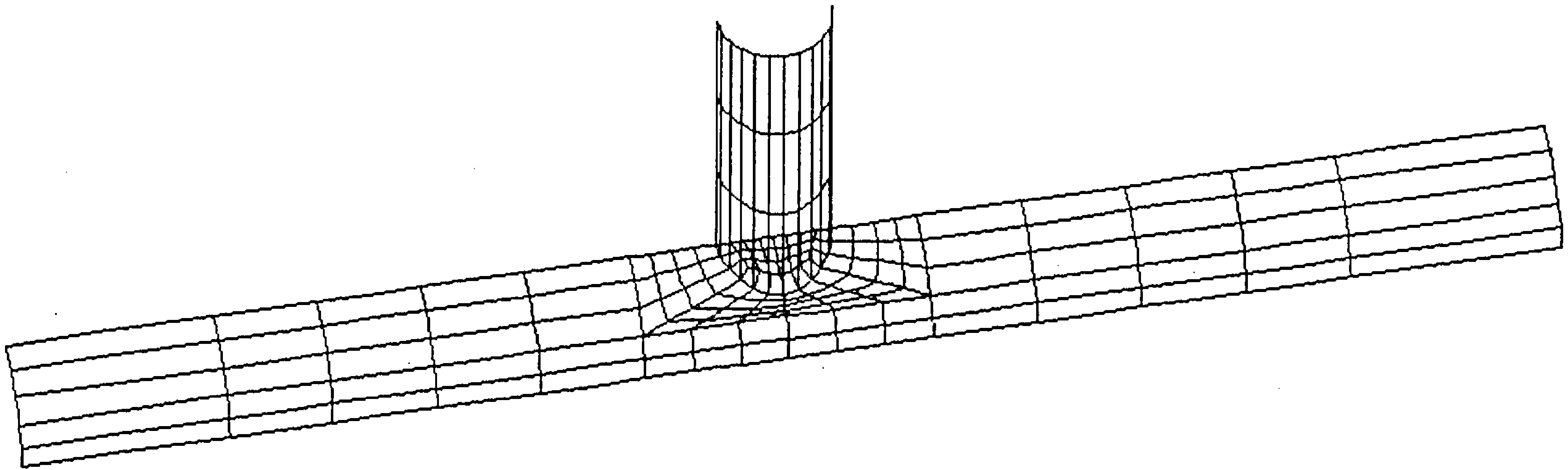

Figure 5.15 DT joint mesh

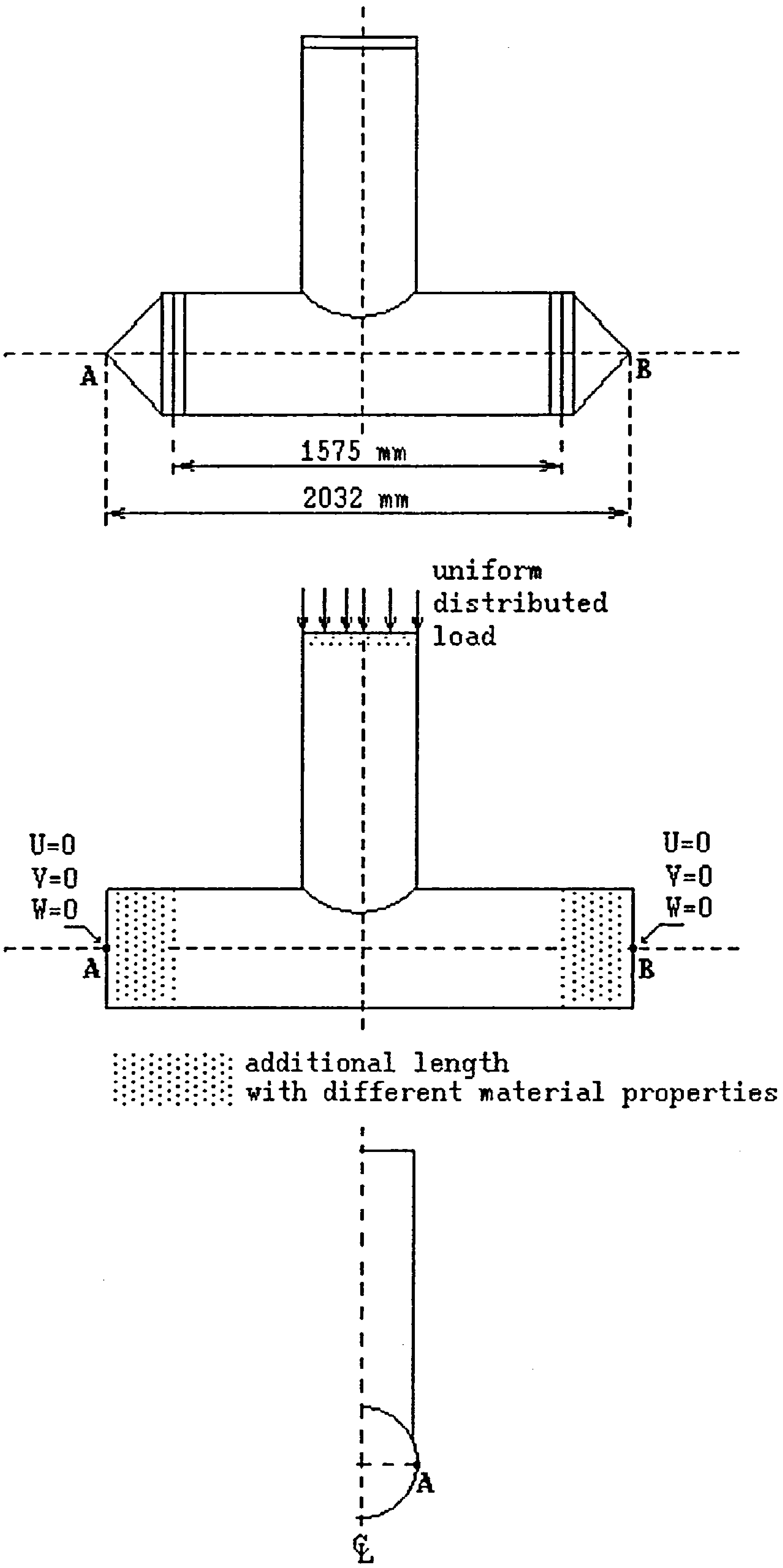

Figure 5.16 Simplification T joint specimen.

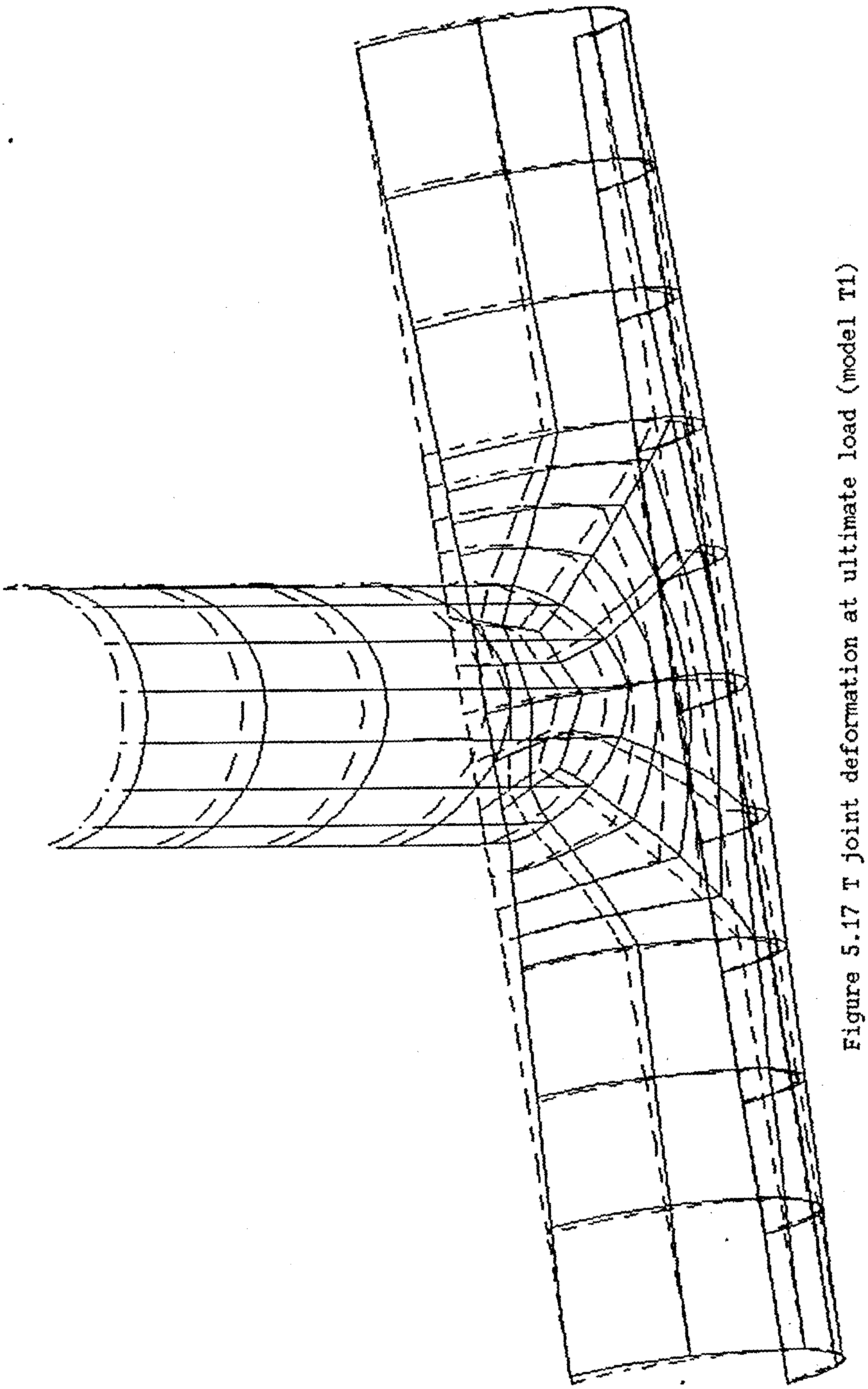

Figure 5.17 T joint deformation at ultimate load (model T1)
(deformation magnification factor = 5)

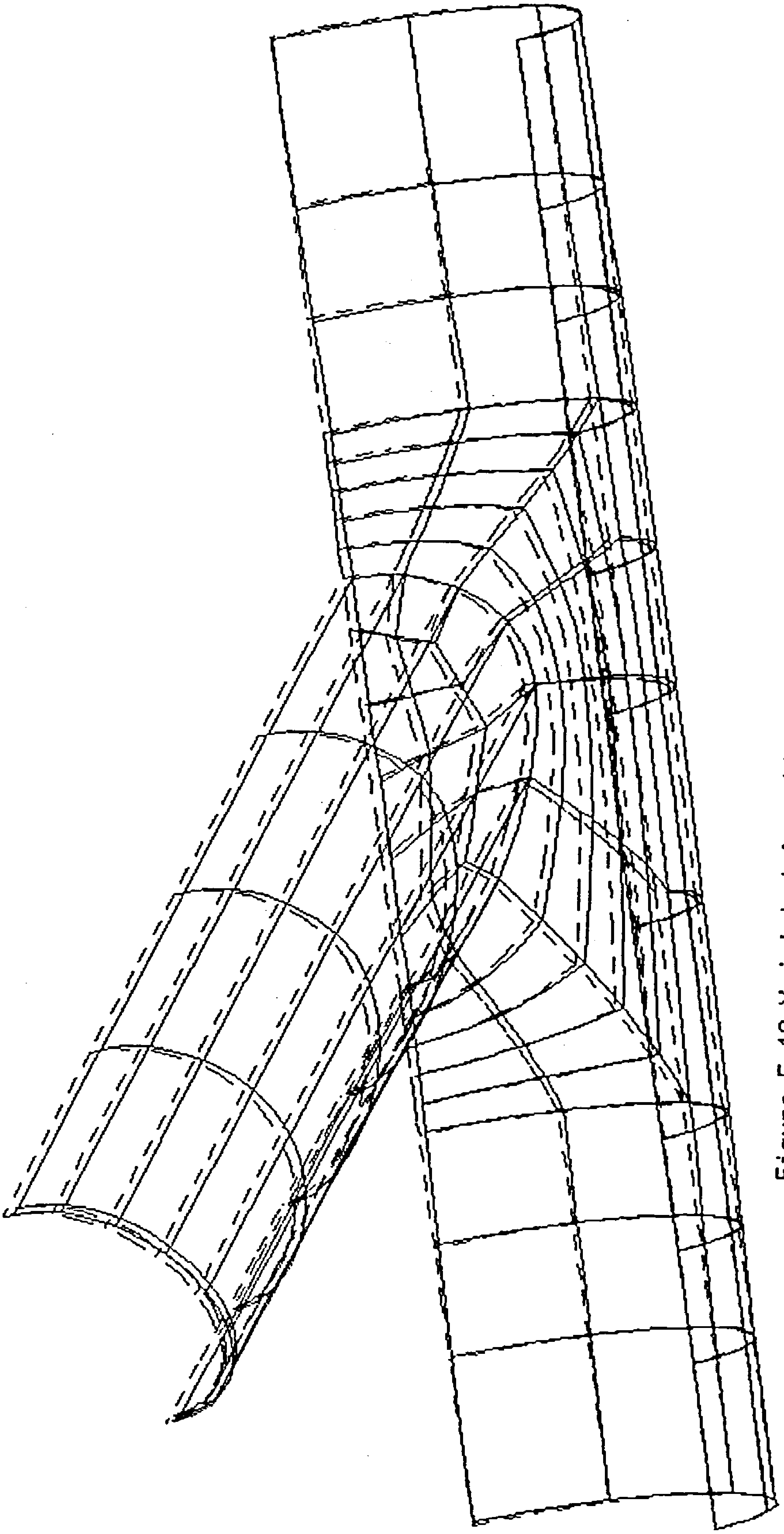

Figure 5.18 Y joint deformation at ultimate load (Model Y2)
(deformation magnification factor = 5)

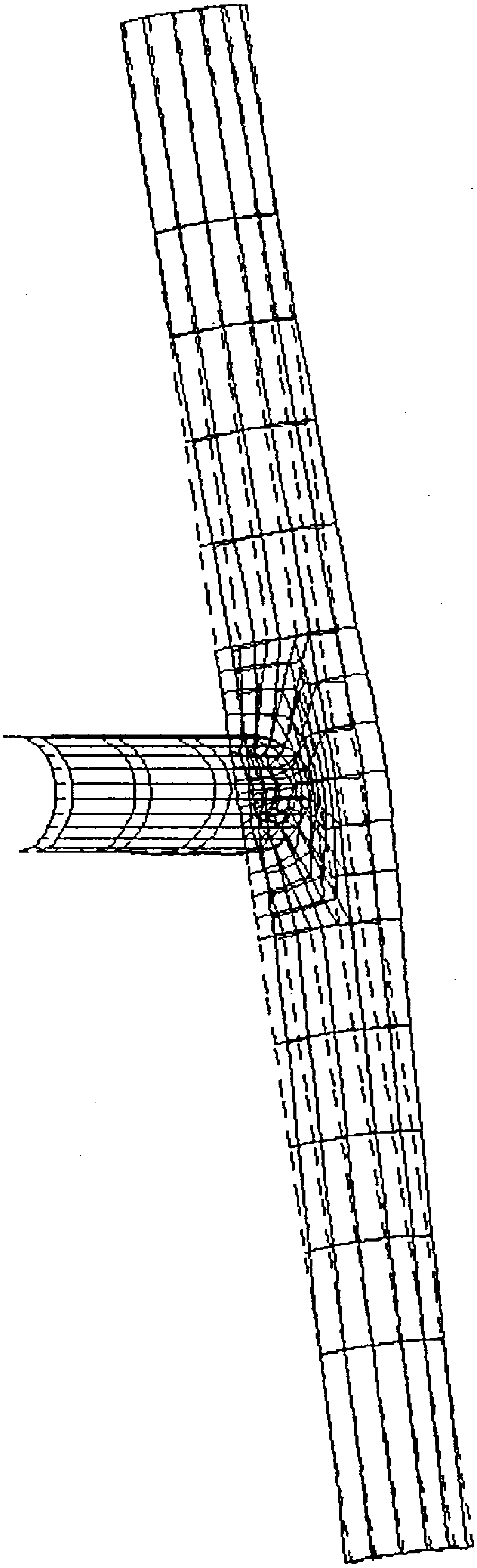

Figure 5.19 DT joint deformation at ultimate load
(deformation magnification factor = 5)

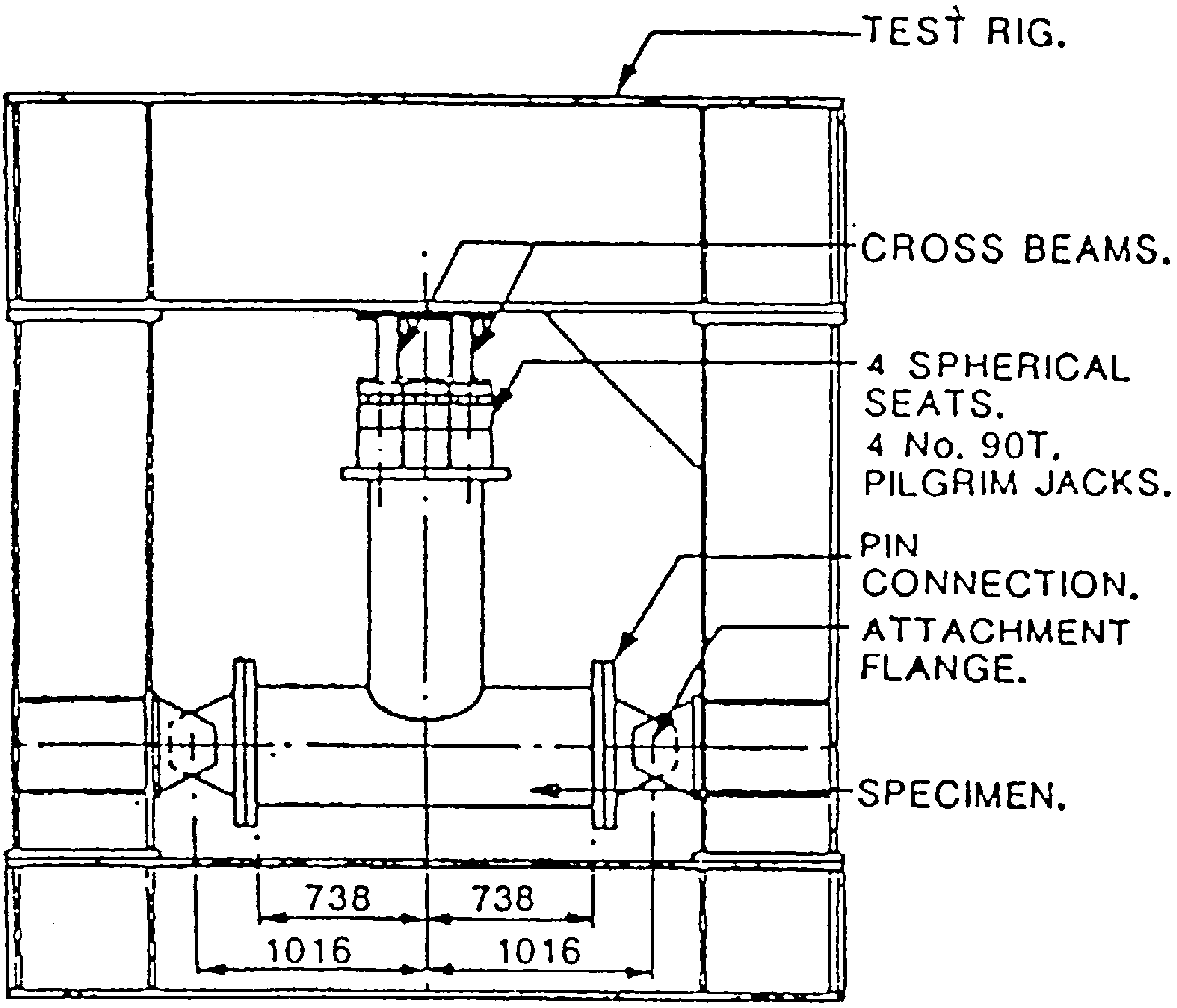

Figure 5.20 : Test arrangement for T joint with axial loading.

Chapter VI

In-plane Bending Moment in K and Y Joints

6.1 Introduction

In this chapter, the ultimate strength of K and Y joints will be calculated using the finite element method and the results will be compared with experimental tests especially those using in-plane bending moment loading. A review of numerical work in ultimate strength of tubular joints under in-plane bending moment is given below.

There are no available numerical results of the ultimate load of K and Y joints subjected to pure in-plane bending moment. The most recent work related to in-plane bending moment was done by Cofer and Will [1990]. As part of the numerical review described in the previous chapter, Cofer and Will analysed a DT joint subjected to a combination of in-plane bending moment in braces and a constant axial compressive force in chord using the finite element method. The loading is a point force on the centre of the chord end plates to impart an overall lateral force along with a constant compressive force and reasonable result is obtained.

6.2 Experimental Studies of Tubular Joint

As part of the testing program [Wimpey Offshore 1989] described in the previous chapter, K and Y joints were loaded to failure with pure in-plane bending moment. The fabrication of specimen was identical to that described in the previous chapter.

As reported by Wimpey Offshore, the jack is applied in the appropriate direction and produces a force perpendicular to the axis of the brace. To ensure that the load direction remained normal to the brace as the brace rotated, a spherical rocker bearing was provided between the load jack and the brace flanges (see Fig. 6.17). The applied bending moment is given by multiplying the force with the lever arm of the jack from the chord surface on the brace centreline. Table 6.1 and 6.2 shows the dimension of the specimen and Fig. 6.17 depicts the test rig.

Mo-del	D (mm)	d (mm)	T (mm)	t (mm)	L (mm)	l1=l2 (mm)	gap (mm)	θ_1/θ_2	β	γ	Fy (N/mm²)		Ft (N/mm²)	
											chord	brace	chord	brace
K1	508	508	12.5	12.5	3200	1100	50.8	$45^0/45^0$	1.0	20.32	349	390	504	556
K2	508	254	12.5	12.5	3200	1100	50.8	$45^0/45^0$	0.5	20.32	280	377	436	555
K3	508	254	12.5	12.5	3200	1100	76.2	$45^0/45^0$	0.5	20.32	274	373	426	552
K4	508	254	12.5	12.5	3200	1100	50.8	$45^0/45^0$	0.5	20.32	310	378	445	555
K5	508	508	12.5	12.5	3200	1100	50.8	$45^0/45^0$	1.0	20.32	356	377	494	548
K6	508	254	12.5	12.5	3200	1100	76.2	$45^0/45^0$	0.5	20.32	294	369	449	489

Table 6.1 — Geometrical and material properties of K joints

Model	D (mm)	d (mm)	T (mm)	t (mm)	L (mm)	l (mm)	θ	β	γ	Fy (N/mm²)		Ft (N/mm²)	
										chord	brace	chord	brace
Y4	508	203	12.5	12.5	1575	1000	45^0	0.4	20.32	322	475	483	577
Y5	508	406	12.5	12.5	1575	1000	45^0	0.8	20.32	317	387	448	527
Y6	508	406	8.0	8.0	1575	1000	45^0	0.8	20.32	278	378	424	479
Y6	508	508	8.0	8.0	1575	1000	45^0	1.0	31.75	300	405	428	570

Table 6.2 — Geometrical and material properties of Y joints

6.3 Simplication in Numerical Models

A numerical model similar to that in section 5.3 is adopted in this work. The numerical model of the K joint can be seen in Fig. 6.11. A uniformly distributed force is applied normal to the brace around the top of the brace. The applied bending moment is given by multiplying the lever arm of the force from the chord surface on the brace centerline. Fig. 6.12 and 6.13 show the mesh of the joints used in the analysis.

6.4 K Joint with In-plane bending Moment

Six sets of experimental results of K joints are compared with numerical tests. From Table 6.1, the joints have nondimensional β between 0.5 and 1.0, ζ between 0.1 and 0.15, and γ equals 20.32. Three of the K joints, K1, K2, K3, are subjected to in-plane bending moment with the same direction of moments. Other K joints, K4, K5, K6, are subjected to in-plane bending moment with opposite directions of moment.

6.4.1 Model K1

As model T1 in section 5.4.1, model K1 is used as a base case study to examine the hardening parameter. This model is chosen because it is the only specimen from six of K joints which exhibited plastic collapse. Three different hardening parameters were used and the total number of elements is 184 (Fig. 6.12a). The hardening parameter is taken between 1% to 10% of Young Modulus (E). Excellent results are obtained when the hardening parameter is given as $1\%E$ or $5\%E$, but other numerical tests also give good results (see Fig. 6.1a-d). Table 6.3 shows the range of ultimate load as the hardening parameter is varied between 0.0 % and 5%. Based on those numerical tests, the density of element was increased by 46% with the hardening parameter at $5\%E$ and the total number of elements equals 268 (Fig. 6.12b). Fig. 6.1d shows that the coarse mesh is stiffer than fine mesh, but both test give the differences of ultimate load in range 2.5% (see Table 6.3).

It can be seen from Fig. 6.1a-d, that the brace displacement of the numerical tests give good comparison with the experimental test in the elastic range. As reported by Wimpey Offshore, yielding was first detected at the chord crown heel position on both braces at a moment of 240.0kNm, and at 520.0kNm plastic deformation of chord wall occurred, in the compression zone, at the heel position. In the numerical analysis, yielding was first found at the chord crown toe position at a moment of 376kNm. At 491.0kNm, yield had occurred at the chord crown heel positions on both braces. The plastic zone spread around the cylinder intersection and the plug of the chord at a moment of 580.0kNm. Even though there is a difference on first yield, the numerical analysis gives excellent comparison for displacement and ultimate load as mentioned above.

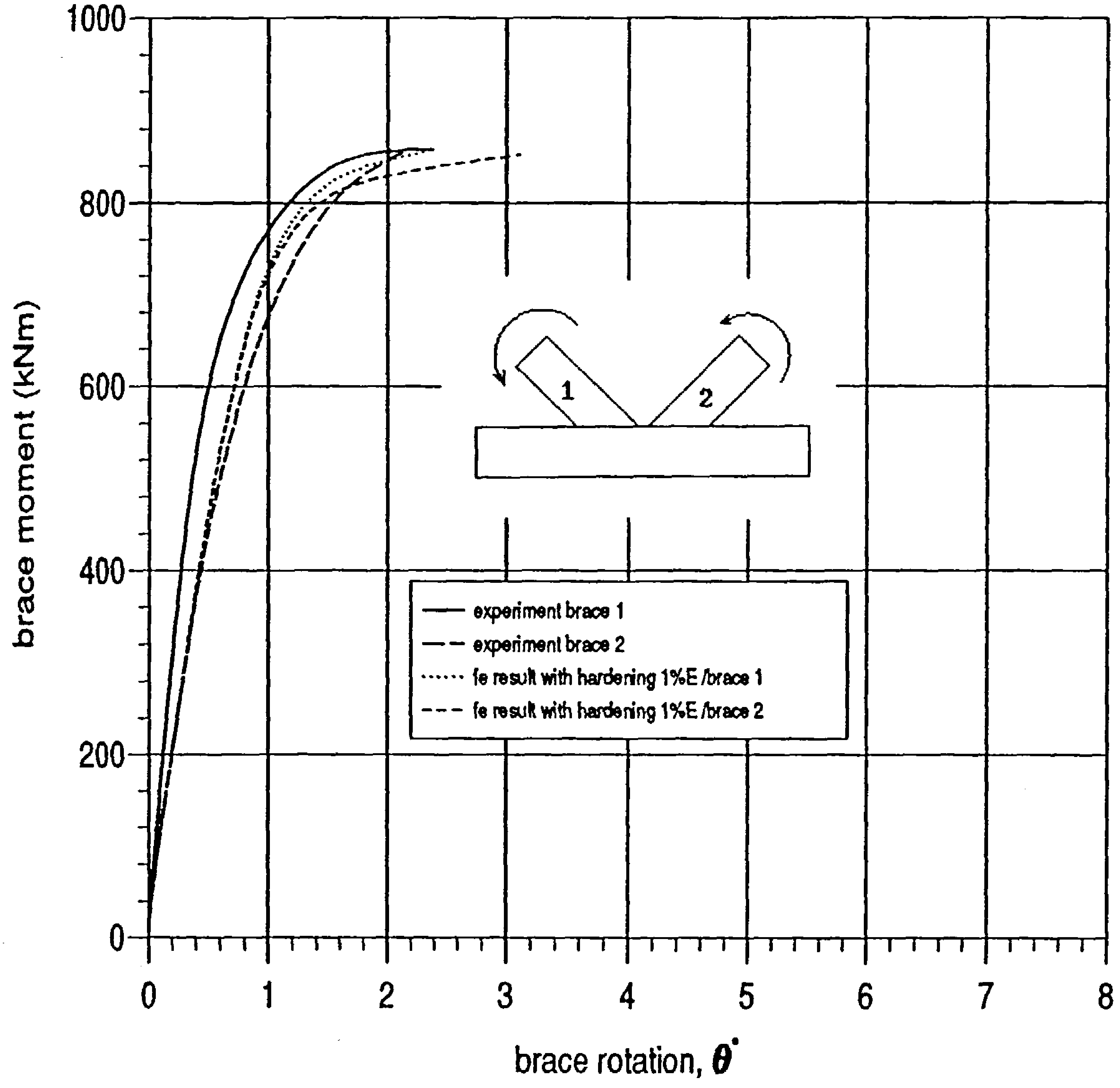

Figure 6.1a : M-θ plot of model K1 with hardening parameter 1%E in numerical model.

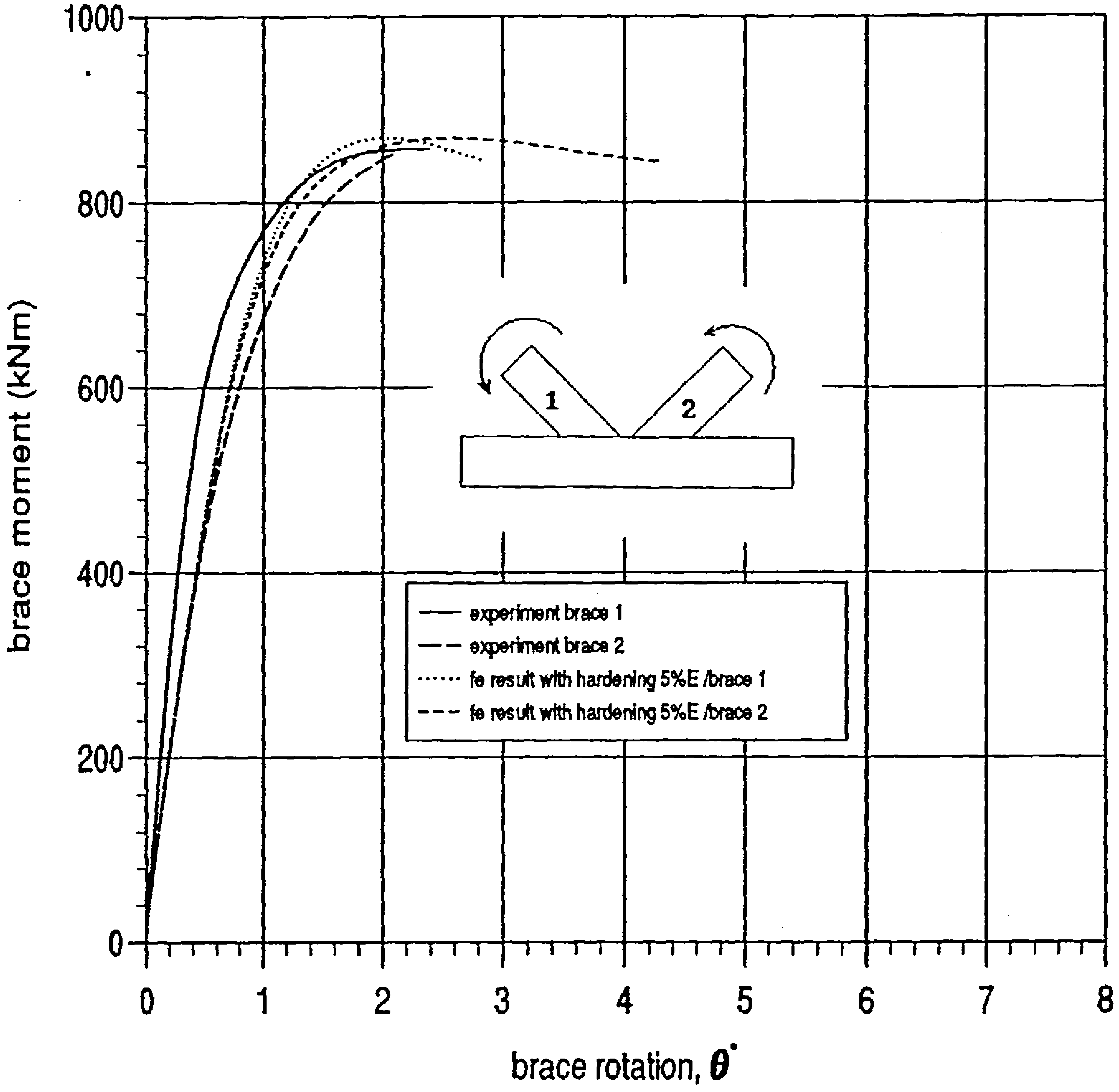

Figure 6.1b : M-θ plot of model K1 with hardening parameter $5\%E$ in numerical model.

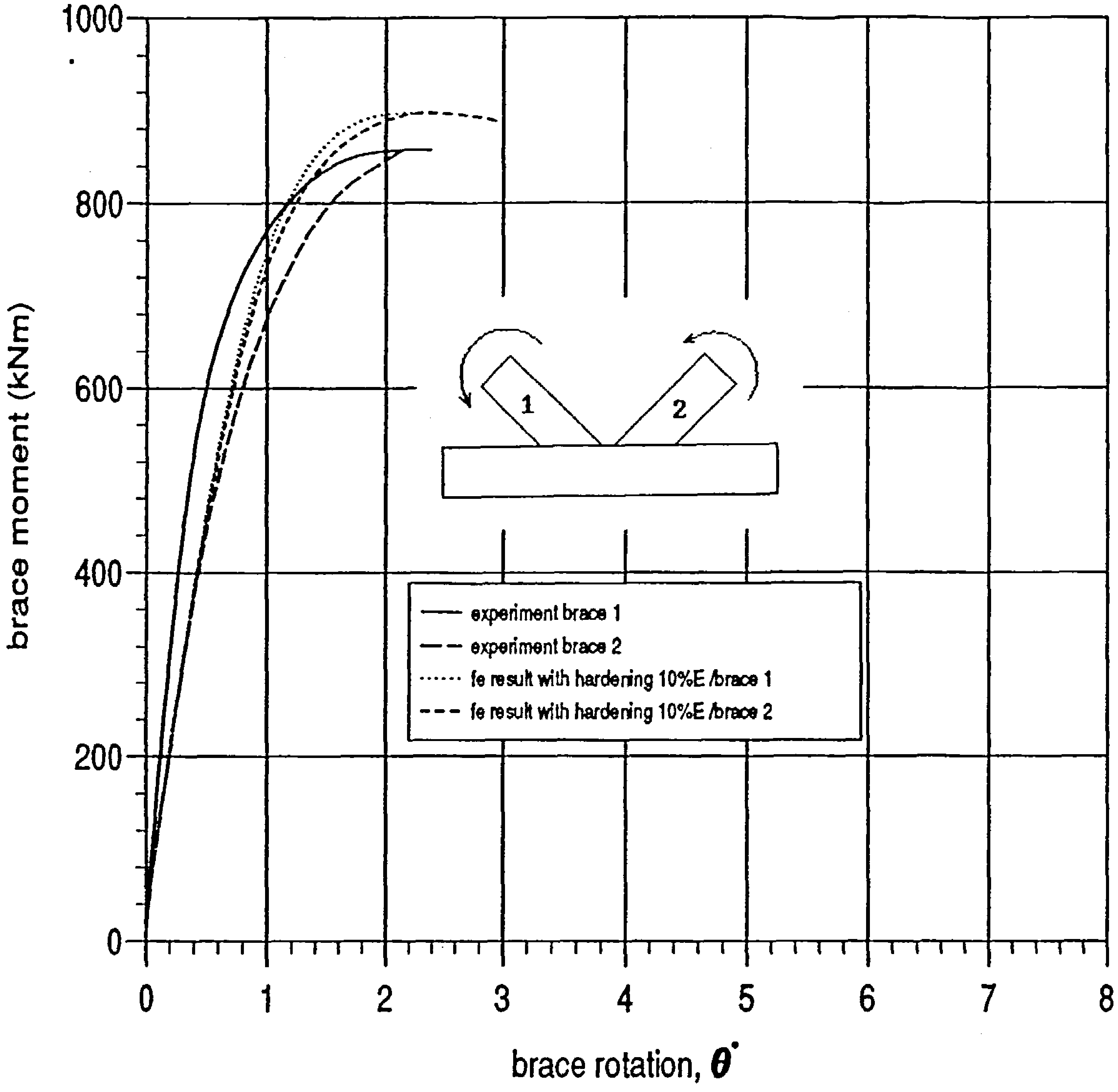

Figure 6.1c : M-θ plot of model K1 with hardening parameter 10%E in numerical model.

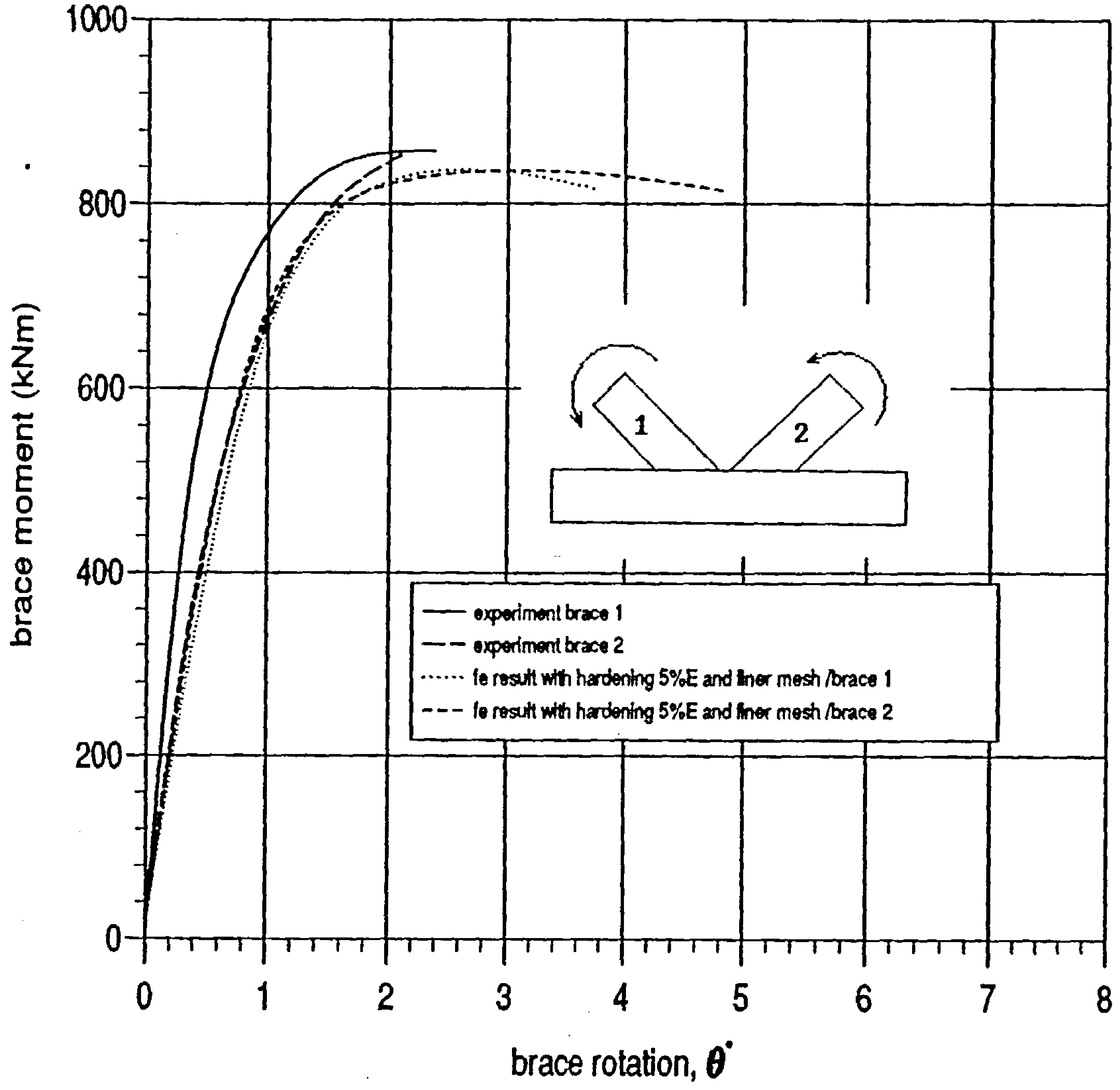

Figure 6.1d : M-θ plot of model K1 with fine mesh.

Case	hardening parameter $(\%E)$	ultimate load (kN)	differences $(\%)$
Experiment	-	857	-
FE coarse mesh	1	851.8	-0.6
FE coarse mesh	5	866.5	1.1
FE coarse mesh	10	899.4	4.9
FE finer mesh	5	835.2	-2.5

Table 6.3 — Model K1 result compare with experiment

6.4.2 Model K2

Based on the numerical test of model K1, 184 elements will be used to analyse other K joints. It can be seen from the M-θ plot (see Fig. 6.2) that the displacement in the numerical test of model K2 is slightly lower than the experimental result in the elastic range. However, the trend of the numerical test in the M-θ plot is generally similar to experimental results.

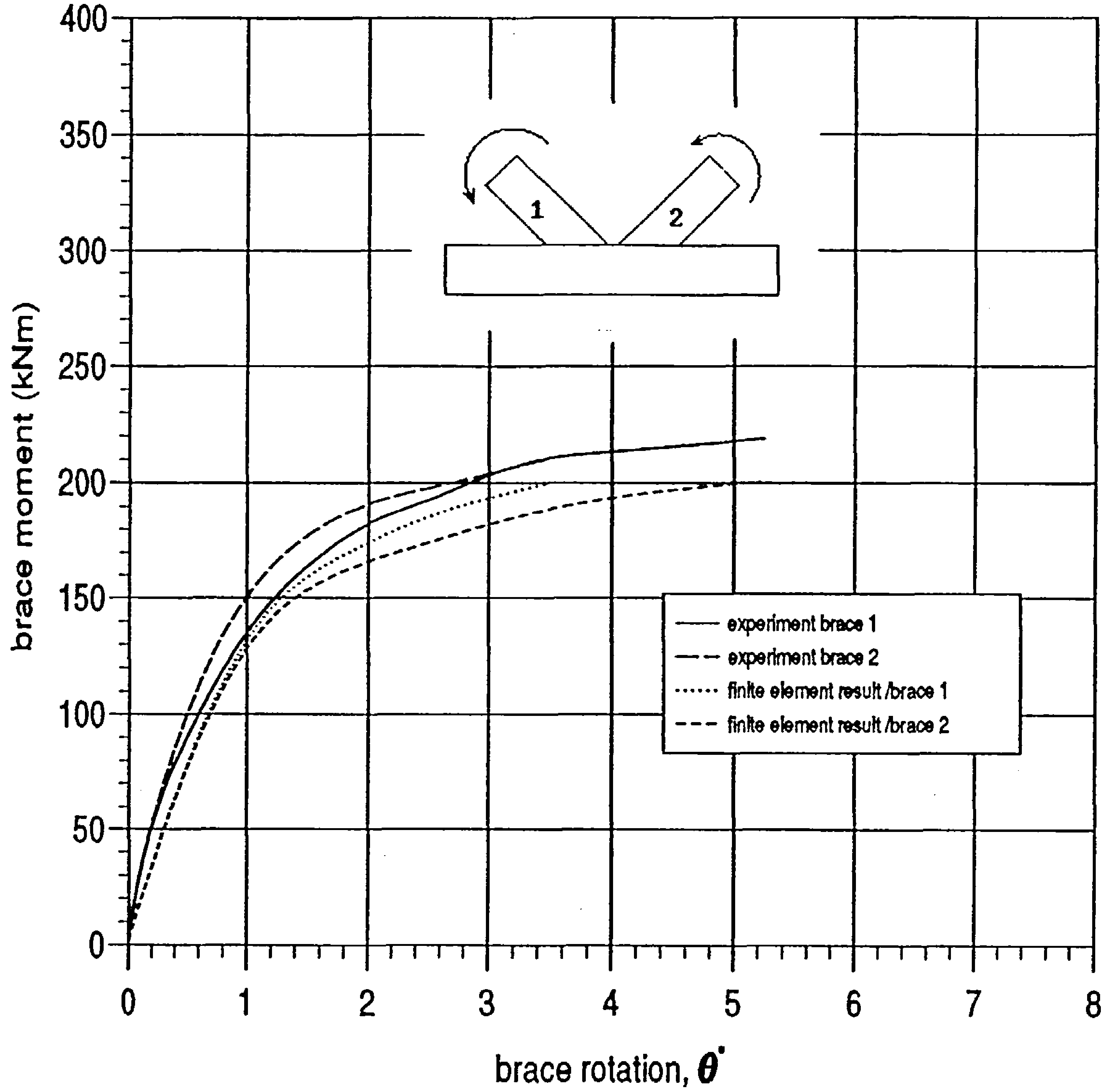

Figure 6.2 : M-θ plot of model K2.

As in the experimental test of specimen K1, yielding was first recorded at the crown heel position on both braces at a moment of 65.0kNm. At 125.0kNm, plastic deformation of chord material, in the compression zone, at the heel of the brace was observed. In the numerical test, first yield was found at the chord crown heel and toe at a moment of 104.0kNm. The plastic zone spread around the cylinder intersection at 130.0kNm.

At 210.0kNm tearing of material initiated at the chord crown heel posistion of brace 2 (see Fig. 6.2) in the experimental test. The specimen failed at 219.0kNm while the numerical model failed at 200.4kNm.

6.4.3 Model K3

As shown in Fig. 6.3 the numerical test displacement gives an excellent comparison to the experimental test. Close to the peak load, braces 1 and 2 in the numerical test give different displacements while braces 1 and 2 of experimental test give the same result. The possible reason for the difference is that the experimental specimen started tearing before reaching the ultimate load. This case also occurred in specimen K2.

In the experimental tests, yielding was first detected at the chord crown heel position on both braces at a moment of 65.0kNm and at 135.0kNm plastic deformation of the chord wall at the heel position of brace 1 was observed. In the numerical test, yielding was found at a moment of 110.0kNm at the chord crown heel position of brace 1, at the chord crown toe position and at the chord saddle position of the braces. The plastic zone spread around the intersection of the cylinder at a moment of 128.0kNm.

As mentioned above, tearing of material initiated at the chord crown heel position of the brace at a moment of 200.0kNm in the experimantal tests. The specimen eventually failed at 208.0kNm while the numerical model reached an ultimate load of 223.0kNm.

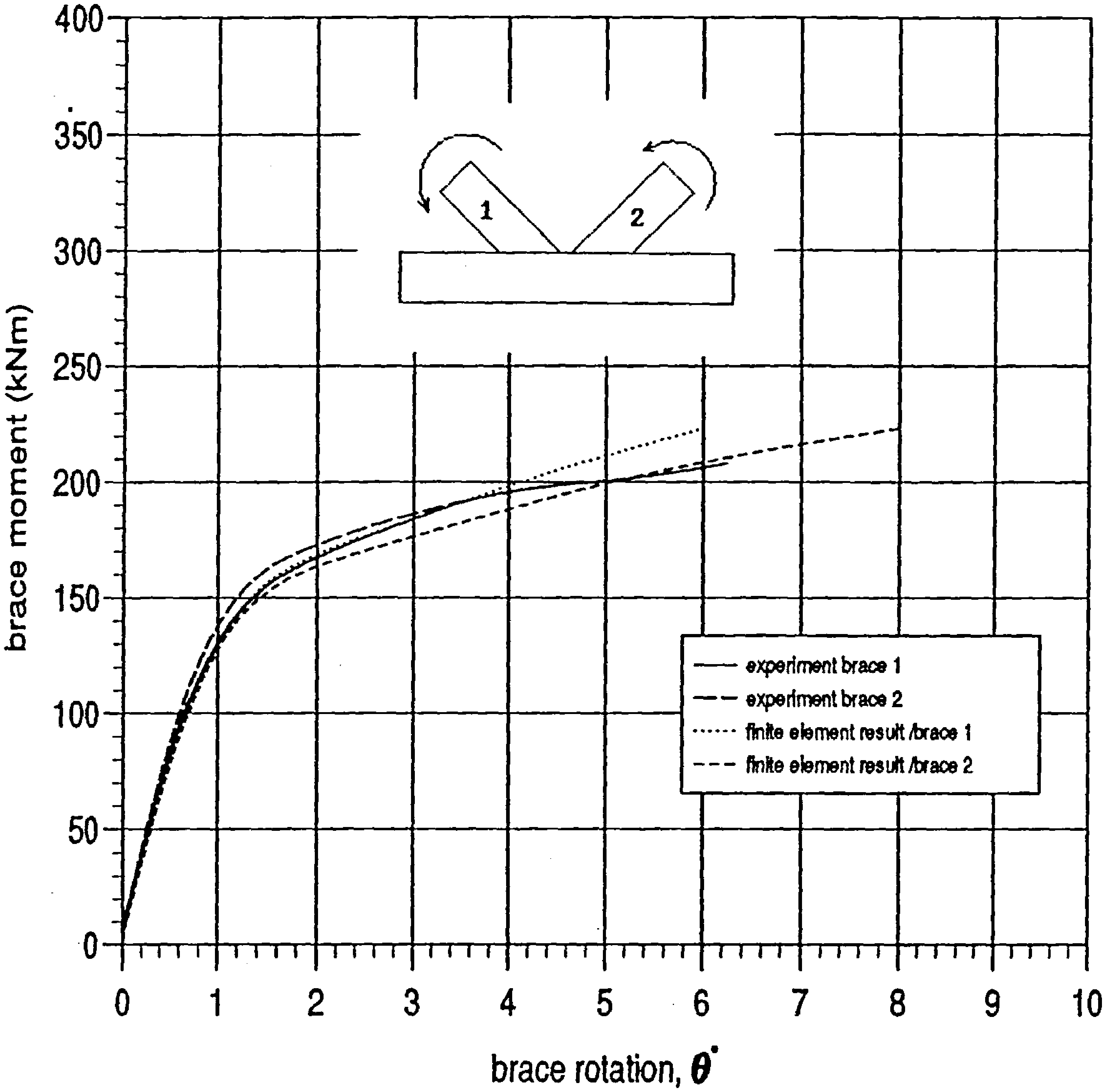

Figure 6.3 : M-θ plot of model K3.

6.4.4 Model K4

The opposite bending moment was applied to the model. From the M-θ plot in Fig. 6.4 excellent results were obtained by the numerical tests compared to experimental tests.

As reported by Wimpey, there were no strain gauges mounted at the 'hot spot' location of the joint. First yield was determined by examining the M-θ plot and occurred at a moment 65.0kNm. Plastic deformation of the chord wall at the crown toe position of both braces was observed at a moment of 150.0kNm. In numerical tests, yielding was found at the chord crown toe position and the chord saddle position of both braces at a moment of 106.0kNm. At a moment of 127.0kNm, the plastic zone extended to the crown heel position.

Tearing of material at the heel position of both braces initiated at a moment of 190.0kNm. The specimen failed at a moment of 198.0kNm in the experimental test while the numerical model reached its ultimate load at a moment of 198.8kNm which is slightly higher than the experimental test (see Table 6.4).

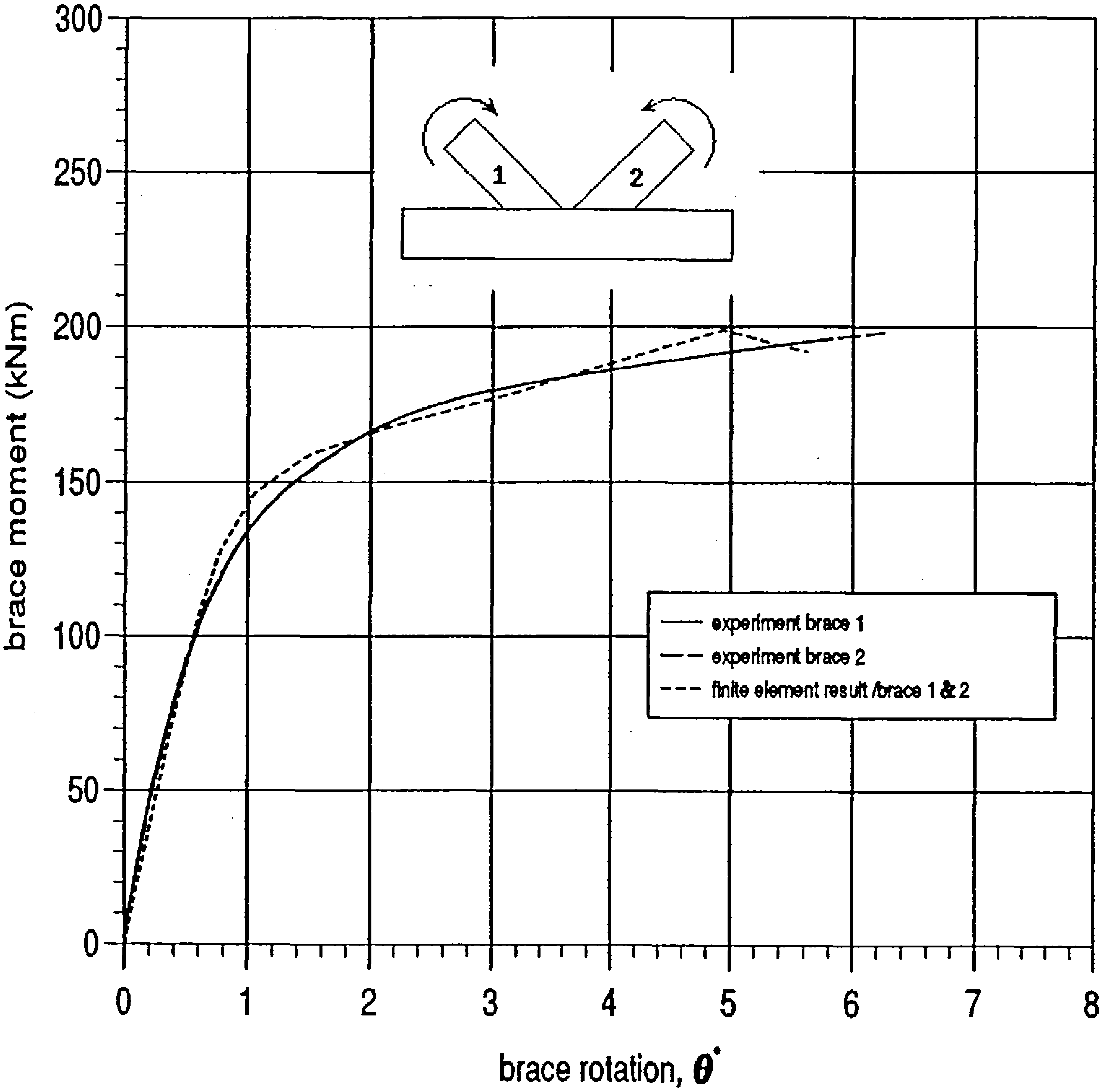

Figure 6.4 : M-θ plot of model K4.

6.4.5 Model K5

Fig. 6.5 shows that the numerical displacement is slightly lower than the experimental result which in this case shows that the numerical model is slightly stiffer than the experimental specimen.

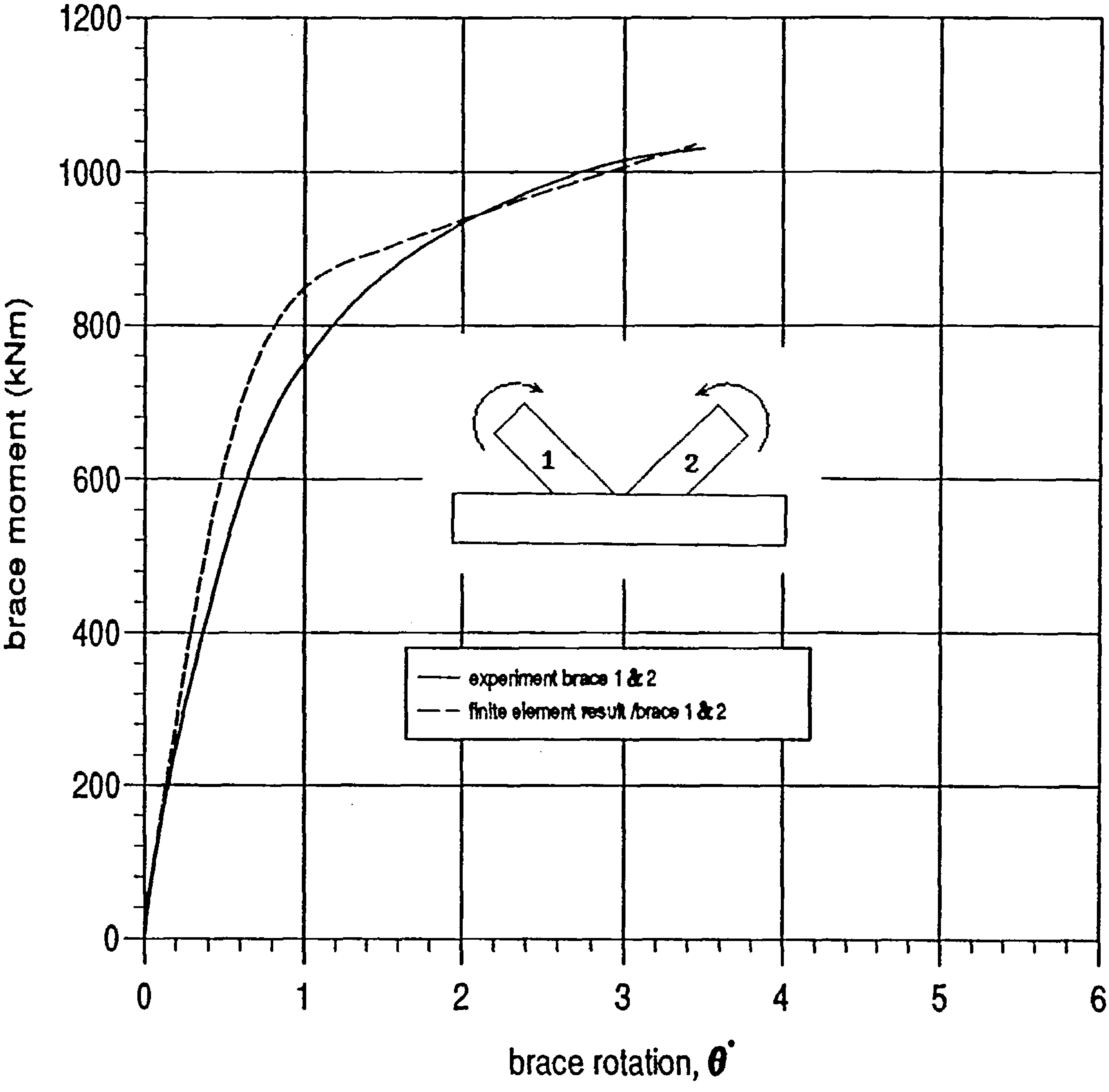

Figure 6.5 : M-θ plot of model K5.

First yield was estimated using the M-θ plot and occurred at a moment of

250.0kNm. At a moment of 780.0kNm, plastic deformation of the chord wall at the crown toe position of the brace was observed. In the numerical test yielding occurred first at the chord crown heel position at a moment of 525.0 kNm and at a moment of 696.0kNm the plastic zone extended around the cylinder intersection of both braces.

Tearing of material at the heel position of the braces initiated at a moment of 1000.0kNm and the specimen failed at a moment of 1030.0kNm. In the numerical test, the ultimate load was reached at the moment of 1035 kNm which is 0.5% higher than in the experimental test (see Table 6.5).

6.4.6 Model K6

From the M-θ plot, Fig. 6.6, good comparison of displacement is obtained from the numerical test. As shown in Fig. 6.6, displacement of brace 1 in experimental test, shown by full line, is slightly different from that of brace 2 in the near transition between elastic and plastic region. Since the structure and loading are symmetrical, the difference shows that there are some imperfection in the specimen.

As with specimens K4 and K5, first yield was estimated using the M-θ plot and occurred at a moment of 78.0kNm. Plastic deformation of the chord at the crown toe position of both braces was observed at a moment of 130.0kNm. In the numerical test, yielding occurred first at the chord crown toe and the chord saddle positions at a moment of 117.0kNm. The plastic zone extended around the cylinder intersection at a moment of 137.0kNm.

In the experimental test, tearing of material initiated at 190.0kNm and the specimen failed at a moment of 191.0kNm. A slightly lower ultimate load was reached by the numerical test at a moment of 175.0kNm. Table 6.5 shows that the diference in ultimate load of numerical test and experimental test is -8.4%.

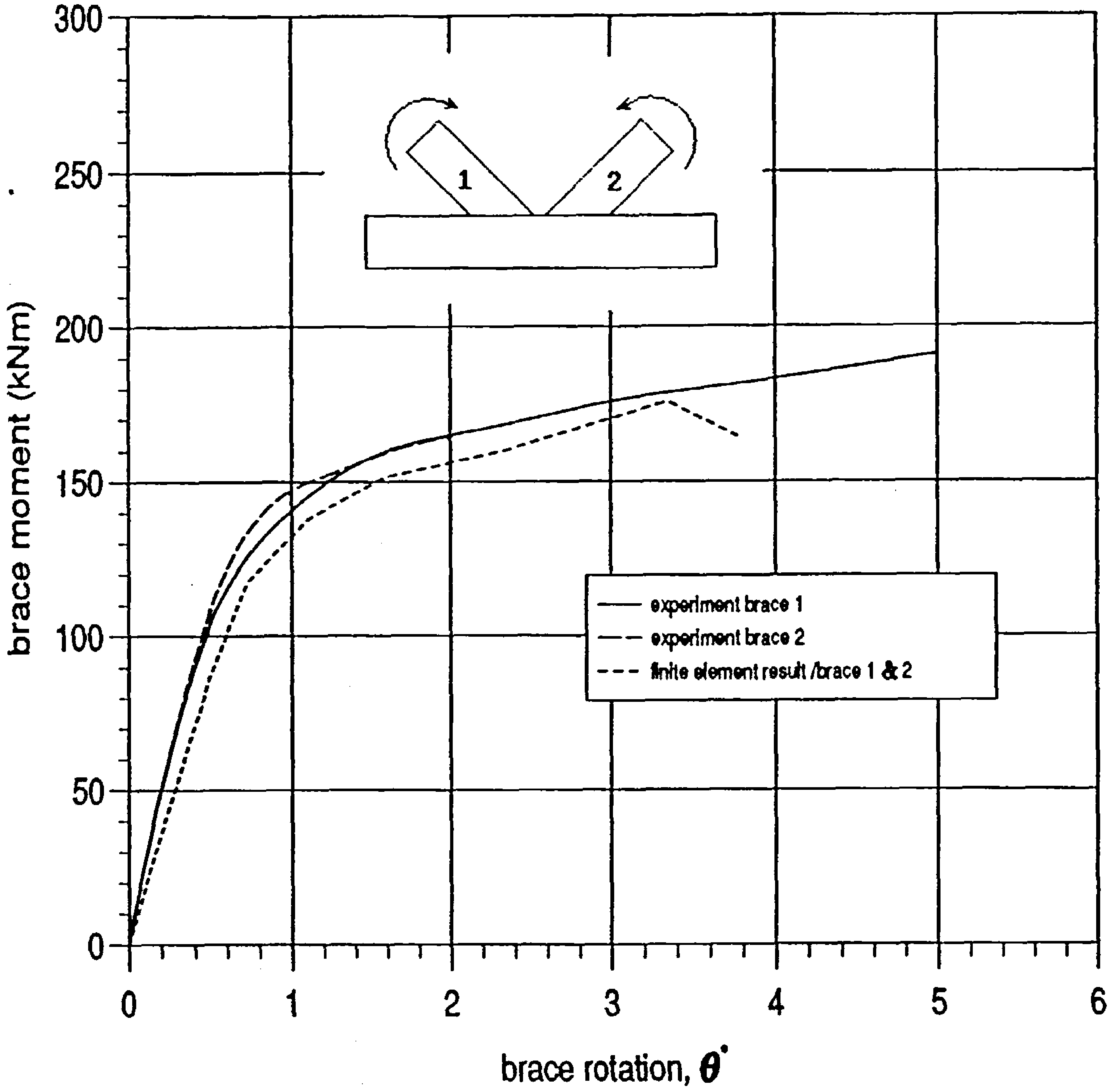

Figure 6.6 : M-θ plot of model K6.

Model	Numerical result (kNm)	Experiment result (kNm)	difference %	initial tearing (kNm)	difference %
K1	866.5	857.0	1.1	-	-
K2	200.4	219.0	-8.7	210.0	-4.6
K3	223.0	208.0	7.2	200.0	11.5
K4	198.8	198.0	0.4	190.0	4.6
K5	1035.0	1030.0	0.5	1000.0	3.5
K6	175.0	191.0	-8.4	190.0	-7.9

Table 6.4 — Ultimate load numerical and experimental test of K joints

6.5 Y Joint with In-plane Bending Moment

Four sets of experimental results of Y joints are compared with numerical results. The joints are analysed using the mesh shown in Fig. 6.13 with 138 elements.

6.5.1 Model Y4

As shown in Table 6.2, the brace diameter is much smaller than the chord diameter which gives a β ratio of 0.4. As a result of an applied bending moment, the displacement in the numerical test is larger than in the experimental test (as shown in Fig. 6.7). As for specimen T3 in the previous chapter (see section 5.4.3), this experimental result is suspect. There is a possibility that a mistake has been made in reading the displacement from the chart. If the displacement reading is multiplied by two, the agreement with the numerical result is very good.

At approximately 60.0kNm, yielding was first detected at both compression and tension zones on the brace in experimental test. Plastic deformation of the chord wall was observed at approximately 100.0kNm in the compression zone at the toe position. It was also reported that deformation of the chord wall was accompanied by flaking of the surface paint at the buckling position at approximately 175.0kNm. In the numerical test, yielding was found in both compression and tension zones on the chord and brace at a moment of 103.0kNm. At the next load increment, 136.0kNm, the plastic zone rapidly extended around the cylinder intersection.

The tensile crack initiated at the chord heel position at a moment of 205.0kNm and the specimen failed at a moment of 206.0kNm. The numerical model reached its ultimate load at a moment of 212.7kNm which is slightly higher than in the experimental test. Table 6.5 shows the diference in ultimate load between numerical test and experimental test.

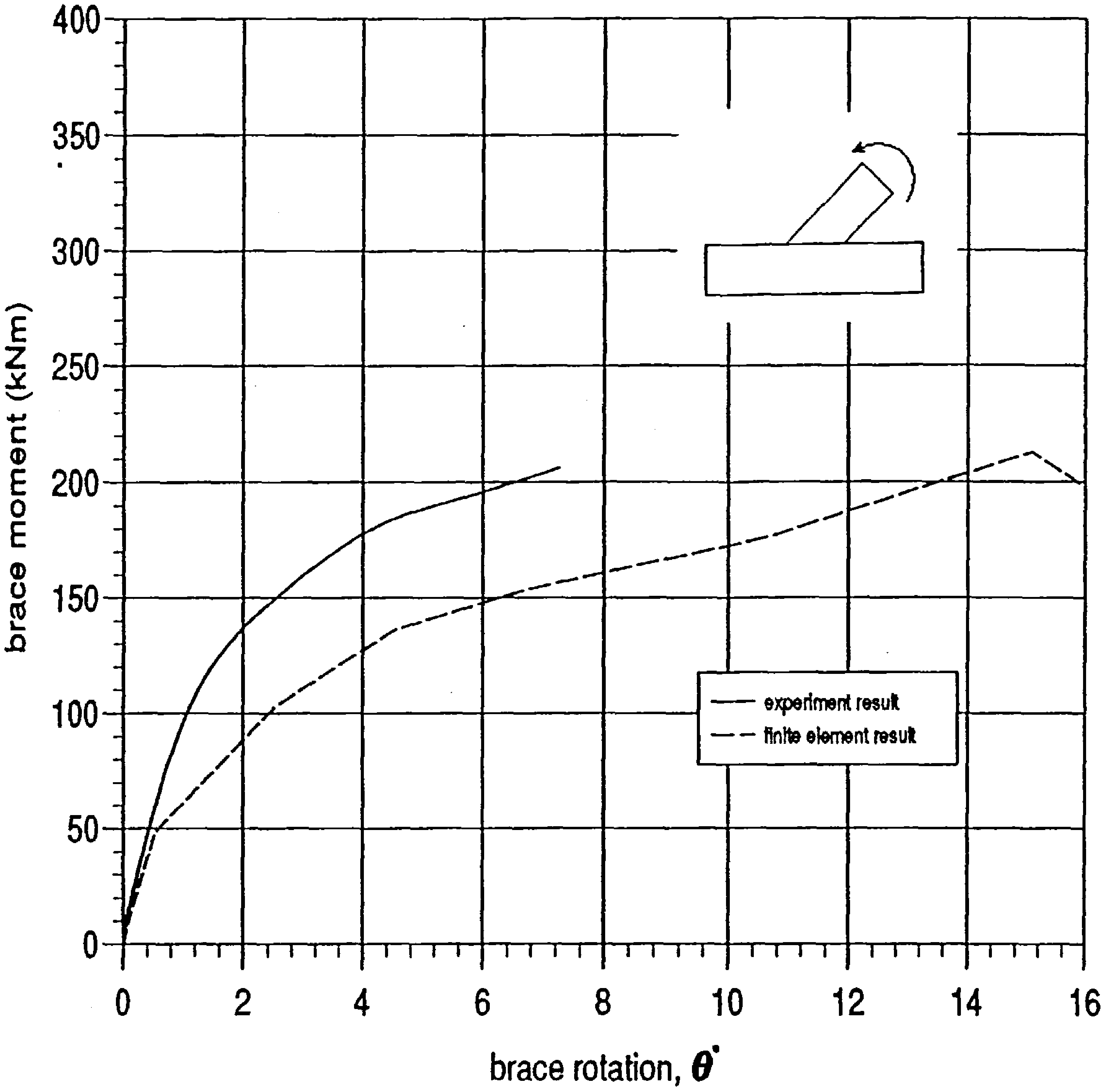

Figure 6.7 : M-θ plot of model Y4.

6.5.2 Model Y5

As shown in the M-θ plot in Fig. 6.8, a good comparison is obtained with the numerical analysis. At the peak load, the numerical displacement is slightly less than the experimental result.

As reported by Wimpey, there were no strain gauges mounted at the 'hot spot' location of the specimen. First yield was determined by examining the M-θ plot and occurred at approximately 175.0kNm. At 400.0kNm plastic deformation of the chord wall occurred on the compression side at the toe position. In the numerical test, yielding was first found at the chord saddle position at a moment increment of 240.0kNm. At a moment of 310.0kNm, yielding occurred in the tension zone at the chord heel position. The plastic zone extended around the cylinder intersection at 349.0kNm.

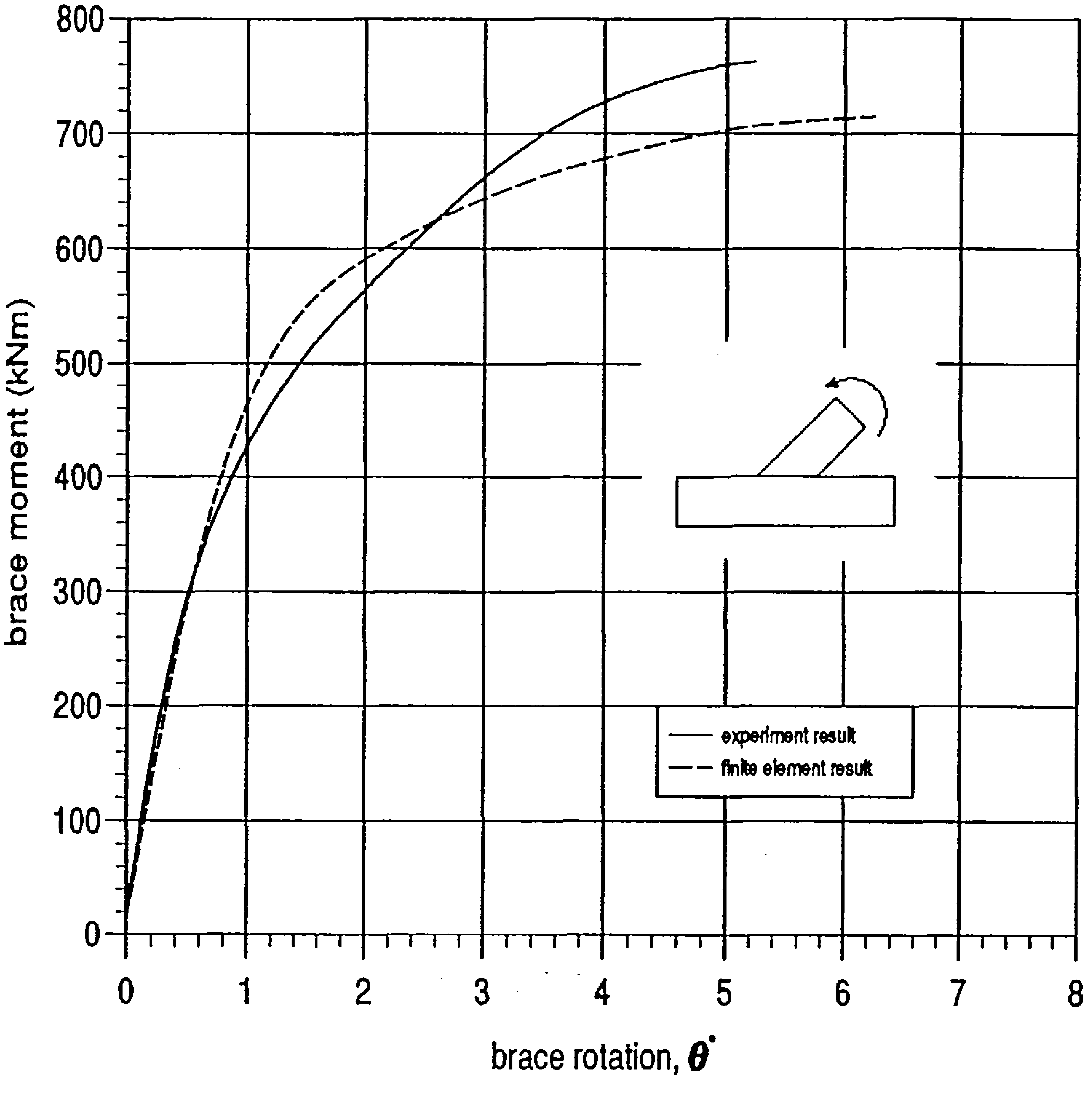

Figure 6.8 : M-θ plot of model Y5.

The tensile crack appeared at the chord heel position at a moment of 762.0kNm in the experimental test. At this point, the specimen could not sustain any futher load. A slightly lower ultimate load of 714.0kNm was obtained from the numerical model.

6.5.3 Model Y6

As with Model Y5, the numerical test displacement is slightly less than experimental result but slightly larger near the peak load. The M-θ plot can be seen in Fig. 6.9.

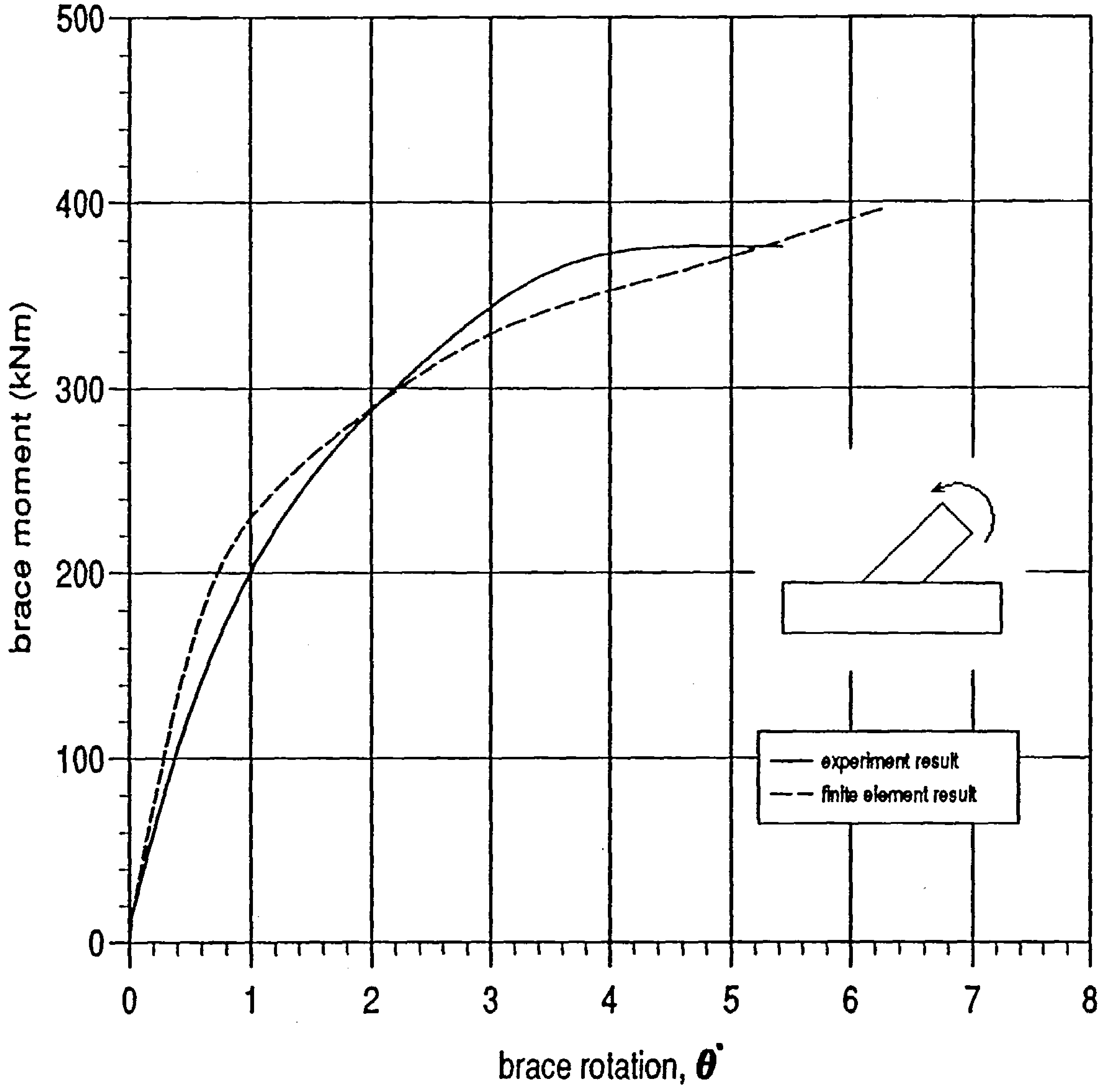

Figure 6.9 : M-θ plot of model Y6.

First yield was estimated using an M-θ plot and occurred at a moment of 85.0kNm in the experimental test. Plastic deformation of the chord wall was observed at 200.0kNm on the compression zone. In the numerical test, first yield occurred in the tensile zone at the chord heel and at the chord saddle position at a moment of 173.0kNm. The plastic zone extended around cylinder intersection at a moment of 206.0kNm.

At 370.0kNm, tearing of chord material at the crown heel position and the weld toe was recorded. The specimen eventually failed at 376.0kNm. The numerical model reached ultimate load at a moment of 397.0kNm, 7% higher than the experimental result (see Table 6.5).

6.5.4 Model Y7

It can be seen from Fig. 6.10, that an excellent result is obtained by the numerical analysis. The displacement of the numerical model is similar with experimental results in elastic range. Near the peak load, the numerical displacement is slightly larger than the experimental result.

Like model Y5 and Y6, first yield was estimated using an M-θ plot and occurred at a moment of 200.0kNm in the experimental test. Plastic deformation of the chord wall was observed at 450.0kNm on the compression zone. In the numerical model, yielding was first found in the tensile zone at the chord crown heel and the plug. Yielding was found at the chord saddle at a moment of 316.0kNm and extended to the compression zone at the chord crown heel position.

A crack was started at the chord crown heel at a moment of 690.0kNm and the specimen failed at 712.0kNm. In the numerical test, the ultimate load reached was 689.8kNm, 3.1% lower than the experimental result.

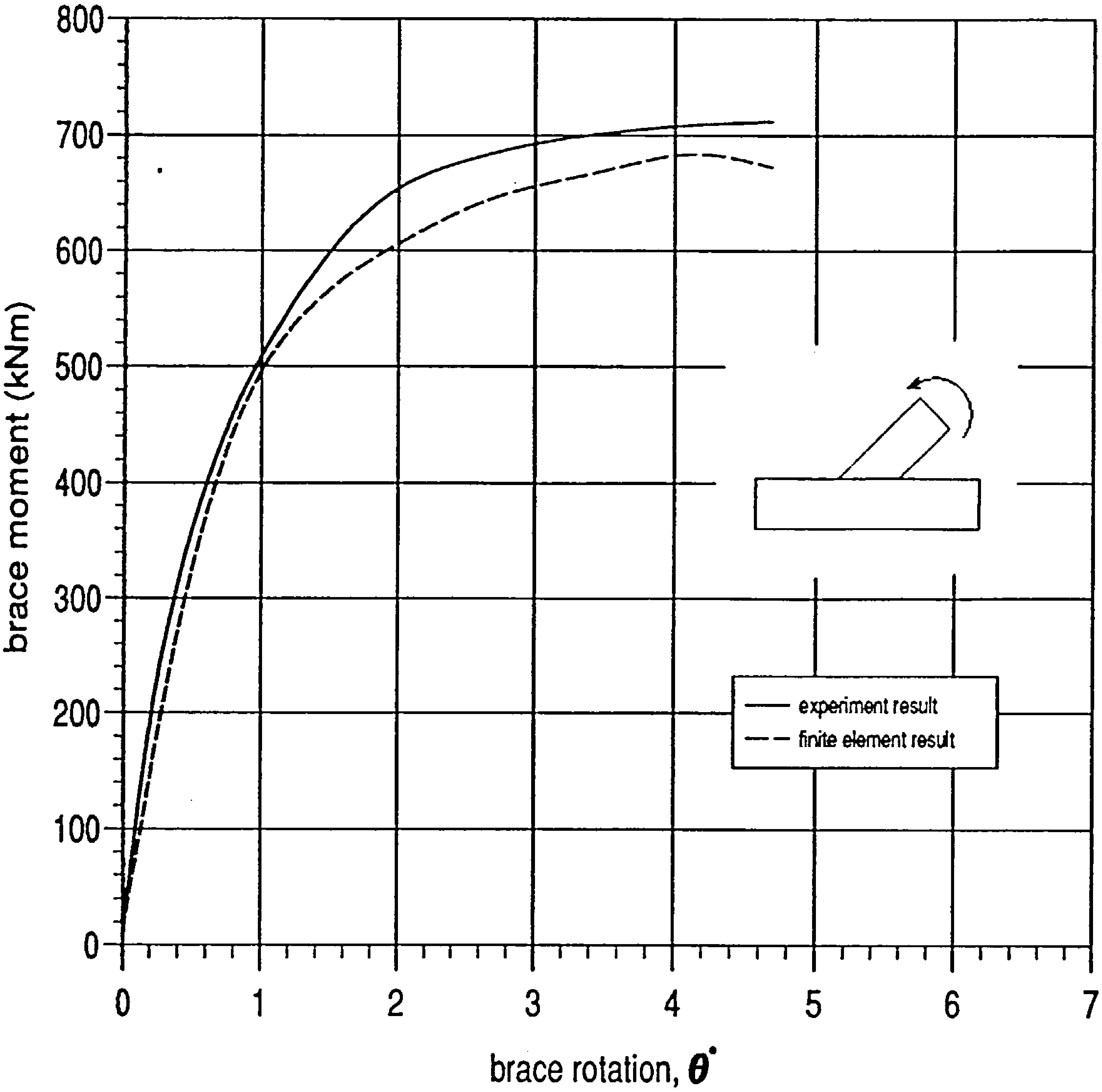

Figure 6.10 : M-θ plot of model Y7.

Model	Numerical result (kNm)	Exp. ultimate load result (kNm)	difference %	Exp. initial crack (kNm)	difference %
Y4	212.7	206.0	5.7	205.0	3.8
Y5	714.0	762.0	-6.3	762.0	-6.3
Y6	397.0	376.0	5.6	370.0	7.3
Y7	712.0	689.8	-3.1	690.0	-0.0

Table 6.5 — Ultimate load numerical and experimental test of Y joints

6.6 Discussion

Six sets of numerical results for **K** joints, show that most of the numerical displacements give excellent comparisons to the experimental results. Fig. 6.14-15 show the deformation of **K** joints under inplane bending moment. Most of the first yield loads of numerical tests are higher than those of experimental tests. This problem will be discussed later. There are some differences in the position of first yield between numerical tests and experimental tests. In the first three of the **K** joints (K1, K2, K3), first yield always occurred at the chord heel on both braces in experimental tests while in numerical tests it always occurred at the chord crown toe (at the gap) and at the chord crown heel of brace 1. This difference can be explained as follows.

In the experimental test specimen, the gap was filled with the welding deposite while in the numerical model the welding toe at the gap. Hence the thickness at the gap is increased in the experimental specimens which increased the area at that position and reduces the stress concentration.

Five of the experimental tests of the **K** joints had tearing failures. All numerical model had plastic collapse since the numerical model cannot deal with tearing. However, the ultimate load in numerical tests give reasonable results in comparison with the experimental tests. The differences between numerical ultimate loads and initial tearing failure in the experiments range between -7.9% and 11.5%. The differences of ultimate load from experimental result range between -8.7% and 7.2%. The average of ultimate load differences is -1.3%.

Generally, the numerical results for displacement of **Y** joints is reasonably good compared to the experiment results. Fig. 6.16 shows the deformation of **Y** joints under inplane bending. Like most other numerical tests, the first yield load is higher than the first yield load in the experimental test. This problem will be discussed later. The first yield position in numerical model Y3 has the same location as specimen Y3. Other first yield position in experimental tests were not reported and they were assumed to have the same location as specimen Y3 by Wimpey. However, it was found that one of the numerical models (Y5) gives a different location for the first yield.

All of the experimental Y joint tests displayed crack failure. The numerical model demonstrated plastic failure. However, the differences between the ultimate load in numerical tests and formation of the initial crack range between -6.3% and 7.8% (see Table 6.5). Compared to the ultimate load of experimental tests, the numerical ultimate load give a reasonable range between -6.3% and 5.7%. The average difference in ultimate load is 0.5%.

Almost all of the first yield points in the numerical models are higher than those in experimental specimens. Two explanations can be given for this fact. The first is that in the numerical method, the actual load that causes the first yield will fall between two load steps. The lower load step does not yet cause first yield, but the next load step will have to overshoot it, and this could be the first time that the program detects the first yield. This problem can be solved approximately by using small increment load steps, but this needs a large computer CPU time.

In the numerical analysis, the point where the stress is calculated does not lie on the surface of the shell. Because of this, a higher load is needed to reach first yield. This problem can be avoided by using multilayer elements. However it will increase computer time and requires a larger memory.

The second point is an experimental one. The residual stress due to fabrication causes the first yield load to occur earlier than when there are no such stresses. However, the differences between experimental and numerical tests generally are not large.

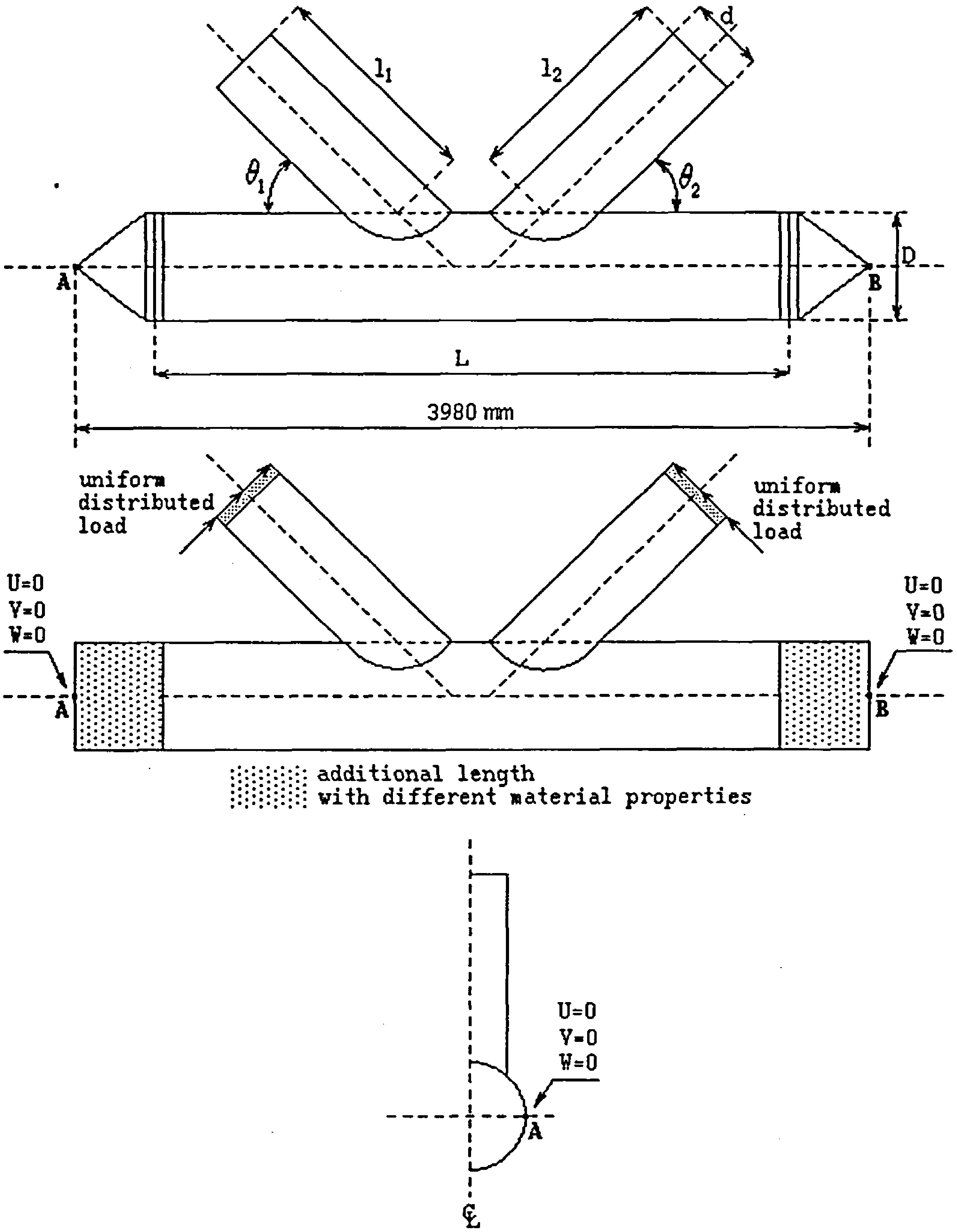

Figure 6.11 : Simplification of K joint specimen

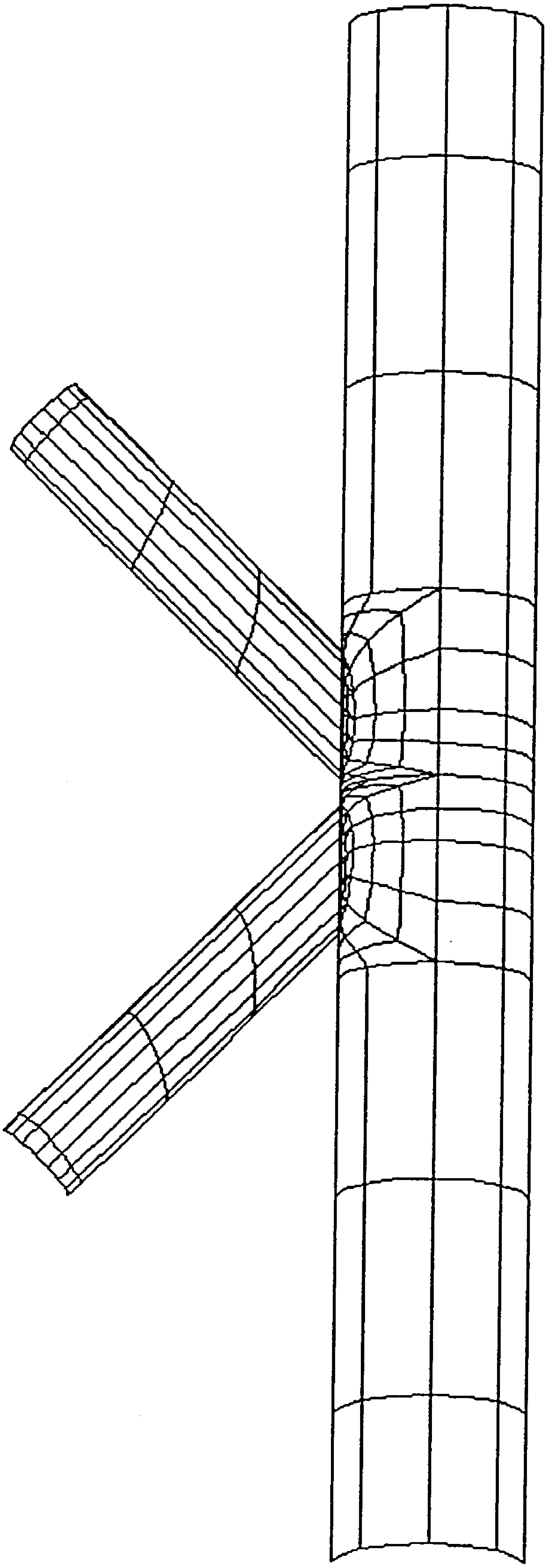

Figure 6.12a K joint mesh with total of 184 elements

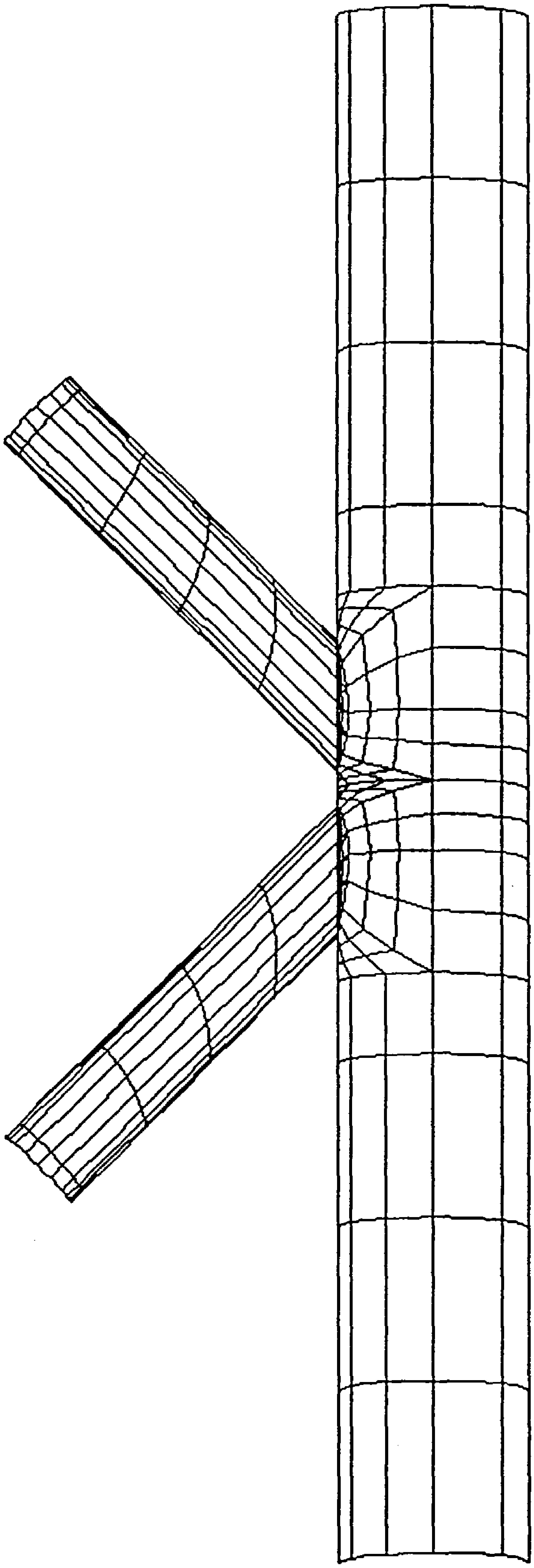

Figure 6.12b K joint mesh with the total of 268 elements

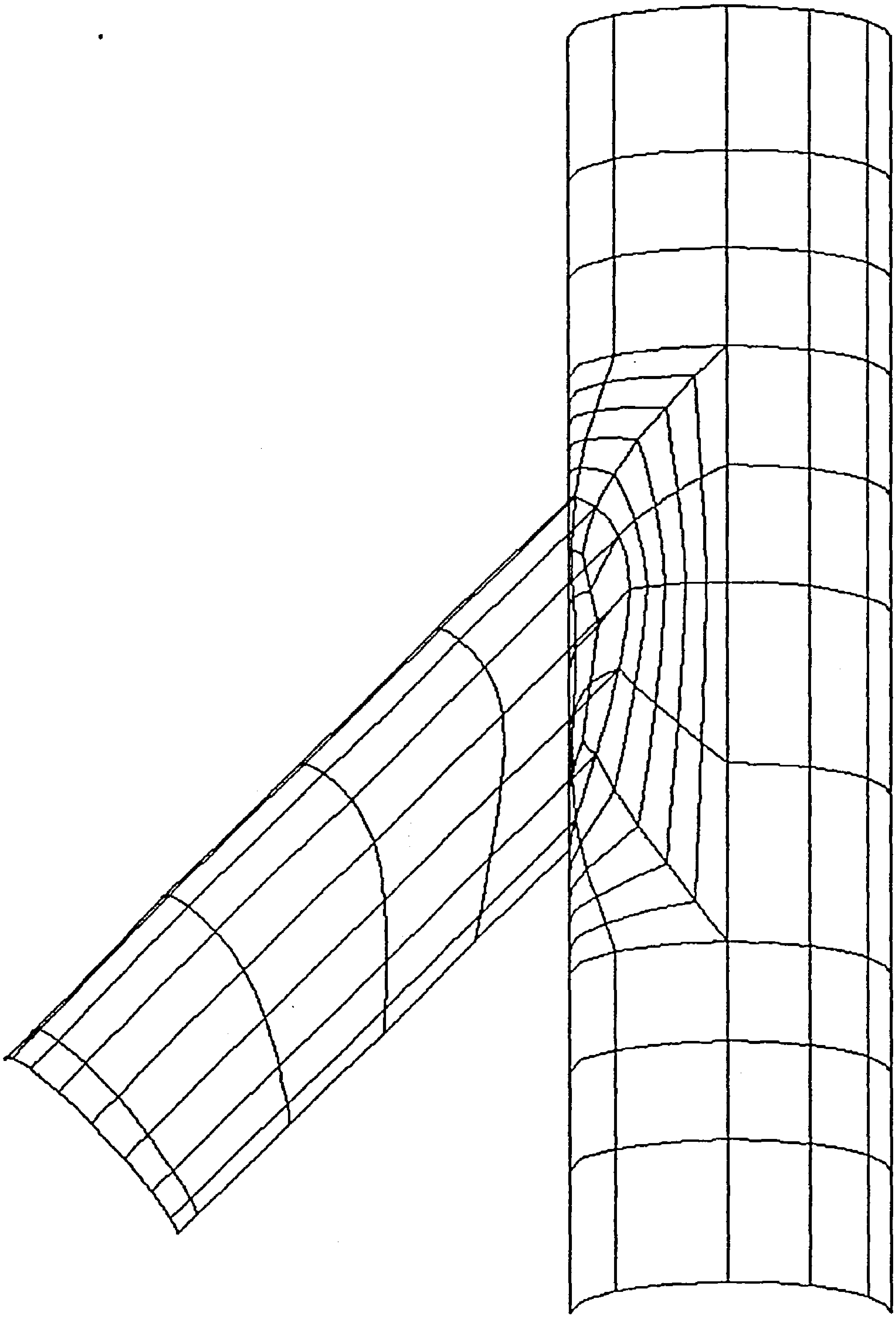

Figure 6.13 Y joint mesh.

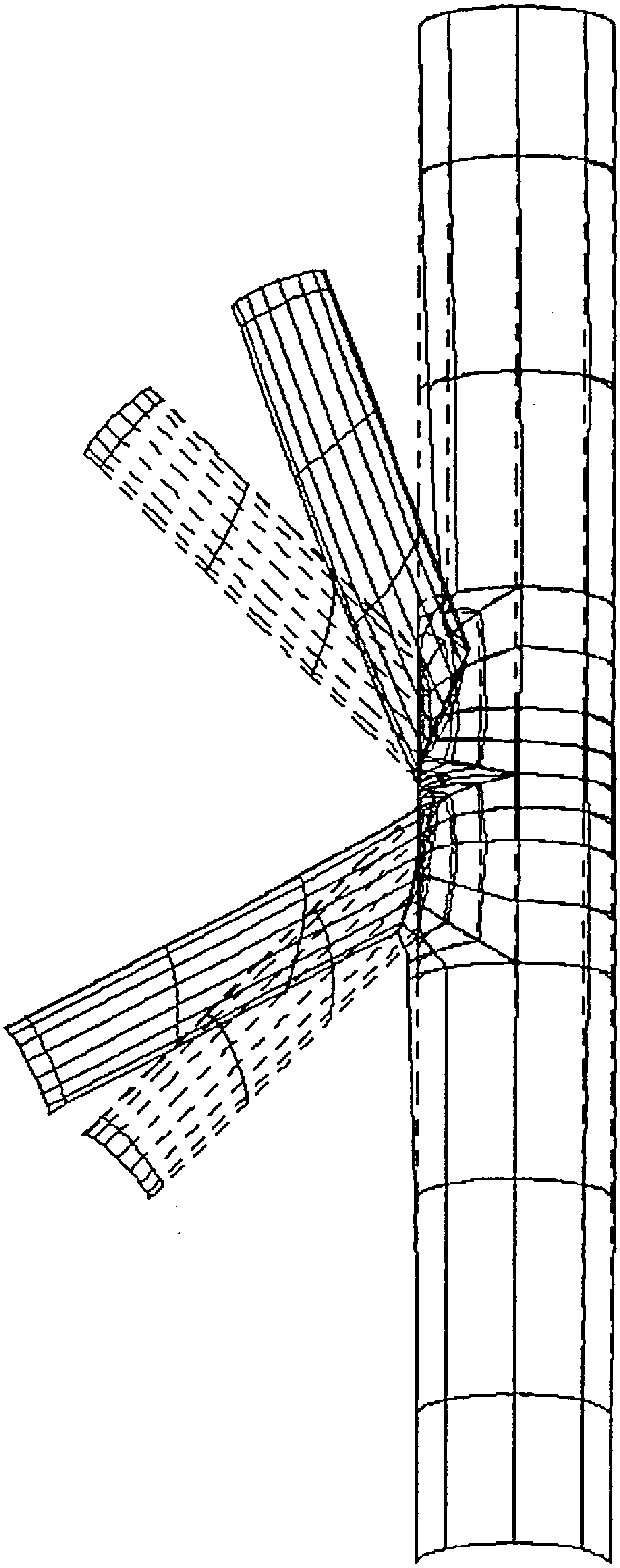

Figure 6.14 Deformation of K Joint at Ultimate load (model K2).
(brace load same sense and deformation magnification factor = 5)

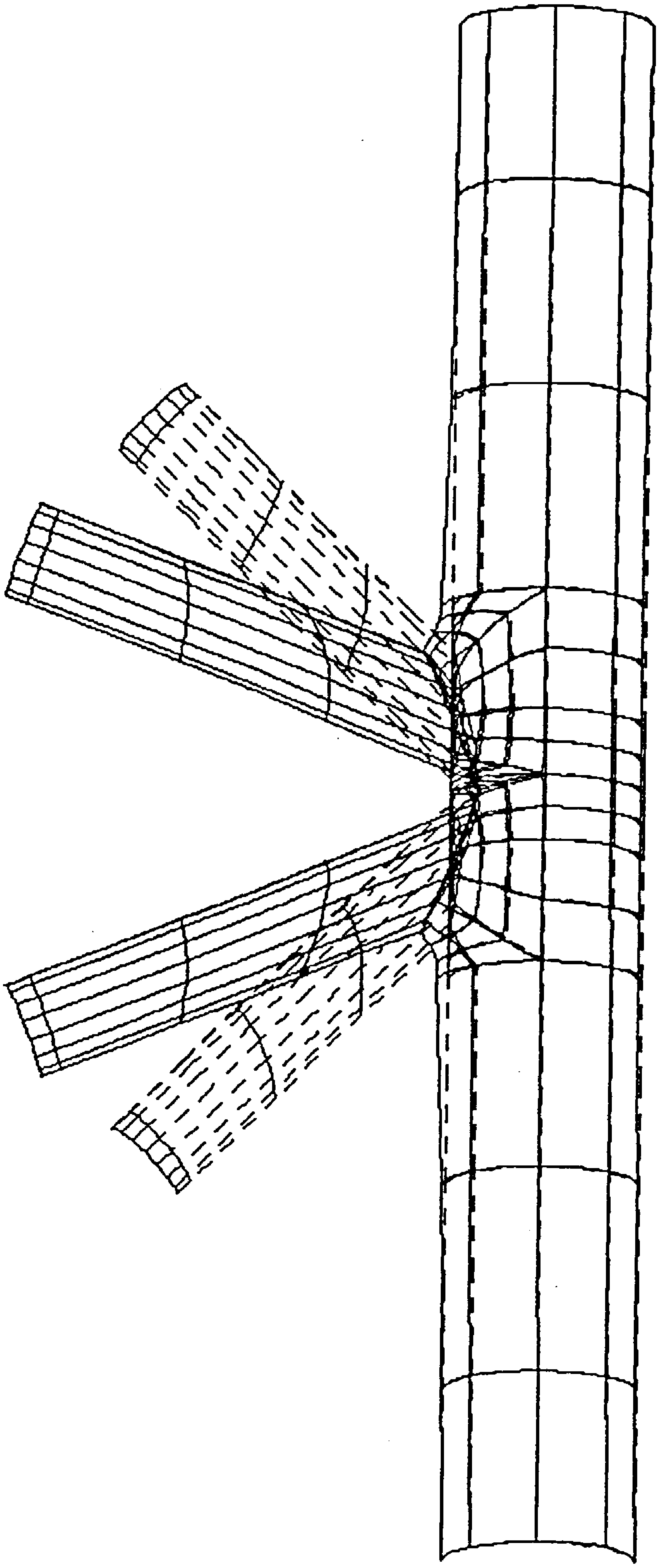

Figure 6.15 Deformation of K joint at Ultimate load (model K4).
(brace load opposite sense and deformation magnification factor = 5)

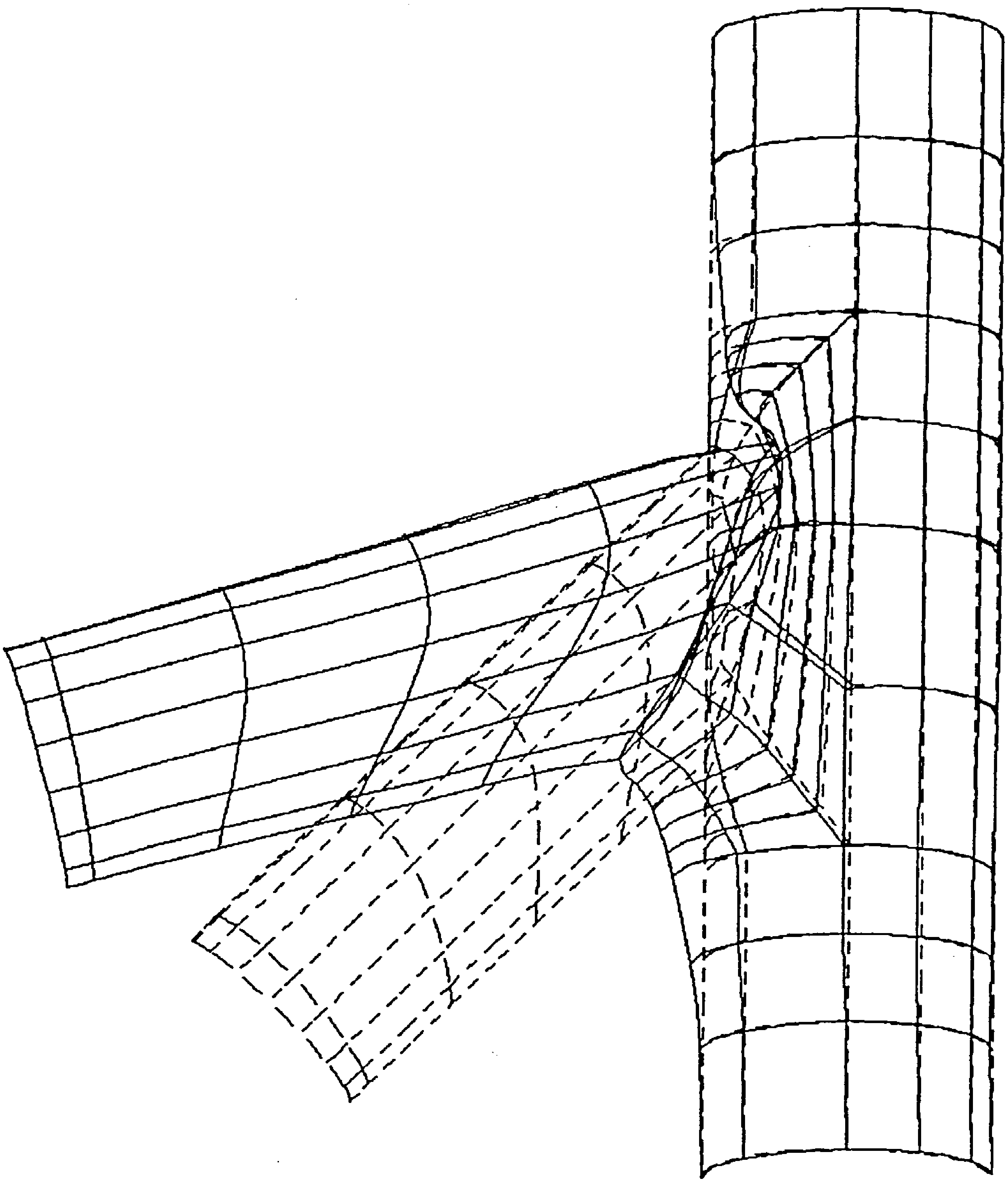

Figure 6.16 Deformation of Y joint at ultimate load.
(deformation magnification factor = 5)

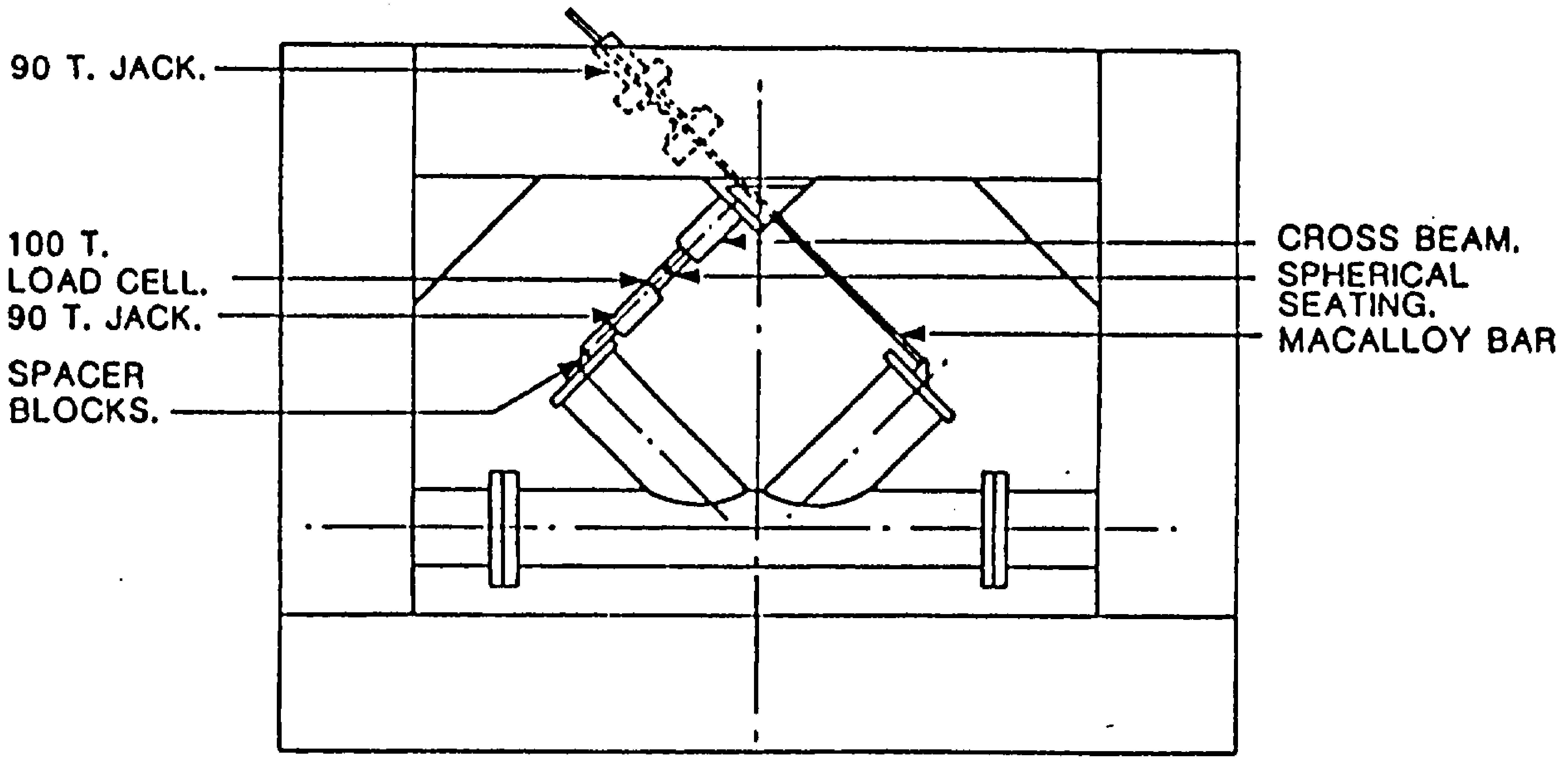

Figure 6.17 : Test arrangement for K joint with in-plane bending moment.

brace load same sense

Chapter VII

Conclusion and Proposal

This study can be divided into three main parts, which are first, the development of shell elastic analysis, and second the development to nonlinear analysis with the solution procedure incorporating automatic incremental load and iterative strategies such as the arc length method. The third part is the application of nonlinear shell finite elements to the analysis of the ultimate load behaviour of tubular joints and a comparison with experimental results. The following summary and conclusions are presented.

7.1 Conclusion

7.1.1 Shell Finite Element

The degeneration concept in shell finite element analysis, coupled with reduced integration technique, produces a shell element which performs accurately in both thick and thin shell situations. Numerical examples show that bending and membrane modes are modelled well. In comparison to the results of other workers, the rate of convergence of the present shell element is excellent. The application of implicit thickness integration is suitable for layer analysis and avoids over straining especially when the element has different material properties which always occurs in material nonlinear analyses.

The application of the updated Lagrangian approach in geometric nonlinearity, produces a geometry nonlinear of shell of reasonable accuracy. Numerical examples in section 4.6 demonstrate that the convergence rate of this nonlinear shell is reasonably good. Coupled with material nonlinear analysis, this shell has advantages due to the number of layers that can be adopted to analyse the stress through the thickness. Combined with automatic incremental load and an iterative solution strategy such as the arc length method, the present nonlinear shell finite element can pass through the maximum point load without any difficulties in some cases studies. analysis.

7.1.2 Ultimate Load of Tubular Joint

A wide range of tubular joints has been analysed using the present shell finite element. The comparison of the experimental and numerical results demonstrates the following. First, the finite element program can predict the ultimate strength of a wide range of offshore tubular joint with a surprisingly high level accuracy. The differences between numerical and experimental ultimate load predictions are of a size typical of the variations in a series of experiment results. The differences are perhaps less than one would expect from the influence of residual stress and imperfections in physical models and prototypes. Most of the load displacement curve predictions are reasonably good compared to the experimental results. There is no significant effect of weld profile elements on the ultimate load of tubular joints, but the stiffness of the numerical model increases by using the weld profile elements and ignoring the weld profile is therefore generally conservative. It can be concluded that the finite element method is a suitable tool for predicting the ultimate strength of such joints and can be used by engineers with some confidence.

7.2 Proposal for Future Works

7.2.1 Shell Finite Element

There is an obvious need for a continuation of research in shell finite elements as well as investigating further their application. Thus, the following future work is outlined as a natural extension of the present study.

In developing the capability for handling geometric nonlinearity, the geometric equation should be modified for large rotation analysis. This can be done by slightly modifying the definition of second term on the right hand side of equation

2.9, representing the linear rotation, to nonlinear rotation. This modification can be seen in references by to Hughes [1981], Milford [1989], and Crisfield [1991].

To obtain more accurate results for material nonlinearity, two problems should be considered. First, the method of crossing the yield surface, an approximate linear interpolation in the present study, should be modified due to the nonlinearity of the yield surface. The nonlinear method, proposed by Bicanic [1988], can be adopted and as a result an accurate value of the crossing point can be obtained. Secondly, the standard predictor 'forward Euler procedure' to return to the yield surface, which is adopted in present study, will give an accumalation error in incremental procedures if the stress and strain increments are not sufficient small [Crisfield 1991]. This procedure can be replaced by the backward Euler procedure which uses the normal at the elastic trial point and is more accurate.

7.2.2 Ultimate Strength of Tubular Joints

Large research programmes have generated a significant number of test data on the ultimate strength of tubular joints. These data have been used in various design codes such as API RP2A, DEn, AWS to develop design recommendations. However, some areas need futher investigation. A feasibility study by Lalani [1987], using the AWS, DEn, and API RP2A codes give significant differences of predicted ultimate load T joint for a β ratio ≥ 0.6. Parametric study is necessary in this area as well as for other regular configurations.

Futher research is also needed to investigate the effect of loading at the chord. Some experiments have been done by Wimpey [1989] for ultimate strength. However there has been no parametric study concerning the above problem, probably, because there is not enough data for such a parametric study. Design codes also give conflicting guidance on complex tubular joints. One of the reasons is lack of data to interpret the behaviour of complex tubular joints.

Nonlinear finite element analysis has been shown to provide good correlation with experimental tests. With decreasing computing cost and the advent of improved finite elements, the nonlinear finite element can be used to generate reasonable data to interpret the behaviour of any configuration of tubular joint.

References

Ahmad, S., Irons, B. M., & Zienkiewicz, O. C., 'Analysys of Thick and Thin Shell Structures by Curved Finite Elements', *Int. J. Num. Meth. Eng.*, **2**, 419-451, 1970

Anon., 'Depth Record Rises by 100m as Bullwinkle Goes in', *Offshore Engineer*, June, 16-18, 1988

Ashwell, D. G. & Sabir, A. B., 'A New Cylindrical Shell Finite Element Based on Simple Independent Strain Functions', *Int. J. Mech. Sci.*, **14**, 171-183, 1972

Baba, S. *et al.*, 'Numerical Evaluation of Stiffening Effect of Tubular Joints', *Trans. ASCE J. Struct. Eng.*, **110**, 316-327, 1984

Bathe, K. J. & Bolourchi, S., 'A Geometrical Material Nonlinear Plate and Shell Element', *Comp. & Struct.*, **11**, 23-48, 1980

Bathe, K. J. & Ho, L. W., 'A Simple and Effective Element for Analysis of General Shell Structures', *Comp. Struct.*, **13**, 1981

Bathe, K. J., *'Finite Element Procedures in Engeering Analysis'*, Prentice-Hall Inc., 1982

Belytschko, T., Stolarski, H., Liu, W. K., Carpenter, N. & Ong, J. S. J., 'Stress Projection for Membrane and Shear Locking in Shell Finite Elemnts', *Comp. Meth. Appl. Mech. Eng.*, **51**, 221-258, 1985

Belytschko, T. & Wong, B. L., 'Assumed Strain Stabilization Procedure for the 9-Node Lagrange Shell Element', *Int. J. Num. Meth. Eng.*, **28**, 385-4141, 1989

Belytschko, T., Ong, J. S., Liu, W. K. & Kennedy, J. M., 'Hourglass Control in Linear and Nonlinear Problems', *Comp. Meth. Appl. Mech. Eng.*, **43**, 251-276, 1984

Bergan, P. G. & Clough, R. W., 'Convergence Criteria for Iterative Processes', *AIAA Journal*, **10**, 1972

Bergan, P. G., Horrigmoe, G., Kråkeland, B. & Søreidas, T. H., 'Solution Techniques For Nonlinear Finite Element Problems', *Int. J. Num. Meth. Eng.*, **12**, 1677-1696, 1978

Bergan, P. G., 'Automated Incremental-Iterative Solution Methods in Structural Mechanics', *Recent Advances in Non-linear Computational Mechanics*, Ed. E. Hinton, D. R. J. Owen & C. Taylor, Pineredge Press, Swansea, U.K., 1982

Bettess, P. & Bettess, J. A., 'A Profile Matrix Solver with Built-in Constraint Facility', *Eng. Comput.*, 209-216, **3**, 1986

Bettess, P., 'Offshore Synthesis', *MSc Course, Dept. Marine Tech. University of Newcastle Upon Tyne*, 1989

Bicanic, N. P., 'Exact Evaluation of Contact Stress State in Computational Elasto-Plasticity', *Eng. Comp.*, **6**, 67-73, 1989

British Petroleum Statistical Review, London, 1988

Burdekin, F. M. and Frodin, J. G., 'Ultimate Failure of Tubular Connections', *Marinetech Northwest Report, University of Manchester Institute of Science and Technology*, November, 1987

Burgoyne, C. J. & Crisfield, M. A., 'Numerical Integration Strategy for Plates and Shells',*Int. J. Num. Meth. Eng.*, **29**, 105-121, 1990

Carmalt, S. W. & John, B. St., 'Giant Oil and Gas Field', *Future Petroleum Province of The World*, Ed. M . T. Halbouty, American Association of Petroleum Geologist, Tulsa, Oklahoma, USA, 1986

Cantin, G., 'Rigid Body Motions in Curved Finite Elements', *AIAA Journal*, **8**, 1252-1255, 1970

Chapman, R. E., '*Petroleum Geology*', Elsevier Science Publisher, 1982

Chang, T. Y., Saleb, A. F. & Graf, W., 'On the Mixed Formulation of a 9-Node Lagrange Shell Element', *Comp. Meth. Appl. Mech. Eng.*, **73**, 259-281, 1989

Chen, W. F. & Han, D. J., *'Plasticity for Structural Engineers'*, Springer-Verlag, 1988

Cofer, W. F. & Will, K. M., 'An Analytical Method for Ultimate Strength Evaluation of Tubular Joints', Proc. 9th Int. Conf. Off. Mech. and Arctic Eng.', **3**, 1990

Cook, R. D., *'Concepts and Applications of Finite Element Analysis'*, 2nd edition, John Wiley & Sons, 1981

Cormeau, I., 'Elastoplastic Thick Shell Analysis by Viscoplastic Solid Finite Elements', *Int. J. Num. Meth. Eng.*, **12**, 203-227, 1978

Crisfield, M. A., 'A Fast Incremental / Iterative Solution Procedure That Handles "Snap-Through" ', *Comp. & Struct.*, **13**, 55-62, 1981

Crisfield, M. A., 'Variable Step Lengths For Non-linear Structural Analysis',*TRRL Report 1049, Transport & Road Res. Lab.*, Crowthorne, Berks., UK, 1982

Crisfield, M. A., 'Criteria for a Reliable Non-linear Finite Element System', *Reali-bility Methods for Engineering Analysis*, Ed. K. J. Bathe *et al.*, Pineridge Swansea, 159-179, 1986

Crisfield, M. A., 'Explicit Integration and Isoparametric Arch and Shell Elements', *Comm. Appl. Num. Meth.*, 2, 181-187, 1986

Crisfield, M. A., *'Non-linear Finite Element Analysis of Solids and Structures'*, Vol.1, John Wiley & Sons, 1991

Dupuis, G. A., Hibbit, H. D., McNamara, S. F. & Marcal, P. V., 'Nonlinear Material and Geometric Behaviour of Shell Structures', *Comp. Struct.*, 1, 223-239, 1971

Ebecken, N. F. F. *et al.*, 'Analysis of the Static Strength of Tubular Joints', Numerical Method for Nonlinear Problems, Ed., C. Taylor *et al.*, Pineridge Press, 421-431, 1984

Ebecken, N. F. F. & Ferrante, A. J., 'Elastoplastic Analysis of Tubular Joints of Offshore Platforms', *Adv. Eng. Software*, 9, 1987

Gerwick, B. C., *'Construction of Offshore Structure', John Wiley & Sons*, 1986

Gibstein, M. B., 'Parametrical Stress Analysis of T Joints', *Paper 26, European Offshore Steel Research Seminar, Cambridge, U.K.*, 1978

Gibstein, M. B., and Moe, E. T., 'Numerical and Experimental Analysis of Tubular Joints with Inclined Braces', Paper TS6.3, Steel in Marine Structures, Paris, 1981

Graff, W. J., 'Introduction to Offshore Structures', *Gulf Publishing Company*, 1981

Halbouty, M. T., 'Basins and New Frontiers: An Overview',*Future Petroleum Province of The World*, Ed. M.T. Halbouty, American Association of Petroleum Geologist, Tulsa, Oklahoma, USA, 1986

Hibbit, H. D., Marcal, P. V. & Rice, J. R., 'A Finite Element Formulation For Problems of Large Strain and Large Displacement', *Int. J. Solid Struct.*, 6, 1069-1086, 1970

Hinton, E. & Owen, D. R. J, *'Finite Elements in Plasticity - Theory and Practice'*, Pineridge Press, Swansea, 1980

Hinton, E. & Owen, D. R. J, *'Finite Element Software for Plates and Shells'*, Pineridge Press, Swansea, 1984

Hoffman, E. *et al.*, 'Accuracy of Different Finite Element Types Analysis of Complex, Welded Tubular Joints', *Offshore Technology Conference*, May, 1980

Huang, H. C. & Hinton, E., 'A New Ninie Node Degenerated Shell Element with Enhanced Shear Interpolation', *Int. J. Num. Meth. Eng.*, **22**, 73-92, 1986

Hughes, T. J. R. & Liu, W. K., 'Nonlinear Finite Element of Shells: Part I. Three Dimensional Shells', *Comp. Meth. Appl. Mech. Eng.*, **26**, 331-362, 1981

Irving, D. J., 'Large Deformation Elasto-Plastic Finite Element Analysis of Plates, Shells, and Tubular joints Using Semiloof Shell Element', *PhD Thesis, Kingston Polytechnic, U.K.* 1982

Kanock-Nukulchai, W., 'A Simple and Efficient Finite Element for General Shell Analysis', *Int. J. Num. Meth. Eng.*, **14**, 179-200, 1979

Kardestuncer, H. *et al.*, *'Finite Element Handbook'*, McGraw-Hill, 1987

Kreyszig, E., *'Advanced Engineering Mathematics'*, 6th edition, John Wiley & Sons, 1988

Kuang, J. G., Potvin, A. B. & Leich, R. D., 'Stress Concentration in Tubular Joints', *Paper OTC 2205 of Offshore Technology Conference*, 1975

Lalani, M., 'Rationalisation of Design Practice for the Ultimate Limit State of Tubular Joints', *Paper 9, Integrity Offshore Structure Conference, Glasgow*, 1987

Lalani, M., Gholkar, S. F. and Ward, J. K., 'Recent Developments in the Ultimate Strength Assessment of Tubular Joints: A Nonlinear Numerical Treatment', *Paper OTC 6158 of Offshore Technology Conference*, 1989

Liaw, C. Y., Litton, R. W., & Reimer, R. B., 'Improved Finite Elements for Analysis of Welded Tubular joints', *Paper OTC 2642 od Offshore Technology Conference*, 1976

MacNeal, R. H. & Harder, R. L., 'A Proposed Standard Set of Problems to Test Finite Element Accuracy', *Finite Elements in Analysis and Design*, **1**, 3-20, 1985

Matthies, H. G., 'A Decomposition for the Integration of the Elasto-Plastic Rate Problem', *Int. J. Meth. Eng.*, **28**, 1-11, 1989

Meek, J. L. & Lognathan, S., 'Geometrically Non-linear Behaviour of Space Frame Structure', *Comp. & Struct.*, **31**, 35-45, 1989

Milford, R. V. & Schnobrich, W. C., 'Degenerated Isoparametric Finite Element Using Explicit Integration', *Int. J. Num. Meth. Eng.*, **23**, 133-154, 1986

Murray, J. C. & Gregory, J. H., 'A Study of Incremental Iterative Strategies for Non-linear Analysis', *Int. J. Num. Meth. Eng.*, **29**, 1365-1391, 1990

Nyssen, C., 'An Efficient and Accurate Iterative Method, Allowing Large Incremental Steps, To Solve Elasto-Plastic Problems', *Comp. & Struct.*, **13**, 63-71, 1981

Owen, D. R. J. & Figueiras, J. A., 'Elasto-Plastic Analysis of Anisotropic Plates and Shells by Semiloof Element', *Int. J. Num. Eng.*, **19**, 521-539, 1983

Ortiz, M. Popov, E. P., 'Accuracy and Stability of Integration Algorithms For Elastoplastic Constitutive Relations', *Int. J. Num. Meth. Eng.*, **21**, 1561-1576, 1985

Parisch, H., 'Large Displacement of Shells Including Material Nonlinearities', *Comp. Meth. Appl. Mech. Eng.*, **27**, 183-214, 1981

Riks, E., 'An Incremental Approach to the Solution of Snapping and Buckling Problems', *Int. J. Solid Struct.*, **15**, 529-551, 1979

Saleeb, A. F., Chang, T. Y., Graf, W. & Yingyeunyong, S., 'A Hybrid/Mixed Model for Non-linear Shell Analysis and Its Application to Large-Rotation Problems', *Int. J. Num. Meth. Eng.*, **29**, 407-446, 1990

Sloan, S. W., 'Substepping Schemes for the Numerical Integration of Elastoplastic Stress-Strain Relations', *Int. J. Num. Meth. Eng.*, **24**, 893-911, 1987

Stolarski, H. and Belytschko, T. 'Membrane Locking and Reduce Integration for Curved elements', *J. Appl. Mech.*, 49, 1982

Thompson, P. A., 'Stiffened Shell Elements: Development and Application to Perforated Structures', *PhD Thesis, University of Newcastle Upon Tyne*, 1989

Timoshenko, S. P. & Woinowsky-Krieger, S., *'Theory of Plates and Shells'*, McGraw-Hill, 1959

Tiratsou, E .N., *'Oilfields of the World'*, 3rd edition, Scientific Press Ltd, Beacons field, England, 1984

Van Der Valk, C. A. C., 'Factors Controlling the Static Strength of Tubular T-Joints', *BOSS'88 Conference*, **3**, 1988

Underwater Engineering Group (UEG), 'Design of Tubular Joints for Offshore Structures', *UR33*, 1985

Urm, H. S., 'Optimum Structural Design of Submersibles', *PhD Thesis, University of Newcastle Upon Tyne*, 1991

Visser, W., 'On the Structural Design of Tubular Joints', *Paper OTC 2117 of Offshore Technology Conference*, 1974

Ward, J. K., & Izzudin, B., 'Ultimate Limit State of Tubular Joints', *OTJ 88 Conference*, Surrey, 1988

Washizu, K., *'Variational Methods in Elasticity & Plasticity'*, 3rd edition, Pergamon Press., 1982

Wempner, G. A., 'Discrete Approximation Related to Nonlinear Theories of Solids', *Int. J. Solid Struct.*, **7**, 1581-1599, 1971

Wimpey Offshore, 'Static Strength of Large Scale Tubular Joints', *OTI 89543*, 1989

Yang, T. Y. & Saigal, S., 'A Curved Quadrilateral Element for Static Analysis of Shells with Geometric and Material Nonlinearities', *Int. J. Num. Meth. Eng.*, **21**, 617-635, 1985

Zienkiewicz, O. C., Taylor,R.L. & Too,J.M., 'Reduced Integration Technique in General Analysis of Plates and Shells', *Int. J. Num. Meth. Eng.*, **3**, 275-290, 1971

Zienkiewicz, O. C., *'The Finite Element Method'*, 3rd edition, McGraw-Hill, 1977

Zienkiewicz, O. C., *'The Finite Element Method'*, Vol. 1, 4th edition, McGraw-Hill, 1989

Zienkiewicz, O. C., *'The Finite Element Method'*, Vol. 2, 4th edition, McGraw-Hill, 1991

Appendix A

Simple Mesh Generator for Symmetric Tubular Joints

To analyse tubular joints using the finite element method, a mesh generator is needed. Structural symmetries are exploited to reduce the number of elements. Here, a tubular joint will be divided into several regions (see Fig.A.2). Then, each region will be divided into a number of elements.

As proposed by Zienkiewiecz [1977], blending functions will be used to generate the mesh in each region. The blending function will interpolate the unknown Φ so that it will exactly satisfy the variations along the edges of the ξ, η domain (see Fig.A.1). This method can be described as follows. Consider the plane curve in Fig. A.1a, for which boundary functions are given on each edge as $\Phi(-1,\eta), \Phi(1,\eta), \Phi(1,\xi), \Phi(-1,\xi)$. Using these boundary functions, the function $\Phi(\xi,\eta)$ will be interpolated linearly so that a smooth surface is produced. The linear interpolation functions can be written as follows :

$$\begin{aligned} N_1(\xi) &= (1+\xi)/2 \\ N_2(\xi) &= (1-\xi)/2 \\ N_1(\eta) &= (1+\eta)/2 \\ N_2(\eta) &= (1-\eta)/2 \end{aligned} \tag{A.1}$$

First, we interpolate the function in the η direction as follows (see Fig.A.1b) :

$$P_\eta \Phi \equiv N_2(\eta)\Phi(\xi,1) + N_1(\eta)\Phi(\xi,-1) \tag{A.2}$$

Similarly, we interpolate the function in the ξ direction as follows (see Fig.A.1c) :

$$P_\xi \Phi \equiv N_2(\xi)\Phi(\eta,1) + N_1(\xi)\Phi(\eta,-1) \tag{A.3}$$

Extending the interpolation to two dimensional Lagrangian interpolation, equation A.4 is obtained (see Fig.A.1d).

$$\begin{aligned} P_\eta P_\xi \Phi =& N_2(\eta)N_2(\xi)\Phi(-1,-1) + N_1(\xi)N_2(\eta)\Phi(1,-1) \\ &+ N_1(\xi)N_1(\eta)\Phi(1,1) + N_1(\eta)N_1(\xi)\Phi(-1,1) \end{aligned} \qquad (A.4)$$

Using eq.(A.2), (A.3) and (A.4), we can construct a smooth surface interpolating exactly the boundary function as :

$$\Phi = P_\eta \Phi + P_\xi \Phi - P_\eta P_\xi \Phi \qquad (A.5)$$

Using the above method, we can generate a mesh for each region of a tubular joint by giving the number of mesh subdivisions along each edge of the region. For a tubular joint, the subdivision will move from one side of the tubular to the opposite as shown in Fig.A.2 by arrow marks. For instance, in region 2, the number of subdivision comes from region 1 and region 3. Blending functions will now be applied to this region. The coordinate of a point at the top of brace can be determined in local coordinate system as follows (see Fig.A.2) :

$$\begin{aligned} x'_b &= r\cos\{\beta_5 - \frac{1}{2}(\xi - 1)(\beta_6 - \beta_5)\} \\ y'_b &= r\sin\{\beta_5 - \frac{1}{2}(\xi - 1)(\beta_6 - \beta_5)\} \\ z'_b &= oa \end{aligned} \qquad (A.6a)$$

where r is radius of brace and line oa' is the length of the brace axis measured from origin. This local coordinate should be transformed to a global coordinate as follows :

$$\begin{bmatrix} x_b \\ y_b \\ z_b \end{bmatrix} = [\theta] \begin{bmatrix} x' \\ y' \\ z' \end{bmatrix} \qquad (A.6b)$$

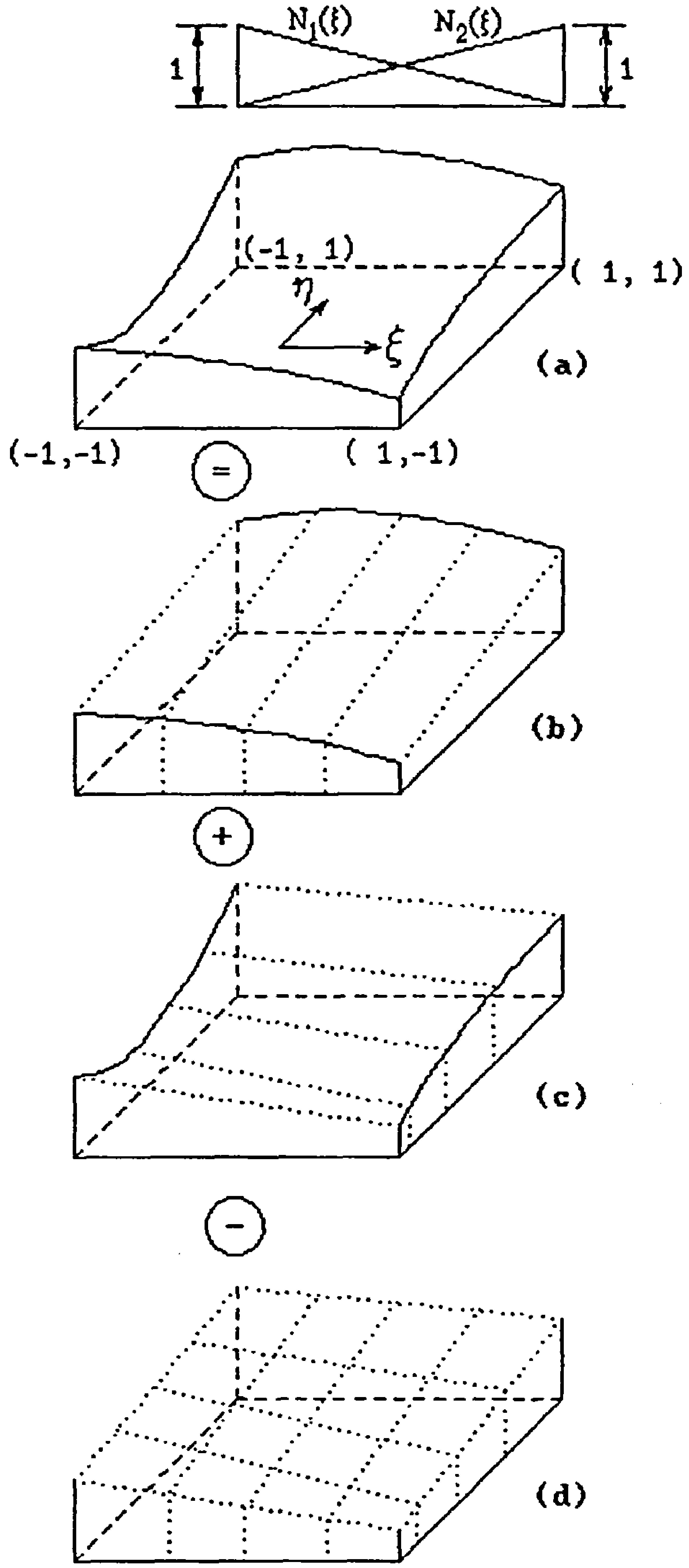

Figure A.1 Stages of construction of a blending interpolation [Zienkiewcz 1977] where θ is the transformation matrix from local to global coordinate systems. The coordinate of any point at the intersection can be calculated as follows. First, determine the equation of line l' as follows :

$$\begin{aligned} x &= x_o + (x_a - x_o)t \\ y &= y_o + (y_a - y_o)t \\ x &= x_o + (x_a - x_o)t \end{aligned} \tag{A.8}$$

where t is the slope of the line. The line through point b (x_b, y_b, x_b) and parallel to line l' can be defined as follows :

$$\begin{aligned} x &= x_b + (x_a - x_o)t \\ y &= y_b + (y_a - y_o)t \\ z &= z_b + (z_a - z_o)t \end{aligned} \tag{A.9}$$

and

$$t = \frac{z - z_b}{z_a - z_o} \tag{A.10}$$

Substituting eq.(A.10) into one of eq.(A.9), we obtain :

$$y = y_b + (y_a - y_o)\frac{z - z_b}{z_a - z_o} \tag{A.11}$$

The equation of the cylinder at any point with an axis x can be written as follows:

$$y^2 + z^2 = R^2 \tag{A.12}$$

The intersection of line l with this cylinder, say at point c, can be obtained by subtituting eq.(A.11) into eq (A.12) as follows,

$$y_b + (y_a - y_o)(\frac{z_c - z_b}{z_a - z_o})^2 + z_c^2 - R^2 = 0 \tag{A.13}$$

Rewriting equation (A.13), we obtain:

$$Az_c^2 + Bz_c + C = 0$$

where

$$A = 1 + (\frac{y_a r - y_o}{z_a - z_b})^2$$

$$B = 2y_b \frac{y_a - y_o}{z_a - z_o} - 2z_b(\frac{y_a - y_o}{z_a - z_o})^2$$

$$C = y_b^2 - 2y_b z_b y_a - y_o \; z_a - z_o + z_b^2(y_a - y_o \; z_a - z_o)^2 - R^2$$

and

$$z_c = \frac{-B \pm \sqrt{B^2 - 4AC}}{2A} \qquad (A.14)$$

z_c is chosen to always have positive value. Using equation (A.14), (A.12) and (A.9) we obtain :

$$y_c = \sqrt{R^2 - z_c^2} \qquad (A.15)$$

and

$$x_c = x_b + (x_a - x_1)\frac{z_c - z_b}{z_a - z_1} \qquad (A.16)$$

The boundary function for each edge of region 2 can be written as follows :

$$\Phi(\xi, 1) = \begin{bmatrix} x_c \\ y_c \\ z_c \end{bmatrix}$$

$$\Phi(\xi, -1) = \begin{bmatrix} x_2 - \frac{1}{2}(\xi - 1)(x_2 - x_1) \\ y_1 \\ z_1 \end{bmatrix}$$

$$\Phi(1, \eta) = \begin{bmatrix} x_2 - \frac{1}{2}(1 - \eta)(x_3 - x_2) \\ R\cos\{\alpha_2 - \frac{1}{2}(1 - \eta)(\alpha_3 - \alpha_2)\} \\ R\sin\{\alpha_2 - \frac{1}{2}(1 - \eta)(\alpha_3 - \alpha_2)\} \end{bmatrix}$$

$$\Phi(-1,\eta) = \begin{bmatrix} x_1 \\ R\cos\{\alpha_1 - \frac{1}{2}(1-\eta)(\alpha_4-\alpha_1)\} \\ R\sin\{\alpha_1 - \frac{1}{2}(1-\eta)(\alpha_4-\alpha_1)\} \end{bmatrix} \quad (A.17)$$

The coordinates of corner nodes can be written as follows :

$$\Phi(-1,-1) = \begin{bmatrix} x_1 \\ y_1 \\ z_1 \end{bmatrix} \qquad \Phi(-1,1) = \begin{bmatrix} x_2 \\ y_2 \\ z_2 \end{bmatrix}$$

$$\Phi(1,1) = \begin{bmatrix} x_3 \\ y_3 \\ z_3 \end{bmatrix} \qquad \Phi(-1,-1) = \begin{bmatrix} x_4 \\ y_4 \\ z_4 \end{bmatrix} \quad (A.18)$$

On rewriting the blending functions in more detail we have

$$\begin{aligned}
\Phi(\xi,\eta) =& P_\eta\Phi + \Phi_\xi\Phi - P_\eta P_\xi\Phi \\
\Phi(\xi,\eta) =& N_1(\eta)\Phi(\xi,1) + N_2(\eta)\Phi(\xi,-1)N_1(\xi)\Phi(1,\eta) + N_2(\xi)\Phi(-1,\eta) \\
& \{N_2(\eta)N_2(\xi)\Phi(-1,-1) + N_1(xi)N_2(\eta)\Phi(1,-1)+ \\
& N_1(\xi)N_1(\eta)\Phi(1,1) + N_1(\eta)N_2(\xi)\Phi(-1,1)\} \\
\Phi(\xi,\eta) =& \frac{1}{2}(1+\eta)\Phi(\xi,1) + \frac{1}{2}(1-\eta)\Phi(\xi,-1)+ \\
& \frac{1}{2}(1+\xi)\Phi(1,\eta) + \frac{1}{2}(1-\xi)\Phi(-1,\eta) \\
& -\{\frac{1}{4}(1-\xi)(1-\eta)\Phi(-1,-1) + \frac{1}{4}(1+\xi)(1-\eta)\Phi(1,-1)\Phi(1,-1)+ \\
& \frac{1}{4}(1+\xi)(1+\eta)\Phi(1,1) + \frac{1}{4}(1+\eta)(1-\xi)\Phi(-1,1)\}
\end{aligned}$$

$$(A.19)$$

On substituting equation (A.17) and (A.18) into equation (A.19), we obtain the blending function of region 2 (see eq.A.20). By using equation (A.20) we can determine the coordinate of any point in region 2. Similarly, the blending function of other region can be defined by subtituting their boundary functions and corner values into equation (A.19). Some results in the use of this method are presented in Fig.A.3-5.

$$\begin{aligned}
\Phi(\xi,\eta) = \begin{bmatrix}\Phi_x\\ \Phi_y\\ \Phi_z\end{bmatrix} = {} & \frac{1}{2}(1+\eta)\begin{bmatrix}x_c\\ y_c\\ z_c\end{bmatrix} + \frac{1}{2}(1-\eta)\begin{bmatrix}x_2 - \frac{1}{2}(\xi-1)(x_2-x_1)\\ y_1\\ z_1\end{bmatrix} + \\
& \frac{1}{2}(1+\xi)\begin{bmatrix}x_2 - \frac{1}{2}(1-\eta)(x_3-x_2)\\ R\cos\{\alpha_2 - \frac{1}{2}(1-\eta)(\alpha_3-\alpha_2)\}\\ R\sin\{\alpha_2 - \frac{1}{2}(1-\eta)(\alpha_3-\alpha_2)\}\end{bmatrix} + \\
& \frac{1}{2}(1-\xi)\begin{bmatrix}x_1\\ R\cos\{\alpha_1 - \frac{1}{2}(1-\eta)(\alpha_4-\alpha_1)\}\\ R\sin\{\alpha_1 - \frac{1}{2}(1-\eta)(\alpha_4-\alpha_1)\}\end{bmatrix} - \\
& \frac{1}{4}(1-\eta)(1-\xi)\begin{bmatrix}x_1\\ y_1\\ z_1\end{bmatrix} - \frac{1}{4}(1+\xi)(1-\eta)\begin{bmatrix}x_2\\ y_2\\ z_2\end{bmatrix} - \\
& \frac{1}{4}(1+\xi)(1+\eta)\begin{bmatrix}x_3\\ y_3\\ z_3\end{bmatrix} - \frac{1}{4}(1+\eta)(1-\xi)\begin{bmatrix}x_4\\ y_4\\ z_4\end{bmatrix}
\end{aligned} \qquad (A.20)$$

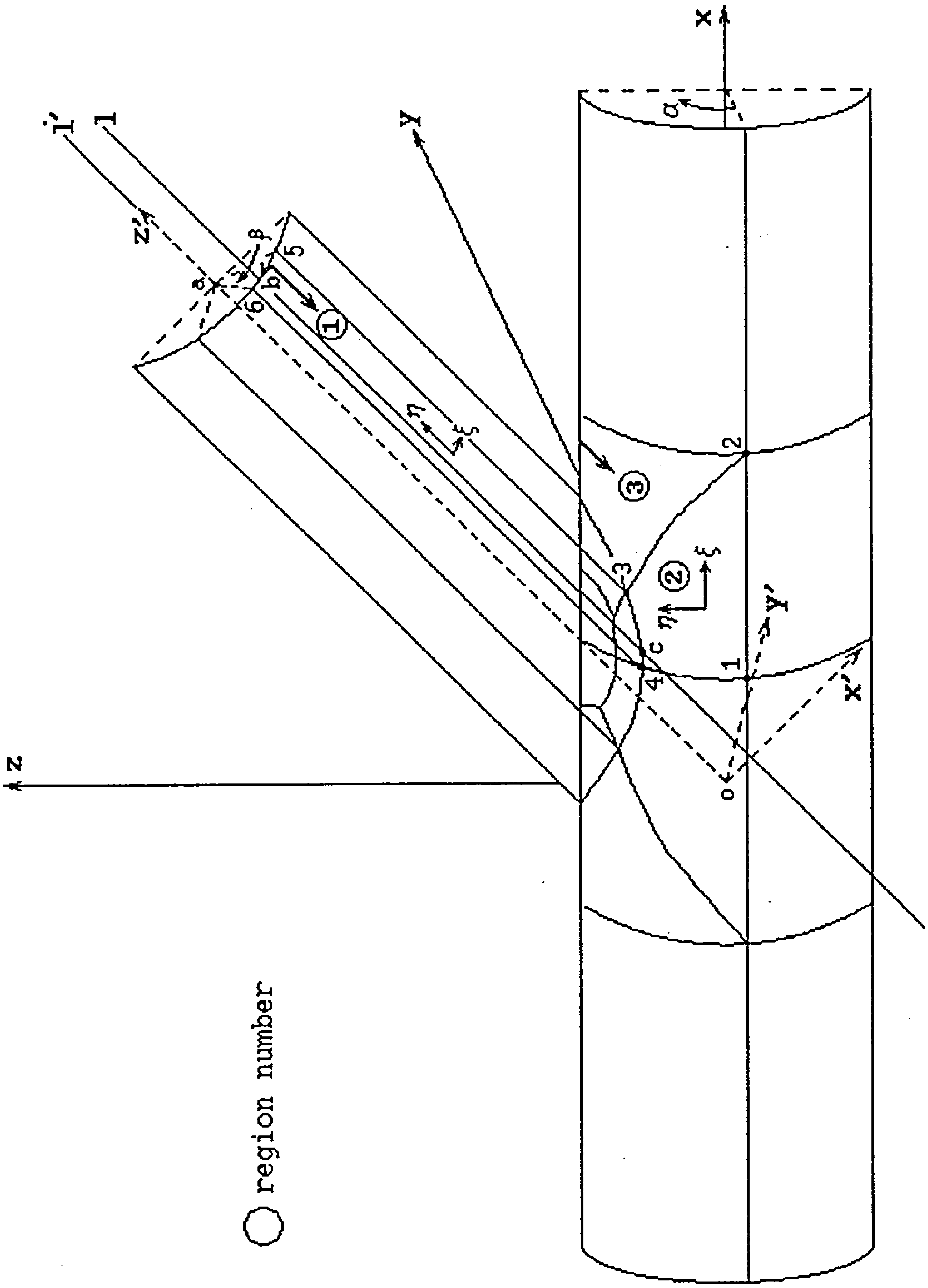

Figure A.2 : Division of Y joint

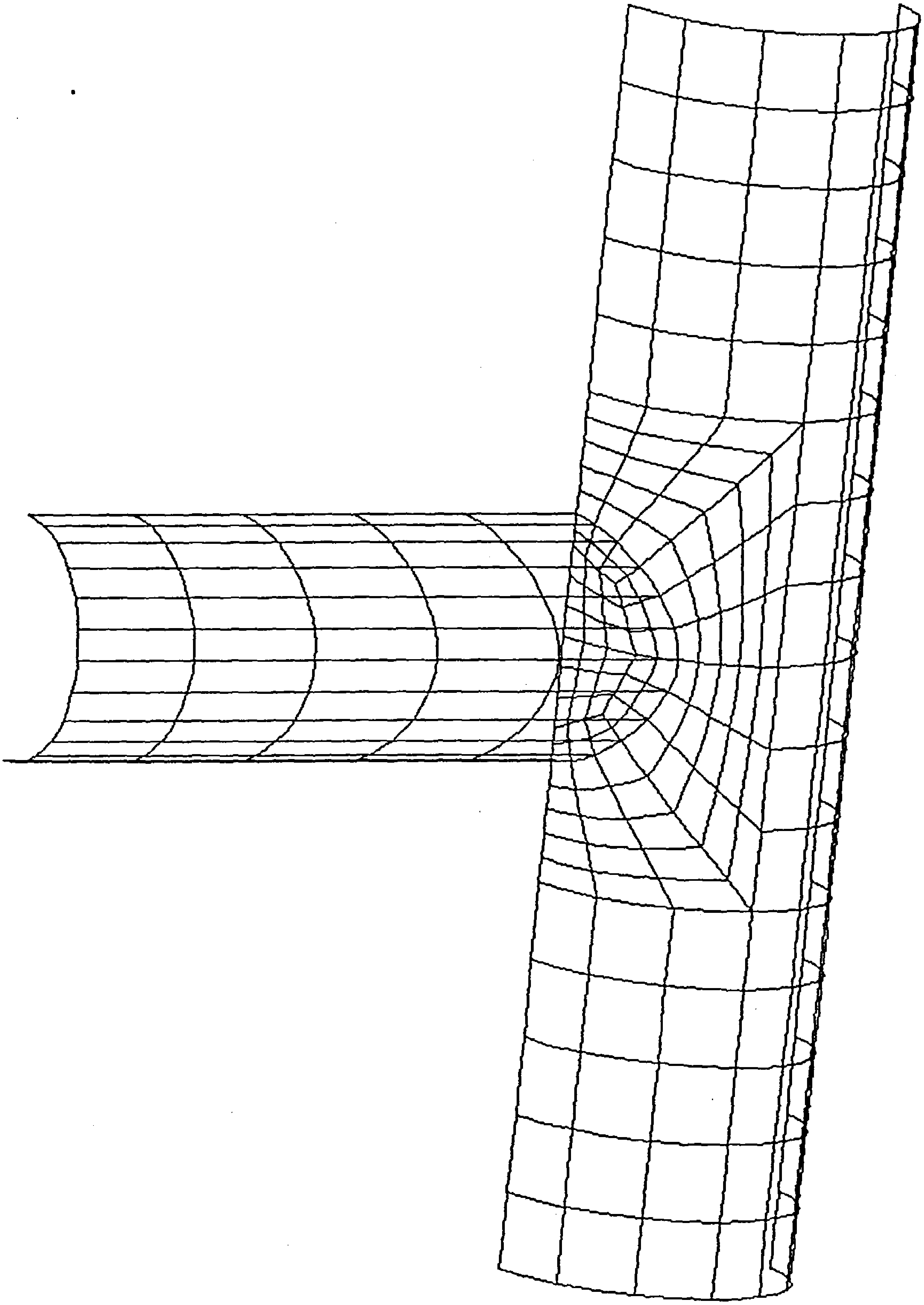

Figure A.3 : Application to blending interpolation at T joint

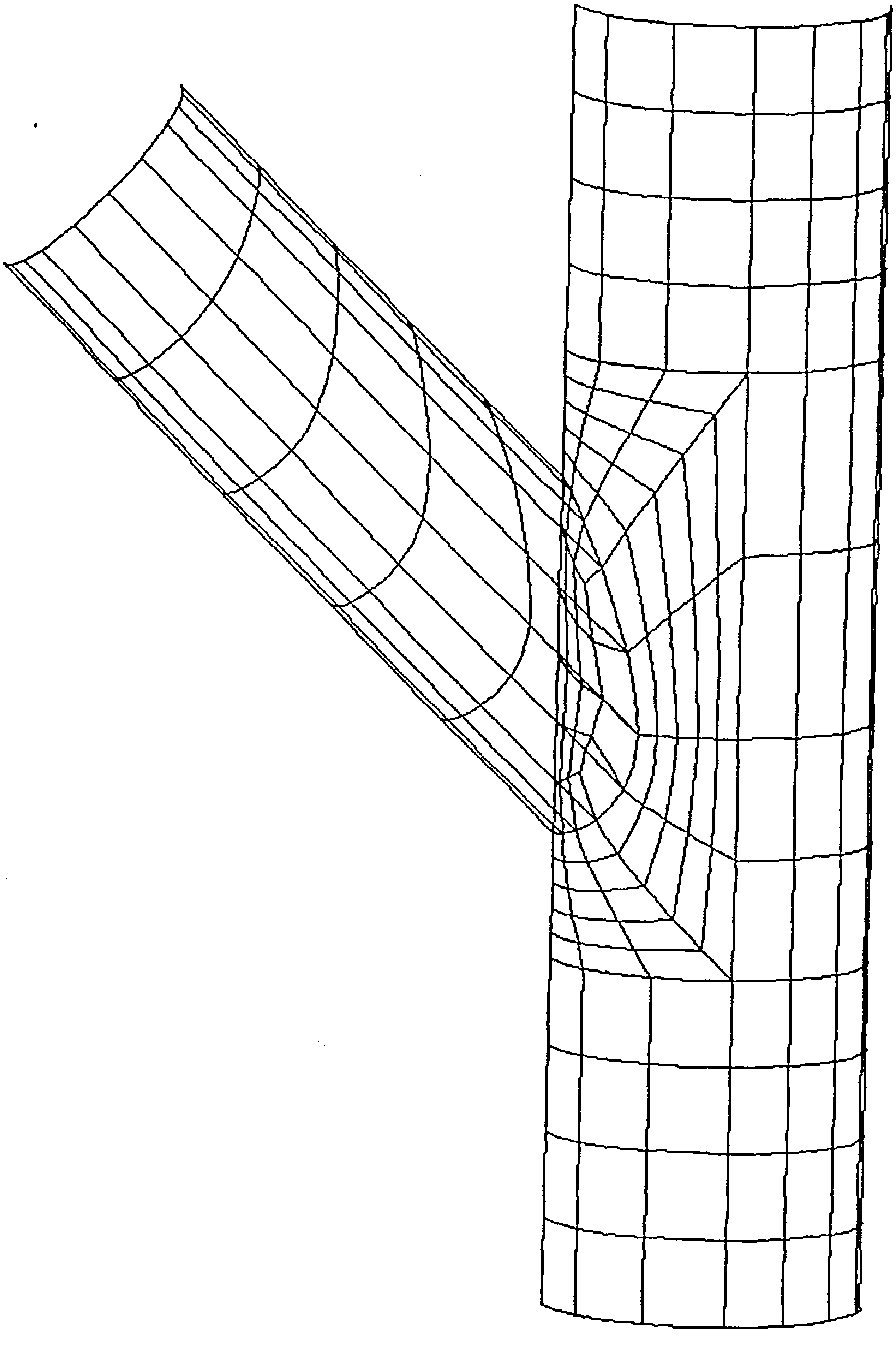

Figure A.4 : Application to blending interpolation at Y joint

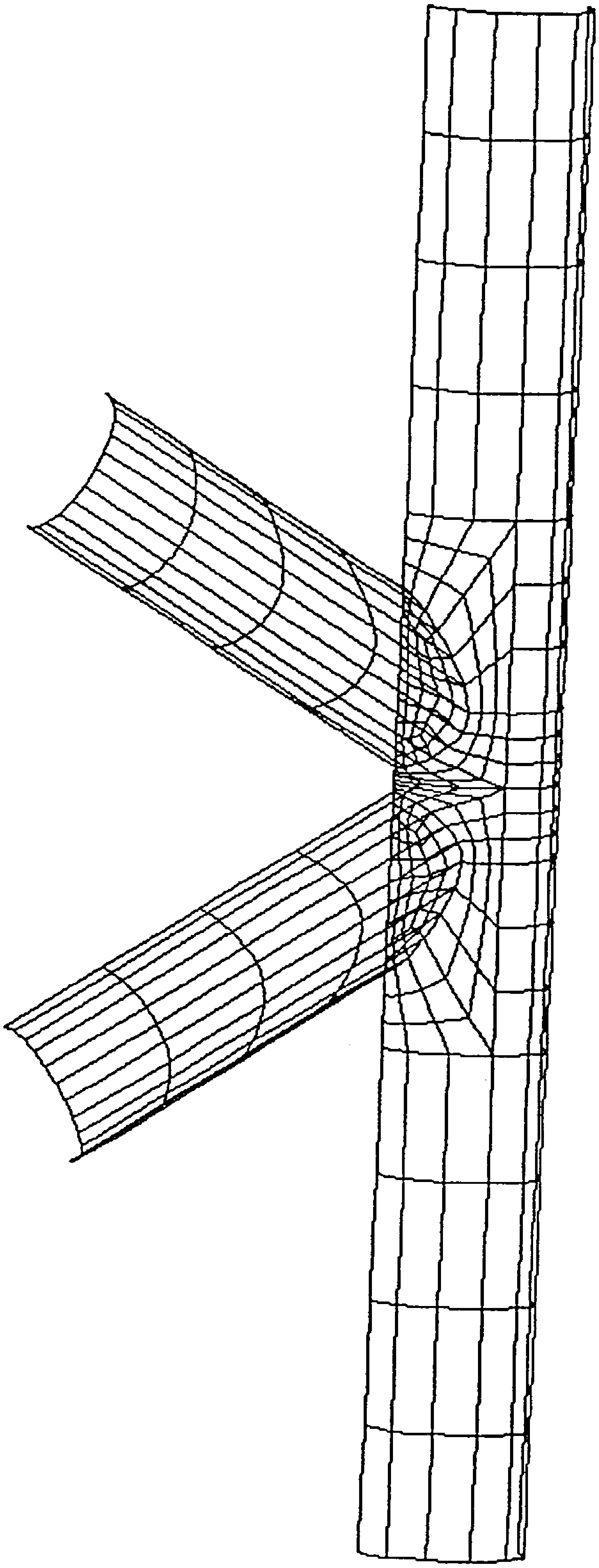

Figure A.5 : Application to blending interpolation at K joint

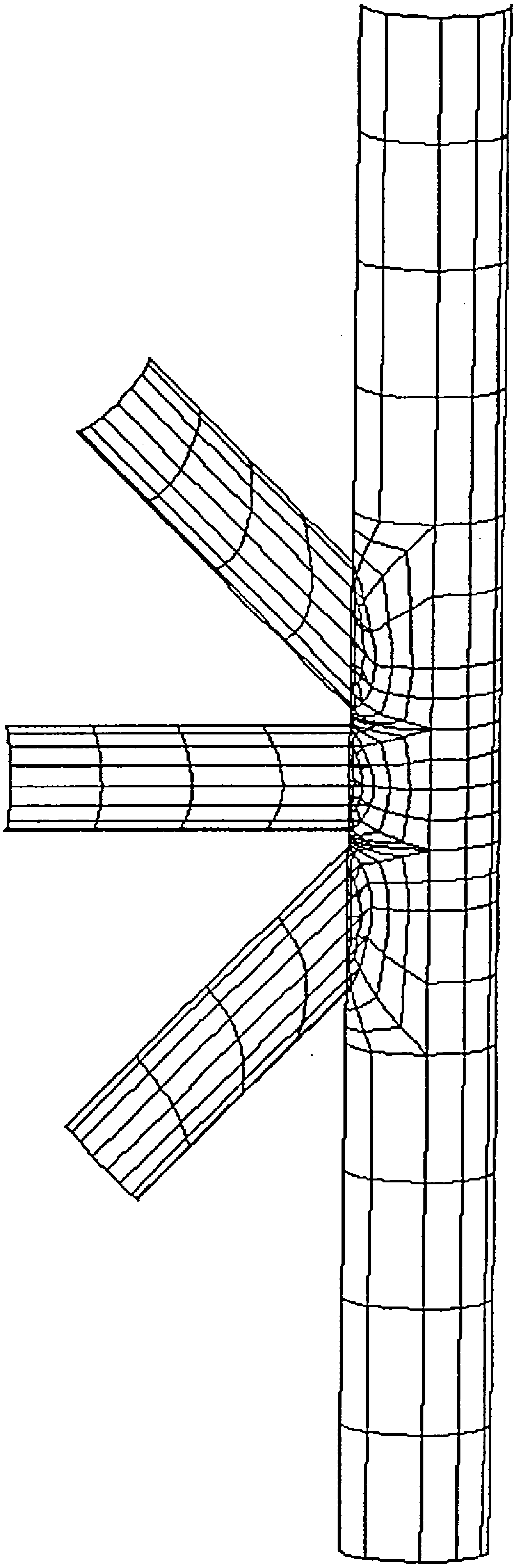

Figure A.5 : Application to blending interpolation at KT joint